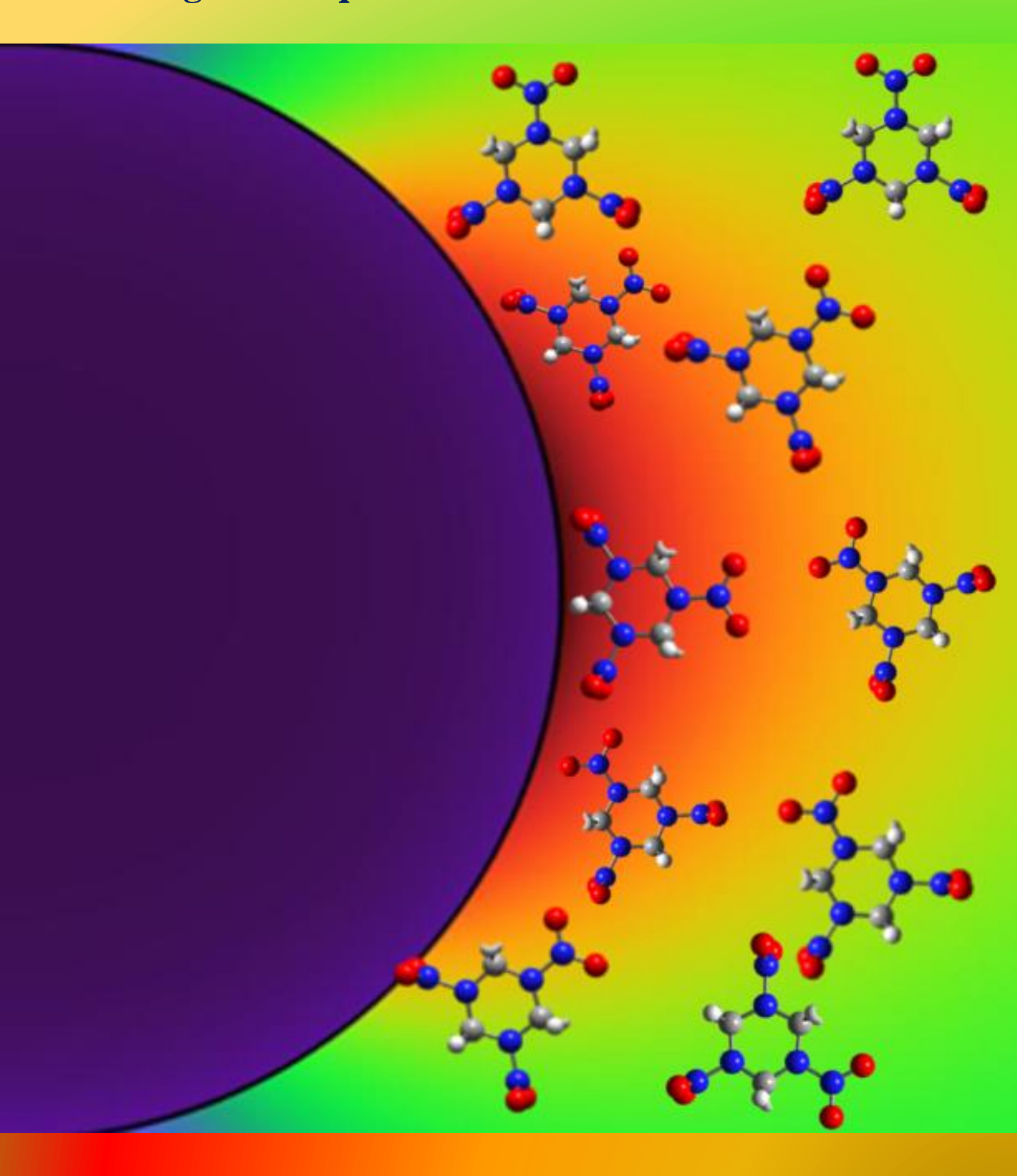
Novel, Hybrid Plasmonic Materials Aided with Machine Learning Techniques for SERS Based Trace Detection



Ph.D. Thesis

Novel, Hybrid Plasmonic Materials aided with Machine Learning Techniques for SERS based Trace Detection

Submitted to

University of Hyderabad

Towards Partial fulfilment for the degree of Doctorate in Physics

By

RESHMA BEERAM (18ACPP01)





Under the supervision of

Prof. Soma Venugopal Rao

Advanced Centre of Research in High Energy Materials (ACRHEM),

DRDO Industry Academia – Centre of Excellence (**DIA-COE**), School of Physics,

University of Hyderabad, Hyderabad 500046, Telangana, India.

July, 2023

Dr. Soma Venugopal Rao Professor

Tel.: +91-40 2313 8811 Fax: +91-40 2301 2800

E-mail: soma_venu@uohyd.ac.in

soma_ venu@yahoo.com
somavenu/@gmail.com



ACRHEM

University of Hyderabad, Prof. C. R. Rao Road, Gachibowli, Hyderabad - 500046, Telangana, India.

Certificate

This is to certify that the thesis entitled "Novel, Hybrid Plasmonic Materials aided with Machine Learning Techniques for SERS based Trace Detection," being submitted to the University of Hyderabad by Ms. Reshma Beeram (Reg. No. 18ACPP01), for the award of the degree of Doctor of Philosophy in Physics, is a record of bonafide work carried out by him under my supervision and is free of plagiarism.

The matter embodied in this report has not been submitted to any other University or Institution for the award of any degree or diploma.

Nempopallano Supervisor: 27/7/23

Prof. SOMA VENUGOPAL RAO FN A Sc., FInst P. FRSC ACRHEM

DRDO Industry Academic-Centre of Excellence (DIA-COE) University of Hyderabad Hyderabad-500046. Telangana, INDIA.

Director:

(ACRHEM)

Director ACRHEM Dean:

(School of Physics)

DEAN

School of Physics University of Hyderabad HYDERABAD - 500 046. **Declaration**

I hereby declare that the thesis titled "Novel, Hybrid Plasmonic Materials aided with

Machine Learning Techniques for SERS based Trace Detection," submitted by me

under the guidance and supervision of **Prof. Soma Venugopal Rao**, is a bonafide research

work and is free from plagiarism. I also declare that it has not been submitted previously,

in part or in full to this university or any other university or institution, for the award of

any degree or diploma. I hereby agree that my thesis can be deposited in Shodhganga/

INFLIBNET.

A report on plagiarism statistics from the university librarian is enclosed.

Hyderabad

Date: 27-07-2023

Reshma Beeram

Restona

(18ACPP01)

ii



This is to certify that the thesis entitled "Novel, Hybrid Plasmonic Materials aided with Machine Learning Techniques for SERS based Trace Detection," submitted by Reshma Beeram bearing registration number 18ACPP01 in partial fulfilment of the requirements for the award of Doctor of Philosophy in physics at ACRHEM, School of Physics, University of Hyderabad is a bonafide work carried out by him under my supervision and guidance. This thesis is free from plagiarism and has not been submitted previously in part or in full to this or any other University or Institution for the award of any degree or diploma.

Further, the student has the following publications before submission of the thesis for adjudication.

- 1) **Beeram Reshma,** Dipanjan Banerjee, Linga Murthy Narlagiri, and Venugopal Rao Soma. "Machine learning for rapid quantification of trace analyte molecules using SERS and flexible plasmonic paper substrates." *Analytical Methods* 14, no. 18 (2022): 1788-1796.
- 2) Beeram Reshma, V. S. Vendamani, and Venugopal Rao Soma. "Deep learning approach to overcome signal fluctuations in SERS for efficient On-Site trace explosives detection." Spectrochimica Acta Part A: Molecular and Biomolecular Spectroscopy 289 (2023): 122218.
- 3) **Beeram Reshma**, and Venugopal Rao Soma. "Ultra-trace detection of diverse analyte molecules using femtosecond laser structured Ag–Au alloy substrates and SERRS." *Optical Materials* 137 (2023): 113615.
- 4) Vendamani, V. S., **Reshma Beeram**, SVS Nageswara Rao, and Soma Venugopal Rao. "Protocol for designing AuNP-capped Ag dendrites as surface-enhanced Raman scattering sensors for trace molecular detection." *STAR protocols* 4, no. 1 (2023): 102068.
- 5) **Beeram Reshma,** Kameswara Rao Vepa, and Venugopal Rao Soma. "Recent trends in SERS-based plasmonic sensors for disease diagnostics, biomolecules detection, and machine learning techniques." *Biosensors* 13, no. 3 (2023): 328.
- 6) Vendamani, V. S., Reshma Beeram, SVS Nageswara Rao, A. P. Pathak, and Venugopal Rao Soma. "Trace level detection of explosives and pesticides using robust, low-cost, freestanding silver nanoparticles decorated porous silicon." *Optics Express* 29, no. 19 (2021): 30045-30061.
- 7) Vendamani, V. S., **Reshma Beeram,** M. M. Neethish, SVS Nageswara Rao, and S. Venugopal Rao. "Wafer-scale silver nanodendrites with homogeneous distribution of gold nanoparticles for biomolecules detection." *iScience* 25, no. 8 (2022): 104849.
- 8) Vendamani, V. S., **Reshma Beeram**, and Venugopal Rao Soma. "MoS₂ nanosheets decorated plasmonic silicon nanowires as SERS substrates for ultra-sensitive multiple analyte detection," *Journal of Alloys and Compounds* 959 (2023): 170573.

- 9) Narlagiri, Linga Murthy, M. S. S. Bharati, Reshma Beeram, Dipanjan Banerjee, and Venugopal Rao Soma. "Recent trends in laser-based standoff detection of hazardous molecules." TrAC, Trends in Analytical Chemistry 153 (2022): 116645.
- 10) Byram, Chandu, Sree Satya Bharati Moram, Dipanjan Banerjee, Reshma Beeram, Jagannath Rathod, and Venugopal Rao Soma. "Review of ultrafast laser ablation for sensing and photonic applications." Journal of Optics 25 (2023): 043001.

Conference Proceedings:

- Beeram Reshma, Dipanian Baneeriee, and Soma Venugopal Rao, "Sand Dune Like Copper Nanostructures Fabricated by Femtosecond Laser Ablation for Trace Explosive Detection." In Frontiers in Optics/Laser Science 2022, 16th – 20th October, Rochester, New York, USA., pp. JTu4A-27. Optica Publishing Group, 2022.
- Beeram Reshma, Dipanjan Banerjee, A. Mangababu, and Soma Venugopal Rao, "Femtosecond Laser Processed Web-like Silicon Nanostructures and Application in Surface Enhanced Raman Spectroscopy." In Conference on Lasers and Electro-Optics/Pacific Rim (CLEO-PR), Sapporo, Japan, 31st July- 5th August, p. CThP5D 04. Optica Publishing Group,
- 3) Beeram Reshma, V. S. Vendamani, and Soma Venugopal Rao. "Flexible Paper Substrate with Silver Dendrites for Trace Detection of Dye and Explosive Molecules using SERS." Workshop on Recent Advances in Photonics (WRAP), 04th - 06th March, 2022, IIT Bombay, 1-2. IEEE, 2022.
- Beeram Reshma, and Soma Venugopal Rao. "Studies on Effects of Size, Morphology and Composition in Ag, Au and Ag-Au Plasmonic Nanoparticles." International Conference on Recent Trends in Photonics' (NPS 2021), 27th February- 1st March, International School of Photonics, Cochin University of Science and Technology.
- Banerjee, Dipanjan, Reshma Beeram, and Venugopal Rao Soma. "Ultrafast Bessel Beam Induced Finger-like Silver Nanostructures for Trace-level Picric Acid Sensing." In Frontiers in Optics/Laser Science 2022, 16 - 20 October, Rochester, New York, USA., pp. LM2B-5. Optica Publishing Group, 2022.

S.No.	Course ID	Course Name	Grade	Credits
1	PY801	Research Methodology	\mathbf{B}^{+}	4
2	PY802	Advanced Quantum Mechanics	\mathbf{B}^{+}	4
3	PY803	Advanced Experimental Techniques	A	4

Supervisor: Prof. Soma Venugonal Rao. ACRHEM, School of Physics, University of Hyderabad, Hyderabad.

Prof. SOMA VENUGOPAL RAO F.N.A.Sc., Finst.P. FRSC ACRHEM **DRDO Industry Academic-Centre of Excellence** (DIA-COE)

University of Hyderabad Hyderabad-500046. Telangana, INDIA.

ACRHEM.

University of Hyderabad, Hyderabad.

Director

Dean: School of Physics. University of Hyderabad, Hyderabad.

DEAN School of Physics

University of Hyderabad HYDERABAD - 500 046

Acknowledgements

I am immensely indebted to Jawahar Navodaya Vidyalaya, and University of Hyderabad for providing me quality education. If not for these institutes, it is almost impossible for a rural girl like me to gain perspectives and be what I am today. I hold immense respect, pride, and responsibility for this privilege. I always wanted to be a scientist and a writer. I was in 3rd standard when the Columbia space disaster happened and India was paying respects to the late Kalpana Chawla. I almost felt like I found an answer to the 'what do you want to become?' question and I said loud and clear that I wanted to be an astronaut. I used to feel like one wearing my dad's helmet and raincoat. I had dreams of exploring the space and its vastness but eventually found my ground in studying tiniest events around electrons, atoms and molecules. Intrigued by the concept of duality and uncertainty principle, I was drawn to physics. I am fortunate to have teachers and parents who encouraged me to pursue my love for basic sciences right from an early age.

Beyond getting a tag, this degree has transformed me as a person in many ways. This Ph.D. period has been a huge opportunity for self-growth. The fact that I look back at my initial work and see a lot of room for improvement, or approach research problems outside my discipline is an indication of that. I vividly remember the disappointment of my first paper rejection, despite the kind reassurances from my supervisor. However, subsequent rejections became easier as I opened myself up to constructive criticism. My invaluable scientific education has trained me to question why things happen and to construct my own understanding of the world. Approaching a new skill felt intimidating before, but now I know doing little by little every day is the key to master. The ability to reason, draw logical conclusions, and troubleshoot are the skills that will accompany me regardless of my chosen path. Balancing familial responsibilities and managing my health, particularly dealing with PCOS, has taught me the importance of prioritizing my mental and physical well-being. If this degree inflates me with any sense of self-importance and grants me the opportunity to offer advice, I would strongly urge prioritizing health over work, as I have learned that everything else falls into place when you do.

I am eternally grateful for my supervisor, Prof. Soma Venugopal Rao, whose professional discipline serves as a constant inspiration. I hope to carry at least a fraction of his

dedication into my professional life. His punctuality, sense of urgency, and generosity have been instrumental in helping me complete my degree on time. Throughout the challenges I faced during these five years, he has shown unwavering kindness and provided reassurance. I would also like to express my gratitude to my DRC members, Prof. B.V.R. Tata, Prof. Prem Kiran, and Prof. Ashok Vudayagiri, for their well wishes and constructive suggestions that have improved the quality of my work. Additionally, I want to seize this opportunity to thank my teacher, Prof. Surajit Dhara, for laying the foundation of my research interest and recognizing my potential. I am indebted to my teacher, Prof. Ashok Kapoor, whose passion for teaching and connecting with his students has been a constant source of inspiration.

Regarding friends and family, I have so many people to thank for and constrained by words and space. My grandmothers, Narsamma, Laxmi and Amrutha have been role models for me for their compassion and hard work. I am certain they would have done a better job at this Ph.D. if given an opportunity. I have an extended world of friends who have been my support systems and sinks. I am fortunate to have friends like Shruti, Buntu and Kranthi who have been my pillars of strength and took pride in my failures and achievements equally. Soham's company was a catalyst to regenerate my curiosity. Selvi's kindness and Raja Sir's warmth have always made me feel home in Hyderabad. My batch mates Naveen, Sardhak, Abinash, Mainur, and Devaparna have always offered me comfort and comradeship through the tough times in Ph.D.

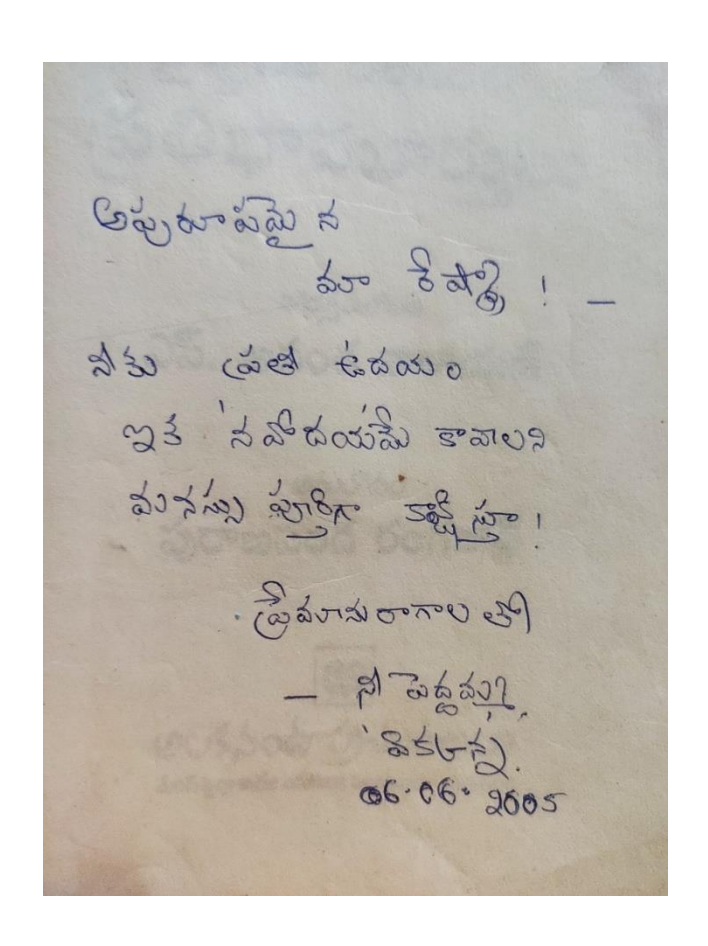
I thank the Directors (past and present) of ACRHEM, Deans (past and present) of the School of Physics for addressing my concerns on time. My lab mates Dr. Bharathi, Dr. Lingamurthy, Dipanjan and Jaganath are always there when I needed their support. It was because of Dr. Vendamani's expertise on Si materials my life was easier, saving me valuable time, and effort. All the technicians who worked with FESEM, TEM, and UV-Visible spectrometer were always kind and helped me to finish my experiments faster. I am also thankful to ACRHEM office and cleaning staff for taking care of the lab and administration. I am grateful to DRDO for fully funding my PhD period without which this would not have been possible.

My thesis is incomplete if I do not thank my wonderful parents, Latha and Ramulu. With no formal education it was difficult for them to understand research, Ph.D., and publications. Nevertheless, they have celebrated all my achievements and have been there

throughout my failures. It was not easy for them to keep away from relatives and neighbours who always questioned my unconventional life regarding career, marriage and choices. Yet, they have always taken pride in my choices and shielded me from relatives and peers. My younger brother Rahul has showered his support whenever I needed him and shared responsibilities to ease me. Our beautiful dogs, and farm has been a reprise for me whenever I needed a break. My god mother, Tanuja, who is no more, would have been immensely proud of the woman I have become, and her blessings continue to guide me.

Last but not the least, I am thankful to the campus trees, rocks, grasses, and birds which were just a walk away to make my rough days brighter. I am grateful for their existence and sincerely hope they will continue to thrive for generations to come.

To,My Mother, Latha, and god mother, Tanuja



List of Figures

- **Figure 1.1:** State of the art in SERS in terms of substrate fabrication, applications and implementation in machine learning techniques.
- Figure 1.2: Schematic of classification of different explosive detection techniques.
- **Figure 1.3:** Schematic of a) LSPR oscillations in metal nanoparticles in the presence of an electromagnetic field, b) Spring-mass model of a molecule with two atoms bound by a spring analogous to the chemical bond.
- **Figure 1.4:** Real and imaginary parts of dielectric functions of gold and silver taken from Johnson and Christy's work [56].
- **Figure 1.5:** Illustration of chemical enhancement in SERS through charge transfer mechanism between analyte molecule and the metal nanostructure a) case of resonant excitation where laser energy is close to the electronic transitions of the analyte molecule. b, c) Photo driven charge transfer mechanisms between the Fermi and HOMO, LUMO energy levels [81].
- **Figure 1.6:** Illustration of a probe molecule at a SERS hotspot and associated electromagnetic and chemical enhancement contribution to signal enhancement in SERS.
- **Figure 1.7:** Flowchart for simulations performed in COMSOL Multiphysics.
- **Figure 1.8:** Plasmonic region of interest for Ag, Au and Cu where there are extensively used in SERS. Figure adapted from the reference [86].
- **Figure 1.9:** Extinction spectra of a) c) Ag-Au alloy nanoparticles of size 10nm with varying compositions. b) Inset shows the LSPR of the alloy nanoparticles as a function of the Au composition. c) Ag@Au core-shell nanoparticles with varying Au thickness. b) Au@Ag core-shell nanoparticles with varying Ag thickness.
- **Figure 1.10:** Calculated extinction (Q_{Ext}), absorption (Q_{Abs}), and scattering (Q_{Scat}) spectra, surrounded by air, of A) Au for a) 20 nm b) 40 nm c) 60 nm and d) extension spectra for all sizes as indicated in the figure. B) Ag nanospheres of size a) 20 nm b) 40 nm c) 60 nm and d) extinction spectra for all sizes.
- **Figure 1.11:** a) LSPR resonance as a function of particle size for Ag and Au nanoparticles, b) Local field intensity as a function of distance from the nanoparticle for Ag sphere.
- **Figure 1.12:** A) Relative electric field along the electric field direction as a function of distance from the centre of the dimer. B) Near field intensity pattern for the dimer with distance a) 0.5 nm b) 2 nm c) 4 nm and d) 6 nm. C) Relative electric field as a function of

- gap between nanoparticles of Ag dimer configuration. Squares the experimental data points while the solid line is a polynomial fit.
- **Figure 1.13:** Near field enhancement around anisotropic NSs a) Ag Cube b) Ag star c) Ag triangle d) Ag Dendrites e) Ag Dendrites with Au. nanoparticles
- **Figure 1.14**: Schematic of classification of different machine learning algorithms.
- **Figure 1.15:** DFT optimized structures of different molecules studied in this thesis.
- **Figure 1.16:** Schematic of different challenges in SERS and different chapters presented in the thesis addressing the challenges.
- **Figure 2.1:** Illustration of top-down and bottom-up methods for the preparation of plasmonic nanostructures.
- **Figure 2.2.** COMSOL simulation of pulsed laser ablation of alumina with a pulse duration of 10 µs and repetition rate of 20 Hz showing a series of heating and cooling of the surface
- **Figure 2.3:** Time scale of different events that occur during laser ablation in liquids for a nanosecond laser. Figure adopted from reference [28].
- **Figure 2.4:** Illustration of formation of anisotropic silver dendrites through electroless etching of Si in the presence of AgNO₃ and HF
- **Figure 2.5**: Electric Field line for a) conductor b) a conductor in the presence of an electric field.
- **Figure 2.6:** Schematic of mechanism for drying of nanoparticles on the surface of hydrophobic filter paper.
- **Figure 2.7:** Absorption and emission spectra of Ti-Sa laser.
- **Figure 2.8:** Illustration of mode locking through saturable absorber in Chameleon a) when the slit is inactive and b) when the slit is active.
- **Figure 2.9:** Beam path for the Coherent femtosecond laser amplifier where green light indication the pump (Evolution), red indicates seed from Vitesse and yellow for the pulse within the regenerative amplifier. The coloured line indicated chirped pulse. The labels for optical components are highlighted in the figure.
- **Figure 2.10:** Schematic of optical path in the a) Stretcher system and b) Compressor system of the amplifier. Images have been reproduced from the manual of Coherent [63].
- **Figure 2.11:** Schematic of experimental setup inside an autocorrelator used to measure femtosecond laser pulses. Figure reproduced from the reference [64].

- **Figure 2.12:** Femtosecond amplifier system pulse width measurement using intensity autocorrelation technique.
- **Figure 2.13:** Experimental setup for laser ablation of Si using femtosecond laser oscillator system.
- Figure 2.14: Schematic of femtosecond laser ablation used in the thesis work for different conditions a) of Ag-Au target using different angles of incidence, b) Irradiation of MoS₂ powder using magnetic stirrer, and c) Au in water.
- **Figure 2.15:** a) Optical alignment inside the Horiba LabRam Raman Spectrometer (Image reproduced from the user manual of the instrument [67], and b) Simplified schematic of the optical path.
- **Figure 2.16:** Schematic to illustrate the working of a) FESEM and b) TEM for imaging.
- **Figure 3.1**: Schematic of laser ablation by a) nanosecond pulses, b) femtosecond pulses and SEM images of laser ablated steel foil with c) nanosecond and d) femtosecond laser of same wavelength. Figure reproduced from [2].
- **Figure 3.2:** FESEM images of laser ablated Si for different scan speeds as indicated in the figure. Left side images are in low-resolution while the right ones are in high-resolution. **Figure 3.3:** Summary of results on studying the effects of scan speed on the density and
- **Figure 3.3:** Summary of results on studying the effects of scan speed on the density and size of the Si nanoparticles comprising the web-like nanostructures.
- **Figure 3.4:** FESEM images of femtosecond laser ablated Si nanostructures for different laser fluencies as indicated in the image.
- **Figure 3.5:** CCD images of emissions during fs laser abaltion of Ti with nearly same fluence but different spot sizes of a) 1×10^{-3} cm² and b) 2.4×10^{-4} cm². Figure reproduced from the reference [14].
- **Figure 3.6:** Summary of effects of fluence on laser ablation of Si showing increase in aggregation with increasing fluence.
- **Figure 3.7:** Schematic of mechanism of formation of nanochains during high repetition rate fs ablation of Si.
- **Figure 3.8:** a, b) FESEM imaging of web-like Si nanostructures as SERS substrate FESEM micrographs of LS-Si used for SERS studies at different magnifications and c) EDX spectrum with quantitative results for the gold coated Si used for SERS.
- **Figure 3.9:** a) SERS spectra of MB with 785 nm excitation, 10s acquisition time and 20 mW laser power a) on LS-Si and plain Au coated Si for 100 μ M concentration b) SERS spectra of MB on LS-Si for different concentrations. The spectrum of 1 μ M concentration

was multiplied by 10 for better visibility c) Intensity variation of 1621 cm⁻¹ peak of MB at 20 random spots on the substrate.

- **Figure 3.10:** FESEM images of laser ablated Ag-Au nanostructures with debris for different angles of incidence a) 00, b)100, c) 200 and d) 300 as indicated in the figure. The images indicate that the number of nanoparticles ablated is different for different angles of incidence.
- **Figure 3.11:** FESEM images of laser ablated Ag-Au nanostructures without debris for different angles of incidence a) 0^0 , b) 10^0 , c) 20^0 and d) 30^0 as indicated in the figure. The images indicate the formation of ripples on Ag-Au surface for all angles of incidence but with varying periodicity. e) and f) Represent EDX data showing the presence of both Ag and Au.
- **Figure 3.12:** a) UV-Visible absorption spectrum of different probe molecules used in SERS studies for this work. The dotted line indicates the laser excitation wavelengths. b) Scatter plot of the absorption peak and excitation wavelength for each probe molecule where $|\Delta\lambda|$ is indicating the absolute difference between the two.
- **Figure 3.13:** UV-Visible reflectance data of Ag-Au sample used in this study indicating plasmonics resonance in the visible range.
- **Figure 3.14:** a) SERRS spectra of femtosecond laser ablated Ag-Au samples for different angles of incidence for 1 μM of R6G with 532 nm laser excitation. Each spectrum is an average of 10 spectra collected at different spots on each sample. b) Bar graph for 1650 cm⁻¹ peak intensity of R6G indicating better performance of D-S10 sample.
- **Figure 3.15:** SERRS mapping studies performed in an area of $100 \, \mu m^2$ with 5 μ M of R6G for D-S10 and ND-S10 substrate with 612 cm⁻¹ peak as reference. a,e) SERRS false color image generated for the peak intensity for a) ND-S10, e) D-S10 substrate. b and f represent corresponding spectra while c,g) show the contour maps of the peak intensity distribution. d,h) Scatterplot of peak intensity for d) ND-S10 and h) D-S10 sample with statistical parameters summarized in the figure. The line in the graphs indicate the mean value.
- **Figure 3.16:** SERRS mapping studies performed in an area of $100 \ \mu m^2$ with $10 \ pM$ of R6G on ND-S10 substrate with $612 \ cm^{-1}$ peak as reference. a) SERRS false color image generated for the peak intensity. b) corresponding spectra while c) show the contour map of the peak intensity distribution. d) Scatterplot of peak intensity for d) with statistical parameters summarized in the figure. The line in the graphs indicate the mean value.
- **Figure 3.17:** a) SERRS spectra of R6G for different concentrations collected on ND-S10 substrate with 532 nm laser excitation and 1mW laser power. The spectrum at 10 fM is collected with D-S10 sample and is multiplied by 10 for better readability. b) The full spectrum of the 10fM of R6G presented for readability. c) SERRS intensity and concentration relation for 1650 cm⁻¹ peak intensity of R6G fitted to a polynomial with an

- R2 value of 0.98. d) Reproducibility of the signal at 10 random spots on the substrate for ND-S10 (black) and D-S10 (red) samples with 5 μM of R6G.
- **Figure 3.18**: a) SERRS spectra of CV for different concentrations collected on ND-S10 substrate with 633 nm laser excitation and 1mW laser power. The spectrum at 100 fM is collected with D-S10 sample and is multiplied by 10 for better readability. b) SERRS intensity and concentration relation for 1618 cm⁻¹ peak intensity of CV fitted to a polynomial with an R^2 value of 0.98. c) Reproducibility of the signal at 10 random spots on the substrate for ND-S10 (black) and D-S10 (red) samples with 1 μ M of CV.
- **Figure 3.19:** SERRS spectra of for different concentrations for a) PA studied with 325 nm laser excitation and 1.3 mW laser power on ND-S10 substrate. The 100 nM spectrum for PA is multiplied by 5 to increase visibility. c) Reproducibility of 1343 cm⁻¹ of PA collected at 10 random spots on the same with RSDs of 16%.
- **Figure 3.20:** SERRS spectra of for different concentrations for a) Cysteine studied with 325 nm laser excitation and 1.3 mW laser power on ND-S10 substrate. b) Intensity and concentration fit c) Reproducibility of 2944 cm⁻¹ peak of Cysteine collected at 10 random spots on the same with RSDs of 18%.
- **Figure 3.21:** FESEM images of laser structured Ag with different energies as indicated in the figure for different magnifications.
- **Figure 3.22:** FESEM images of laser structured Ag that was used as SERS substrate for different magnifications as indicated in the figure. The inset image shows a tree bark with ripples resembling the nano-ripples on Ag. Inset show EDX spectrum with Ag peak. Tetryl, RDX and cytosine, respectively.
- **Figure 3.23:** SERS spectra of a) Tetryl, b) RDX and, c) Cytosine for different concentrations collected using portable Raman spectrometer with laser power of 10mW and acquisition time of 10s. d) Intensity and concentration relation for prominent peaks of the three analyte molecules.
- **Figure 3.24**: a) SERS mapping image of Tetryl of concentration $5\mu M$ generated using the intensity of 1358 cm^{-1} peak of Tetryl in an area of $65 \mu m^2$. b) Corresponding SERS spectra of the mapping region and, c) Intensity distribution of the mapping area.
- **Figure 3.25:** a) SERS spectra of different E. coli species as indicated in the image, b) PCA for classification and identification of the species using SERS data
- **Figure 3.26:** a)-c) FESEM micrographs of laser ablated Cu nanostructures at different magnifications indicate the presence of sand dune-like laser-induced periodic structures. d) Quantitative results of the EDX spectrum of a selected area on laser structured Cu.
- **Figure 3.27**: a) SERS spectra of Tetryl for a concentration at 100 μ M on laser structured Cu (LS-Cu) (black line, top) and plain Cu (red line, bottom) (multiplied by 3 to enhance

- the readability) b) Intensity of the 1358 cm⁻¹ peak collected at 10 random spots on the substrate demonstrating an RSD of 5%. c) SERS spectra of Tetryl, MB and AN for concentrations 10 μ M, 5 μ M and 50 μ M, respectively, collected with portable Raman spectrometer with 785 nm laser excitation and 30 mW laser power.
- **Figure 4.1:** Results of COMSOL simulation showing a) Geometry of Ag dendrites constructed b) Near field simulation of the Ag dendrites showing enhancement at the tips. c) Geometry of Au@Ag nano-dendrites constructed. d) Near field simulation of Au@Ag nano-dendrites clearly showing additional enhancement relative to the plain Ag dendrites. Image taken from [26].
- **Figure 4.2:** Optical images of the bare three-inch Si wafer (left), AgNDs on Si wafer (middle), and AuNPs@AgNDs on Si wafer (right). The AuNPs were decorated in ~3 hours (i.e., AuNPs@AgNDs-3).
- **Figure 4.3:** FESEM images of (a) as prepared AgNDs and AuNPs decorated AgNDs at various molar concentrations of Au seed solutions at b) 0.05 mM, c) 0.1 mM, d) 0.5 mM, e) 1 mM, f) 1.5 mM (g) 3 mM, h) 5 mM, i) 7 mM at room temperature.
- **Figure 4.4**: SEM images displaying morphology of the AgNDs decorated with 1 mM AuNPs at various times of deposition, a) 30 minutes (i.e., AuNPs@AgNDs-0.5), b) 1 hour (i.e., AuNPs@AgNDs-1), c) 2 hours (i.e., AuNPs@AgNDs-2) and, d) 3 hours (i.e., AuNPs@AgNDs-3) (highlighted yellow-coloured circles represent the AuNPs decoration on AgNDs at a few places for clarity).
- **Figure 4.5:** SEM images of the AuNPs (on AgNDs) decorated at 3 hours' reaction time (AuNPs deposited at 1 mM concentration) (i.e., AuNPs@AgNDs-3) viewed at different magnifications.
- **Figure 4.6:** EDX mapping presents the elemental composition of the AuNPs@AgNDs-3 sample, which depicts a high concentration of Ag, Au, and Si, and a lower concentration of O as expected.
- **Figure 4.7:** Reflectance spectra of AgNDs and AuNPs decorated AgNDs at various deposition times (inset shows the magnified SPR band 1 in 400-500 nm).
- **Figure 4.8:** SERS spectra of CV (dye) on AuNPs@AgNDs-3 at (a) (i) 10 μ M (ii) 5 μ M (iii) 1 μ M, and (iv)100 nM (v) 10 nM and (vi) 1 nM concentrations and (b) corresponding linear fit of log (intensity) versus log (lower concentration) of the 918 cm⁻¹ Raman peak.
- **Figure 4.9:** SERS spectra of adenine (DNA bases) on AuNPs@AgNDs-3 at (a) (i) 1 mM (ii) 100 μ M (iii) 50 μ M, and (iv)10 μ M, and (v) 100 nM concentrations, (b) corresponding linear fit of log (intensity) Versus log (lower concentration) of the 722 cm⁻¹ Raman peak, (c) Cytosine (i) 1 mM (ii) 100 μ M (iii) 50 μ M, and (iv) 10 μ M M, (v) 100 nM, and (vi) 10 nM concentrations, and (d) corresponding linear fit of log (intensity) Versus log (lower concentration) of the 792 cm⁻¹ Raman peak.

- **Figure 4.10:** SERS spectra of penicillin G on AuNPs@AgNDs-3 at (a) (i) 1 mM (ii) 100 μM (iii) 50 μM, and (iv) 10 μM M, (v) 100 nM, and (vi) 10 nM concentrations, and (b) corresponding linear fit of log (intensity) vs log (lower concentration) of the 985 cm⁻¹ Raman peak (c) Kanamycin (i) 1 mM (ii) 100 μM (iii) 50 μM, and (iv)10 μM, and (v) 100 nM concentrations, and (d) corresponding linear fit of log (intensity) vs log (lower concentration) of the 975 cm⁻¹ peak, (e) Ampicillin (i) 1mM (ii) 100 μM (iii) 50 μM, and (iv)10 μM, (v) 100 nM, and (vi) 10 nM concentrations, and (f) corresponding linear fit of log (intensity) versus log (lower concentration) of the 988 cm⁻¹ peak.
- **Figure 4.11:** SERS spectra of AN (explosive) on AuNPs@AgNDs-3 at (a) (i) 50 μ M (ii) 10 μ M (iii) 5 μ M, and (iv) 1 μ M, and (v) 100 nM concentrations, and (b) corresponding linear fit of log (intensity) versus log (lower concentration) of the 1045 cm⁻¹ Raman peak.
- **Figure 4.12.** SERS spectra of thiram (pesticide) on AuNPs@AgNDs-3 at (a) (i) 10 μ M, (ii) 5 μ M, (iii) 300 nM, (iv)100 nM, and (v) 10 nM concentrations, and (b) corresponding linear fit of log (intensity) versus log (lower concentration) of the 1384 cm⁻¹ Raman peak.
- **Figure 4.13:** Spectral reproducibility of (a) CV at 5 μ M, and (b) cytosine at 50 μ M concentrations, (c) corresponding histogram with RSD values, (d) Stability estimation of AuNPs@AgNDs-3 substrate at 5 μ M CV over 120 days.
- **Figure 4.14:** (a) Selected large-area Raman mapping $(45 \times 45 \ \mu m^2)$ of SERS substrate with 532 nm laser excitation, 10X microscope objective, 25 mW laser power with CV as probe molecule for 918 cm⁻¹ Raman mode with 3s acquisition time, averaged over 3 spectra (b) Small area $(20\times20 \ \mu m^2)$ SERS mapping of CV (c) corresponding representative spectra of the mapping region, (d) Selected large-area Raman mapping $(100\times100 \ \mu m^2)$ -cytosine as probe molecule for the 792 cm⁻¹ Raman mode [with similar acquisition parameters mentioned in (a)] (e) Small area $(20\times20 \ \mu m^2)$ SERS mapping of 10 μM cytosine (f) Corresponding representative spectra of the mapping region [presented in (e)]. The background (grey color) in (a) and (d) depicts the optical microscope images of the substrates.
- **Figure 4.15:** Schematic of application of MoS2 decorated plasmonic SiNWs for SERS based sensing.
- **Figure 4.16:** FESEM images of laser-irradiated MoS2 in different liquid environments (a) Water, (b) Ethanol, (c) Methanol, and (d) Corresponding absorption spectra.
- **Figure 4.17:** FESEM image of (a) AgNPs decorated SiNWs, (b) Ag-AuNPs decorated SiNWs, (c) MoS₂ coated Ag-AuNPs/SiNWs, (d-e) higher magnifications of (b and c) images respectively, and (f) EDS spectrum of figure (c).
- **Figure 4.18:** Bright-field images of (a) AgNPs distributed on the walls of SiNWs, (b) Ag-AuNPs distributed on the walls of SiNWs (c) SAED pattern of figure (b), (d) Dark-filed

- image of figure (b), (e) HRTEM image and the red rectangular line directs the area of selection for IFFT, and (f) IFFT data obtained from a selected area of figure (e).
- **Figure 4.19:** (a) SERS signal sensitivities of MG detected on various SERS-active substrates indicating signal enhancement at each stage (the spectra are shifted for clarity) (b) Bar-chart showing the quantitative CM and EM enhancements of MG detection [data has been taken from Fig. 4.19 a)].
- **Figure 4.20:** (a) SERS spectra of MG at various level of concentrations as indicated in the image, and (b) linear plot of log(concentration) vs log(intensity) of the peak 1617 cm⁻¹.
- **Figure 4.21:** (a) SERS spectra of melamine at various concentrations (spectra are shifted for clarity) (b) Linear plot of log (intensity) versus log (concentration) of the peak at 677 cm⁻¹ (c) SERS spectra of naphthalene at various concentrations as indicated in the Fig. (spectra are shifted for clarity) and (d) Linear plot of log (intensity) versus log (concentration) of the peak at 1386 cm⁻¹.
- **Figure 4.22:** (a) SERS spectra of BSA at various concentrations (b) Linear plot of log (concentration) versus log (intensity) of the peak at 998 cm⁻¹ (c) SERS spectra of adenine at various concentrations (d) Linear plot of log (intensity) versus log (concentration) of the peak at 722 cm⁻¹ (e) SERS spectra of cysteine at various concentrations and (f) Linear plot of log (intensity) versus log (concentration) of the peak 679 cm⁻¹.
- **Figure 4.23:** Whole organism SERS spectrum of B1121 strained E. coli bacteria detected on hybrid MoS2/Ag-AuNPs/SiNWs substrate.
- **Figure 4.24:** (a) SERS spectra of tetryl at various concentrations (spectra are shifted for clarity) and (b) Linear plot of log (intensity) versus log (concentration) of the Raman peak at 1362 cm⁻¹.
- **Figure 4.25:** a) SERS mapping area $(50 \times 50 \, \mu\text{m}2)$ of 5 μ M Tetryl with false colors for the peak intensity of 1362 cm-1 mode b) Scatterplot for the peak intensity of ~ 500 spectra collected in mapping with RSD of 6%. The line indicates the mean value c) SERS spectra of the mapping region. d) The corresponding contour plot for the spectra depicted no significant peak shift at all collection points.
- **Figure 4.26:** (a) SERS durability of melamine (100 μ M) as a function of the aging interval, and (b) Intensity variations as a function of aging time.
- **Figure 4.27:** Schematic of HFP in combination with machine learning for rapid quantification of trace analyte molecules.
- **Figure 4.28:** a) and b) TEM images of Au nanoparticles at different magnifications. c) and d) HRTEM images with different magnifications. Inset in a) and b) depicts the particle size distribution fitted to a Gaussian distribution and inset in d) shows the SAED pattern.

- **Figure 4.29:** a), b), c) FESEM micrographs of HFP at different magnifications. Inset in a) shows contact angle measurement and b) shows a drop of CV on HFP and normal FP.
- **Figure 4.30:** UV-Visible absorption spectrum of laser ablated Au NPs. Inset shows near field simulation of randomly spaced Au NPs of different sizes with 785 nm excitation using COMSOL.
- **Figure 4.31:** SERS spectra on HFP for different concentrations of a) CV, b) PA collected with a portable Raman spectrometer with laser excitation 785 nm and 10 mW laser power. Figures represent average and standard deviation of 100 spectra collected at random sites on the substrate for each concentration. The prominent peaks for each analyte molecule are highlighted in yellow colour. 'Arb.u.' means arbitrary units.
- **Figure 4.32:** Individual SERS spectra of each concentration for the two molecules studied in the work.
- **Figure 4.33:** Cumulative variance as a function of number of Principal components for a) CV, b) PA.
- **Figure 4.34:** Principal component analysis for a) CV and b) PA for different concentrations as indicated in the labels.
- **Figure 4.35:** Processing steps for the fabrication of AgNPs@FS-pSi layer by anodicetching followed by electro-polishing.
- **Figure 4.36:** Photographs of FS-pSi (a) floating on water (b) freely held by a tweezer, and (c) mounted on a flexible scotch tape.
- **Figure 4.37:** (a) The morphology of as-anodized FS-pSi layer and (b) the histogram of the pore size distribution (solid line indicates the Gaussian fit).
- **Figure 4.38:** AgNPs decoration of FS-pSi at various deposition times (a) 30 min, (b) 60 min, (c) 4 hours, and (d) EDS spectrum of AgNPs@FSpSi-60min sample. [Inset of the figure (d) illustrates the distribution of AgNPs over the sample surface of FSpSi-60min [shown in (b)] and the solid line is a Gaussian fit].
- **Figure 4.39:** The SERS spectra of MB molecules on AgNPs@FS-60min substrate at a concentration of (a)-(i) 100 μ M (ii) 50 μ M (iii) 10 μ M (iv) 5 μ M (v) 1 μ M and (vi) 100 nM concentration (b) SERS spectra of MB (5 μ M) at various AgNPs deposition time on FS-pSi. Spectra in (a) and (b) are stacked in Y-axis to avoid ambiguity in the data.
- **Figure 4.40:** The SERS spectra of PA, an explosive molecule, on AgNPs@FSpSi-60min substrate at concentration of (a)-(i) 100 μ M, (ii) 50 μ M, (iii) 30 μ M, (iv) 10 μ M, and (v) 5 μ M concentrations, (b) SERS spectra of PA (30 μ M) at various AgNPs deposition time on FSpSi, and (c) corresponding linear calibration [log (SERS intensity) versus log

- (concentration)] of the different Raman modes observed at 832 cm^{-1} , 1177 cm^{-1} , and 1346 cm^{-1} .
- **Figure 4.41:** (a) Reproducibility of the SERS spectra of 10 μM MB molecules detected at 10 different spots on AgNPs@FSpSi-60min, and (b) the corresponding standard analysis with RSD values.
- **Figure 4.42:** (a) Reproducibility of the SERS spectra of 50 μM PA molecules detected at 10 different spots on AgNDs@FSpSi-60min, and (b) the corresponding histogram with RSD values.
- **Figure 4.43:** The SERS spectra of AN molecule on AgNPs@FSpSi-60min substrate at (a)-(i) 100 μM, (ii) 50 μM, (iii) 10 μM, (iv) 5 μM, and (v) 1 μM concentrations, (b) The SERS spectra of AN (50 μM) at various AgNPs deposition time on FS-pSi, and (c) corresponding linear calibration [log (SERS intensity) versus log (concentration)] of the Raman modes at 711 cm⁻¹, and 1042 cm⁻¹ (d) Reproducibility of AN (50 μM) on AgNDs@FSpSi-60min substrate and inset shows the corresponding standard deviation.
- **Figure 4.44:** The SERS spectra of thiram (pesticide) on AgNPs@FSpSi-60min at (a) (i) $10 \,\mu\text{M}$ (ii) $5 \,\mu\text{M}$ (iii) $1 \,\mu\text{M}$ and (iv) $100 \,\text{nM}$ concentrations (b) SERS spectra of thiram (10 $\,\mu\text{M}$) at various AgNPs deposition time on FSpSi and (c) corresponding linear relationship of log (SERS intensity) versus log (concentration).
- **Figure 4.45:** (a) Linear dependence of log (SERS intensity) versus log (analyte concentration) for the principal modes of MB molecules, (b) The stability estimation of AgNPs@FSpSi-60min substrate with 50 μ M concentration of MB over a period of 90 days.
- **Figure 4.46:** The SERS intensity versus analyte concentration for (a) MB 1626 cm⁻¹ (b) PA -1346 cm⁻¹ (c) AN 1042 cm⁻¹ (d) thiram-1385 cm⁻¹, and (e)-(h) Linear dependence of the log SERS intensities verses lower molecular concentrations.
- **Figure 5.1:** Schematic of flow of training mechanism in NNs through a series of mathematical operations classified as forward and backward propagation.
- **Figure 5.2:** a) Representation of a single neuron with input and output (Image taken from Wikipedia), b) A single node of a NN with input, activation function and an output.
- **Figure 5.3:** a) Sketch of cerebral cortex showing scheme of layers of interconnected neurons. Image taken from Wikipedia (https://en.wikipedia.org/wiki/Cerebral_cortex). b) Architecture of NNAS used in this study with two hidden layers, input and output layers.
- **Figure 5.4:** Schematic of distribution of probe molecules on a SERS substrate with hotspots and associated signal fluctuations.

- **Figure 5.5:** Different scenarios of SERS spectra of picric acid measured on same substrate of Au@Ag nanodendrites under experimental indication selective enhancement/quenching of peaks, effects of oxidation and photo bleaching.
- **Figure 5.6:** Graphical representation of the goal of NNAS model to bridge the gap between lab and field performance removing the reliance of expert by automating the identification of representative SERS spectra of trace explosives.
- **Figure 5.7:** End to end streamlined workflow for the NNAS model starting from data collection to model evaluation.
- **Figure 5.8:** Schematic of preparation of AuNPs decorated on AgNDs (AuNPs@AgNDs) and their application for SERS.
- **Figure 5.9:** a) Flowchart showing data analysis and splitting for training, evaluation and out of sample evaluation, b) Code snippet of the NNAS model showing implementation of various techniques discussed in the section.
- **Figure 5.10:** a) A representative spectrum of CV with prominent peaks used for calculating SNR labelled in blue. b) Swarm plot showing distribution of the prominent peaks highlighted in blue. c) Input SERS data for CV that is used for modelling.
- **Figure 5.11:** a) A representative spectrum of tetryl with prominent peaks used for calculating SNR labelled in grey. b) Swarm plot showing distribution of the prominent peaks highlighted in grey. c) Input SERS data for tetryl that is used for modelling.
- **Figure 5.12:** a) A representative spectrum of picric acid with prominent peaks used for calculating SNR labelled in pink. b) Swarm plot showing distribution of the prominent peaks highlighted in blue. c) Input SERS data for picric acid that is used for modelling.
- **Figure 5.13:** Learning curves for training and validation data of NNAS model with loss as a parameter for a) CV, b) Tetryl, and c) Picric Acid.
- **Figure 5.14:** Learning for different random states resulting similar accuracy indicating that the accuracy of the model is not an event of chance.
- **Figure 5.15:** Spatial representation of a) actual and b) NNAS predicted validation SERS data set for CV with green representing RS and red representing NRS, c) Confusion matrix of the validation data set indicating an accuracy of 0.983, d) Confusion matrix of 284 out of sample SERS spectra for a different concentration than the testing data set (50 nM) depicting an accuracy of 0.982.
- **Figure 5.16:** Spatial representation of a) actual and b) NNAS predicted validation SERS data set for Tetryl with blue representing RS and green representing NRS, c) Confusion matrix of the validation data set indicating an accuracy of 0.984, d) Confusion matrix of

777 out of sample SERS spectra for a different concentration than the testing data set (50 nM) depicting an accuracy of 0.981.

Figure 5.17: Spatial representation of a) actual and b) NNAS predicted validation SERS data set for picric acid with yellow representing RS and dark blue representing NRS, c) Confusion matrix of the validation data set indicating an accuracy of 0.993, d) Confusion matrix of 1026 out of sample SERS spectra for a different concentration than the testing data set (100 nM) depicting an accuracy of 0.985

Figure 5.18: Spatial mapping of representative and non-representative spectra for actual, predicted data for a, b) CV, c, d) Tetryl, e,f) Picric Acid

Figure 5.19: Confusion matrix for the classification based on SVM for a) CV, b) Tetryl and c) Picric Acid indication accuracy of 0.889, 0.874, and 0.887, respectively.

Figure 6.1: Summary of different contributions made in SERS in this thesis work.

Figure 6.2: Images of drop of Au nanoparticles and CuSO₄ on HFP taken using home built contact angle setup.

List of Tables

- **Table 2.1:** Summary of materials and different characterization techniques used in this study.
- **Table 3.1:** Summary of analytes and SERS parameters for this study.
- Table 4.1: Summary of analytes detected and SERS parameter for AuNPs@AgNDs.
- **Table 4.2:** Summary of regression metrics for SVR
- **Table 4.3:** Summary of analytes detected and the SERS parameter for studies on pSi.
- **Table 5.1:** Summary of experimental parameters that were systematically varied during data collection.
- **Table 5.2:** Comparison of performance of SVM and NNAS model.
- **Table 6.1**: Summary of all the substrates, analyte molecules and highlights of the study.
- **Table C1:** Summary of scale of parameters.

Table of Contents

1) Introduction and Thesis Motivation	1
1.1. Introduction	2
1.2. Trace Detection of Explosives	5
1.3. Localized Surface Plasmon Resonance	9
1.3.1. Optical Properties of Coinage Metals	12
1.4. SERS Enhancement Mechanism	13
1.4.1. Electromagnetic Enhancement	16
1.4.2. Chemical Enhancement	18
1.4.3. Calculating Enhancement Factor	19
1.5. Factors that influence SERS	21
1.5.1. Effects of Material	22
1.5.2. Effects of Size of Nanoparticles	23
1.5.3. Effects of distance between the Nanoparticles	26
1.5.4. Effects of Shape of the Nanoparticles	27
1.5.5. Experimental Parameters	28
1.6. Machine Learning for SERS	28
1.7. Molecules Studied in This Thesis	30
1.8. Challenges and Thesis Motivation	32
1.9. Rest of the Thesis Outline	34
Chapter 2: Synthesis and Characterization Techniques	34
Chapter 3: Ultrafast Laser Ablated Plasmonic NSs for SERS	35
Chapter 4: Novel Flexible, Hydrophobic, Hybrid and Low-cost SERS Substrate	es36
Chapter 5: Overcoming Signal Fluctuations in the SERS for Improved Applications	
Chapter 6: Conclusion and Scope	38
2) Synthesis and Characterization Techniques	51
2.1. Introduction	52
2.2. Fabrication and Synthesis of NSs	53
2.2.1. Ultrafast Laser Ablation	53
2.2.2. Chemical Methods for NP Synthesis	56
2.3. Experimental Techniques	59
2.3.1. Ti:Sapphire as a Gain Medium	59
2.3.2. Femtosecond Laser Oscillator	61

	2.3.3. Femtosecond Amplifier System	63
	2.4. Experimental Setups	68
	2.4.1. Ultrafast Laser Ablation	68
	2.4.2. Raman Systems	69
	2.5. Characterization Techniques	71
	2.5.1. FESEM and TEM	71
	2.5.2. UV-Visible Spectroscopy	72
	2.5.3. Energy Dispersive X-Ray Spectroscopy	74
	2.5.4. SERS Measurements	74
3)	Ultrafast Laser Ablated Plasmonic NSs for SERS	84
	3.1. Introduction	85
	3.2. Structures Prepared using Femtosecond Laser Oscillator	86
	3.2.1. Experimental Setup	88
	3.2.2. Effects of Scan Speed	88
	3.2.3. Effects of Fluence	89
	3.2.4. Mechanism of Laser Ablation	91
	3.2.5. SERS Measurements	94
	3.3. Metal Nanostructures Using Femtosecond Amplifier	95
	3.3.1. Femtosecond Laser Ablation of Ag:Au Alloy and Application in SERS	95
	3.3.2. Femtosecond Ablation with Cylindrical Focusing	108
	3.4. Conclusions	115
4)	Novel Flexible, Hydrophobic, Hybrid and Low-cost SERS Substrates	125
	4.1. Introduction	126
	4.2. Anisotropic and Hybrid SERS Substrates	127
	4.2.1. Highly Anisotropic Ag Dendrites for SERS	127
	4.2.2. Sample Preparation	128
	4.2.3. Application for Detection of Diverse Analytes	132
	4.3. 2-D, Hybrid SERS Substrates	141
	4.3.1. Preparation and Characterization	142
	4.3.2. SERS Measurements	147
	4.4. Flexible SERS Substrates	153
	4.4.1. Novel Hydrophobic Filter Paper as SERS Substrate	153
	4.4.2. Flexible Porous Si for SERS	162
	4.6. Conclusion and Scope	170

5) Overcoming Signal Fluctuations in the SERS for Improved Field A	
5.1. Introduction	
5.1.1. Machine Learning Algorithms	179
5.2. Signal fluctuations in the SERS	183
5.3. Neural Network Aided SERS (NNAS)	186
5.3.1. Signal to Noise Ratio Approach	190
5.3.2 Sample Preparation	190
5.3.3 Data collection	191
5.3.4 Results and Discussion	193
5.3.5 Spatial Representation of the Data	197
5.4. Conclusion and Scope	200
6) Conclusion and Scope	211
6.1. Summary	212
6.1.1. Machine Learning for Quantification in SERS	213
6.1.2. Femtosecond Laser Ablation of Metals and Semiconductors	214
6.1.3. Anisotropic Ag-Au dendrites for SERS	215
6.1.4. 2-D materials for SERS	216
6.1.5. Flexible, Free Standing Porous Si Substrate for SERS	218
6.2. Future Scope	218
Appendix A	223
Support Vector Machine	223
Appendix B	226
Guide to Implementing Machine Learning Using Python	226
Appendix C	229
Five Axis Representation of SERS Performance	229
List of Publications	231

Chapter 1

INTRODUCTION AND THESIS OUTLINE

Abstract

This chapter provides a comprehensive overview of the motivation behind the work performed and the results presented in the thesis. It is set to focus on the basics and theory of physics involved in this thesis methods. It begins with focusing on the significance of plasmonic materials and their recent applications, including the preparation methods. Various trace detection techniques in vogue for the detection of different molecules like explosives, pesticides, dyes are examined, particularly emphasising the advantages of surface-enhanced Raman spectroscopy (SERS) over other techniques. The chapter then delves into the theoretical underpinnings of the Raman scattering and SERS enhancement, exploring the influence of materials (Ag, Au, and Ag-Au alloys), nanoparticle size, material, shape, and interparticle distance using COMSOL simulations. The challenges currently facing SERS and their origins are also discussed. State-of-the-art in the SERS techniques in substrate fabrication, applications, and implementation of machine learning techniques is also detailed. An introduction to machine learning techniques and their applications in SERS is presented, along with an overview of the different molecules studied in the thesis, including explosives and biomolecules.

1.1. Introduction

"There is a plenty of room at the bottom," claimed Prof. Richard Feynman at the American Physical Society conference in 1959, introducing the term 'Nanotechnology' and emphasising the importance of its study [1]. He called nanoparticles 'tiny machines' and as he rightly predicted, they have revolutionised many fields in science. But the usage of nanoparticles can be traced back to fourth century AD in the Roman civilization through the popularly known Lycurgus cup in the present British museum. The dichroism observed in the cup was ascertained to the presence of Ag-Au alloy nanoparticles of different sizes in specific ratio of 7:3, along with 10 percent of Cu nanoparticles [2]. Stained glass windows of churches in the late medieval period were found to contain Ag-Au nanoparticles giving them distinct luminous colours [3]. Ag or Cu nanoparticles were found in ceramic gazes of the Islamic world and Europe during the 9th-17th centuries [4]. A number of Renaissance pots produced during the 16th century was encrusted with nanoparticles by the Italians [5]. Nanomaterials such as carbon nanotubes, "Damascus" blades with distinct patterns, cementite nanowires were extensively used to improve strength and performance of different materials [6]. However, throughout this period there was no understanding of the properties of the nanoparticles. In 1857, a colloidal gold containing nanoparticles was prepared by Faraday and from then it was known that metallic nanoparticles exhibit different optical properties than the bulk [7]. This was the first attempt to understand the properties of nanoparticles and soon a field of study called 'nanoscience' has emerged. Further, the theory developed by Gustav Mie in 1908 provided a full understanding of the scattering of light in small metallic particles [8]. Advancements in characterization techniques like Scanning Tunnelling Microscope (STM), Atomic Force Microscope (AFM), Scanning Electron Microscope (SEM), Field Emission Scanning Electron Microscope (FESEM), and Transmission Electron Microscope (TEM) has further revolutionised the study of nanoparticles progressively.

Advents in nanotechnology lead to the emergence of many new fields, one of the crucial fields being plasmonics. Plasmonics deals with the study of the oscillations of conduction electrons in metallic nanostructures and at the metal-dielectric interfaces, including their potential applications [9]. The free conduction electrons in metals are constantly moving under the influence of fixed positive charge centred at the nucleus. The oscillations of

these free electrons can be understood through Drude and Lorentz models [10]. The quantum of these collective oscillations of the conduction electrons is called as a "plasmon" and the study of these oscillations and related applications is called as 'plasmonics'. Upon interaction with electromagnetic field, there are two important resonances that occur in plasmons, Localised Surface Plasmon Resonance (LSPR) and propagating Surface Plasmon Resonance (SPR) [11]. Propagating Surface Plasmons (PSP) are evanescent electromagnetic waves that are only present at flat, metal-dielectric interfaces and are caused by the oscillations of conduction electrons within the metal. Under optimum conditions, like angle of incidence, dielectric constant, and wavelength of light, that satisfy the conditions of conservation of energy and momentum, exciting PSPs lead to resonant oscillations called as SPR. SPRs are very sharp resonances and are function of many experimental parameters. Specific configuration like Otto or Kretschmann setups are used in order to excite SPR [12]. They are capable of travelling relatively larger distances (10-100 µm) and have very sharp resonances making them a reliable choice for plasmonic waveguides and sensors respectively [13]. LSPR refers to resonances in nanostructures where surface plasmons are confined and often need only the conservation of energy criteria thus removing the need for complex experimental setup. LSPR resonances are relatively broader than SPR and are hence advantageous for certain applications like SERS. SPR always needs a planar interface to facilitate PSPs whereas LSPR can be excited in 3D volumes like the case of nanoparticles dispersed in water. LSPR applications also have greater flexibility to tune the resonances by changing the shape, size as opposed to SPR [14]. The distinct properties of metal nanostructures are attributed to the occurrence of LSPR originating from collective as well as coherent oscillations of electrons on the surface in these structures. This often leads to field localization and hence enhancement in electric field to small regions. These oscillations and the filed enhancement caused by LSPR are highly dependent on the shape, size and surrounding media of the nanoparticles [15] [16]. Additionally, it offers the chance to modify the nanoparticles' characteristics according to the specific application.

SERS and plasmonics share a symbiotic relationship where development in one field is aiding the other. A good SERS substrate can be used as a tool to comprehend the fundamentals of plasmonics, and a good plasmonic material is always a good SERS substrate. SERS is a potent analytical approach that increases the Raman scattering signal of molecules when they are adsorbed on metallic or dielectric nanostructured surfaces by

several orders of magnitude. SERS is both a quantitative and qualitative spectroscopic technique for the unique identification of various materials through their vibrational fingerprint. Fleischmann made the initial discovery of the phenomenon accidently in 1974 while examining pyridine adsorbed on a roughened silver electrode [17]. However, the enhancement in his experiment was credited to a larger adsorption surface area that was available to the molecules. The origin of the enhancement was only discovered through additional research conducted in 1977 by two separate research groups, Jeanmaire and van Duyne [18] and Albrecht and Creighton [19]. It is now well known that the two mechanisms of electromagnetic enhancement (EE) and chemical enhancement (CE) account for the majority of the contributions to the enhancement. The CE mechanism arises from the chemical interaction between the adsorbed molecule and the surface. This interaction can modify the molecular polarizability and induce charge transfer, resulting in an enhancement of the Raman scattering signal [17]. The electromagnetic enhancement in SERS primarily arises from the strong electromagnetic fields produced by the LSPRs of the metal nanostructures. These LSPRs are a consequence of the conduction band electrons' collective oscillations in response to incoming light stimulation. The resulting enhanced electromagnetic fields can be used to excite Raman-active molecules, leading to the amplification of their vibrational signals [18]. The scattering intensity of the molecule in this case is bound to grow by several orders of magnitude as a result of the two enhancements, which is the product of these two [10]. Understanding the origin of SERS enhancements and its influence on various parameters such as shape, size, and material of the nanoparticles, including the experimental parameters, is important to maximize the SERS enhancement [19] and for translating the research to practical applications. Under such optimized conditions, SERS has the potential to detect trace analytes in the regime of Attomolar [20], femtomolar [21], picomolar [22] and nanomolar [23] and even single molecule [24] or a cell [25]. With this potential, SERS has seen many applications for trace detection of explosives [26] [27] [28][29], biomolecules [30], pesticides [31], [32], microorganisms [33], drugs [34], and disease biomarkers [35] to name a few. The current research in SERS is focused on three main aspects, a) Innovations in plasmonics for SERS, b) Taking SERS to different applications and developing SERS based devices, and c) Usage of machine learning techniques to overcome some of the challenge sin SERS as shown in figure 1.1.

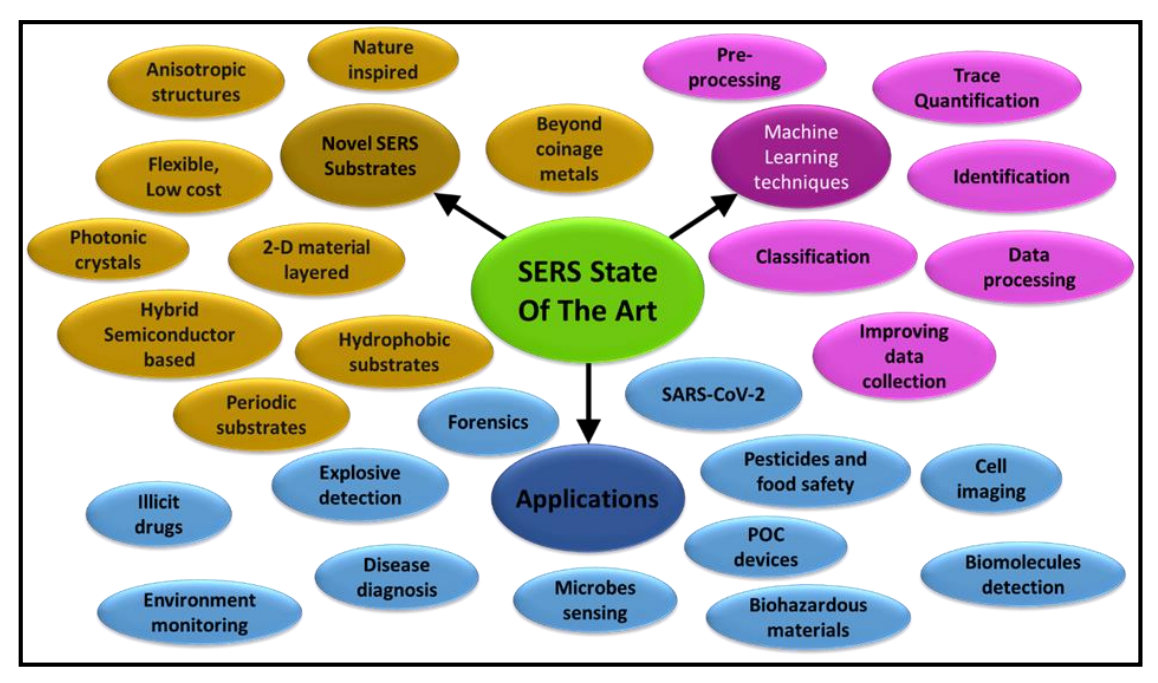


Figure 1.1: State of the art in SERS in terms of substrate fabrication, applications and implementation in machine learning techniques.

1.2. Trace Detection of Explosives

With growing terrorism and threats to world peace, homeland security is a challenge for every nation. Detection/sensing of high energy materials (HEMs), often called as explosives, in public places in view of safety is an important aspect of a country's security. Trace detection of explosives is important to identify early threat and further save lives. Bulk detection and trace detection are the two broad categories into which explosive detection can be divided. Bulk detection refers to detection of bulk explosives and is now very well established with existing techniques such as Raman Spectroscopy, terahertz (THz) spectroscopy, Laser-induced Breakdown Spectroscopy (LIBS), neutron based technologies, X-ray imaging, and computed tomography etc. [36]. Trace explosive detection refers to detection of explosives that one cannot see with the naked eye and is often used as an indication of handling bulk explosives prior [37] [38]. There are many trace explosive detection techniques like ion mobility spectroscopy (IMS), Chemiluminescence (CL), gas chromatography (GC), mass spectroscopy (MS), photoacoustic spectroscopy (PAS), and SERS [39]. These techniques can further be classified on the basis of sample collection technique or if it offers a fingerprint signature, near field or standoff and so on as shown in the figure 1.2. IMS identifies ions based on their mobility in a gas phase. It works by ionizing a sample and subjecting the resulting ions to an electric field, which causes them to drift through a gas-filled chamber at different speeds depending on their size and shape, allowing for their identification. Though quick, IMS does not give fingerprint response, is not compatible for multiplexing, destructive and the result depends on the length of drift tube and atmospheric conditions [40]. CL is based on a chemical reaction that when an electronically excited state of a chemical de-excites to ground state it generates electromagnetic radiation as light. There are different techniques that make use of CL for trace detection like thermal energy analyser (TEA), luminal based CL, electrochemiluminescence as such or in combination with an immunoassay with or without a fluorophore [41]. These techniques are always coupled with a separation technique to detect explosives in a complex matrix because of the lack of selectivity. For example, gas chromatography coupled TEA is widely used for explosive detection exploiting the fact that most of the explosives containing nitrate or nitro groups [41]. In MS, the charge to mass ratio of the components present in the sample are analysed in the presence of a magnetic field and a mass spectrum is generated to identify the sample. PAS involves the use of a laser to excite a sample and generate acoustic waves, which are detected by a microphone. The resulting signal provides information about the sample's properties, such as its absorption spectrum and concentration. Each of the techniques comes with its own challenges and limitations when it comes to preventing false alarms, sensitivity, detection in complex matrices and multiplexing. In real world situations, safe, non-destructive, label-free, cost-effective, and rapid detection is imperative for any explosive detection technique.

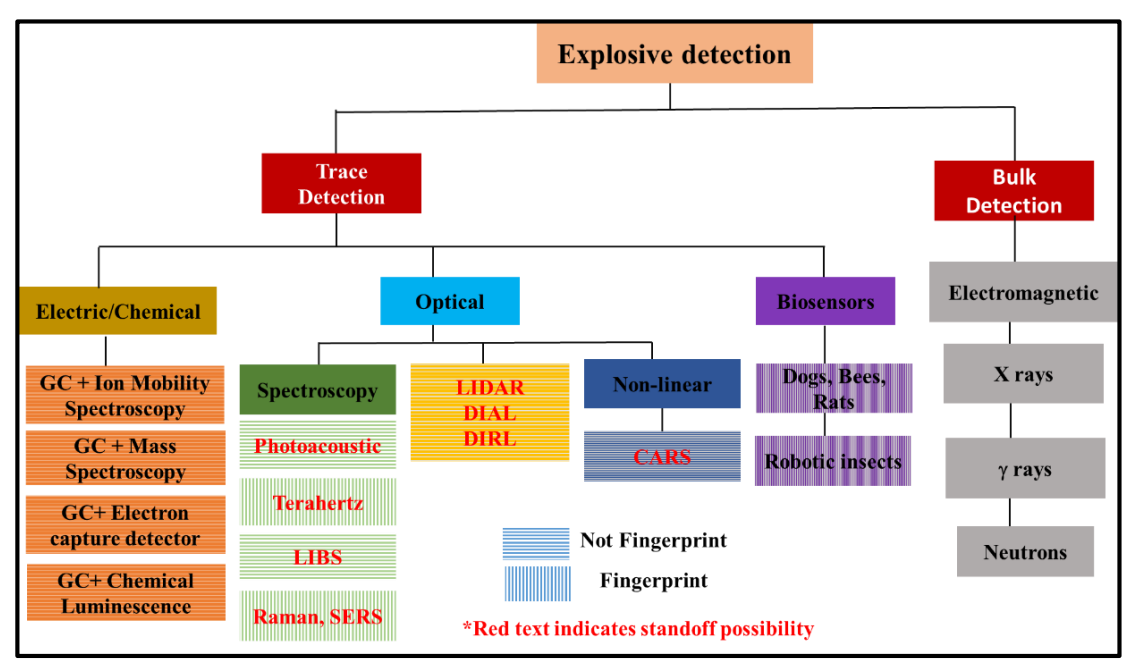


Figure 1.2: Schematic of classification of different explosive detection techniques.

Biomolecules are defined as chemical substances present or produced by living organisms including proteins, nucleic acids (DNA, RNA, and their bases), lipids, carbohydrates, and vitamins [42]. Detection of biomolecules is important to understand different biochemical processes, optimise drug delivery mechanisms in pharmaceutical applications, and for early diagnosis of diseases [35]. Existing popular techniques like enzyme-linked immunosorbent assay (ELISA) and polymerase chain reaction (PCR) are known to be time consuming and cost-ineffective. Specifically, for biomolecules trace detection techniques that can track minute changes in cells/tissues or in complex bio fluids, help in early disease diagnosis thus saving lives. It is also ideal to have a tool that is water compatible and offers high signal to noise ratio despite the presence of huge background as is the case for biomolecules. Recent pandemic (COVID-19) and growing cancers, has invoked new interest in developing SERS based detections systems for non-invasive, rapid and early detection [43].

The performance of any trace detection is characterised by the following parameters.

- 1) **Selectivity:** It is the ability of a detection system to detect a specific analyte despite the presence of other molecules interfering with its detection.
- 2) **Sensitivity:** Sensitivity is technically defined as the minimum change in input parameter that can show detectable change in the output parameter. In the case of trace detection, it is the smallest change in concentration that can be detected by the detection technique.
- 3) **Limit of Detection (LOD):** Limit of detection is defined by the standard definition [44]. It is given as the relation between standard deviation of the intensity of the blank sample, σ and the slope of the intensity vs concentration calibration curve, b,

$$LOD = \frac{3\sigma}{b} \tag{1.1}$$

4) **Reproducibility:** Reproducibility means the variation in the intensity of a selected signature peak/response of the molecule under study. It is usually measured in terms of relative standard deviation (RSD), which is a ration of mean to the standard deviation of the signal. Lower RSD indicates better reproducibility.

SERS overcomes the existing challenges in the detection of both, explosives and biomolecules by offering portable, rapid, non-destructive, and fingerprint detection. It is

an excellent tool for trace detection because it enables identification of molecules present at extremely low concentrations due to the high field amplification caused by the interaction between the analyte molecules and the plasmonic material. SERS is also known for its selectivity making it an ideal tool for identifying trace amounts of target molecules in complex matrices, which is crucial for various types of field applications in explosive and biomolecule detection. SERS also allows for rapid analysis with detection times as less as 2-5 minutes [45], multiplexing allowing simultaneous detection of two analyte molecules [46], and versatility meaning one SERS substrate can be used for detection of different molecules [47]. SERS is also non-destructive, indicating that samples can be analysed without altering their chemical or physical properties. This is important for explosive and biomolecule sensing where samples need to be preserved for further analysis, prevent damage of tissues/cells or operator's safety is a concern. Along with these advantages, recent developments in portable instrumentation and compact lasers have made SERS desirable for on-site analysis [48]. This means that samples can be analysed in the field, rather than being transported to a laboratory for analysis making it possible to pursue onsite and remote detection.

Using different criteria such as velocity of detonation, chemical properties and energy released, explosives are classified into different groups in order study their properties. First and foremost, as explosives have varying destructive capacities depending on their velocity, the categorization of explosives based on detonation velocity is often employed in a variety of industries, including the military, mining, and building destruction [49]. If the velocity of detonation is greater than 4000 m/sec, the explosives are classified as high energy explosives. Further depending on the sensitivity, they are classified into primary, secondary and tertiary. Primary explosives are extremely sensitive to heat, spark and friction and hence detonate easily. They are often used as triggering agents for secondary explosives in small quantities. Mercury fulminate, lead azide, lead styphnate, and tetracene are some of the examples of primary explosives. Secondary explosives are the most commonly studied and used explosives as they are not very sensitive to external stimuli. They are often triggered by a primary explosive and have high detonation velocities. Some of the commonly studied secondary explosives include 1,3,5-Trinitroperhydro-1,3,5triazine (RDX), 1,3,5,7-Tetranitro-1,3,5,7-tetrazocane (HMX), 5 Amino,3-nitro,1,3,5nitrozole (ANTA), 2,4,6,8,10,12-Hexanitro-2,4,6,8,10,12-hexaazaisowurtzitane (CL-20), Trinitrotoluene (TNT), and 1,1-diamino-2,2-dinitroethene (FOX-7). Tertiary explosives

have very low detonation velocities and are often used for demolition and mining. Low are also characterised by low velocity of detonation and used as propellants in various applications. Black powder, gun powder and amputations in firearms are some of the examples of tertiary explosives [50].

1.3. Localized Surface Plasmon Resonance

Understanding LSPR is important to understand SERS and the factors that influence the enhancement in SERS. SERS primarily uses LSPR for enhancing the Raman signal through mechanisms discussed in later sections. There are reports where both SPR and LSPR are used in SERS for dual mode enhancement [51–53]. However, the work done in this thesis has focused exclusively on LSPR based SERS for the advantages discussed in the introduction. In order to understand the LSPR, one has to look into the interaction of electromagnetic radiation with metal nanoparticles whose size is less than the wavelength of the light and hence is often treated as an electrostatic problem. When electromagnetic radiation strikes a metal nanoparticle, the displacement of the conduction electrons from the positive ions causes the system to become polarised. But Columbic attraction causes the displaced negative and positive charges to be brought together, producing a restoring force. In response to the periodic electric field and the restoring force produced by the Columbic attraction between the positive and negative charges, the conduction electrons in the nanoparticle experience coherent oscillation, as seen in figure 1.3 a). This may be described in a manner similar to the mass-spring oscillator model, as seen in figure 1.3 b). The coherent oscillations in metal nanoparticles are referred to as LSPR, which is called "localised" because the electron oscillations are spatially constrained in three dimensions.

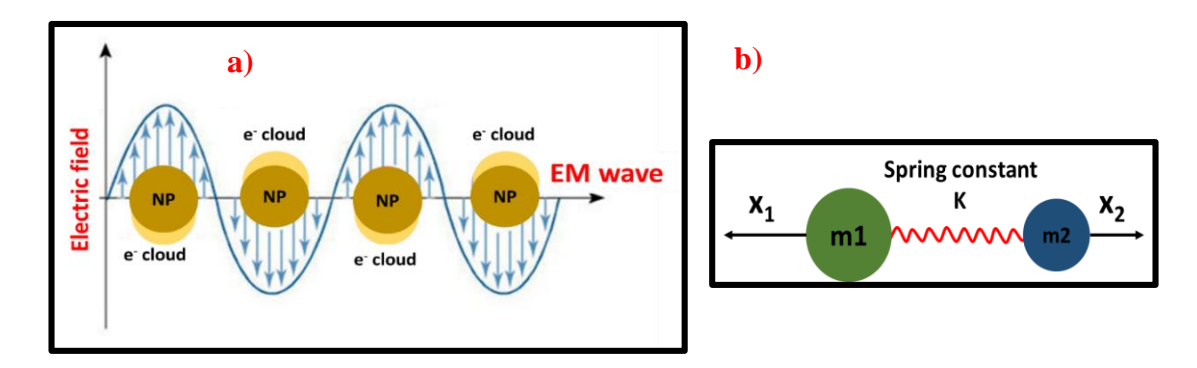


Figure 1.3: Schematic of a) LSPR oscillations in metal nanoparticles in the presence of an electromagnetic field, b) Spring-mass model of a molecule with two atoms bound by a spring analogous to the chemical bond.

In order to develop a theoretical formulation for the origin of LSPR, the simplest model at hand is a spherical metallic nanoparticle. Instead of solving the Maxwell's equations fully, we can restore to the electrostatic approximation. In real life situations, where the excitation wavelength is approximately around 500-800 nm, is much larger than the size of the nanoparticles, which is approximately 10-100 nm, this approximation is justified. LSPR in a metallic sphere can thus be understood with electrostatic approximation by solving the Laplace equation with appropriate boundary conditions.

The Laplace equation for a potential, V, is given as,

$$\nabla^2 V = 0 \tag{1.2}$$

In the spherical coordinates, the solution of the above equation is a series of Legendre polynomials and is a function of radial distance, r and the polar angle, θ [54].

$$V(r,\theta) = \sum_{l=0}^{\infty} (A_l r^l + \frac{B_l}{r^{l+1}}) P_l(\cos\theta)$$
 (1.3)

Consider a metallic sphere of radius, R, dielectric function ε , placed in a medium of dielectric constant, ε_m . The potential inside (V_{in}) and outside (V_{out}) this metallic sphere in the presence of an external electromagnetic field, E_{Inc} , is obtained by solving equation (1.3).

$$V_{in} = \sum_{l=0}^{\infty} (A_l r^l) P_l(\cos \theta)$$
 (1.4)

$$V_{out} = \sum_{l=0}^{\infty} \left(\frac{B_l}{r^{l+1}}\right) P_l(\cos\theta)$$
 (1.5)

Using the appropriate boundary conditions, the constants A₁ and B₁ can be derived as [54],

$$A_l = B_l = 0$$
 for $l \neq 1$

$$A_1 = \frac{-3\varepsilon_{\rm m}}{\varepsilon + 2\varepsilon_{\rm m}} E_{\rm Inc}$$
, $B_1 = \frac{\varepsilon - \varepsilon_{\rm m}}{\varepsilon + 2\varepsilon_{\rm m}} R^3 E_{\rm Inc}$ (1.6)

From equations (1.4), (1.5) and (1.6), the potential inside and outside the sphere can be written as,

$$V_{in} = \frac{-3\varepsilon_{\rm m}}{\varepsilon + 2\varepsilon_{\rm m}} \, E_{\rm Inc} \, r cos \, \theta \tag{1.7}$$

$$V_{out} = -E_{Inc}rcos\theta + \frac{\varepsilon - \varepsilon_m}{\varepsilon + 2\varepsilon_m} R^3 E_{Inc} \frac{cos\theta}{r^2}$$
 (1.8)

From the multipole expansion of the electric field potential, the first term indicates the monopole contribution while the second term indicates the dipole contribution where the dipole moment can be written as,

$$p = 4\pi \varepsilon \varepsilon_m \frac{\varepsilon - \varepsilon_m}{\varepsilon + 2\varepsilon_m} R^3 E_{\text{Inc}} = \varepsilon \varepsilon_m \alpha E_{\text{Inc}}$$
 (1.8)

 α here is the polarizability of the sphere and is a measure of 'responsiveness' of the molecule to the electromagnetic radiation, can be written as,

$$\alpha = 4\pi \frac{\varepsilon - \varepsilon_m}{\varepsilon + 2\varepsilon_m} R^3 \tag{1.9}$$

From the potential the electric field inside the metallic sphere can be derived as,

$$E_{In} = \frac{3\varepsilon_{m}}{\varepsilon + 2\varepsilon_{m}} E_{Inc}$$
 (1.10)

The absorption, scattering and extinction cross sections of the sphere can be derived using the above equations [55] and all of them have $\epsilon + 2\epsilon_m$ in the denominator.

It has to be noted that the dielectric function for metals is a function of wavelength and is a complex function which can be written as a sum of real and imaginary parts as,

$$\varepsilon \approx \varepsilon(\lambda) = \text{Re}\varepsilon(\lambda) + i\text{Im}\varepsilon(\lambda)$$
 (1.12)

In a case where $\text{Im}[\epsilon(\lambda)]$ is small implying $\text{Im}[\epsilon(\lambda)] \sim 0$ and $\text{Re}[\epsilon(\lambda)] \sim (-2\epsilon_m)$, the denominator in equation 1.11 tends to infinity. This is the resonance condition where the optical response of the metallic sphere is huge and is called as a LSPR. The field that is generated and hence the denominator in equation 1.11 is hugely dependent on the shape of the metal nanostructure. The resonance condition that is obtained here is purely a consequence of the geometry of the sphere and the boundary conditions that have been used in the derivation. This validates the dependence of LSPR on the shape of the metal nanostructures studied, as for example for a cylinder the denominator changes to $\epsilon(\lambda) + \epsilon_m$, changing the resonance condition [18]. The equation also suggests the dependence of LSPR on the surrounding medium (ϵ_m), for example LSPR is red shifted in the presence of medium with higher dielectric function like water than air. We will study the specific case of gold and silver in later sections. There are many important inferences on LSPR that can be drawn from the sphere model and are summarised below. The nature and quality of LSPR depends on,

- Nature of dielectric function of the metal $\varepsilon(\lambda)$.
- Shape of the nanoparticle as it results to different resonance condition in the denominator of the electric field.
- Wavelength, as a consequence that the dielectric function of the metal is a function of wavelength.
- Surrounding medium through the variable ε_m in the term including the presence of other nanoparticle in the vicinity.

In the coming sections we will introduce the aspects of LSPR that will influence the enhancements in the SERS.

1.3.1. Optical Properties of Coinage Metals

The optical properties of coinage metals such as Ag, Au, and Cu are essential to understanding their widespread usage as SERS substrates. In this thesis we have extensively worked on Ag, Au and their combinations and hence will restrict the discussion to Ag and Au. The Drude model provides a good approximation for the dielectric function of these metals in the region of interest [10]. In this thesis work for the simulations, we have used the dielectric function provided by the widely cited Johnson and Christy's work [56]. Figure 1.4 shows real and imaginary parts of dielectric functions of gold and silver taken from their work.

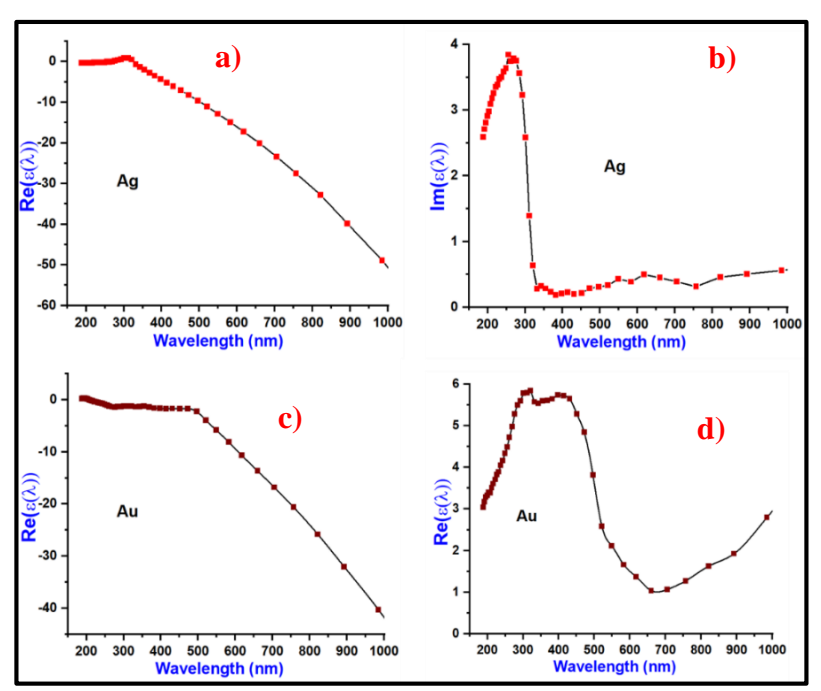


Figure 1.4: Real and imaginary parts of dielectric functions of gold and silver taken from Johnson and Christy's work [56].

The resonance condition derived in equation 1.11 has constraints on the dielectric function through the denominator. It implies that the real part of the dielectric function is largely negative. Figures 1.4 a), 1.4 c) indicate exactly the same for the real part of the dielectric function along with a monotonous decrease in the visible region. The denominator also signifies that the imaginary part has to be small and this condition is met by both the metals as shown in figures 1.4 b), 1.4 d). A small imaginary part also implies a superior quality factor. It has to be noted that imaginary part of Ag is smaller than Au, which indeed makes Ag a better performer in terms of enhancement in SERS. At higher wavelengths in the IR regions, both Ag and Au are known to perform equally par because of the similarity in dielectric function in this region [57]. However, Au is known to exhibit greater stability, low toxicity [58] and compatibility and hence is a preferred choice especially for SERS based biology applications [59]. There is also a recent surge in usage of materials beyond metals like doped semiconductors and dielectrics that have similar dielectric functions as SERS substrates [60] [61] [62] [63] [64].

1.4. SERS Enhancement Mechanism

It is crucial to first take a step back and comprehend Raman Scattering before moving on to comprehend the mechanism of SERS. SERS, after all, is an essentially Raman scattering with enhancement in signal through plasmonic nanostructures. Raman scattering refers to inelastic scattering of light by materials resulting in change in frequency of the incident light. This shift in frequency is called 'Raman shift' and is a vibrational signature of the materials under study. It is referred to as "Stokes Raman" (down conversion) if the frequency of the scattered light is lower than the incident frequency, and as "anti-Stokes Raman" (up conversion) if it is greater. Anti-Stokes scenario occurs if the molecules are already in an excited state and hence is not a common occurrence at room temperature. Throughout this thesis we are only referring to stokes shift. Raman spectroscopy has huge potential for many applications given it is label free, rapid and also offers fingerprint spectra enabling unique identification of samples under study. Classically the Raman scattering can be explained using the oscillating electric dipole where the scattered radiation is treated as radiation emitted by the dipole. When electromagnetic radiation interacts with a molecule, it interacts with the electron cloud associated with a chemical bond and induces a dipole moment. The induced dipole moment, p_{induced}, is proportional to the incident electromagnetic field, E_{inc} , and has a proportionality constant polarizability, α as given by the equation (1.13).

$$p_{induced} = \alpha \times E_{inc} \tag{1.13}$$

Raman scattering can be explained using a classical model using the spring-mass analogy and Newton mechanics. Consider a diatomic molecule which can be modelled using a spring mass system [figure 3 b)]. The force between the atoms can be written as in equation 1.14 using the Hook's law, where x_1 , x_2 are the displacements from the origin, m_1 , m_2 are the atomic masses and K is the spring constant which is equivalent to bond strength.

$$\frac{m_1 m_2}{m_1 + m_2} \left(\frac{d^2 x_1}{dt^2} + \frac{d^2 x_2}{dt^2} \right) = -K(x_1 + x_2) \tag{1.14}$$

By introducing total displacement, q, as the sum of displacements x_1 , x_2 and reduced mass, μ , the above equation can be rewritten as,

$$\mu \frac{d^2q}{dt^2} = -\mathbf{K} \mathbf{q} \tag{1.15}$$

The solution of the above differential equation with boundary condition at t=0 can be written as,

$$q = q_0 \cos(2\pi v_m t) \tag{1.16}$$

Where, $v_m = \frac{1}{2\pi} \sqrt{\frac{K}{\mu}}$ is the frequency of the vibration from the mean position and is, hence, dependent on the bond strength and the reduced mass of the atoms. The induced polarizability given in equation 1.13 for an incident electric field $E_0 \cos(2\pi v_0 t)$ can be rewritten as,

$$p_{induced} = \alpha \times E_{inc} = \alpha \times E_0 \cos(2\pi v_0 t)$$
 (1.17)

The polarizability is a tensor and is a function of displacement of the atoms present in the molecule. Under the small displacement caused in the presence of electric field, it can be approximated by the Taylor expansion as,

$$\alpha = \alpha_0 + q \left(\frac{d\alpha}{da}\right)_{q=0} + \dots$$
 (1.18)

Combining the equations 1.16, 1.17 and 1.18, one can write the induced diploe moment as,

$$p_{induced} = \alpha_0 \, E_0 \cos(2\pi v_0 t) + q_0 \, \cos(2\pi v_m t) \, E_0 \cos(2\pi v_0 t) \, \left(\frac{d\alpha}{dq}\right)_{q=0} + \cdots \, (1.19)$$

The first term is equivalent to Rayleigh scattering, where the frequency of the dispersed light is the same as the frequency of the incoming light. Using trigonometric identities, the second term may be stretched to produce two distinct terms that represent the sum and difference of frequencies, as illustrated below.

$$p_{induced} = \alpha_0 E_0 \cos(2\pi v_0 t) + q_0 E_0 \left(\frac{d\alpha}{dq}\right)_{q=0} \left[\cos(2\pi \{v_0 - v_m\}t) + \cos(2\pi \{v_0 + v_m\}t)\right] + \cdots$$
(1.20)

As can be seen, the sum and difference frequencies generated in the equation highlight the contribution of anti-Stokes and Stokes frequencies in the Raman scattering event, respectively. It is important to note that for Raman scattering, $\frac{d\alpha}{dq}$ must be non-zero meaning only the vibrational modes that result in change in polarizability are Raman active. The intensity of the Raman signal is proportional to the Raman cross-section of the molecule and the incident power density. The scenario is same in the case of SERS except with an enhancement factor originating from both electromagnetic and chemical enhancement. The Raman power, P_{Raman} emitted in an event is proportional to the intensity of the input laser power, I, number of molecules in the excitation region, N, and scattering cross section of the k^{th} mode, σ_k .

$$P_{Raman} = KN \sigma_k I \tag{1.21}$$

K here is the proportionality constant that accounts for instrument parameters like detector efficiency in converting photons into electrons. In the case of SERS, the output power, P_{SERS} is proportional to the Raman power with an additional enhancement factor, G_{SERS} , which is further a product of electromagnetic enhancement, G_{EM} , and chemical enhancement, G_{CM} .

$$P_{SERS} = G_{SERS}P_{Raman} = G_{EM}G_{CM}P_{Raman}$$
 (1.22)

1.4.1. Electromagnetic Enhancement

After the discovery of anomalously intense Raman signal of pyridine adsorbed on silver electrodes in early 1970s, there were many theories which attempted to understand the origin of enhancement. Electromagnetic enhancement is an important contribution to SERS and with optimum plasmonic material it could be as high as 10¹⁰ [65]. The understanding of EM enhancement (EME) was a progress of different works over the years which lead it to the current form. Through his work, Moskovits proposed that the roughed electrodes can be approximated as nanoparticles and are hence contributing to the enhancement through plasmonic effects [66]. Further, he suggested that colloidal nanoparticles can also be used for such enhancements [67]. Eventually in 1979, Creighton et al. have demonstrated SERS with Ag/Au colloids and went further to study the effects of size and wavelength of SPR on SERS. They argued that the enhancement is from the surface plasmon resonance in metallic nanostructures and called it 'plasmon resonanceenhanced Raman' in their studies [68]. His group significantly contributed in the progress of SERS substrates beyond roughened surfaces and eventually concluded that the dielectric function of the metals has a role to play in the efficiency of SERS [69]. The idea of SERS hotspots has also been conceptualised by Creighton during his studies on the effects of aggregation of gold nanoparticles on SERS enhancement [70]. This observation was reinforced by a different study performed to calculate the field enhancement for Ag and Au dimers establishing the concept of SERS hotspots. The idea was conceptualised later for the detection of single molecule detection like that of haemoglobin in between two Ag nanoparticles [71]. Eventually, the electromagnetic enhancement in SERS is now well understood and is formulated below. The EME in SERS is mainly attributed to the nature of LSPR and its effects on the presence of probe molecules in the vicinity. As any LSPR technique, it is a near field enhancement and is dependent on different factors that influence the quality of LSPR. In SERS substrates the probe molecules are adsorbed on the surface of metal nanoparticles/nanostructures either through physisorption or chemisorption. The enhancement is formulated by solving the electric field around these probe molecules in the presence of the metal nanoparticles. The EME can be understood in terms of two events [17] [18],

1.4.1.1. Local Field Enhancement (LFE)

In the sections described above, it is clear that metal nanoparticles under certain conditions experience field enhancement in their vicinity. The enhancement of incident electric field in the presence of nanoparticles is called as LFE. This field enhancement is localized in the vicinity of the nanoparticle and these areas of dense electric field are often called as 'hotspots' in SERS. The field enhancement this case can be understood using the classical dipole approximation described earlier where the power of dipole radiation of the oscillating Raman dipole is given as,

$$P_{Raman} = \frac{\omega^4}{12\pi\varepsilon_0 c^3} |p_{induced}|^2 = \frac{\omega^4}{12\pi\varepsilon_0 c^3} |\alpha E_{inc}|^2$$
 (1.23)

The equation above suggests that the power is proportional to the square of incident filed intensity using which we can define a LF intensity enhancement factor (LFIEF), M_{LFIE} for a local field of E_{Loc} (ω_L) as (where ω_L is the frequency of incident radiation),

$$M_{LFIE} = \frac{|E_{Loc}(\omega_L)|^2}{|E_{inc}(\omega_L)|^2}$$
 (1.24)

The local filed enhancement depends on many factors originating from the dependence of LSPR on different parameters. It is generally intense at tips, sharp edges, and cervices similar to the popular lightening rod effect in metals. It is also a function of orientation of the molecule, wavelength, polarization of the field with respect to the metal nanoparticle of interest.

1.4.1.2. Re-radiation Enhancement (RE)

While the LFE is from the perspective of the metal nanoparticle and associated LSPR, reradiation effect is from the perspective of the molecule. This results from the fact that, as equation 1.23 illustrates, the power emitted by an oscillating dipole relies on its surrounding environment [72]. Depending on its electromagnetic environment, a fixed oscillating dipole amplitude will extract more or less energy. If a dipole oscillates close to a metal surface with a frequency of ω_R , its power can, for example, be many orders of magnitude greater than if it were radiated in free space. This is often described as modified spontaneous emission and is described in detail elsewhere [73]. In the presence of metal nanoparticle and the local field enhancement, the power radiated by the molecule, P_{Rad} is enhanced and the radiation enhancement factor, M_{REF} , relative to the free space, P_0 is given as,

$$M_{REF} = \frac{P_{Rad}}{P_0} = \frac{|E_{Loc}(\omega_R)|^2}{|E_{inc}(\omega_L)|^2}$$
(1.25)

The total EM enhancement, G_{EM} in SERS is the product of LFIE and REF and is often known as $|E|^4$ approximation of SERS enhancement.

$$G_{EM} = M_{LFIE} M_{RE} = \frac{|E_{Loc}(\omega_L)|^2}{|E_{inc}(\omega_L)|^2} \frac{|E_{Loc}(\omega_R)|^2}{|E_{inc}(\omega_L)|^2}$$
(1.26)

Under the approximation that the Raman shift is small which implies $\omega_L \approx \omega_R$, this can further be simplified as below. The approximation is also justified by the optical reciprocity theorem discussed elsewhere [74].

$$G_{EM}\alpha \left| \mathcal{E}_{Loc}(\omega_L) \right|^4 \tag{1.27}$$

It has to be noted that the origin of EME is same for both the cases i.e., the excitation of LSPR in metal nanoparticles by the incident electromagnetic field.

1.4.2. Chemical Enhancement

While EME is an attribute of metal nanostructures, CME depends on the molecule and nanostructure interaction and hence the enhancement is subjective. The origin of CME in SERS is believed to be the change in polarizability of the molecule due to chemical/physical changes after its interaction with the plasmonic material. The exact magnitude of this enhancement, G_{CME} , depends on the molecule and metal combination and often ranges between 10^2 - 10^4 in magnitude. Though the contribution is relatively small compared to EME, it plays a crucial role in SERS as it often causes anomalies like shifts in expected Raman modes, and enhancement of specific modes while quenching few. The details of the mechanism and the different ways in which the polarizability is changed are discussed elsewhere [75], [76], [77], [78]. Broadly, these are described as 'charge transfer mechanisms' in which the electronic charge around the molecule is slightly perturbed in the presence of the nanostructure as shown in figure 1.5 depending on the interacting between the two [77].

Molecules in the SERS technique are adsorbed on the metal nanostructure either through physisorption on chemisorption, the distinction of which is made on the basis of enthalpy of the process [79], [80]. Chemisorption often involves formation of a chemical bond and, hence, causes a stronger perturbation in the molecule's structure than physisorption. In

both the cases the change in charge distribution relative to that of free molecules induces change in the Raman polarizability and, hence, in the Raman modes cross section.

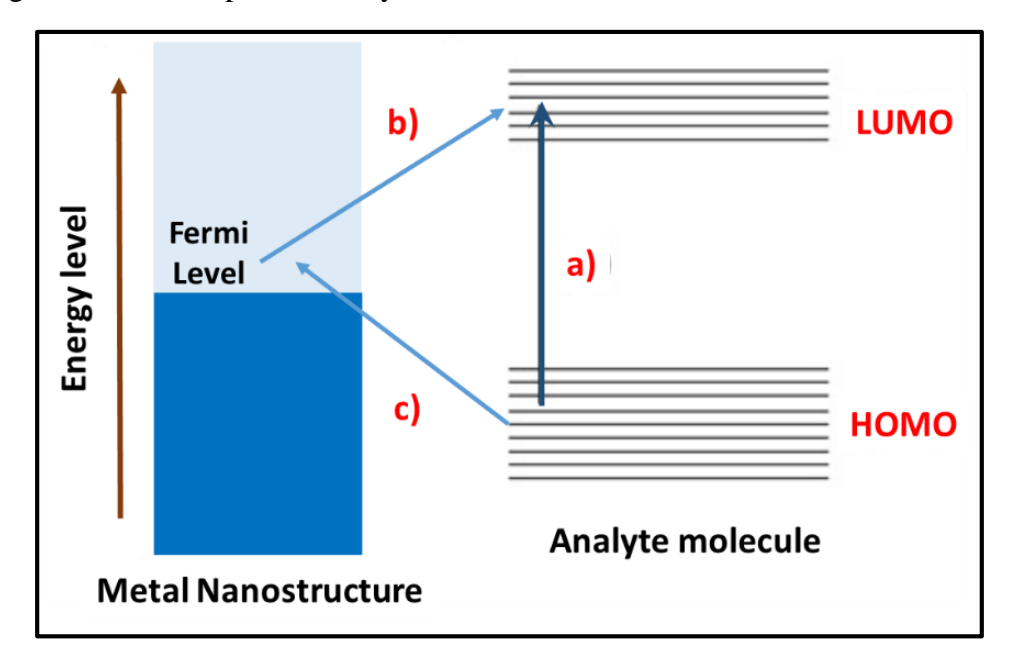


Figure 1.5: Illustration of chemical enhancement in SERS through charge transfer mechanism between analyte molecule and the metal nanostructure a) case of resonant excitation where laser energy is close to the electronic transitions of the analyte molecule. b, c) Photo driven charge transfer mechanisms between the Fermi and HOMO, LUMO energy levels [81].

The total enhancement in SERS, G_{SERS} , is a product of both electromagnetic and chemical enhancements and is summarised in figure 1.6.

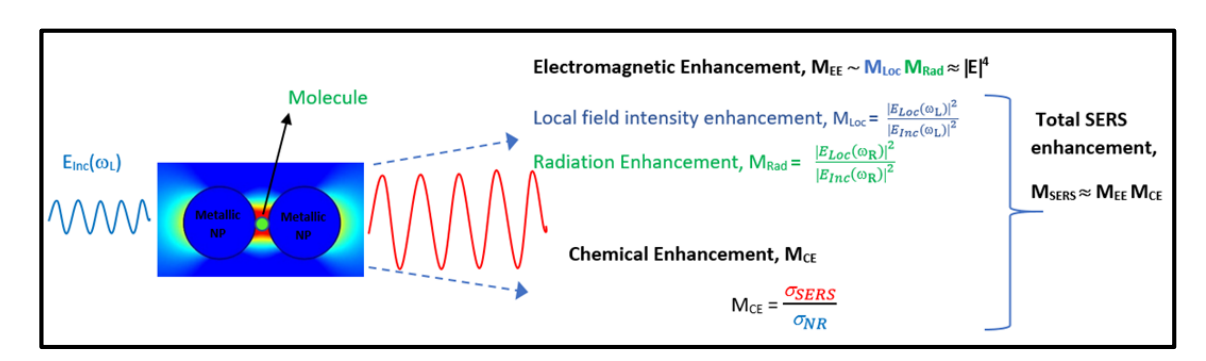


Figure 1.6: Illustration of a probe molecule at a SERS hotspot and associated electromagnetic and chemical enhancement contribution to signal enhancement in SERS.

1.4.3. Calculating Enhancement Factor

The SERS Enhancement factor (EF), is defined as,

$$EF = \frac{I_{SERS}/C_{SERS}}{I_{NR}/C_{NR}}$$
 (1.27)

Where I_{NR} , I_{SERS} stands for intensity under normal Raman and SERS conditions respectively while C_{NR} and C_{SERS} represents concentration of the analyte in normal Raman

and SERS respectively. C_{SERS} is the lowest concentration of analyte that has been detected using the substrate. I_{SERS} is the peak intensity of prominent vibrational mode for the analyte under study. It has to be noted that the I_{NR} and C_{NR} have to be measured under same experimental conditions like power, acquisition time and spot size as SERS. C_{NR} is the concentration of the same analyte as SERS and is usually in milli molar. I_{NR} is the peak intensity of prominent vibrational mode under Raman conditions [65]. These measurements have to be performed on the blank i.e., structure without the plasmonic nanostructures.

The enhancement factor calculated this way is only a lower limit and is often the modest way to have an estimate. Not all molecules in the collection area contribute to the SERS effect. Only a fraction of molecules adsorbed on the nanostructures will result in the enhancement. In order to estimate the fraction of adsorbed molecules, adsorption studies become relevant. An upper estimate can be calculated by modelling the adsorption of the molecules on the SERS substrate. The Analytical Enhancement Factor is defined as,

$$AEF = \frac{I_{SERS}/N_{SERS}}{I_{NR}/N_{NR}}$$
 (1.28)

Here, I_{NR} , I_{SERS} stands for intensity under normal Raman and SERS conditions respectively while N_{NR} and N_{SERS} represents number of molecules contributing to I_{NR} and I_{SERS} , respectively. N_{SERS} is calculated as follows [82],

$$N_{SERS} = \eta \ N_A \ C_{SERS} \ V_a \frac{A_{laser}}{A_{total}} \tag{1.29}$$

Where, η is the adsorption factor found by fitting the concentration and intensity data to an adsorption isotherm like Langmuir. C_{SERS} is the lowest concentration detected in SERS and A_{laser} , A_{total} are the laser spot size and area covered by the analyte molecule, respectively. N_A is the Avogadro number and V_a is the volume of the analyte drop casted. N_{NR} is measured on the blank substrate as follows,

$$N_{NR} = N_A C_{NR} V_a \frac{A_{laser}}{A_{NR}} \tag{1.30}$$

From equations (1.28), (1.29) and (1.30), AEF is given as,

$$AEF = \frac{I_{SERS}}{I_{Raman}} \frac{N_{Raman}}{N_{SERS}} = \frac{I_{SERS}}{I_{Raman}} \frac{C_{NR} \times A_{NS}}{\eta \times C_{SERS} \times A_{total}}$$
(1.31)

The adsorption factor is always less than one and hence the EF calculated this way is always higher than the one calculated without taking adsorption into account. This method of calculating EF ensures that we take into account only those molecules that are adsorbed on the nanostructure.

1.5. Factors that influence SERS

In order to understand different factors like size, shape, material and distance between nanoparticles on SERS enhancement, COMSOL Multiphysics based simulations have been performed. The simulations were performed in RF module with Electromagnetic Wave physics. This module solves Maxwell's equations for a given system in the frequency domain. The simulations steps performed are described below and illustrated in figure 1.7.

- Geometry of the problem is built including the perfectly matching layers (PML) layer. Only a quarter of the geometry was simulated to reduce memory usage and time. Boundary conditions were imposed at the interfaces to account for the symmetry of the problem. A PML shell of half the wavelength is used for the study. Changing the thickness however did not change the output parameters except the quality of the near field of the nanoparticle.
- Materials of the domains under study were defined. Optical constants of gold and silver were defined using values from the most widely used literature by Johnson and Christy [56]. Interpolation function was used to incorporate the same. The surrounding medium is defined as air ε=1 for both the cases.
- The geometry was discretized using physics-based meshing in COMSOL. The sequence generated was edited to optimise the results. Mesh size was chosen such that the output parameters are unchanged on further fine meshing. A detailed mesh refinement study can be pursued with a parametric sweep on element size; however, this comes at a cost of memory and computation time.
- Physics of the problem is defined with an input plane wave sweeping a range of wavelengths under study. The problem is formulated for scattered field and accordingly scattering boundary conditions were defined.
- The extension, scattering, absorption coefficients and cross sections were defined.

 The quantities were derived from Mie theory and taken as it is [83]. The absorption cross section region is defined as the volume of the nanoparticle because it is a near

field property. Similarly scattering cross sections are defined at the internal PML layers because it is a far field property. The relation between absorption/extinction/scattering coefficient and cross section is given as,

$$Q_{NP} = \frac{\sigma_{abs/scat/ext}}{\sigma_{geometric}}$$
 (1.32)

• A parametric sweep across wavelengths of interest is defined in the study section.

The wavelength is varied in steps of two for both gold and silver.

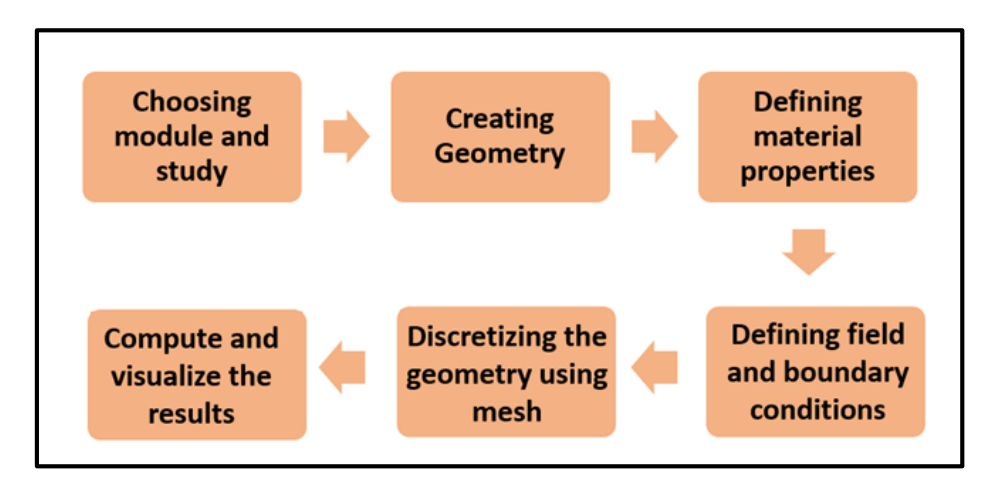


Figure 1.7: Flowchart for simulations performed in COMSOL Multiphysics.

1.5.1. Effects of Material

The choice of right material is key for SERS applications and a good plasmonic material is characterised by its enhancement, ease of use and durability. Ag, Au and Cu are the widely used plasmonic materials in the visible and near-IR region while aluminium is preferred in the UV region [84] [85] owing to the desirable nature of the dielectric functions of these metals in those regions as shown in figure 1.8. Different combinations of these metals as alloys and in different morphologies like spheres, triangles, stars, dendrites and cubes were used to maximise the enhancement in SERS.

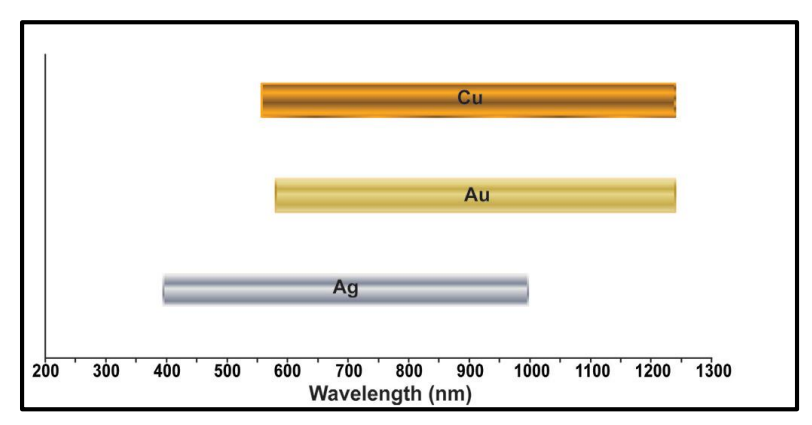


Figure 1.8: Plasmonic region of interest for Ag, Au and Cu where there are extensively used in SERS. Figure adapted from the reference [86].

Using COMSOL, we have studied the LSPR in the case of Ag, Au, Ag-Au core-shell, and alloy nanoparticles. This is because recently there has been an increase in usage of bimetallic Ag-Au nanoparticles employing their synergic benefits of enhanced stability and optimum enhancement with a choice of tunability in the SERS [87]. The dielectric function for simulating the alloy nanoparticles is taken from elsewhere [88]. For alloy nanoparticles, it is seen that the LSPR red shifts with increasing Au composition as shown in figures 1.9 a), 1.9 b). This knowledge is often used in choosing the right alloy nanoparticles with suitable resonance in order to increase the SERS enhancement. Similarly, Ag@Au and Au@Ag core-shell nanoparticles also offer a wide range of tunability in the visible region by varying the thickness of the shell as shown in figures 1.9 c), 1.9 d). Recently there has been a growing interest in usage of hybrid and flexible plasmonic materials as enhancers in SERS [89]. Ag-TiO₂ based SERS trace detection has been shown to achieve higher sensitivity through photo induced mechanisms in the transition metals [90]. Shell isolated nanoparticle enhanced Raman spectroscopy (SHINERS) have also been used with a combination of coinage metals, transition metals and semiconductors [91] [92]. The usage of 2-D materials such as graphene oxide, hBN, and MoS₂ in hybrid SERS substrates for greater stability and enhancement through chemical mechanism has also seen a rise [93] [94]. In this thesis, Ag, Au and their combinations are extensively used as SERS substrates both in colloidal form and as rigid substrates. In one study Cu nanostructures were also used for trace detection of explosives as a low-cost alternative to Ag and Au.

1.5.2. Effects of Size of Nanoparticles

The LFIE is the main mechanism that governs the enhancement in SERS. As size of the nanoparticle increases the restoring force decreases resulting in the red shift of the LSPR resonance. This shift in LSPR with the size of the nanoparticles and is studied using COMSOL Multiphysics for both Ag and Au nanoparticles. The red shift in resonance with increasing size can be seen in both the cases. However, the shift is greater in the case of Ag than Au. Also, silver has higher quality of resonance than gold, accounting for the fact that $Im[\epsilon(\lambda)]$ is relatively high for gold in the visible region. This leads to increased absorption and hence damping of oscillations in the case of gold. It can also be seen that the resonance broadens with increasing size implying decreased quality factor. The broadening is due to radiation effects. This can further be noticed with increase in scattering cross-section with increasing size. Absorption dominates for small particles and

scales slower whereas scattering is greater for bigger particles. Multipole resonances can also be seen with increasing size. The longest resonance in this case corresponds to the dipole resonance. The red shift in dipolar resonances reduces the overlap of the multipolar resonances. Figure 1.10 shows the extinction spectra of Ag and Au nanospheres for different sizes. It can be seen that the redshift in resonance is greater for silver than gold. This can be ascertained to higher optical absorption in gold in the visible region. From equation (32), the extinction cross-section for 10 nm Ag sphere at resonance can be estimated as, 10^{-15} m². Similarly, for 10 nm sized Au nanosphere the extinction cross-section is estimated as 10^{-16} m².

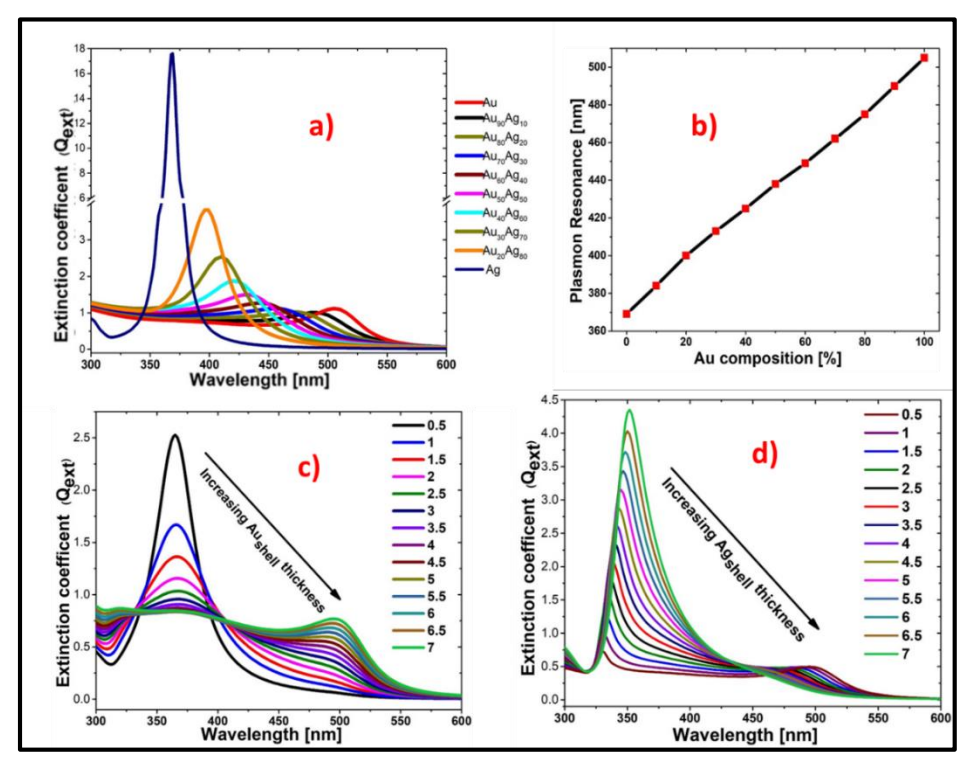


Figure 1.9: Extinction spectra of a) c) Ag-Au alloy nanoparticles of size 10nm with varying compositions. b) Inset shows the LSPR of the alloy nanoparticles as a function of the Au composition. c) Ag@Au core-shell nanoparticles with varying Au thickness. b) Au@Ag core-shell nanoparticles with varying Ag thickness.

The red shift in resonance with increasing size is plotted in figure 1.11 a) for both Ag and Au. It can be seen that the shift is greater in the case of Ag (360 to 470 nm) than Au (510 to 560nm). This is attributed to the low radiation/retardation effects in Au as opposed to Ag attributing to the difference in the $Im[\epsilon(\lambda)]$ in both [10]. The field enhancement along the polarization direction of the incident field is also studied and the relative field is plotted in figure 1.11 b). The field characteristics indicate a sharp enhancement in the vicinity of the nanoparticle followed by an exponential decay in the intensity with distance from the

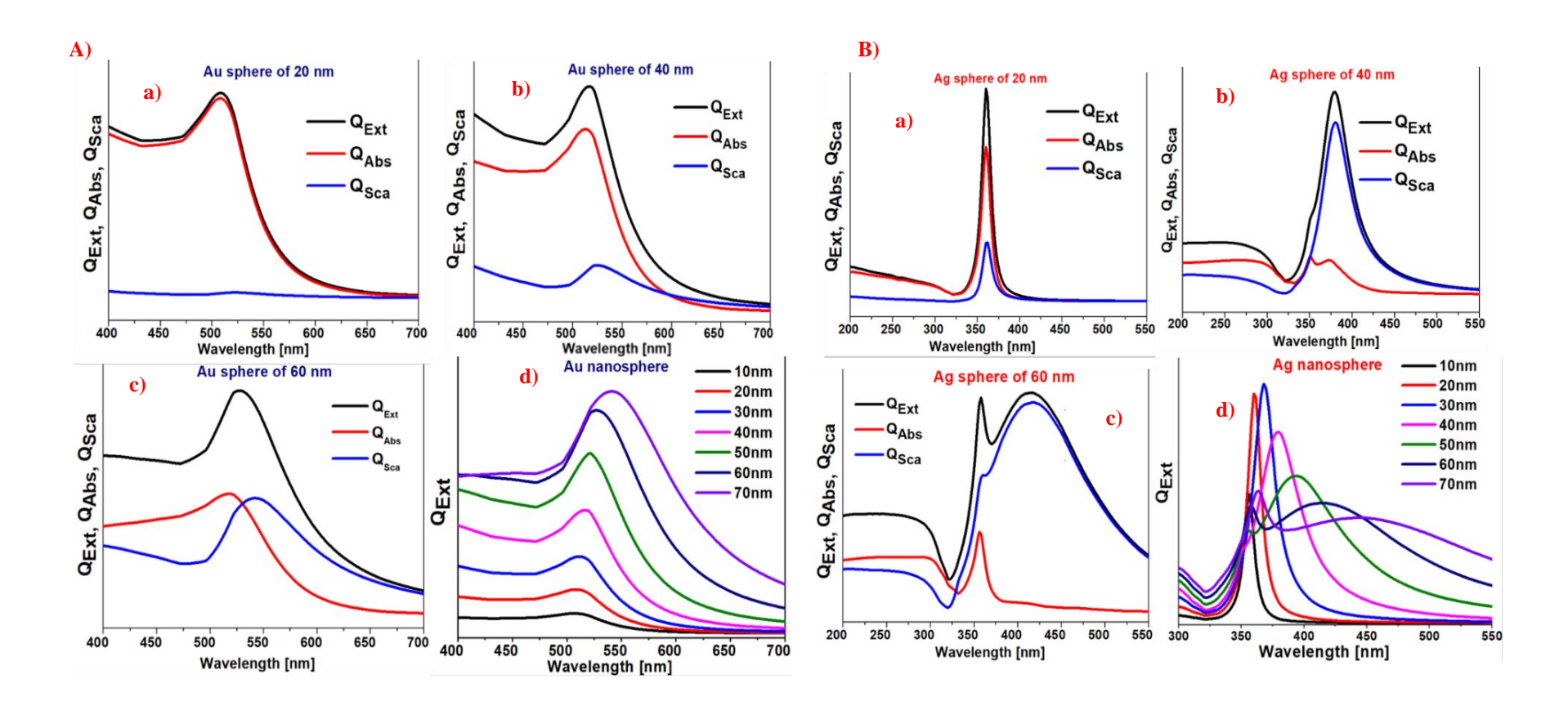


Figure 1.10: Calculated extinction (Q_{Ext}), absorption (Q_{Abs}), and scattering (Q_{Scat}) spectra, surrounded by air, of A) Au for a) 20 nm b) 40 nm c) 60 nm and d) extension spectra for all sizes as indicated in the figure. B) Ag nanospheres of size a) 20 nm b) 40 nm c) 60 nm and d) extinction spectra for all sizes.

nanoparticle. This re-emphasis the localization of hotspots in SERS and the importance of having a substrate with high density of hotspots for achieving trace detection.

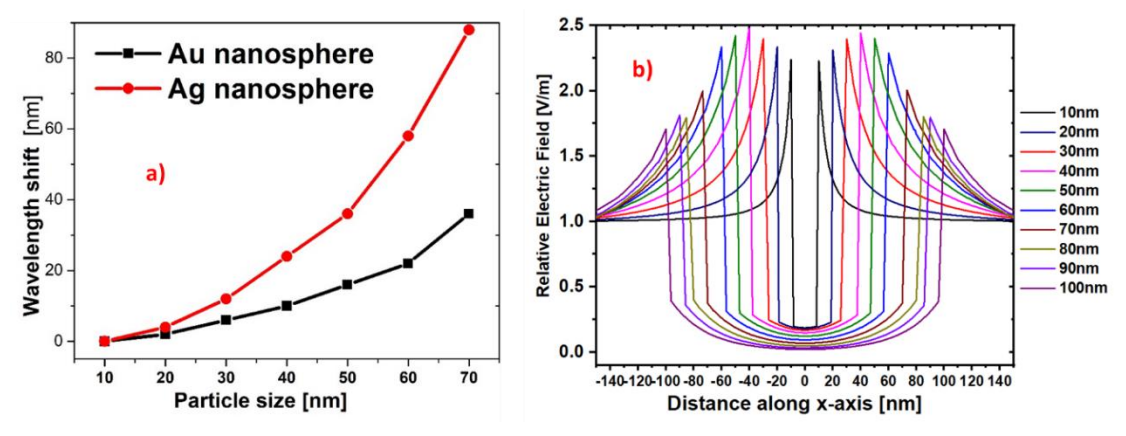


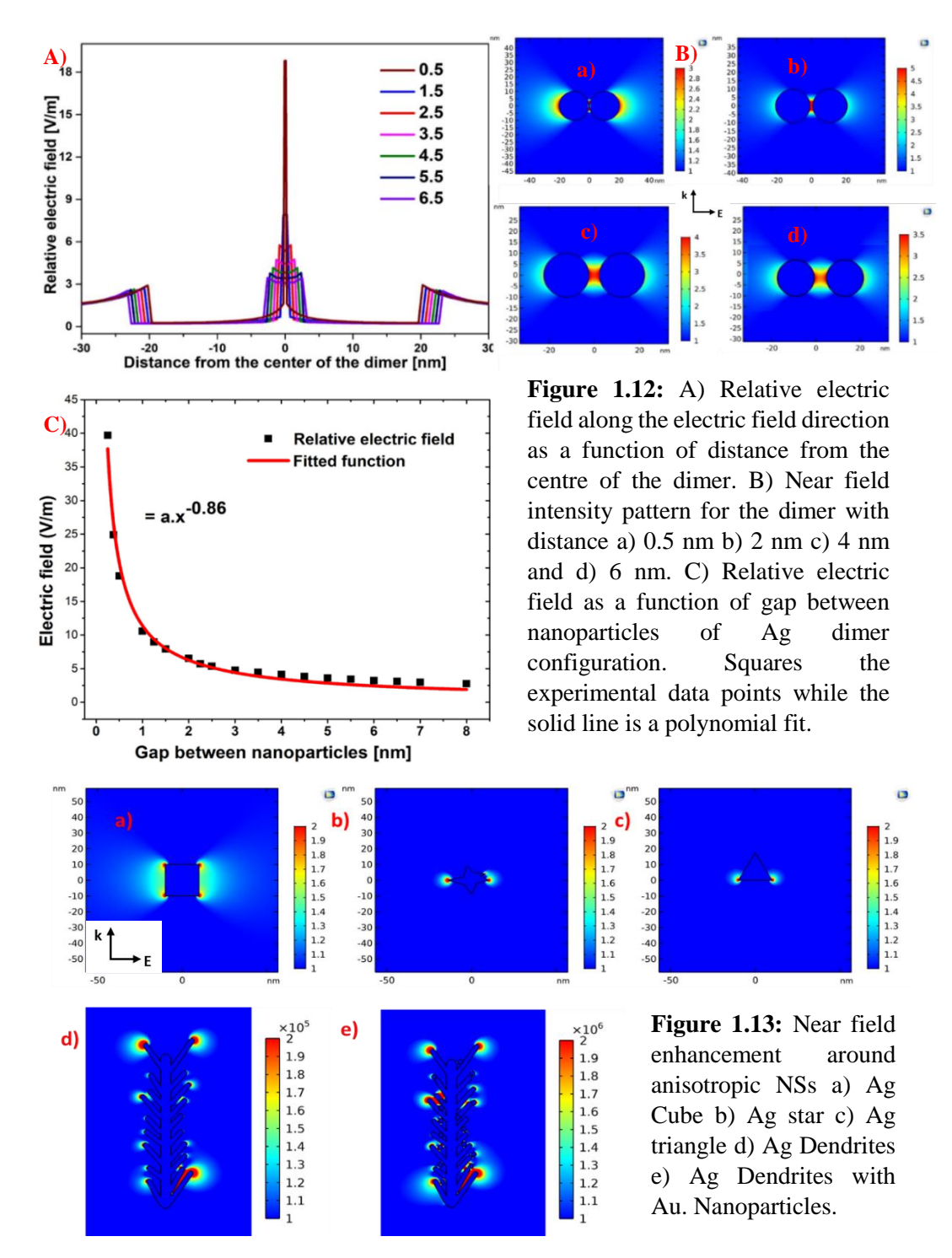
Figure 1.11: a) LSPR resonance as a function of particle size for Ag and Au nanoparticles, b) Local field intensity as a function of distance from the nanoparticle for Ag sphere.

1.5.3. Effects of distance between the Nanoparticles

Trace detection in SERS hugely benefits from the localized intense electric field regions called as hotspots. Hotspots are formed between the junction of two or more nanoparticles and a molecule is in the vicinity of these hotspots benefits from the intense field. SERS signal generated by a single molecule at a hotspot is the same as the SERS signal generated by 580 molecules randomly adsorbed on the surface [95] [10]. These hotspots, however, are commonly distributed randomly on the substrate surface and the inhomogeneous adsorption of the molecules adds further to the randomness. SERS suffers from poor reproducibility because of the localization of these hotspots. Laser illumination also changes the shape, size, and distance of these hotspots, contributing to further signal variations [96]. Using COMSOL, we have studied the effects of distance between the nanoparticles on the field intensity for the case of two 10 nm Ag spheres. Field intensity plotted in figure 1.12 a) clearly indicates that aggregation of nanoparticles indeed facilitates high density and quality hot spots facilitating lower detection limits [97]. Figure 1.12 b) presents the near field intensity pattern for different distances between the dimer configurations. In order to understand the near field enhancement in case of a dimer configuration, we have simulated two Ag nanospheres by varying the gap between the two nanoparticles. The maximum field enhancement as a function of distance is shown in the Figure 1.12 c). It has been found the relative the relative electric field varies as $1/r^{0.86}$ where r is the distance between the nanoparticles.

1.5.4. Effects of Shape of the Nanoparticles

The intensity of the local field enhancement through the localised surface plasmon resonance depends hugely on the morphology of the NP [98] [99] [100]. Lightning rod effects are thought to be responsible for the enhancement of electric fields at metallic tips [101]. In a study using star, triangular and spherical nanoparticles, it was found that the star nanoparticles outperformed the other two in terms of enhancement and limit of detection [97]. Surface area to volume ratios are useful indicators of electron density,



which is proportional to electrostatic fields. Owing to this, the electric field enhancement effect of metallic nanoparticles increases as their edges sharpen. COMSOL Multiphysics has been used in order to simulate near field enhancement around different anisotropic structures as shown in figure 1.13.

1.5.5. Experimental Parameters

SERS efficiency depends on various experimental parameters like excitation wavelength, spot size of the laser on the substrate, laser power, and polarization. Choosing a right wavelength is crucial for SERS to maximise the enhancement. As suggested by equation (23), Raman power is inversely proportional to λ^4 and, hence, it may appear that shorter wavelengths are suitable for higher signals. However, in order to quench fluorescence, which is a major competitor for SERS during measurements, it is always better to choose longer wavelengths like the IR. Longer wavelengths, in addition, are also known to offer better signal to noise ratio. Shorter wavelengths also mean a smaller Raman shift which demands a spectrometer with higher resolution. Choosing a wavelength close to the LSPR resonance of the metal substrate or to the absorption of the probe molecule is known to enhance the signal further through what is popularly called as SERS [21]. Spot size of the laser on the substrate determines the number of probe molecules that are contributing to the signal. A larger spot size would average signal over large number of molecules in various hotspots and all result in good reproducibility. A small spot size just at the hotspot is ideal for trace detection and single molecule SERS. In order to supress fluorescence and also prevent the damage of the substrate, it is always ideal to work at low powers in SERS.

1.6. Machine Learning for SERS

Human brain identifies and predicts through observations and learnings. Through machine learning, this job is outsourced to a computer through a program or an algorithm. The programs are trained though large data sets in order to recognise patterns and make accurate predictions on things that are unknown. An early example of a machine learning algorithm is a model that filters spam emails through key words. Depending on the type of datasets and the models used, machine learning techniques are broadly classified into supervised, unsupervised and reinforcement models as shown in figure 1.14. In supervised models labelled data is given to the model for training and educated predictions were made on unlabelled data sets. Unsupervised models are built to discover patterns and relationships in unlabelled data sets and are often used for clustering and dimensionality

reduction. Reinforcement models attempt to solve real world problems through a path that maximises reward and minimises the error.

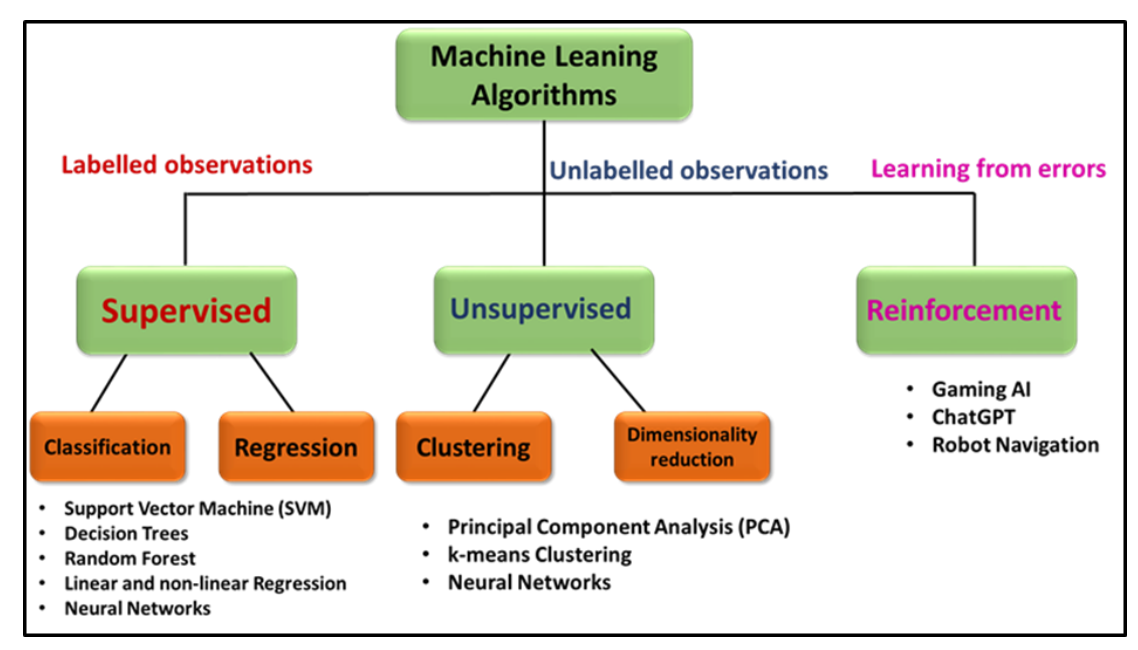


Figure 1.14: Schematic of classification of different machine learning algorithms.

Machine learning (ML) techniques have gained popularity in different fields including spectroscopy for pre and post data processing recently. The wide availability of Raman/SERS data and computation facilities has enabled this rapid progression [102]. SERS has witnessed a huge surge in the usage of different ML algorithms both supervised and unsupervised, to overcomes many existing challenges and improve data collection and analysis. This trend is desirable given the complexity of existing SERS challenges, including trace detection, signal fluctuations, quantification, and identification, which involve many variables and require an analytical tool that can capture patterns without expert input [103]. Trace detection involves identifying faint signals from a noisy background, making it a task that can benefit from ML assistance. In the case of biomolecules, background contributions from undesirable components interfere with the signal, necessitating ML algorithms to extract useful information [104]. SERS also experiences inherent signal fluctuations due to the localization of hotspots and the dynamics of molecules and substrate adsorption which can be circumvent by using appropriate ML models [105] [96]. The intrinsic signal variations in SERS makes it challenging to quantify the analyte under where simple linear analysis is not promising given that the intensity and analyte concentration is dominantly nonlinear. Thus quantification and the process of identification of chemical composition can be addressed by using ML [23]. In addition, ML in SERS can also be used to improve data collection,

overcome signal fluctuations, enhance on-site usability, estimate the effect of scattering, and even enhance the SERS signal itself [106] [107] [108] [109]. Principal component analysis (PCA), support vector machine (SVM), partial least squares (PLS), decision trees (DTs), and convolutional neural networks (CNNs) are a few common ML approaches. Figure 1.14 illustrates these techniques. PCA is a dimensionality reduction method that maintains components that are typical of the data with high variance. It is frequently applied as a pre-processing step to simplify models or as a classification method. [110]. SVM is a nonlinear machine learning approach that may be used for both regression and classification. It works by employing a kernel function to find a hyperplane that separates two or more classes. [111]. PLS is useful for quantitative studies when the data set is small and the number of variables is large, as it still extracts useful information [112] [113]. DTs are commonly used for data classification using bootstrapping [114], while CNNs employ filters and pooled layers in their architecture, often used for modelling large data sets with images [115].

1.7. Molecules Studied in This Thesis

Different molecules including explosives, biomolecules and dyes have been studied in this thesis works. Each SERS substrate that has been fabricated has been first characterised using dye molecules as they offer higher Raman cross sections due to the presence of free electrons. Explosive molecules can have various structures depending on the type of explosive. However, most explosive molecules share some common characteristics. They typically contain a large amount of potential energy stored in their chemical bonds, which can be rapidly released in an exothermic reaction. One common structural feature of explosive molecules is the presence of a highly reactive functional group, such as nitro (-NO₂) or azide (-N₃). These groups contain high-energy nitrogen-oxygen or nitrogennitrogen bonds that can be easily broken, releasing a large amount of energy in the process. Explosive molecules can exist in different states, such as solid, liquid, or gas, and their chemical and physical properties can vary depending on their state. Kanamycin, penicillin, and ampicillin are three different types of antibiotics with distinct chemical structures and modes of action studied in this thesis. Kanamycin is an aminoglycoside antibiotic that is effective against a wide range of gram-negative and some gram-positive bacteria. It consists of a complex ring structure with several amino groups and sugar residues. The active functional groups allow kanamycin to bind to the bacterial ribosome and inhibit protein synthesis, leading to bacterial cell death [116]. Penicillin is a beta-lactam antibiotic

that is effective against a variety of bacterial infections. It is composed of a beta-lactam ring fused to a thiazolidine ring [117]. The beta-lactam ring is crucial to the antibiotic's function, as it binds to and inhibits the activity of bacterial enzymes called penicillinbinding proteins (PBPs). These enzymes are responsible for synthesizing the bacterial cell wall, and inhibition of their activity leads to the disruption of bacterial cell wall formation, eventually leading to cell death. Ampicillin is a semi-synthetic penicillin derivative that is similar in structure to penicillin, but with an additional amino group. This modification increases the antibiotic's effectiveness against gram-negative bacteria by allowing it to penetrate the outer membrane of these bacteria. Adenine and cytosine are two of the four nitrogenous bases that make up the genetic code of DNA (the other two being guanine and thymine). Adenine and cytosine are both classified as purine and pyrimidine bases, respectively. The structure of adenine consists of a purine ring system, which is composed of two fused rings. Adenine also contains two functional groups - an amine group and a carbonyl group - attached to the purine ring. The amine group is responsible for forming hydrogen bonds with the thymine base in DNA, while the carbonyl group participates in the formation of the phosphodiester bonds between nucleotides in the DNA backbone. The structure of cytosine, on the other hand, consists of a single pyrimidine ring with a carbonyl group and an amine group attached to it. Like adenine, cytosine can form hydrogen bonds with its complementary base in DNA (guanine). Thiram is a chemical compound belonging to the class of fungicides in agriculture to control various fungal diseases in crops. The chemical structure of thiram is also notable for its Sulphur atoms, which are responsible for the compound's strong odour. The distinctive smell of thiram is often used as a warning signal to indicate the presence of the chemical in products such as treated seeds. Naphthalene is an aromatic hydrocarbon with the chemical formula and is a common water contaminant [118]. The structure of naphthalene consists of two fused benzene rings. Each benzene ring is composed of six carbon atoms and six hydrogen atoms arranged in a hexagonal ring structure. In naphthalene, these two benzene rings are fused together by sharing two adjacent carbon atoms, forming a structure that resembles a figureeight. Melamine is an organic compound with the chemical formula and is a white crystalline solid. It is a common food adulterant especially in the milk raising health concerns recently [119]. The molecule has six amine functional groups (-NH₂) attached to the nitrogen atoms and three carbonyl functional groups (-C=O) attached to the carbon atoms. Figure 1.15 depicts the structures of all the molecules studied in this thesis using the molecules studied in this thesis using Gaussian software with appropriate basis

function optimised for the state of minimum ground state energy. In addition to these molecules, SERS substrates were also used for the detection of live bacteria, Escherichia coli, commonly known as E. coli. E. coli is a rod-shaped bacterium that is commonly found in the lower intestines of warm-blooded organisms and is also a common water contaminant raising public health concerns. It is a single-celled prokaryotic organism with a simple internal structure and made up of different proteins, lipids, nucleoid, ribosomes, and plasmids. The whole organism Raman spectra depends on the composition of these contents and varies from species to species and, hence, offers a way to identify them through vibrational spectrum.

1.8. Challenges and Thesis Motivation

SERS, as discussed above, is a powerful evolving tool for trace detection of explosives and biomolecules. Despite all its advantages, there are many challenges associated with SERS standing in the way of translating the benefits to the real world [96]. SERS signals are known to have poor spatial reproducibility owing to inhomogeneous distribution of hotspots, random adsorption of molecules on the metal structure, coupling of the molecule with the substrate etc. [120], [121]. Periodic and predictable structures like those produced by e-beam lithography and laser ablation that are ligand free (pure) are promising in this regard [29]. The SERS substrates as they involve noble metals like Ag, Au and Pt are known to be expensive and are often not reusable and durable as they are prone to rapid oxidation. The cost of the substrates can be brought down drastically if instead a semiconductor material like Si is used as the base material with deposition of Ag/Au by different methods [122]. The combination of Ag and Au is also known to prevent rapid oxidation of the substrates thus increasing their durability [21]. Often on field it is advantageous to have a flexible substrate that would enable swabbing the surface. A flexible substrate is defined as something that is easy to bend and fold [123], [124], [125].

SERS is also known to have inherent signal fluctuations because of very factors that are known to enhance the SERS signal. The hotspots that lead to signal enhancement through electromagnetic effects are localised to small areas causing point to point signal variations in SERS [126], [127]. These hotspots are also known to evolve under the presence of laser light causing signal 'blinking' in SERS [96]. The vibrational spectrum in SERS is also different from Raman with significant peak shifts and enhancement/quenching of certain modes depending on the adsorption, orientation of the molecule with respect to the metal

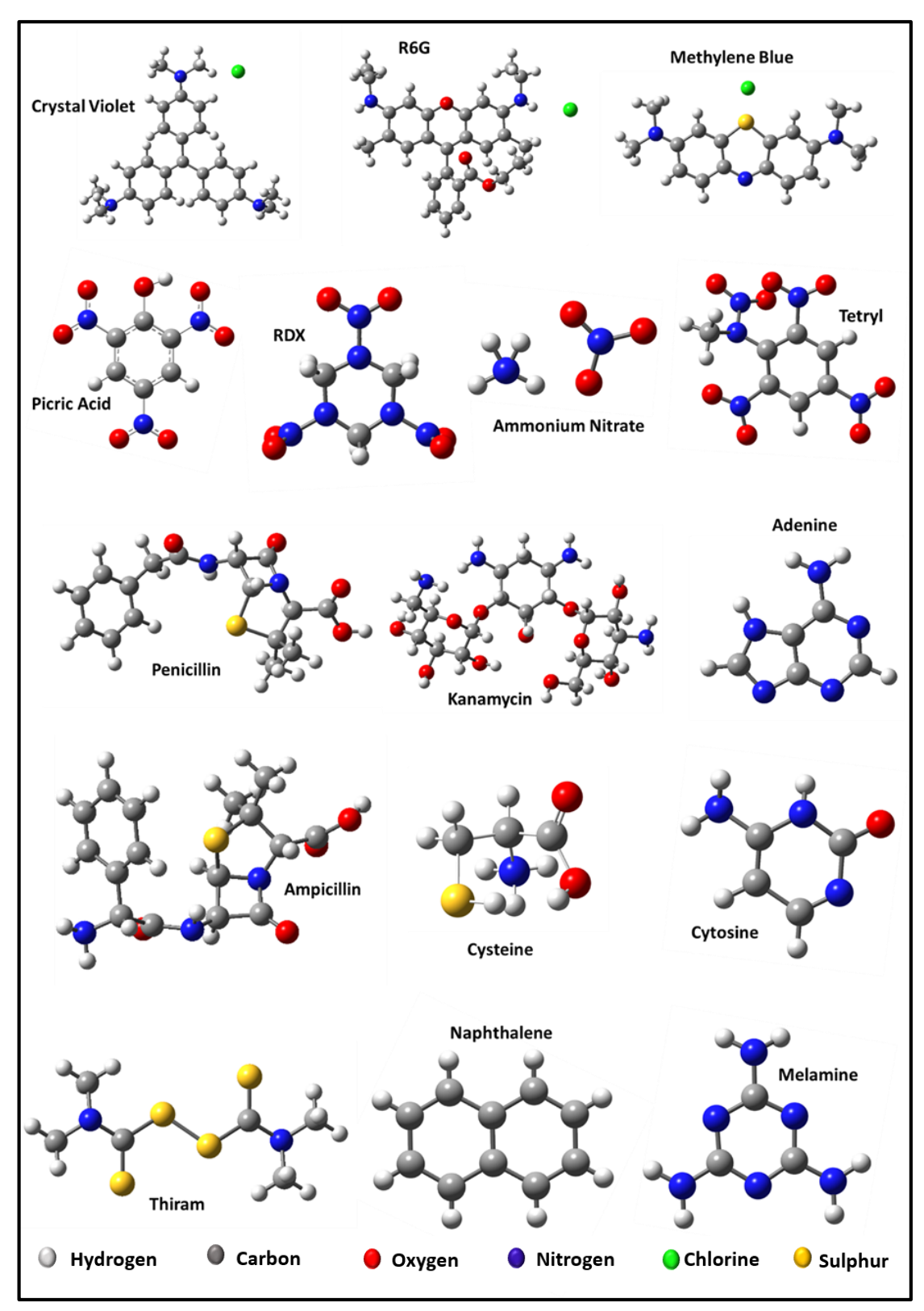


Figure 1.15: DFT optimized structures of different molecules studied in this thesis.

nanostructure. In many applications, it is also useful to quantify the trace analyte that is being studied using SERS. However, the signal intensity and quantity of analyte is non-linear and is complex for the signal blinking effects in SERS. Going beyond the detection

limit of fabricated plasmonic substrates to achieve ultra-trace sensitivity involves changing the experimental parameters like choosing the right wavelength. Resonant excitation in the case of SERS is known to enhance the SERS signal further by at least 10^6 times [10]. With a combination of ultrafast lasers, novel methods for low-cost synthesis of durable and flexible SERS substrates and machine learning techniques, this thesis attempts to address these challenges at various levels as discussed in detail in each chapter as shown in figure 1.16.

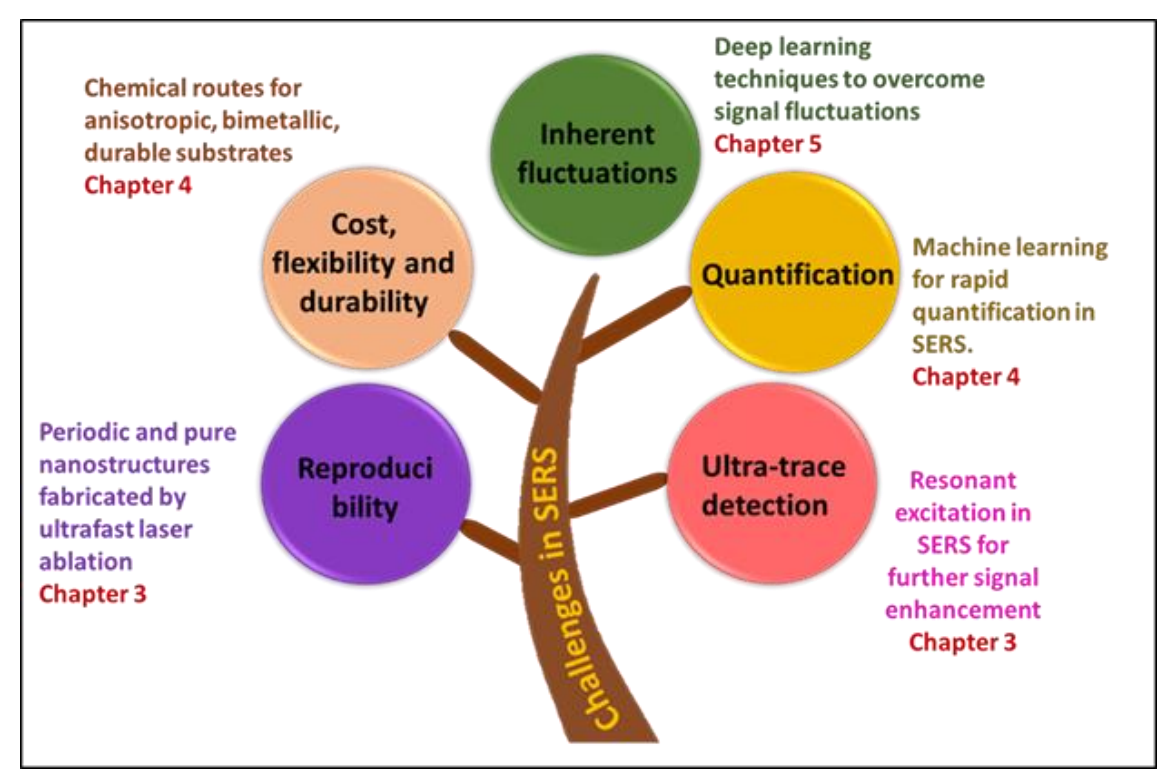


Figure 1.16: Schematic of different challenges in SERS and different chapters presented in the thesis addressing the challenges.

1.9. Rest of the Thesis Outline

Chapter 2: Synthesis and Characterization Techniques

This chapter primarily focuses on various techniques for fabrication/synthesis and characterization that were utilized throughout the study. Specifically, the synthesis and mechanisms for the formation of plasmonic nanostructures through ultrafast laser ablation in air and different chemical methods are discussed in detail. Additionally, different characterization techniques such as FESEM, TEM, UV-Visible spectroscopy, and contact angle measurements are elaborated upon, as they were used to analyse the nanoparticles. The chapter also includes comprehensive descriptions of two Raman instruments, a portable system and micro-Raman system, along with the procedures utilized for SERS

measurements on both rigid and flexible substrates. Finally, the chapter provides detailed information on ultrafast laser systems (femtosecond amplifier and oscillator) and various pulse characterization techniques.

Chapter 3: Ultrafast Laser Ablated Plasmonic NSs for SERS

This chapter exclusively focuses on ultrafast laser ablated nanostructures and their application as highly reproducible SERS substrates. Different nanostructures were prepared using laser ablation of Si, Ag, Ag-Au and Cu using both femtosecond laser amplifier and oscillator. The work done in this chapter attempts to overcome the challenge of reproducibility in SERS using the advantage of periodic structures resulting from the ultrafast laser ablation.

Chapter 3.1: Using femtosecond laser oscillator (140 fs, 800 nm, 80 MHz), web-like structures were fabricated on Si via laser ablation in air. The nanostructures formed on Si exhibited unique web-like structures where the nanoparticles self-assembled into nanochains, interweaving closely. The effects of different laser parameters like fluence, scan speed (number of pulses per spot) on the formation of these structures were studied in detail. It was understood that there is a threshold fluence for the formation of these web-like structures. The size of the nanoparticles within the nanochains was found to increase with increasing the scan speed. The mechanism for the formation of these web-like structures in the case of high repetition rate is understood and is presented in detail. These structures were further coated with thin layer of Au (~10nm) using thermal vapour evaporation and used as SERS substrate with methylene blue as the probe molecule. The web-like structures demonstrated better enhancements than plain Au coated Si substrates owing to the chemical enhancement from the Si nanostructures and resulted in 1 μM sensitivity. As opposed to conventional laser ablation using amplifier systems, this is low-cost alternative for plasmonic SERS substrates.

Chapter 3.2 describes the SERS substrates that were prepared for these studies using femtosecond laser (800 nm, 50 fs, 1kHz) ablation of Ag-Au (1:1) in air. The effect of angle of incidence on the formation of the nanostructures for 0°, 10°, 20°, and 30° has been studied. The investigation of a potentially explosive chemical (picric acid), two dye molecules (rhodamine 6G, crystal violet), and an amino acid (cysteine) using surface enhanced resonance Raman spectroscopy (SERRS) is the main emphasis of this study. These molecules were first analysed using UV-Visible spectroscopy to understand the

absorption regions. Accordingly, laser excitation close to the resonance were chosen in order to achieve ultra-trace detection limits. It has been investigated how the SERRS performance of the laser-ablated structures changes with the ablation angle. The ideal structure was applied to more studies on different analytes. Surface debris is frequently produced by laser ablation in the air and is eliminated before employing them for the application. But here, we have looked at the widely contested link between enhancement and repeatability, with the benefit of having randomly stacked nanoparticles in debris and periodic substrates without debris. An inverse link between enhancement and repeatability in SERS has been discovered using statistically significant data (5000 spectra for each), employing the benefit of two substrates from a single experiment. Rhodamine 6G, crystal violet, picric acid, and cysteine were shown to have substrate sensitivity values of 10 fM, 100 fM, 100 nM, and 100 nM, respectively, with high repeatability [21].

Chapter 3.3 presents studies carried out on ultrafast laser ablation, using an amplifier system (50 fs, 1kHz, 800 nm), of Ag and Cu in air using cylindrical focusing conditions. Under cylindrical focusing novel sand-dune like structures were observed on both Ag and Cu. The effects of laser fluence on the formation of these structures is studied. Further, the Cu nanostructures were utilised for the detection of two explosive molecules, Ammonium Nitrate and Tetryl (2, 4, 6-trinitrophenylmethylnitramine) and a dye molecule, Methylene Blue with sensitivities of 50 μ M, 100 μ M and 5 μ M. The Ag nanostructures exhibited superior reproducibility in the trace detection of two explosives, Tetryl and RDX, and one biomolecule, cytosine with sensitivity of 50 nM, 1 μ M and 100 nM respectively. The Ag structures have shown a superior reproducibility of 6% implying practical usability. These structures were also used for identification of different E. coli species based on SERS data using PCA.

Chapter 4: Novel flexible, Hydrophobic, Hybrid and Low-Cost SERS Substrates

The work presented in this chapter focuses on low-cost and durable SERS substrates that
were synthesised by simple chemical and physical methods.

Chapter 4.1 discusses anisotropic Ag and Ag-Au nanostructures that were fabricated by etching the Si in the presence of AgNO₃/ HAuCl₄ (metal salts). Effects of salt concentrations, duration of etching on the formation of highly anisotropic nanostructures were studied. These nanostructures were further coated with Au in a single step reaction which has significantly increased the durability and performance of the nanostructures as

SERS substrates. Extensive SERS mapping studies along with trace detection of different hazardous and bio molecules like dyes, DNA bases, antibiotics, pesticide and explosive will be presented. The sensitivity for CV, adenine, cytosine, penicillin G, kanamycin, ampicillin, AN, and thiram were found to be in the nanomolar regime for all the molecules. SERS data collected at regular intervals indicate that the substrates were stable for a period of 120 days when stored in ambient atmosphere. COMSOL studies to understand the near field enhancement in these structures will also be presented [30].

Chapter 4.2 focuses on Si nanostructures decorated with 2-D laser ablated MoS₂ as SERS substrates. Interesting MoS₂ morphologies were generated by femtosecond laser ablation of commercial MoS₂ powder in water, ethanol and methanol. Si nanowires decorated with bimetallic Ag-Au nanoparticles were synthesised by electroless etching method. These structures were characterised by FESEM, TEM and after layering with laser fabricated 2-D MoS₂ these hybrid substrates were utilised for trace detection of diverse analyte molecules like malachite green (MG) (0.5 nM), melamine (100 nM), naphthalene (300 nM), L-Cysteine (100 nM), tetryl (50 nM) and bacteria (Escherichia coli). The durability of the samples measured by collecting SERS data on different days indicated the stability of samples for 200 days. The results indicate that the MoS₂ has offered dual benefit of signal enhancement and increasing the durability of the substrates.

Chapter 4.3 highlights the novel hydrophobic plasmonic substrate that has been fabricated by a simple method of spin coating filter paper with Si oil. This is so far the cheapest and single step method to modify the wettability of filter paper. The spin coating time has been optimised to achieve a contact angle of 110° . Au nanoparticles that were fabricated by femtosecond laser ablation of gold in water were used as the plasmonic material. SERS data has been collected using portable Raman system for different concentrations of Picric Acid and Crystal Violet, sampling the whole substrate collecting nearly 900 spectra. Using non-linear machine learning models like principal component analysis (PCA) and support vector regression (SVR), the intensity and concentration SERS data has been modelled with an accuracy of 96% for CV and 94% for PA. This is a quick and inexpensive way to measure analytes by employing a portable Raman Spectrometer with a calculation time of less than 10 seconds [23]. This chapter also presents free standing porous Si decorated with Ag nanoparticles synthesised by wet etching method for trace detection of methylene blue, picric acid, ammonium nitrate, and thiram with sensitivities of 50 nM, 1 μ M, 2 μ M, and 1 μ M [124].

Chapter 5: Overcoming Signal Fluctuations in the SERS for Improved Field Applications

This chapter focuses on addressing the challenge of trace quantification and signal fluctuations in SERS using machine learning techniques. The work done in this chapter emphases on developing a deep learning model to overcome signal fluctuations in SERS and hence bridge the gap between lab and onsite performance. Three molecules, tetryl, crystal violet and picric acid were studied using Ag decorated Au nanodendrites (AuNPs@AgNDs) synthesised by chemical methods described in chapter 4. The experimental parameters of SERS like excitation wavelength, laser power, and spot size were systematically varied in order to simulate the general variation of experimental parameters in SERS across instruments. A deep learning model called Neural Network Aided SERS (NNAS) has been developed using the SERS data collected with mapping tool from the micro-Raman setup for three molecules, tetryl, picric acid and crystal violet. Using a signal to noise ratio threshold, each spectrum is labelled as representative and nonrepresentative devoid of expert's opinion. Out of sample predictions were also made to evaluate the model's performance and resulted in accuracy of 0.982, 0.981 and, 0.985 for CV, tetryl and, picric acid, respectively. The model has been compared with standard classification algorithm, SVM (accuracy 89%) and was found to outperform. The model has also been evaluated with a portable Raman spectrum and resulted in 100% accuracy indicating the cross functionality of the model. We think that our NNAS can close the performance gap that exists between onsite detection and lab-based SERS substrates [106].

Chapter 6: Conclusion and Scope

This chapter provides a comprehensive summary of the work carried out in the thesis, emphasizing the encountered challenges and potential for future improvements. It explores the possibilities of enhancing the COMSOL simulations described in chapter 1 to incorporate real-world scenarios, thus further optimizing the nanostructures. Furthermore, it outlines the potential for broadening the versatility of the substrates by extending their application to detect vapours and direct liquid samples and also the aspect of commercializing. Additionally, the discussion highlights the scope for improving chemical methods by extending their use to flexible substrates. Suggestions for enhancing the hydrophobic filter paper substrate, as detailed in chapter 5, are also presented. Moreover, the chapter elaborates on the possibilities of improving the machine learning models to

better suit real-world applications, while also exploring the limitations of the methods utilized for substrate preparation and characterization. We will discuss the scope of expanding the SERS applications towards diseases diagnosis as it has immense potential in enabling early detection of disease biomarkers [35][128].

References

- [1] R.P. Feynman, Plenty of room at the bottom, in APS annual meeting, (1959),1-7. Boston, MA, USA: Little Brown.
- [2] Barber D.J., Freestone I.C. An investigation of the origin of the colour of the Lycurgus Cup by analytical transmission electron microscopy, Archaeometry. 32 (1990) 33–45. https://doi.org/10.1111/j.1475-4754.1990.tb01079.x.
- [3] Church Architecture, New York Times, Availbale Online, https://archive.nytimes.com/www.nytimes.com/imagepages/2005/02/21/science/2 0050222_NANO1_GRAPHIC.html (accessed 18 March 2023).
- [4] T. Pradell, A. Climent-Font, J. Molera, A. Zucchiatti, M.D. Ynsa, P. Roura, D. Crespo, Metallic and nonmetallic shine in luster: An elastic ion backscattering study, J. Appl. Phys. 101 (2007) 103518. https://doi.org/10.1063/1.2734944.
- [5] S. Bayda, M. Adeel, T. Tuccinardi, M. Cordani, F. Rizzolio, The history of nanoscience and nanotechnology: From chemical-physical applications to nanomedicine, Molecules. 25 (2020) 112. https://doi.org/10.3390/molecules25010112.
- [6] M.D. Reibold M, Paufler P, Levin AA, Kochmann W, Pätzke N, Carbon nanotubes in an ancient Damascus sabre, Nature, 444 (2006), 286-286. https://doi.org/10.1038/444286a.
- [7] M. Faraday, On the relations of gold and other metals to light, Proc. R. Soc. London. 8 (1857) 356–361. https://doi.org/10.1098/rspl.1856.0094.
- [8] G. Mie, Beiträge zur Optik trüber Medien, speziell kolloidaler Metallösungen, Ann. Phys. 330 (1908) 377–445. https://doi.org/10.1002/andp.19083300302.
- [9] G. Barbillon, Plasmonics and its applications, Materials. 12 (2019) 10–13. https://doi.org/10.3390/ma12091502.
- [10] E.C.L. Ru, Principles of Surface Enhanced Raman Spectroscopy and Related Plasmonic effects, Elsevier (2008).
- [11] H. Yu, Y. Peng, Y. Yang, Z.Y. Li, Plasmon-enhanced light–matter interactions and applications, Npj Comput. Mater. 5 (2019) 45. https://doi.org/10.1038/s41524-019-0184-1.
- [12] S. Nivedha, P. Ramesh Babu, K. Senthilnathan, Surface plasmon resonance: Physics and technology, Curr. Sci. 115 (2018) 56–63. https://doi.org/10.18520/cs/v115/i1/56-63.
- [13] J.E.S. Fonsaca, M.P. Moreira, S. Farooq, R.E. de Araujo, C.J.S. de Matos, D. Grasseschi, Surface Plasmon Resonance Platforms for Chemical and Bio-Sensing, in: Encycl. Sensors Biosens., (2023), 316–353. https://doi.org/10.1016/b978-0-12-822548-6.00036-4.
- [14] Y. Chen, H. Ming, Review of surface plasmon resonance and localized surface plasmon resonance sensor, Photonic Sensors. 2 (2012) 37–49. https://doi.org/10.1007/s13320-011-0051-2.
- [15] M.E. Stewart, C.R. Anderton, L.B. Thompson, J. Maria, S.K. Gray, J.A. Rogers, R.G. Nuzzo, Nanostructured plasmonic sensors, Chem. Rev. 108 (2008) 494–521.

- https://doi.org/10.1021/cr068126n.
- [16] P.K. Jain, K.S. Lee, I.H. El-Sayed, M.A. El-Sayed, Calculated absorption and scattering properties of gold nanoparticles of different size, shape, and composition: Applications in biological imaging and biomedicine, J. Phys. Chem. B. 110 (2006) 7238–7248. https://doi.org/10.1021/jp057170o.
- [17] R. Pilot, R. Signorini, C. Durante, L. Orian, M. Bhamidipati, L. Fabris, A review on surface-enhanced Raman scattering, Biosensors. 9 (2019) 57. https://doi.org/10.3390/bios9020057.
- [18] P.G. Etchegoin, E.C.L. Ru, Basic Electromagnetic Theory of SERS, Surface Enhanced Raman Spectroscopy: analytical, biophysical and life science applications (2010), 1-37. https://doi.org/10.1002/9783527632756.ch1.
- [19] N.D. Israelsen, C. Hanson, E. Vargis, Nanoparticle properties and synthesis effects on surface-enhanced Raman scattering enhancement factor: An introduction, Sci. World J. (2015). https://doi.org/10.1155/2015/124582.
- [20] S. Fateixa, H.I.S. Nogueira, T. Trindade, Surface-Enhanced Raman Scattering Spectral Imaging for the Attomolar Range Detection of Crystal Violet in Contaminated Water, ACS Omega. 3 (2018) 4331–4341. https://doi.org/10.1021/acsomega.7b01983.
- [21] R. Beeram, V.R. Soma, Ultra-trace detection of diverse analyte molecules using femtosecond laser structured Ag Au alloy substrates and SERRS, Opt. Mater. 137 (2023) 113615. https://doi.org/10.1016/j.optmat.2023.113615.
- [22] Dipanjan Banerjee, Mangababu Akkanaboina, Subhasree Ghosh, V.R.Soma, Picosecond Bessel Beam Fabricated Pure, Gold-Coated Silver Nanostructures for Trace-Level Sensing of Multiple Explosives and Hazardous Molecules, Materials. 15 (2022) 4155. https://doi.org/https://doi.org/10.3390/ma15124155.
- [23] R. Beeram, D. Banerjee, L.M. Narlagiri, V.R. Soma, Machine learning for rapid quantification of trace analyte molecules using SERS and flexible plasmonic paper substrates, Anal. Methods. 14 (2022) 1788–1796. https://doi.org/10.1039/d2ay00408a.
- [24] Katrin Kneipp, Yang Wang, Harald Kneipp, Lev T. Perelman, Irving Itzkan, Ramachandra R. Dasari, Single Molecule Detection Using Surface-Enhanced Raman Scattering (SERS), Phys. Rev. Lett. 78 (1997) 1667. https://doi.org/10.1103/PhysRevLett.78.1667.
- [25] H.Y. Lin, C.H. Huang, W.H. Hsieh, L.H. Liu, Y.C. Lin, C.C. Chu, S.T. Wang, I.T. Kuo, L.K. Chau, C.Y. Yang, On-line SERS detection of single bacterium Using Novel SERS Nanoprobes and a microfl uidic Dielectrophoresis device, Small. 10 (2014) 4700–4710. https://doi.org/10.1002/smll.201401526.
- [26] J. Wu, L. Zhang, F. Huang, X. Ji, H. Dai, W. Wu, Surface enhanced Raman scattering substrate for the detection of explosives: Construction strategy and dimensional effect, J. Hazard. Mater. 387 (2020) 121714. https://doi.org/10.1016/j.jhazmat.2019.121714.
- [27] F. Zapata, M. López-López, C. García-Ruiz, Detection and identification of explosives by surface enhanced Raman scattering, Appl. Spectrosc. Rev. 51 (2016) 207–242. https://doi.org/10.1080/05704928.2015.1118637.

- [28] A. Hakonen, P.O. Andersson, M. Stenbæk Schmidt, T. Rindzevicius, M. Käll, Explosive and chemical threat detection by surface-enhanced Raman scattering: A review, Anal. Chim. Acta. 893 (2015) 1–13. https://doi.org/10.1016/j.aca.2015.04.010.
- [29] S.V. Rao, G.K. Podagatlapalli, S. Hamad, Ultrafast laser ablation in liquids for nanomaterials and applications, J. Nanosci. Nanotechnol. 14 (2014) 1364–1388. https://doi.org/10.1166/jnn.2014.9138.
- [30] V.S. Vendamani, R. Beeram, M.M. Neethish, S.V.S.N. Rao, S.V. Rao, Wafer-scale silver nanodendrites with homogeneous distribution of gold nanoparticles for biomolecules detection, IScience. 25 (2022) 104849. https://doi.org/10.1016/j.isci.2022.104849.
- [31] C. Byram, S.S. Bharathi Moram, S. Venugonal Rao, Femtosecond Laser-patterned and Au-coated Iron Surfaces as SERS Platforms for Multiple Analytes Detection, 2019 Work. Recent Adv. Photonics, WRAP 2019. (2019) 1–3. https://doi.org/10.1109/WRAP47485.2019.9013717.
- [32] D. Zhang, P. Liang, W. Chen, Z. Tang, C. Li, K. Xiao, S. Jin, D. Ni, Z. Yu, Rapid field trace detection of pesticide residue in food based on surface-enhanced Raman spectroscopy, Microchim. Acta. 188 (2021),1-28, https://doi.org/10.1007/s00604-021-05025-3.
- [33] R.M. Jarvis, R. Goodacre, Characterisation and identification of bacteria using SERS, Chem. Soc. Rev. 37 (2008) 931–936. https://doi.org/10.1039/b705973f.
- [34] P.H.B. Aoki, L.N. Furini, P. Alessio, A.E. Aliaga, C.J.L. Constantino, Surface-enhanced Raman scattering (SERS) applied to cancer diagnosis and detection of pesticides, explosives, and drugs, Rev. Anal. Chem. 32 (2013) 55–76. https://doi.org/10.1515/revac-2012-0019.
- [35] R. Beeram, K.R. Vepa, V.R. Soma, Recent Trends in SERS-Based Plasmonic Sensors for Disease Diagnostics, Biomolecules Detection, and Machine Learning, 13 (2023) 328. https://doi.org/10.3390/bios13030328
- [36] L.M. Narlagiri, M.S.S. Bharati, R. Beeram, D. Banerjee, V.R. Soma, Recent trends in laser-based standoff detection of hazardous molecules, TrAC Trends Anal. Chem. 153 (2022) 116645. https://doi.org/10.1016/j.trac.2022.116645.
- [37] L. Senesac, T.G. Thundat, Nanosensors for trace explosive detection, Mater. Today. 11 (2008) 28–36. https://doi.org/10.1016/S1369-7021(08)70017-8.
- [38] D.S. Moore, Recent advances in trace explosives detection instrumentation, Sens. Imaging. 8 (2007) 9–38. https://doi.org/10.1007/s11220-007-0029-8.
- [39] Z. Bielecki, J. Janucki, A. Kawalec, J. Mikolajczyk, N. Palka, M. Pasternak, T. Pustelny, T. Stacewicz, J. Wojtas, Sensors and systems for the detection of explosive devices An overview, Metrol. Meas. Syst. 19 (2012) 3–28. https://doi.org/10.2478/v10178-012-0001-3.
- [40] M.S. Marko Makinen, Marjaana Nousiainen, Ion spectrometric detection technologies for ultra-traces of explosives: A review. Mass spectrometry reviews 30 (2011), 940-973. https://doi.org/10.1002/mas.20308.
- [41] A.M. Jiménez, M.J. Navas, Chemiluminescence detection systems for the analysis of explosives, J. Hazard. Mater. 106 (2004) 1–8.

- https://doi.org/10.1016/j.jhazmat.2003.07.005.
- [42] D. Cialla, S. Pollok, C. Steinbrücker, K. Weber, J. Popp, SERS-based detection of biomolecules, Nanophotonics. 3 (2014) 383–411. https://doi.org/10.1515/nanoph-2013-0024.
- [43] B.A. Taha, Y. Al Mashhadany, N.N. Bachok, A. Ashrif A Bakar, M.H. Hafiz Mokhtar, M.S. Dzulkefly Bin Zan, N. Arsad, Detection of covid-19 virus on surfaces using photonics: Challenges and perspectives, Diagnostics. 6 (2021) 1119. https://doi.org/10.3390/diagnostics11061119.
- [44] A. Shrivastava, V. Gupta, Methods for the determination of limit of detection and limit of quantitation of the analytical methods, Chronicles Young Sci. 2 (2011) 21. https://doi.org/10.4103/2229-5186.79345.
- [45] S.X. Leong, Y.X. Leong, E.X. Tan, H.Y.F. Sim, C.S.L. Koh, Y.H. Lee, C. Chong, L.S. Ng, J.R.T. Chen, D.W.C. Pang, L.B.T. Nguyen, S.K. Boong, X. Han, Y.C. Kao, Y.H. Chua, G.C. Phan-Quang, I.Y. Phang, H.K. Lee, M.Y. Abdad, N.S. Tan, X.Y. Ling, Noninvasive and Point-of-Care Surface-Enhanced Raman Scattering (SERS)-Based Breathalyzer for Mass Screening of Coronavirus Disease 2019 (COVID-19) under 5 min, ACS Nano. 16 (2022) 2629–2639. https://doi.org/10.1021/acsnano.1c09371.
- [46] D. Lin, C.L. Hsieh, K.C. Hsu, P.H. Liao, S. Qiu, T. Gong, K.T. Yong, S. Feng, K.V. Kong, Geometrically encoded SERS nanobarcodes for the logical detection of nasopharyngeal carcinoma-related progression biomarkers, Nat. Commun. 12 (2021) 3430. https://doi.org/10.1038/s41467-021-23789-3.
- [47] I. Haidar, A. Day, U. Martino, A. Chevillot-Biraud, N. Félidj, L. Boubekeur-Lecaque, Bottom-up assembly of Au@Ag plasmonic nanocrystals: Issues to be addressed to achieve a good SERS substrate, Appl. Mater. Today. 15 (2019) 462–471. https://doi.org/10.1016/j.apmt.2019.02.015.
- [48] A. Ali, E.E. Nettey-Oppong, E. Effah, C.Y. Yu, R. Muhammad, T.A. Soomro, K.M. Byun, S.H. Choi, Miniaturized Raman Instruments for SERS-Based Point-of-Care Testing on Respiratory Viruses, Biosensors. 12 (2022). https://doi.org/10.3390/bios12080590.
- [49] F. Zapata, C. García-Ruiz, Chemical Classification of Explosives, Crit. Rev. Anal. Chem. 51 (2021) 656–673. https://doi.org/10.1080/10408347.2020.1760783.
- [50] G.K. Podagatlapalli, Ultrafast laser ablation of metals in liquids for explosives detection using SERS and development of CARS experiments, University of Hyderabad, 2014.
- [51] S.A. Meyer, E.C. Le Ru, P.G. Etchegoin, Combining Surface Plasmon Resonance (SPR) spectroscopy with surface-enhanced Raman scattering (SERS), Anal. Chem. 83 (2011) 2337–2344. https://doi.org/10.1021/ac103273r.
- [52] Y.H. Jang, K. Chung, L.N. Quan, B. Špačková, H. Šípová, S. Moon, W.J. Cho, H.Y. Shin, Y.J. Jang, J.E. Lee, S.T. Kochuveedu, M.J. Yoon, J. Kim, S. Yoon, J.K. Kim, D. Kim, J. Homola, D.H. Kim, Configuration-controlled Au nanocluster arrays on inverse micelle nano-patterns: Versatile platforms for SERS and SPR sensors, Nanoscale. 5 (2013) 12261–12271. https://doi.org/10.1039/c3nr03860b.
- [53] C. Chen, Z. Liu, C. Cai, Z.M. Qi, Facile fabrication of nanoporous gold films for

- surface plasmon resonance (SPR) sensing and SPR-based SERS, J. Mater. Chem. C. 9 (2021) 6815–6822. https://doi.org/10.1039/d1tc01046h.
- [54] D.J. Griffiths, C. Inglefield, Introduction to Electrodynamics, Am. J. Phys. 73 (2005) 574–574. https://doi.org/10.1119/1.4766311.
- [55] H.D. Bohren CF, Absorption and scattering of light by small particles, John Wiley & Sons, 2008.
- [56] R.W.C. Christy, P. B. Johnson, Optical Constants of the Noble Metals, Phys. Rev. B. 6 (1972) 4370. https://doi.org/10.1021/acs.jpcc.6b03785.
- [57] E. Cottancin, G. Celep, J. Lermé, M. Pellarin, J.R. Huntzinger, J.L. Vialle, M. Broyer, Optical properties of noble metal clusters as a function of the size: Comparison between experiments and a semi-quantal theory, Theor. Chem. Acc. 116 (2006) 514–523. https://doi.org/10.1007/s00214-006-0089-1.
- [58] A. Kunzmann, B. Andersson, T. Thurnherr, H. Krug, A. Scheynius, B. Fadeel, Toxicology of engineered nanomaterials: Focus on biocompatibility, biodistribution and biodegradation, Biochim. Biophys. Acta Gen. Subj. 1810 (2011) 361–373. https://doi.org/10.1016/j.bbagen.2010.04.007.
- [59] R. Shukla, V. Bansal, M. Chaudhary, A. Basu, R.R. Bhonde, M. Sastry, Biocompatibility of gold nanoparticles and their endocytotic fate inside the cellular compartment: A microscopic overview, Langmuir. 21 (2005) 10644–10654. https://doi.org/10.1021/la0513712.
- [60] G. V. Naik, V.M. Shalaev, A. Boltasseva, Alternative plasmonic materials: Beyond gold and silver, Adv. Mater. 25 (2013) 3264–3294. https://doi.org/10.1002/adma.201205076.
- [61] G. Demirel, H. Usta, M. Yilmaz, M. Celik, H.A. Alidagi, F. Buyukserin, Surface-enhanced Raman spectroscopy (SERS): An adventure from plasmonic metals to organic semiconductors as SERS platforms, J. Mater. Chem. C. 6 (2018) 5314–5335. https://doi.org/10.1039/c8tc01168k.
- [62] W. Ji, B. Zhao, Y. Ozaki, Semiconductor materials in analytical applications of surface-enhanced Raman scattering, J. Raman Spectrosc. 47 (2016) 51–58. https://doi.org/10.1002/jrs.4854.
- [63] I. Alessandri, J.R. Lombardi, Enhanced Raman Scattering with Dielectrics, Chem. Rev. 116 (2016) 14921–14981. https://doi.org/10.1021/acs.chemrev.6b00365.
- [64] P.R. West, S. Ishii, G. V Naik, N.K. Emani, V.M. Shalaev, Searching for better plasmonic materials, 808 (2010) 795–808. https://doi.org/10.1002/lpor.200900055.
- [65] E.C. Le Ru, E. Blackie, M. Meyer, P.G. Etchegoint, Surface enhanced raman scattering enhancement factors: A comprehensive study, J. Phys. Chem. C. 111 (2007) 13794–13803. https://doi.org/10.1021/jp0687908.
- [66] M. J. Dignam, Influence of Surface Roughness on the Transmission and Reflectance Spectra of Adsorbed Species, J. Chem. Soc. Faraday Trans. 2 Mol. Chem. Phys. 69 (1972) 65–78. 10.1039/F29736900065.
- [67] M. Moskovits, Surface roughness and the enhanced intensity of Raman scattering by molecules adsorbed on metals, J. Chem. Phys. 69 (1978) 4159–4161. https://doi.org/10.1063/1.437095.
- [68] J.A. Creighton, C.G. Blatchford, M.G. Albrecht, Plasma resonance enhancement of

- Raman scattering by pyridine adsorbed on silver or gold sol particles of size comparable to the excitation wavelength, J. Chem. Soc. Faraday Trans. 2 Mol. Chem. Phys. 75 (1979) 790–798. https://doi.org/10.1039/F29797500790.
- [69] J.A. Creighton, Surface Raman electromagnetic enhancement factors for molecules at the surface of small isolated metal spheres: The determination of adsorbate orientation from SERS relative intensities, Surf. Sci. 124 (1983) 209–219. https://doi.org/10.1016/0039-6028(83)90345-X.
- [70] C.G. Blatchford, J.R. Campbell, J.A. Creighton, Plasma resonance enhanced raman scattering by absorbates on gold colloids: The effects of aggregation, Surf. Sci. 120 (1982) 435–455. https://doi.org/10.1016/0039-6028(82)90161-3.
- [71] H. Xu, E.J. Bjerneld, M. Käll, L. Börjesson, Spectroscopy of single hemoglobin molecules by surface enhanced raman scattering, Phys. Rev. Lett. 83 (1999) 4357–4360. https://doi.org/10.1103/PhysRevLett.83.4357.
- [72] K.H. Drexhage, Influence of a dielectric interface on fluorescence decay time, J. Lumin. 1–2 (1970) 693–701. https://doi.org/10.1016/0022-2313(70)90082-7.
- [73] K.H. Drexhage, H. Kuhn, F.P. Schäfer, Variation of the Fluorescence Decay Time of a Molecule in Front of a Mirror, Berichte Der Bunsengesellschaft Für Phys. Chemie. 72 (1968) 329–329. https://doi.org/10.1002/bbpc.19680720261.
- [74] L.D. Landau, E.M. Lifshitz, A.L. King, Electrodynamics of Continuous Media, Am.
 J. Phys. 29 (1961) 647–648. https://doi.org/10.1119/1.1937882.
- [75] E.C. Le Ru, P.G. Etchegoin, Quantifying SERS enhancements, MRS bulletin 38 (2013) 631–640. https://doi.org/10.1557/mrs.2013.158.
- [76] K. Kneipp, Chemical Contribution to SERS Enhancement: An Experimental Study on a Series of Polymethine Dyes on Silver Nanoaggregates, J. Phys. Chem. C. 120(2016) 21076-21081. https://doi.org/10.1021/acs.jpcc.6b03785.
- [77] J. Lombardi, Charge-transfer theory of surface enhanced Raman spectroscopy: Herzberg-Teller contributions, J. Chem. Phys. 84(1986) 4174-4180. https://doi.org/10.1063/1.450037.
- [78] A. Otto, The 'chemical' (electronic) contribution to surface-enhanced Raman scattering, J. Raman Spectrosc. 36 (2005) 497-509. https://doi.org/10.1002/jrs.1355.
- [79] A. Ricardo, Surface-enhanced vibrational spectroscopy, John Wiley & Sons, 2006.
- [80] F.L. Pilot R, Signorini R, Surface-enhanced Raman spectroscopy: Principles, substrates, and applications. Metal Nanoparticles and Clusters: Advances in Synthesis, Properties and Applications, Springer, 2018.
- [81] A. Campion, P. Kambhampati, A. Campion, C. Harris, Surface-enhanced Raman scattering, Chemical society reviews, 27 (1998) 241–250. 10.1039/A827241Z.
- [82] S. Hamad, G.K. Podagatlapalli, M.A. Mohiddon, V.R. Soma, Cost effective nanostructured copper substrates prepared with ultrafast laser pulses for explosives detection using surface enhanced Raman scattering, Appl. Phys. Lett. 104 (2014). https://doi.org/10.1063/1.4885763.
- [83] K.C.K. Sergei Yushanov, Jeffrey S. Crompton, Mie Scattering of Electromagnetic Waves, Proc. COMSOL Conf. 116 (2013). https://doi.org/10.1364/rpa.1983.mc2.
- [84] D.O. Sigle, E. Perkins, J.J. Baumberg, S. Mahajan, Reproducible deep-UV SERRS

- on aluminum nanovoids, J. Phys. Chem. Lett. 4 (2013) 1449–1452. https://doi.org/10.1021/jz4004813.
- [85] W. Li, K. Ren, J. Zhou, Aluminum-based localized surface plasmon resonance for biosensing, TrAC Trends Anal. Chem. 80 (2016) 486–494. https://doi.org/10.1016/j.trac.2015.08.013.
- [86] B. Sharma, R.R. Frontiera, A.I. Henry, E. Ringe, R.P. Van Duyne, SERS: Materials, applications, and the future, Mater. Today. 15 (2012) 16–25. https://doi.org/10.1016/S1369-7021(12)70017-2.
- [87] T.T. Ha Pham, N.D. Dien, X.H. Vu, Facile synthesis of silver/gold alloy nanoparticles for ultra-sensitive rhodamine B detection, RSC Adv. 11 (2021) 21475–21488. https://doi.org/10.1039/d1ra02576g.
- [88] D. Rioux, S. Vallières, S. Besner, P. Muñoz, E. Mazur, M. Meunier, An analytic model for the dielectric function of Au, Ag, and their Alloys, Adv. Opt. Mater. 2 (2014) 176–182. https://doi.org/10.1002/adom.201300457.
- [89] M.S.S. Bharati, V.R. Soma, Flexible SERS substrates for hazardous materials detection: recent advances, Opto-Electronic Adv. 4 (2021) 210048–210048. https://doi.org/10.29026/oea.2021.210048.
- [90] J. Shondo, S. Veziroglu, T. Tjardts, T. Bin Sarwar, Y.K. Mishra, F. Faupel, O.C. Aktas, Nanoscale Synergetic Effects on Ag–TiO 2 Hybrid Substrate for Photoinduced Enhanced Raman Spectroscopy (PIERS) with Ultra-Sensitivity and Reusability (Small 50/2022), Small. 18 (2022) 2270271. https://doi.org/10.1002/smll.202270271.
- [91] X.D. Lin, V. Uzayisenga, J.F. Li, P.P. Fang, D.Y. Wu, B. Ren, Z.Q. Tian, Synthesis of ultrathin and compact Au@MnO2 nanoparticles for shell-isolated nanoparticle-enhanced Raman spectroscopy (SHINERS), J. Raman Spectrosc. 43 (2012) 40–45. https://doi.org/10.1002/jrs.3007.
- [92] X.D. Tian, B.J. Liu, J.F. Li, Z.L. Yang, B. Ren, Z.Q. Tian, SHINERS and plasmonic properties of Au Core SiO2 shell nanoparticles with optimal core size and shell thickness, J. Raman Spectrosc. 44 (2013) 994–998. https://doi.org/10.1002/jrs.4317.
- [93] Z. Yin, K. Xu, S. Jiang, D. Luo, R. Chen, C. Xu, P. Shum, Y. Jun, Recent progress on two-dimensional layered materials for surface enhanced Raman spectroscopy and their applications, Mater. Today Phys. 18 (2021) 100378. https://doi.org/10.1016/j.mtphys.2021.100378.
- [94] T.K. Naqvi, A. Bajpai, M.S.S. Bharati, M.M. Kulkarni, A.M. Siddiqui, V.R. Soma, P.K. Dwivedi, Ultra-sensitive reusable SERS sensor for multiple hazardous materials detection on single platform, J. Hazard. Mater. 407 (2021) 124353. https://doi.org/10.1016/j.jhazmat.2020.124353.
- [95] E.C. Le Ru, J. Grand, I. Sow, W.R.C. Somerville, P.G. Etchegoin, M. Treguer-Delapierre, G. Charron, N. Félidj, G. Lévi, J. Aubard, A scheme for detecting every single target molecule with surface-enhanced raman spectroscopy, Nano Lett. 11 (2011) 5013–5019. https://doi.org/10.1021/nl2030344.
- [96] A.I. Pérez-Jiménez, D. Lyu, Z. Lu, G. Liu, B. Ren, Surface-enhanced Raman spectroscopy: Benefits, trade-offs and future developments, Chem. Sci. 11 (2020)

- 4563–4577. https://doi.org/10.1039/d0sc00809e.
- [97] S.S.B. Moram, C. Byram, V.R. Soma, Gold-nanoparticle- and nanostar-loaded paper-based SERS substrates for sensing nanogram-level Picric acid with a portable Raman spectrometer, Bull. Mater. Sci. 43 (2020) 1–8. https://doi.org/10.1007/s12034-019-2017-8.
- [98] A.S.D.S. Indrasekara, S. Meyers, S. Shubeita, L.C. Feldman, T. Gustafsson, L. Fabris, Gold nanostar substrates for SERS-based chemical sensing in the femtomolar regime, Nanoscale. 6 (2014) 8891–8899. https://doi.org/10.1039/c4nr02513j.
- [99] H. Wang, N.J. Halas, Mesoscopic au 'meatball' particles, Adv. Mater. 20 (2008) 820–825. https://doi.org/10.1002/adma.200701293.
- [100] S. Nie, S.R. Emory, Probing single molecules and single nanoparticles by surface-enhanced Raman scattering, Science. 275 (1997) 1102–1106. https://doi.org/10.1126/science.275.5303.1102.
- [101] W.Y. Ma, H. Yang, J.P. Hilton, Q. Lin, J.Y. Liu, L.X. Huang, J. Yao, A numerical investigation of the effect of vertex geometry on localized surface plasmon resonance of nanostructures, Opt. Express. 18 (2010) 843. https://doi.org/10.1364/oe.18.000843.
- [102] R. Luo, J. Popp, T. Bocklitz, Deep Learning for Raman Spectroscopy: A Review, Analytica. 3 (2022) 287–301. https://doi.org/10.3390/analytica3030020.
- [103] F. Lussier, V. Thibault, B. Charron, G.Q. Wallace, J.F. Masson, Deep learning and artificial intelligence methods for Raman and surface-enhanced Raman scattering, TrAC Trends Anal. Chem. 124 (2020) 115796. https://doi.org/10.1016/j.trac.2019.115796.
- [104] Y. Ding, Y. Sun, C. Liu, Q.Y. Jiang, F. Chen, Y. Cao, SERS-Based Biosensors Combined with Machine Learning for Medical Application, ChemistryOpen. 12 (2023) e202200192. https://doi.org/10.1002/open.202200192.
- [105] T. Rojalin, D. Antonio, A. Kulkarni, R.P. Carney, Machine Learning-Assisted Sampling of Surfance-Enhanced Raman Scattering (SERS) Substrates Improve Data Collection Efficiency, Appl. Spectrosc. 76 (2022) 485–495. https://doi.org/10.1177/00037028211034543.
- [106] R. Beeram, V.S. Vendamani, V.R. Soma, Deep learning approach to overcome signal fluctuations in SERS for efficient On-Site trace explosives detection, Spectrochim. Acta Part A Mol. Biomol. Spectrosc. 289 (2023) 122218. https://doi.org/10.1016/j.saa.2022.122218.
- [107] G. Moon, T. Son, H. Lee, D. Kim, Deep learning approach for enhanced detection of surface plasmon scattering, Anal. Chem. 91 (2019) 9538–9545. https://doi.org/10.1021/acs.analchem.9b00683.
- [108] A.K. Gupta, C.H. Hsu, C.S. Lai, Enhancement of the Au/ZnO-NA plasmonic SERS signal using principal component analysis as a machine learning approach, IEEE Photonics J. 12 (2020). https://doi.org/10.1109/JPHOT.2020.3015740.
- [109] S.K. Seongyong Park, Abdul Wahab, Minseok Kim, Self-Supervised learning for inter-laboratory variation minimization in surface-enhanced Raman scattering spectroscopy Seongyong, Analys. 148(2023),1473-1482.

- https://doi.org/10.1039/D2AN01569B.
- [110] L.M. Narla, S.V. Rao, Identification of metals and alloys using color CCD images of laser-induced breakdown emissions coupled with machine learning, Appl. Phys. B Lasers Opt. 126 (2020) 113. https://doi.org/10.1007/s00340-020-07469-6.
- [111] B. Boehmke, B. Greenwell, Hands-On Machine Learning with R, CRC press, 2019. https://doi.org/10.1201/9780367816377.
- [112] A.L. Boulesteix, K. Strimmer, Partial least squares: A versatile tool for the analysis of high-dimensional genomic data, Brief. Bioinform. 8 (2007) 32–44. https://doi.org/10.1093/bib/bbl016.
- [113] D. Li, Q. Zhang, B. Deng, Y. Chen, L. Ye, Rapid, sensitive detection of ganciclovir, penciclovir and valacyclovir-hydrochloride by artificial neural network and partial least squares combined with surface enhanced Raman spectroscopy, Appl. Surf. Sci. 539 (2021) 148224. https://doi.org/10.1016/j.apsusc.2020.148224.
- [114] W. Deng, Z. Huang, J. Zhang, J. Xu, A Data Mining Based System for Transaction Fraud Detection, 2021 IEEE Int. Conf. Consum. Electron. Comput. Eng. ICCECE (2021) 542–545. https://doi.org/10.1109/ICCECE51280.2021.9342376.
- [115] X. Fan, W. Ming, H. Zeng, Z. Zhang, H. Lu, Deep learning-based component identification for the Raman spectra of mixtures, Analyst. 144 (2019) 1789–1798. https://doi.org/10.1039/c8an02212g.
- [116] W.K. Kim, N. Karabasil, S. Bulajic, K.D. Dunkley, T.R. Callaway, T.L. Poole, S.C. Ricke, R.C. Anderson, D.J. Nisbet, Comparison of spontaneous antibiotic resistance frequency of Salmonella typhimurium growth in glucose amended continuous culture at slow and fast dilution rates, J. Environ. Sci. Heal. Part B Pestic. Food Contam. Agric. Wastes. 40 (2005) 475–484. https://doi.org/10.1081/PFC-200047598.
- [117] Pencillin Structure, http://www.antimicrobe.org/d24.asp#:~:text=The basic chemical structure of,within the beta-lactam ring. (Accessed 5 April 2023).
- [118] A. Shores, M. Laituri, G. Butters, Produced Water Surface Spills and the Risk for BTEX and Naphthalene Groundwater Contamination, Water. Air. Soil Pollut. 228 (2017) 1-13. https://doi.org/10.1007/s11270-017-3618-8.
- [119] K. Sharma, M. Paradakar, The melamine adulteration scandal, Food Secur. 2 (2010) 97–107. https://doi.org/10.1007/s12571-009-0048-5.
- [120] D.P. Dos Santos, M.L.A. Temperini, A.G. Brolo, Intensity Fluctuations in Single-Molecule Surface-Enhanced Raman Scattering, Acc. Chem. Res. 52 (2019) 456–464. https://doi.org/10.1021/acs.accounts.8b00563.
- [121] D. Cialla, A. März, R. Böhme, F. Theil, K. Weber, M. Schmitt, J. Popp, Surface-enhanced Raman spectroscopy (SERS): Progress and trends, Anal. Bioanal. Chem. 403 (2012) 27–54. https://doi.org/10.1007/s00216-011-5631-x.
- [122] V.S. Vendamani, S.V.S. Nageswara Rao, S. Venugopal Rao, D. Kanjilal, A.P. Pathak, Three-dimensional hybrid silicon nanostructures for surface enhanced Raman spectroscopy based molecular detection, J. Appl. Phys. 123 (2018). https://doi.org/10.1063/1.5000994.
- [123] M.S.S. Bharathi, C. Byram, K. Nehra, P. Senthil Kumar, S.V. Rao, Filter paper loaded with gold nanoparticles as flexible SERS substrates for sensing applications,

- AIP Conf. Proc. 2265 (2020). https://doi.org/10.1063/5.0016882.
- [124] V.S. Vendamani, R. Beeram, S.V.S. Nageswara Rao, A.P. Pathak, V.R. Soma, Trace level detection of explosives and pesticides using robust, low-cost, free-standing silver nanoparticles decorated porous silicon, Opt. Express. 29 (2021) 30045. https://doi.org/10.1364/oe.434275.
- [125] R. Beeram, V.S. Vendamani, S.V. Rao, Flexible Paper Substrate with Silver Dendrites for Trace Detection of Dye and Explosive Molecules using SERS, Work. Recent Adv. Photonics, WRAP (2022) 1-2. https://doi.org/10.1109/WRAP54064.2022.9758296.
- [126] C. Farcau, S. Astilean, Mapping the SERS efficiency and hot-spots localization on gold film over nanospheres substrates, J. Phys. Chem. C. 114 (2010) 11717–11722. https://doi.org/10.1021/jp100861w.
- [127] E.C. Le Ru, M. Meyer, E. Blackie, P.G. Etchegoin, Advanced aspects of electromagnetic SERS enhancement factors at a hot spot, J. Raman Spectrosc. 39 (2008) 1127–1134. https://doi.org/10.1002/jrs.1945.
- [128] K.C. Bantz, A.F. Meyer, N.J. Wittenberg, H. Im, Ö. Kurtuluş, S.H. Lee, N.C. Lindquist, S.H. Oh, C.L. Haynes, Recent progress in SERS biosensing, Phys. Chem. Chem. Phys. 13 (2011) 11551–11567. https://doi.org/10.1039/c0cp01841d.

Intentional Blank Page

Chapter 2

Synthesis and Characterization Techniques

Abstract

This chapter primarily focuses on various techniques for fabrication/synthesis and characterization that were utilized throughout the study. Specifically, the synthesis and mechanisms for the formation of plasmonic nanostructures through ultrafast laser ablation in air/water and chemical/physical methods are discussed in detail. Additionally, different characterization techniques such as FESEM, TEM, UV-Visible spectroscopy, and contact angle measurements are elaborated upon, as they were used to analyse the nanoparticles. The chapter also includes comprehensive descriptions of two Raman instruments, a portable system and micro-Raman system, along with the procedures utilized for SERS measurements on both rigid and flexible substrates. Finally, the chapter provides detailed information on ultrafast laser systems (femtosecond amplifier and oscillator) and various pulse characterization techniques.

2.1. Introduction

Plasmonic structures are being fabricated by plethora of techniques that best suit the material and application of interest. Broadly these techniques can be classified as top-down or bottom-up approaches depending on their assembly. The top-down method begins with a bulk material that eventually breaks down under any external agent like intense light or heat into nanoscale structures. In the bottom-up method, particles at atomic or molecular scale assemble to form a nanostructure (NS) [1], as illustrated in Figure 2.1. Laser ablation, ball milling, thermal evaporation, and sputtering are popular top-down approaches. At the same time, chemical vapour deposition, hydrothermal methods, and sol-gel are some examples of bottom-up methods [2]. Bottom-up methods are mediated mainly by chemicals, while top-down methods are mediated through force, pressure, light, or heat. By monitoring the reaction conditions, the bottom-up method gives enormous flexibility to control the size, shape, and yield of the top-down method is more suitable for the fabrication of nanostructures on a bulk surface and is known to yield inhomogeneous distribution of NPs [3]. Further, these nanomaterials are classified based on the material and the dimension of the particles. Based on dimension, there are 0D, 1D, 2D, and 3D nanostructures with a constraint on dimension being from 1-100 nm [4]. Based on the material, they are broadly classified as carbon-based, metal NSs, semiconductor nanoparticles (NPs), and nanocomposites [5].

The aim of NP fabrication techniques with a view of application in SERS is to have a) ligand free particles that does not interfere with the probe molecules, b) have morphologies for maximum enhancement, c) provide flexibility for easy sample collection in view of field applications, and d) be stable against oxidation. This thesis focuses on all these aspects by using different techniques for each case with a focus on SERS based applications. Laser ablation in liquid and air is a ligand free, green technique that results in precise and pure nanoparticles and nanostructures in the same experiment [6]. The mechanisms of laser ablation and the effects of different laser parameters are discussed in detail in the later sections. Anisotropic nanostructures with sharp edges and crevices are known to offer higher enhancement in SERS through what is popularly known as the 'lightening rod effect' [7] [8]. We will discuss a bottom-up chemical methods based on electroless etching for synthesis of Au and Ag nanodendrites on a semiconductor surface. Effects of reaction time, temperature, and concentration of the metal salts on the formation of these metal nanostructures is also discussed. This chapter starts with understanding the

different NP fabrication techniques used in this study followed by detailed description of the characterization techniques that have been used. Different characterization techniques that are preliminary to characterize SERS substrates before measurements are also discussed.

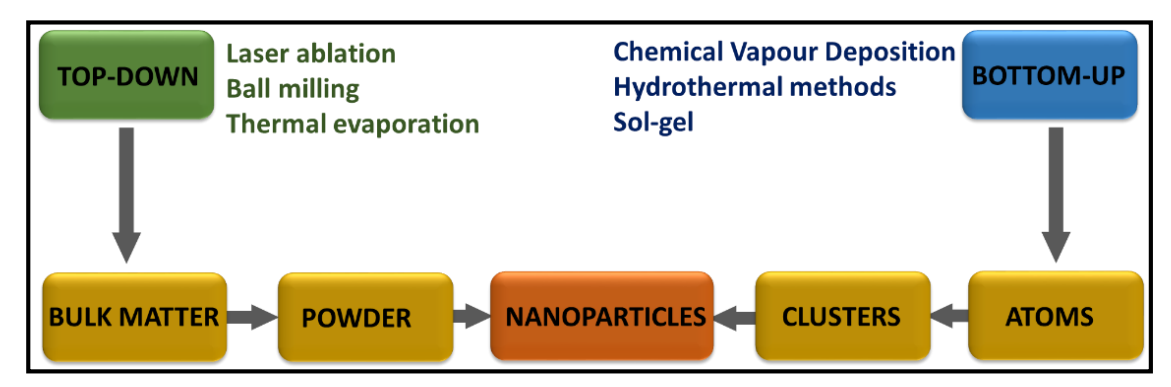


Figure 2.1: Illustration of top-down and bottom-up methods for the preparation of plasmonic nanostructures.

2.2. Fabrication and Synthesis of NSs

Throughout the thesis we have extensively used ultrafast laser ablation and chemical methods for the fabrication of SERS substrates.

2.2.1. Ultrafast Laser Ablation

Science has taken a huge leap after the invention of laser by Maiman in 1960 [9]. To the fascination of the research communities across disciplines, the invention was explored to study astronomy and atoms, cells and celestial objects, medicine and machinery. The entry of the ultrafast lasers further revolutionized science and technology both in labs and on field. ULAL and SERS are both two novel applications that emerged from this excitement. Laser ablation is a subtractive processing technique in which material of interest is exposed to laser radiation with a goal of generating nanoparticles or patterns or both in a single experiment. It is derived from the Latin word 'ablatio' meaning 'carrying away'. Laser ablation in liquids is an improvement over laser ablation in gases for its residue free process. To our knowledge, ultrafast laser ablation in liquids was first reported by Henglein in 1993 [10]. Ultrafast laser ablation is known to result in minimum debris and heat affected zone and would hence lead to precise structure modifications [11] [12]. Intuitively, the laser parameters like wavelength, pulse duration, fluence, focusing conditions influence the efficiency of the process [13] [14] [15]. Experimental conditions like the solvent, number of pulses per spot, presence of external field also influence the

results. In addition, ablation is hugely dependent on the material under study and the mechanism, laser requirements are different for insulators, metals and semiconductors [16]. Addition of surfactants and salts [17], presence of electric or magnetic field during ablation [18–20], focusing conditions [21–23] and temperature [24] are also known to influence the ablation outcome.

The mechanism of laser ablation is described by a series of events which needs interdisciplinary approach to understand. Laser ablation is understood through the interaction of ultrafast pulses with electrons followed by energy exchange process between atoms and ions. The events during ablation can be summarised as below,

- 1) Upon incidence of high intensity laser pulses, the incident energy is absorbed by the free or conduction electrons through inverse Bremsstrahlung (IBS) absorption process.
- 2) This is quickly followed by a relaxation of energy through thermal conduction or diffusion facilitated by electron-phonon coupling.
- 3) At the level of lattice, the exchange of energy eventually leads to different events like heating, breaking of chemical bonds leading to the formation of plasma and ablation eventually.

Classically, the ablation is explained using the two temperature model [25] [26]. Two temperature model describes the distribution of laser energy in the ablation area in one dimension taken as z in this case. It describes the evolution of lattice temperature (T_i) and electron temperature (T_e) .

$$C_{e} \frac{\partial T_{e}}{\partial t} = -\frac{\partial Q(z)}{\partial z} - \gamma \left(T_{e} - T_{i} \right) + S \tag{2.1}$$

$$C_{i} \frac{\partial T_{i}}{\partial t} = \gamma \left(T_{e} - T_{i} \right) \tag{2.2}$$

Q(z) here is the heat flux and is given by the below equation,

$$Q(z) = -k_{e} \frac{\partial T_{e}}{\partial t}$$
 (2.3)

S represents heating contribution by the laser source and is written as,

$$S = I(t)A\alpha e^{-\alpha z} \tag{2.4}$$

Here, A stands for surface absorptivity, I(t) for laser intensity, and for material absorption coefficient. For the electron and lattice systems, respectively, C_e and C_i represent the heat

capacity per unit volume. In the equation, k_e is the thermal conductivity of the electron system, and is a measure of coupling between the electron and lattice systems.

The formation of NPs and NSs is understood by studying the evolution and condensation of the plasma plume formed during ablation. Continuous exposure to laser and heating causes high temperature and density in plasma leading to the expansion of the same and also ejection from the surface if the recoil pressure is high [27]. This is followed by rapid quenching because of collisions between the particles in the plasma leading to nucleation or condensation and eventual formation of NPs [28]. The mechanism of heat exchange during laser ablation has been simulated using COMSOL for the case of alumina based on the parameters given in the reference and the results depict the summary of the mechanism described above [29].

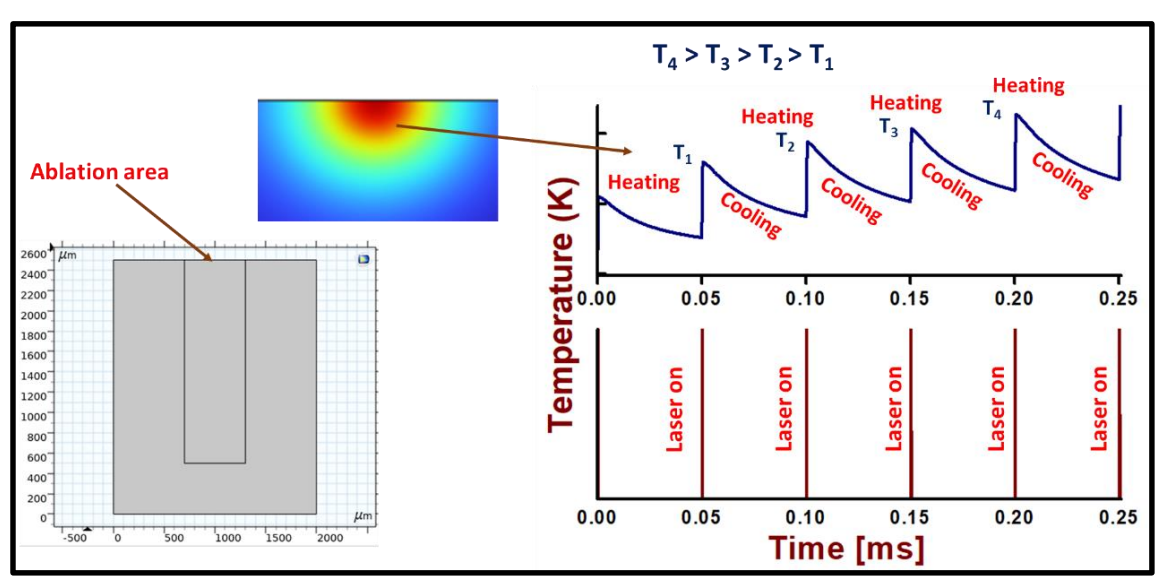


Figure 2.2. COMSOL simulation of heat exchange during LA of alumina with a pulse duration of 10 μs and repetition rate of 20 Hz showing a series of heating and cooling of the surface.

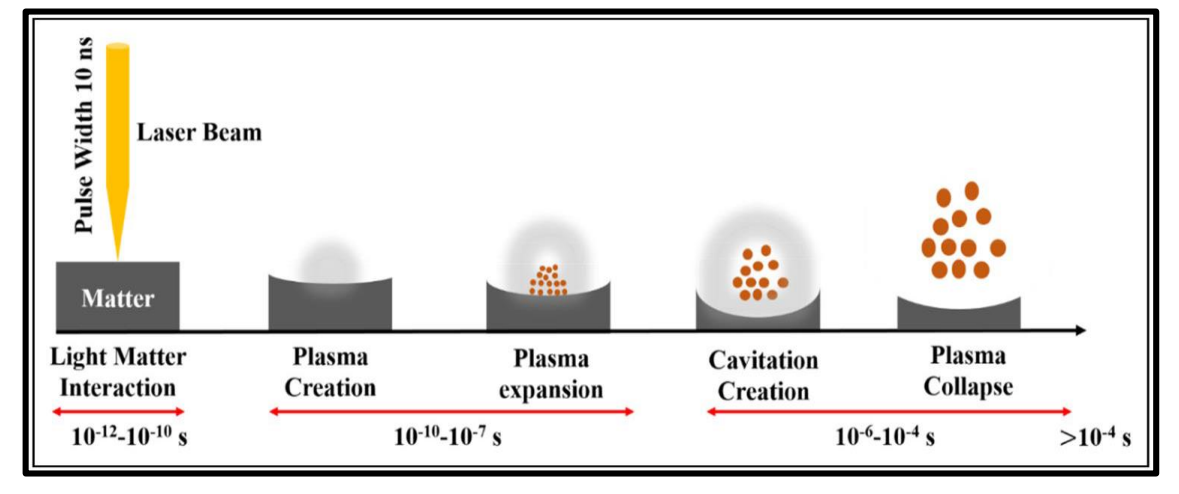


Figure 2.3: Time scale of different events that occur during laser ablation in liquids for a nanosecond laser. Figure adopted from reference [31].

Laser ablation in the presence of liquids will result in the confinement of plasma plume resulting in drastic difference in the process of plasma evolution and condensation [30]. LAL can be described as a 'two birds with one stone' methods which will result in formation of NSs and NPs in a single experiment. The first two steps described for laser ablation in air being the same, after rapid heating of the surface by the laser the material vaporizes and creates a high-pressure vapour bubble just above the surface. This bubble expands rapidly due to the heat generated by the laser, and then collapses due to the pressure of the surrounding liquid. The collapse of the vapour bubble generates a shock wave that ejects the vaporized material from the surface and into the surrounding liquid. The ejection of the material can cause secondary effects, such as cavitation bubbles and shock waves, that can affect the surrounding liquid and the material being ablated. Figure 2.3 presents time scale of different events that occur during laser ablation in liquids with a nanosecond laser. The time scale of the events hugely depends on the pulse duration, material and the surround liquid [31] [32].

2.2.2. Chemical Methods for NP Synthesis

Chemical methods provide a flexibility for the fabrication of flexible and anisotropic nanostructures which are of interest for SERS based traced detection concerning field applications. In order to synthesis highly branched, fractal Ag structures, we have used a cost effective and table top method that is popularly called as electroless etching.

2.2.2.1. Electroless Etching

Since 1990s silver dendrites have attracted lot of attention for their unique morphology and applications in catalysis, fuel cells and storage devices [33] [34]. They are known to provide large surface area and optical properties that are desirable for signal enhancement in different applications including SERS. There are many methods for the fabrication of Ag dendrites which can be broadly classified as electrochemical or chemical routes [35]. In an electrochemical process there is a usage of potential or current in order to reduce the Ag reduction. The formation of dendrites depends on the applied field/current, presence of surfactants and the reaction time [36] [37]. Electroless deposition process on another hand works by simultaneous reduction and oxidation reactions on the surface of the template used. The method can be extended to different metals, for example, zinc and CuSe nano-dendrites have also been reported by Matsushita et al. and Zheng et al. [38] [39].

In 2005, Qiu et al. have first proposed the use of Si wafer as a template for the fabrication of Ag dendrites with HF as an etching agent [40]. The formation of these dendrite structures is better explained by diffusion limited aggregation theory (DLA) [41]. The central idea of the theory is that particles move freely through random walk and eventually settle at a site contributing to the growth of it. The formation of fractal structures is initiated by the formation of a seed particle from the metal salt. Particles formed at different site diffuse through random walk and will stop once they reach and attach to the low energy sites close to the seed. This process continues and the particles continue to add to the growth of the static structure as shown in figure 2.4. Until they arrive at the specified low energy sites on the substrate and are deposited there, the Ag²⁺ nuclei released from random sites move randomly throughout the substrate. The cluster is formed by the nuclei sequentially aggregating [42]. The Si surface is initially etched in the presence of HF leading to the formation of Si nanowires. The Ag nuclei that are simultaneously formed during the redox reaction assemble on the Si nanowires and lead to the formation of clusters. Through the transfer of electrons from the Si atoms underneath, the Si atoms constantly reduced the Ag ions in the solution, and the reduced Ag atoms were subsequently deposited on the Si surface. In our later work, the dendrites formed were removed by dipping in NH₄OH to regain the Si NW structure which was further coated with gold and silver and is used for SERS in combination with MoS₂ [43].

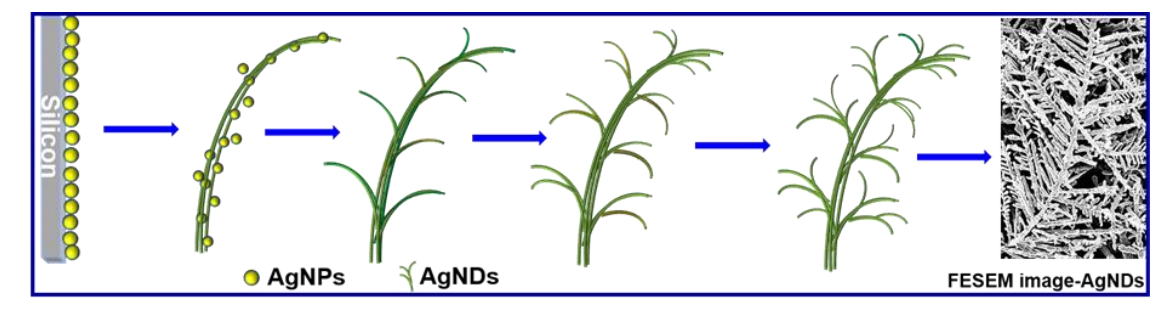


Figure 2.4: Illustration of formation of anisotropic silver dendrites through electroless etching of Si in the presence of AgNO₃ and HF [44].

The reactions explaining the mechanism of formation of these structures are as below [45],

$$4Ag^{+} + Si + 6F^{-} \rightarrow 4Ag + SiF_{6}^{-2}$$
 (2.5)

$$Ag^+ + e^- \to Ag \tag{2.6}$$

$$Si + 6HF \rightarrow SiF_6^{-2} + 4H^+ + 4e^-$$
 (2.7)

Metal nanostructures with sharp edges and crevices are known to contribute further for the electromagnetic enhancement in SERS through the 'lightening rod effect' [46]. The electric field lines for a conductor are very well known to be normal to the surface. On a

flat surface the field lines are evenly spaced and are hence less dense whereas for curved surfaces, the density of the field lines emerging from the surface are concentrated as shown in figure 2.5 [47].

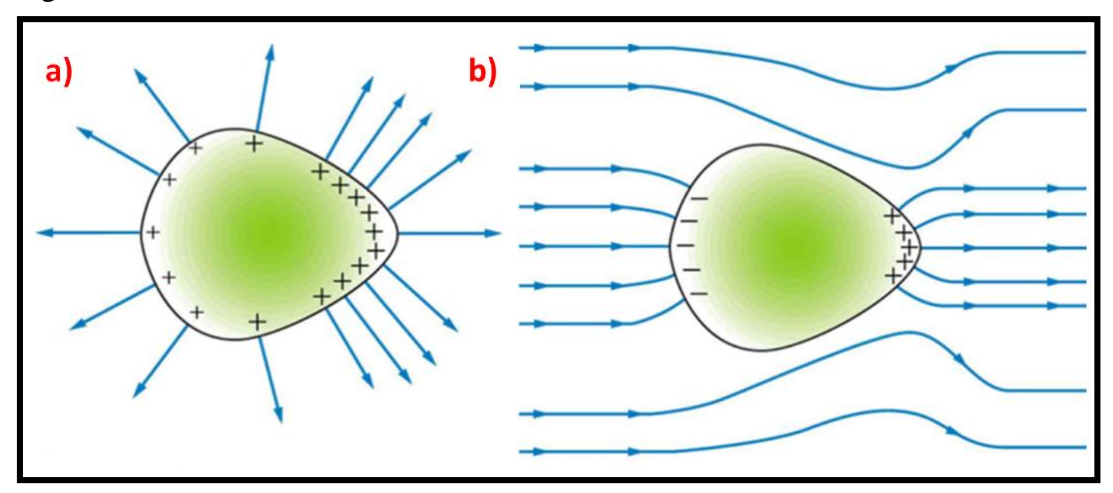


Figure 2.5: Electric Field line for a) conductor b) a conductor in the presence of an electric field. Reproduced from https://courses.lumenlearning.com/suny-physics/chapter/18-7-conductors-and-electric-fields-in-static-equilibrium/.

2.2.2.2. Other Methods

Etching of Si in the presence of an electric field leads to the formation of different structures and also induces porosity in the material [48]. In the presence of an etch cell and by applying a current density in the presence of HF, free standing porous Si has also been fabricated [49]. This porous Si was further decorated with Ag nanoparticles by electroless etching [50]. Recently hydrophobic and super hydrophobic substrates have gained tremendous interest for their ability to concentrate the analyte and NPs to a small area facilitating higher density of

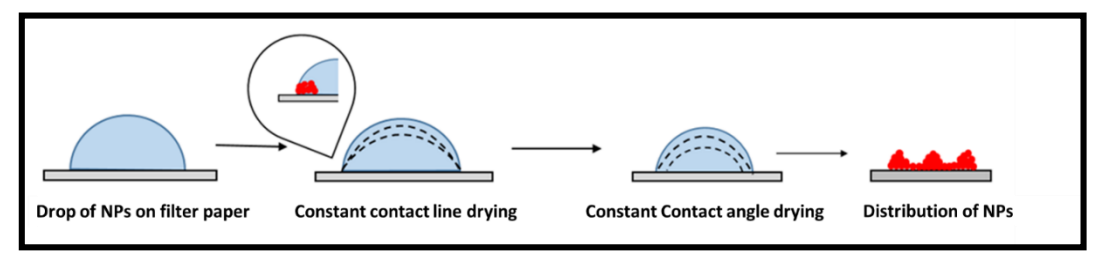


Figure 2.6: Schematic of mechanism for drying of nanoparticles on the surface of hydrophobic filter paper.

hotspots and lower detection limits [51] [52] [53]. Normal filter paper, owing to its porosity spreads the analyte and nanoparticles leading to poor enhancement. In order to fabricate hydrophobic filter paper (HFP), previously different techniques involving coating alkyl ketene dimer[52], 2-dodecen-1-yl)-succinic anhydride[54], agar[55], spin-coating diluted polydimethylsiloxan (PDMS)[56], perfluoroalkyltriethoxysilanes [57] was

used. All these methods involve extensive pre-treatment, possibility for interference with SERS probes and are not cost efficient. Different drying mechanisms of the hydrophobic surface are also known to remove the undesirable coffee ring patterns during drying of the colloids [58][59]. We have used a simple spin coating method for the fabrication of hydrophobic filter paper that was used for quantification of trace explosives along with plasmonic Au NPs [60]. The detailed wetting mechanism has been studied using contact angle measurements. It was discovered that the initial contact angle was 110° after the nanoparticles were dropped. As the drop dries, the contact angle reduced gradually rather than suddenly. The periods of continuous contact angle imply that there is no pinching of the contact lines, and hence, no single coffee ring. As a result, the drying pattern, which is shown in figure 2.6, combines constant contact line drying with constant contact angle drying. A drop of CuSO4 was used to see the drying pattern. CuSO4 was chosen because it has the ability to form colour crystals when dried thus facilitating the visibility when dried. The materials and characterization equipment used that have been used in the thesis work including the chemicals used in synthesis, analyte molecules are summarised in table 2.1.

2.3. Experimental Techniques

2.3.1. Ti:Sapphire as a Gain Medium

Ever since its discovery by Moulton, Ti:Sapphire (Ti:Sa) was widely explored for its ability to produce ultrafast pulses [61]. It has quickly replaced the existing dye laser to generate ultrafast pulses through mode locking [62] and became the go to laser gain medium for the tunable ultrafast laser systems [63]. The lasing occurs in the Ti^{+3} atoms of the crystal. Ti sapphire has very wide bandwidth which consequently facilitates the generation of ultrafast pulses also gibing an opportunity to tune wavelengths (600- 100 nm) as shown in figure 2.7. Its excellent thermal conductivity circumvents the thermal effects caused during lasing. It is also known to have good mechanical strength, rigidity and inertness to external chemicals. It is frequently pumped using a frequency doubled Nd doped solid state laser with emission close to 532 nms. The pumping requires intense, high beam quality source given the upper state lifetime of Ti^{+3+} is very small (3.8 μ s). The doping concentration of Ti^{+3} in Al_2O_3 is often kept very low (\sim 0.2%) in order to preserve the crystal quality as a consequence of which longer crystals and high intensity pump beams are required to obtain higher output. Mode locking in the Ti:Sa system often

happens through the Kerr effect facilitated by the high intensity of the output beam. A large bandwidth is desirable for producing ultrashort pulses as given by the equation (1.8). **Table 2.1:** Summary of materials and different characterization techniques used in this study.

Material/Tool	Chemical formula/details	Specifications
Silver Nitrate	AgNO ₃	Finar
Hydrofluoric Acid	HF	Sigma-Aldrich
Chloroauric Acid	HAuCl ₄ .3H ₂ O	Sigma-Aldrich
Si wafers (1-10 Ωcm)	Si	Macwin
Ammonium Nitrate	NH ₄ NO ₃	HEMRL, Pune
Picric Acid	C ₆ H ₃ N ₃ O ₇	HEMRL, Pune
Tetryl	C ₇ H ₅ N ₅ O ₈	HEMRL, Pune
Gold, Silver, Alloys	Ag, Au, Ag-Au (1:1)	Purchased locally
Filter paper	-	Whatman
Antibiotics	-	Sigma-Aldrich
(Penicillin G,		
Kanamycin,		
Ampicillin)		
DNA Bases (Adenine,	9H-purin-6-amine	Sigma Aldrich
Cytosine)	6-amino-1H-pyrimidin-2-one	
Thiram	Tetramethylthiuram disulfide	Sigma Aldrich
Escherichia coli	-	Lab grown
Crystal Violet	C ₂₅ N ₃ H ₃₀ Cl	Sigma-Aldrich
Rhodamine 6G	$C_{28}H_{31}N_2O_3Cl$	
Methylene Blue	$C_{16}H_{18}CIN_3S$	
Python	https://www.python.org/downloa	Version 3.8.3
	ds/release/python-383/	
COMSOL	https://www.comsol.com/	Version 6.0
Origin	https://www.originlab.com/	Origin 2018
FESEM	https://www.felmi-	Carl ZEISS, Ultra 55
	zfe.at/instrumentation/sem/zeiss-	
	<u>ultra-55</u>	
TEM	https://www.fei.com/products/te	Technai
	m/tecnai-g2-spirit-for-life-	
	sciences/#gsc.tab=0	
UV-Visible	https://www.jasco.de/en/content/	Jasco V-670
spectrometer	V-670/~nm.13~nc.407/V-670-	
	UV-VIS-NIR-	
	Spectrophotometer.html	
Micro-Raman	https://www.horiba.com/ind/scien	Horiba LabRam
spectrometer	tific/products/detail/action/show/	

	Product/labram-hr-evolution-	
	1083/	
fs Oscillator	https://www.coherent.com/lasers/	Coherent
(Chameleon)	<u>oscillators</u>	
fs laser amplifier	https://www.coherent.com/lasers/	Coherent
(Libra)	<u>amplifiers</u>	

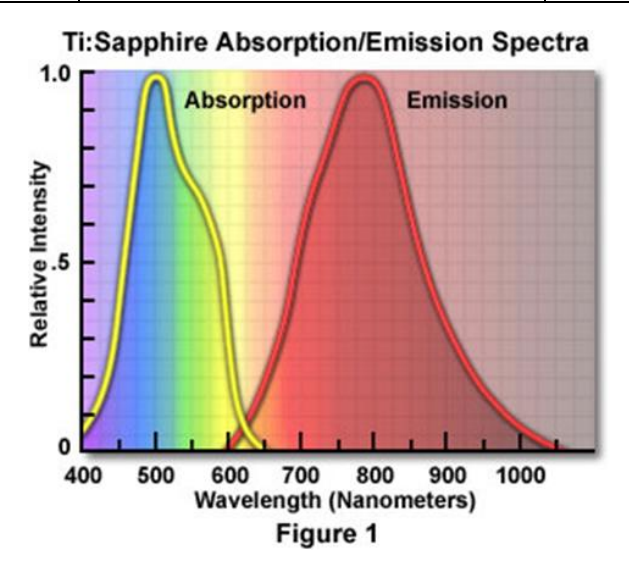


Figure 2.7: Absorption and emission spectra of Ti-Sa laser. Image reproduced form https://micro.magnet.fsu.edu/primer/java/lasers/tsunami/index.html.

$$\Delta\omega\Delta t \geq K \tag{1.8}$$

 $\Delta\omega$ here is the FWHM of the band width of the medium and Δt is the FWHM of the pulse duration and K is a constant that depends on the pulse duration. The relation is derived from the Fourier relations of frequency and time dependent electric fields. The relation indicates that a large bandwidth material like Ti:Sa is needed for generation of ultrashort pulses.

2.3.2. Femtosecond Laser Oscillator

Femtosecond laser ablation of Si has been performed using a coherent femtosecond laser oscillator (Chameleon). It is a tunable Ti-Sa laser with maximum power at 800 nm, pulse width of 140 fs, and repetition rate of 80 MHz. The Ti-Sa laser is pumped with a diode pumped Nd-YVO₄ laser (Verdi). The chameleon oscillator system consists of two laser heads, Verdi and the ultra-fast laser with Ti-Sa as the gain medium. The repetition rate of the laser is determined by the time it takes for one pulse to emerge out of the cavity and this time is around 11 ns for the chameleon laser resulting in the repetition rate of 80 MHz. Femtosecond pulses are generated by mode locking which involves synchronizing the

oscillation of multiple longitudinal laser modes in order to achieve constructive interference. Depending on the mechanism, mode locking is classified as active and passive mode locking. In active mode locking, a precisely timed electric/acoustic optical shutter is used to synchronise the modulation time with that of round-trip time to facilitate mode locking. This often needs precise and sophisticated setups and require monitoring if there is change in round trip or the cavity length of the laser. In contrast, for the case of passive mode locking the modulation is self-adjusted with the arrival of the high intensity laser pulses and often use saturable absorbers. Saturable absorber consists of non-linear material whose optical properties change as a function of laser intensity. When a saturable absorber is incorporated into the laser cavity, it modulates the laser's optical properties in a way that favours the formation of short pulses. Initially, when the laser starts operating, the saturable absorber exhibits high absorption for the incident light. As the light intensity increases, the absorber saturates, leading to a decrease in its absorption capability. This reduced absorption allows the laser to build up energy within the cavity over multiple round trips. As the energy increases, the saturable absorber reaches a point where its absorption decreases significantly, and it behaves more like a transparent medium. At this stage, the gain provided by the laser cavity compensates for the loss incurred, and the laser starts emitting a pulse of light. The pulse generated then travels through the laser cavity and interacts with the saturable absorber again. The absorber recovers its high absorption capabilities and removes the excess energy from the pulse, effectively preventing it from growing indefinitely. This process repeats, allowing the laser to produce a train of welldefined, ultrafast pulses. Mode locking through saturable absorption happens in the chameleon system through the optical Kerr effect. The optical Kerr effect refers to the phenomenon where the refractive index of a material changes in response to the intensity of incident light as given by equation (2.9).

$$n(I) = n_0 + n_2 I (2.9)$$

Here n_0 is the linear refractive index and n_2 is the non-linear refractive index and I is the intensity of the laser light. Kerr lens effect and different optical components present in the laser system leads to chirping of the pulse though group velocity dispersion. Inverted prism combinations are used in order to compensate for the GVD and make the effective GVD zero. One of the significant consequences of Kerr effect is optical self-focusing where because of the intensity peaking at the centre of the beam, the refractive index also increases leading to the formation of 'Kerr lens'. The larger the number of modes locked,

higher the intensity of the pulse. As suggested, the Kerr lens is formed only at high intensities like the case of mode locked pulses and is absent for continuous pulse. This lens, like the case of an optical lens, narrows the beam diameter. The laser system is also equipped with a slit that is tuned to allow only the narrowed mode locked pulse while gating the continuous beam as shown in the figure 2.8. where the continuous laser is blocked and mode locked pulse is allowed when the slit is active [64].

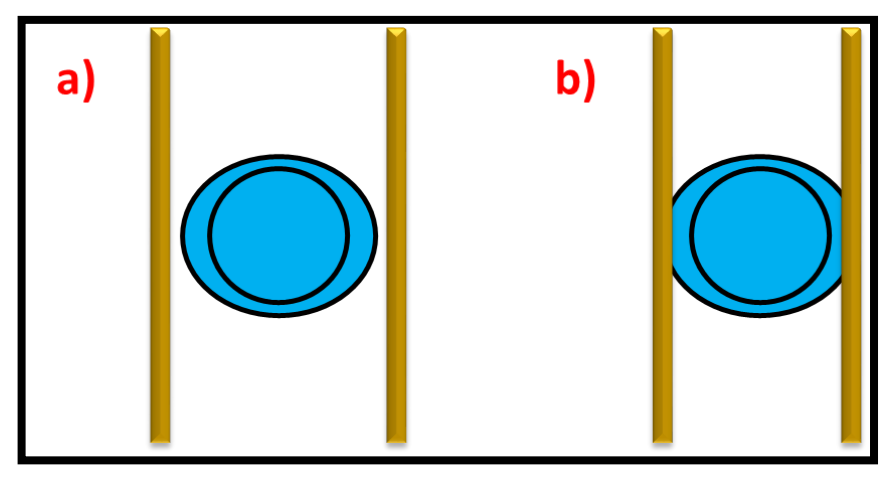


Figure 2.8: Illustration of mode locking through saturable absorber in Chameleon a) when the slit is inactive and b) when the slit is active.

2.3.3. Femtosecond Amplifier System

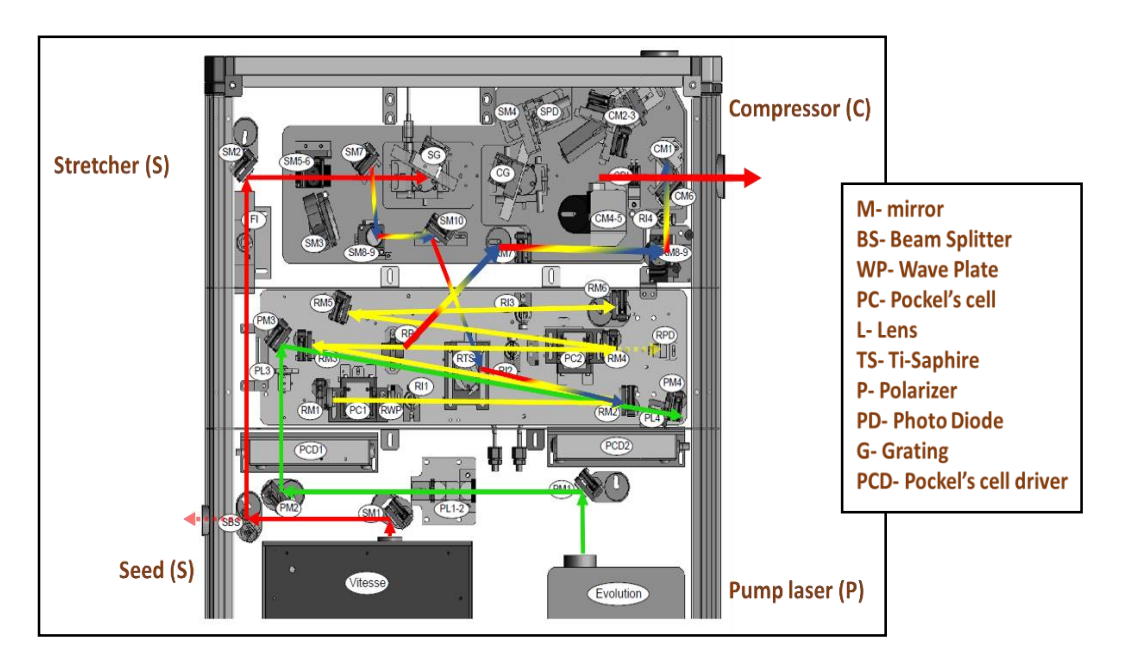


Figure 2.9: Beam path for the Coherent femtosecond laser amplifier where green light indication the pump (Evolution), red indicates seed from Vitesse and yellow for the pulse within the regenerative amplifier. The coloured line indicated chirped pulse. The labels for optical components are highlighted in the figure.

Typical values of energy per pulse generated by a femtosecond laser oscillator is around a few nanojoules and is insufficient for many applications like ablation of metals or laser induced breakdown spectroscopy. An amplifier system overcomes this by having in addition to a routine laser cavity with gain medium and mirrors, an ultrafast laser amplifier comprising of an amplifying unit and chirped pulse amplification unit in order to amplify the seed pulse from

2.3.3.1. Amplification Mechanism

An ultrafast amplifier system consists of an amplifier unit along with an oscillator system in order to amplify the pulses further. An amplifier system can be a multi-pass system or a regenerative amplifier but the latter is always preferred given the simplicity in the alignment. It also consists of chirped pulse amplification system, an innovative way to expand and then compress the ultrafast pulses in order to prevent damage to the optical components and the crystal.

The Libra femtosecond laser amplifier system consists of four modules namely, a) Vitesse, b) Evolution, c) Regenerative amplifier and d) pulse stretcher-compressor units. Vitesse is a Ti-Sa oscillator system that serves as a seed laser for amplification. Evolution is a Q-switched 527 nm laser that serves as a pump for the amplifier system. Regenerative amplifier facilitates amplification of the ultrafast pulses through making multiple passes through the gain medium coupled with an optical shutter. In a regenerative amplifier, initially the laser gain medium is pumped until enough energy is accumulated. The seed pulse is injected into the amplifier through the shutter whose duration is less than the round-trip time of the seed laser. This pulse will make multiple passes through the gain medium and is then amplified significantly. Once enough energy is accumulated, it is eventually released again through an optical switch.

An amplified pulse in the regenerative amplifier, given the high intensity is capable of damaging the crystal and the optics inside the cavity. In 1980s the problem was addressed by the invention of chirped pulse amplification by Donna Strickland, which has eventually won her noble prize in 2018 [65]. The idea in its simplicity is to stretch the pulse before amplification and compress it before ejection using different dispersive elements. Once the pulse is stretched in order to reduce the peak intensity, the pulse is ready to be amplified as the intensity will be less than the damage crystal of the gain medium. After amplifying, a compressor with opposite GVD is employed to eject an unchirped, amplified pulse. The

compressor also compensates for the dispersion introduced during the amplification process. So the distance between gratings is different for stretcher and compressor. A prism pair is the simplest combination of optics that can function as stretcher and compressor in right combinations. However, a grating pair is used in the to avoid material losses. Once the pulse is stretched it is released into the regenerative amplifier using a time gated Pockel's cell.

The detailed beam path for the Libra system is shown in figure 2.9. The seed pulse from the Vitesse oscillator is passed through a series of mirrors into the stretcher system. The stretcher system consists of a grating, in order to introduce GVD, along with other optical components as shown in figure 2.10 a). The stretched pulse is then fed into the Ti-Sa crystal in the regenerative amplifier at a Brewster angle. The pump laser (Evolution) creates excited state population in the Ti-Sa crystal in the amplifier unit. The Pockel's cells in the regenerative amplifier are controlled externally by a synchronization and delay generator (SDG). The regenerative amplifier amplifies the stretched pulse. The output of the regenerative is compressed in the compressor system as shown in figure 2.10 b) and the output unchirped, amplified fs pulse is ejected. The whole system is connected to a water chiller that dissipate s the heat generated by different lasers in the system and is maintained at 21°C.

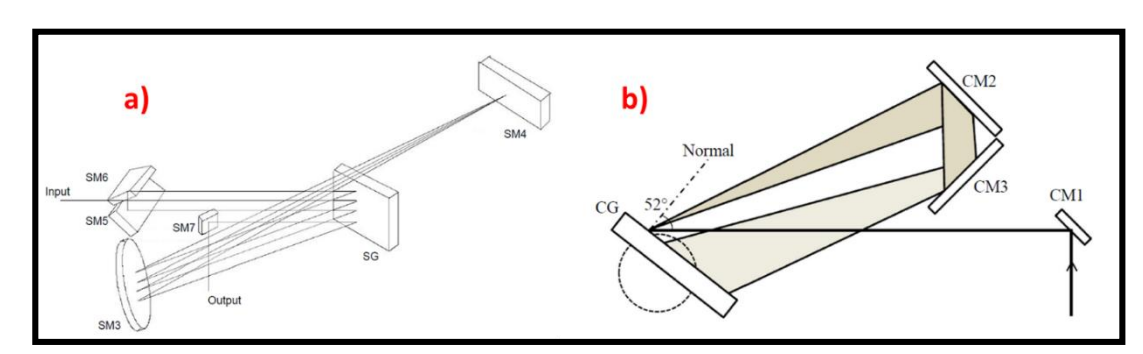


Figure 2.10: Schematic of optical path in the a) Stretcher system and b) Compressor system of the amplifier. Images have been reproduced from the manual of Coherent [66].

2.3.3.2. Autocorrelation

Measuring the pulse duration of an ultrafast pulse is extremely important in order to estimate the time resolution that the pulse can offer and to gate specific events during the experiments. Conventional photodiodes have a response time in the order of few nanoseconds are not useful in measurement of ultrashort pulses. A pulse autocorrelation technique, as the names suggests, measures the temporal correlation of the pulse with itself. A beam splitter is used to divide the pulse into two identical pulses, which are then made to cross into a second order nonlinear crystal, where second harmonic production

takes place, as illustrated in figure 2.11. To introduce a temporal shift in the pulses, the two beams' travel lengths are maintained apart. If the arm length difference is reduced to the point where the pulses collide within the nonlinear crystal, the process of sum frequency generation takes place, producing an output with a shorter wavelength. When the relative time delay is increased, the mixing product becomes weaker and the overlap of the two pulses in the crystal decreases. Intuitively, for shorter pulses, the overlap lasts for very short time. This delay, τ , is controlled by motorized translational stages. In order to measure pulse duration, the path length and the intensity of the second harmonic output are plotted. The field strength of the mixed beam can be written as,

$$E_{sig}^{SHG} \alpha E(t)E(t-\tau)$$
 (2.10)

Since the intensity is proportional to the square of field and it is always intensity that we measure in lab, the equation can also be written as,

$$I_{sig}^{SHG} \alpha I(t)I(t-\tau) \tag{2.11}$$

The intensity autocorrelation is then written as,

$$A(\tau) = \int_{-\infty}^{\infty} I(t)I(t-\tau)$$
 (2.12)

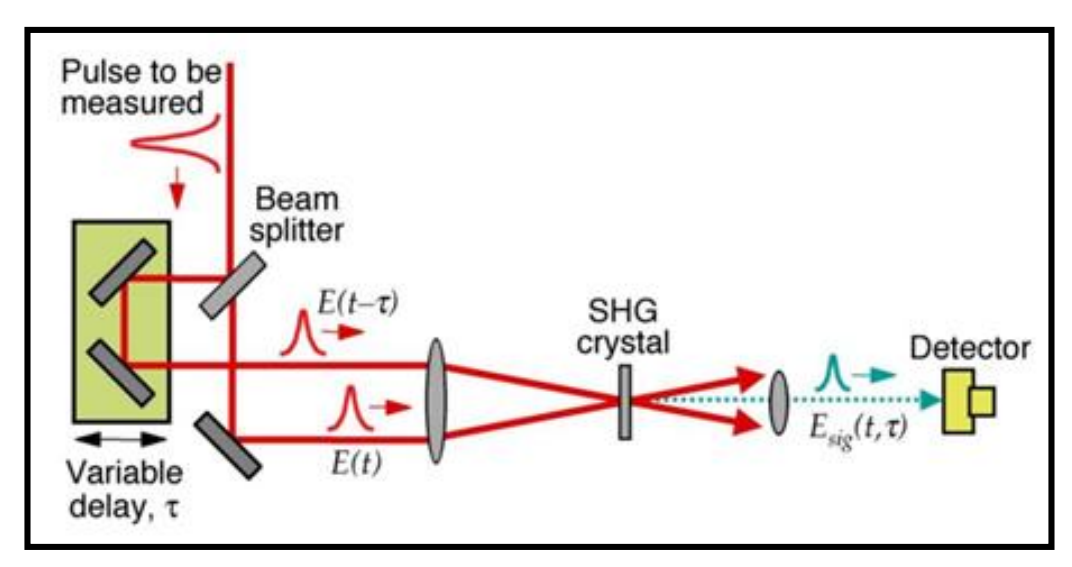


Figure 2.11: Schematic of experimental setup inside an autocorrelator used to measure femtosecond laser pulses. Figure reproduced from the reference [67].

Coherent single shot autocorrelator (SSA) has been employed in order to measure the pulse duration of the fs amplifier system. The laser is incident on a mirror at the entrance slit and is guided into the experimental setup. A 50:50 beam splitter splits the beam into two paths one of whose path lengths is controlled using a delay generator. The two beams are then made to overlap and cross inside the non-linear KDP crystal. The crystal angle needs to be optimized for the overlapping of the beams. A CCD detector is used to the detect the intensity of the second harmonic pulse. Bandpass filter and neutral density filters are used before the CCD in order to filter the 800 nm radiation and prevent overexposure of the CCD.

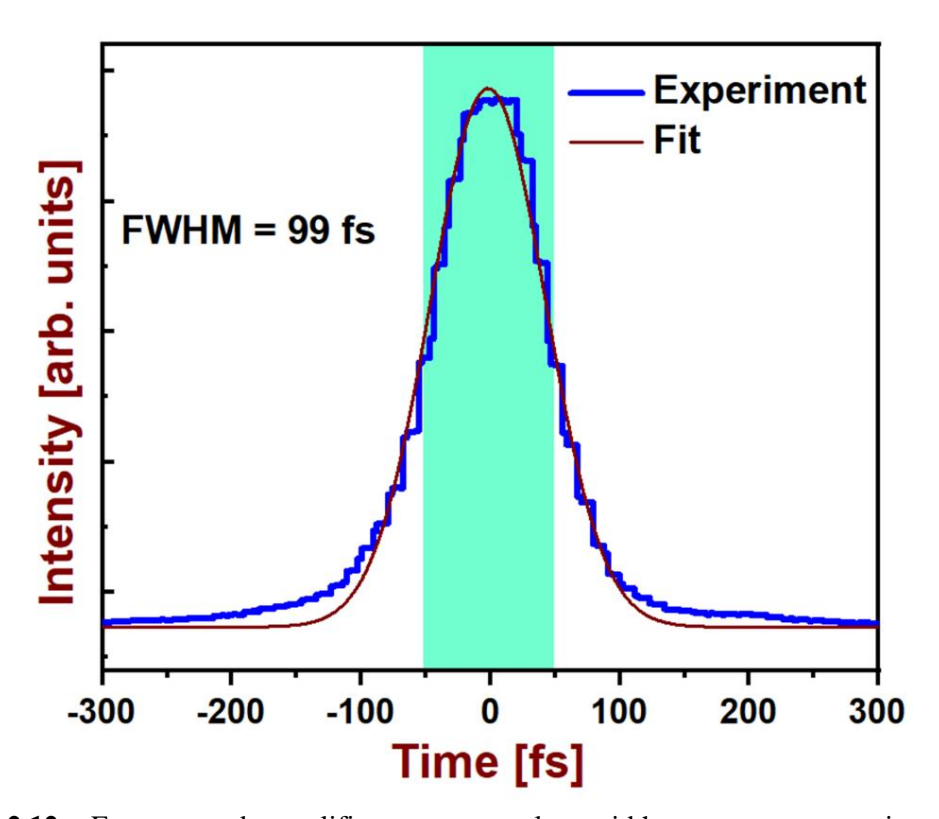


Figure 2.12: Femtosecond amplifier system pulse width measurement using intensity autocorrelation technique

The FWHM of the pulse was found to be 99 fs and taking into account the correction for the Gaussian shape of the pulse, the pulse duration was calculated to be ~70 fs (figure 2.12). The discrepancy between the reported duration of ~50 fs and the experimentally measured pulse can be attributed to group velocity mismatch and group velocity dispersion of the ultrafast pulses when they pass through different optical components.

2.4. Experimental Setups

2.4.1. Ultrafast Laser Ablation

The laser was aligned using different reflective mirrors and was focused on the sample using long working distance objectives (50X and 100X) as shown in figure 2.13. The sample was moved on a computer controlled translational stages to make patterns on the Si substrate. We have studied the effects of different experimental parameters and characterized by FESEM. A square pattern was used for SERS studies as it was proven to be advantageous in our previous study using a femtosecond amplifier [68]. A combination of Brewster wave plate and half wave plate was used in order to adjust the power to the required value. Effects of number of pulses per spot have been studied by changing the scan speed using the programmable stages. Web-like Si structures were observed at a particular scan speed and fluence. Laser fluence has been changes by changing the working objective to 100x keeping the scan speed fixed and the resulting morphology was studied using FESEM. Systematic experiments indicate that there is a threshold fluence for the formation of the web like structures and the mechanism is discussed in chapter 3. Laser ablated Si structures with 50X, 1.5 mm/s, laser power of 2.5 W, and fluence of 1 J/cm² were used for SERS after coating it with thin layer of Au (~10 nm) by thermal evaporation method.

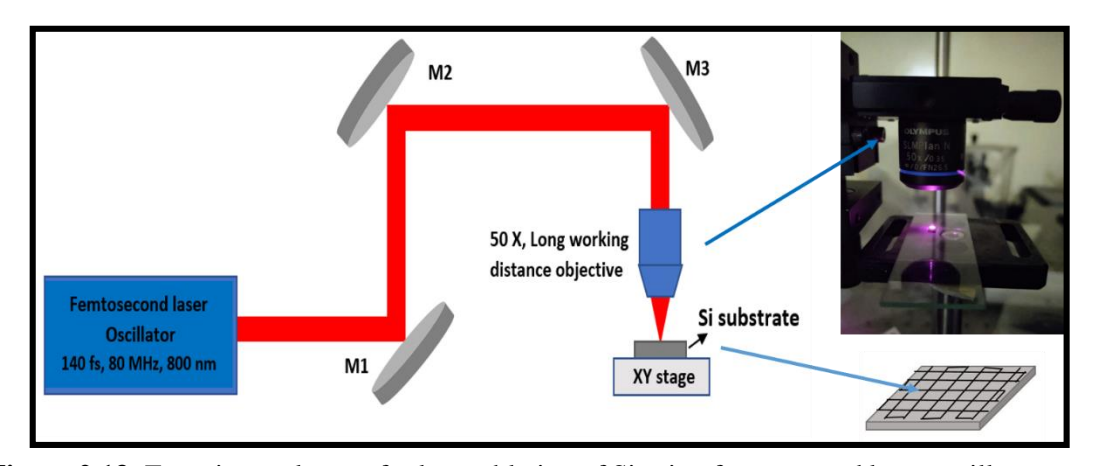


Figure 2.13: Experimental setup for laser ablation of Si using femtosecond laser oscillator system.

The femtosecond laser amplifier was used for different experiments with slight modifications in the setup for different ablation conditions. Ablation of Ag-Au (1:1) alloy

has been performed in air using different angle of incidence. The mirror just above the sample has been placed on a rotation mount in order to rotate to change the angle of

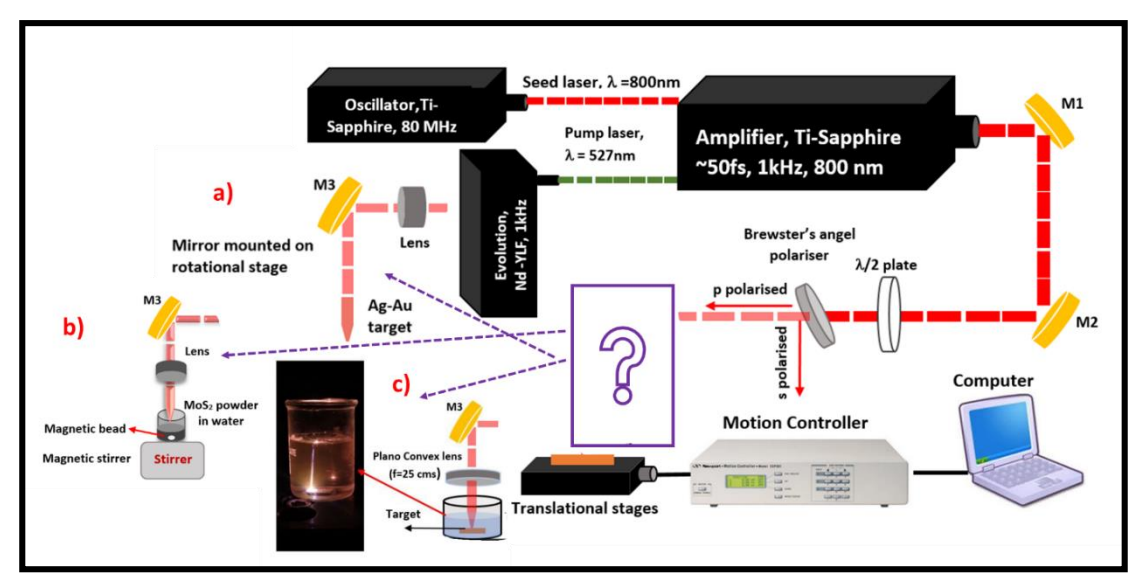


Figure 2.14: Schematic of femtosecond laser ablation used in the thesis work for different conditions a) of Ag-Au target using different angles of incidence, b) Irradiation of MoS₂ powder using magnetic stirrer, and c) Au in water.

incidence on the sample. The lens this case has been placed above the mirror as shown in figure 2.14. Instead of using a plano-convex lens, a cylindrical lens has been used for the ablation of Ag and effects of different experimental conditions has been studied. MoS₂ powder ablation was performed by dispersing the sample in three different solvents, ethanol, methanol and water and by using a magnetic stirrer in order to facilitate homogeneous irradiation.

2.4.2. Raman Systems

Horiba Raman Spectrometer

The initial experiment performed by Prof. C.V. Raman that eventually lead to the discovery of Raman effect and Noble prize was very rudimentary and used sun light as an excitation source. He used a green filter to filter the sunlight and excite the chloroform sample which was found to give away yellow light through inelastic scattering [69]. But modern-day Raman systems have come a long way and now are extremely portable (weighing less than 5 Kgs and transportable in a small suitcase) and stable. A Raman measurement typically consists of an excitation source, optics for sample illumination and signal collection, appropriate filters to filter Rayleigh and anti-stokes shifts, spectrometer and a detector.

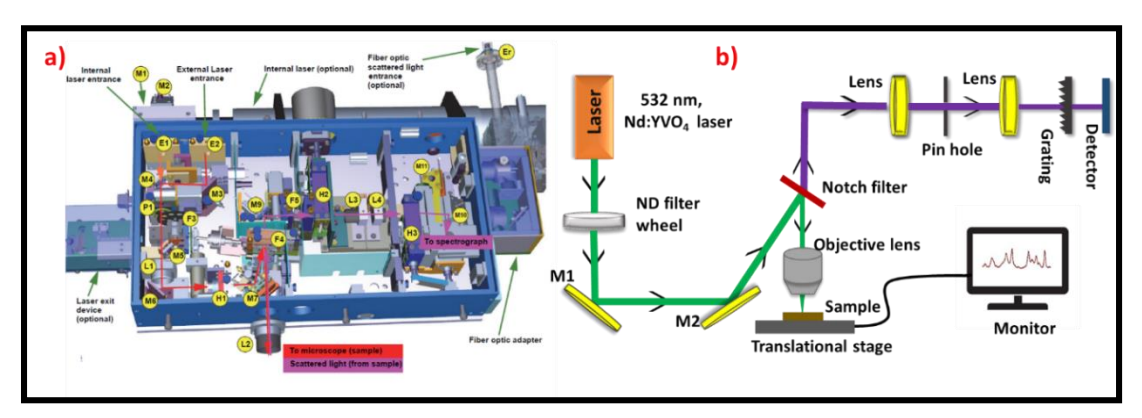


Figure 2.15: a) Optical alignment inside the Horiba LabRam Raman Spectrometer (Image reproduced from the user manual of the instrument [70], and b) Simplified schematic of the optical path.

This thesis majorly used Horiba LabRam Raman Spectrometer for data collection and a BWTEK portable Raman spectrometer for one study. Horiba Raman spectrometer consists of four excitation sources of wavelengths 532 nm (Nd:YVO₄), 633 nm (He-Ne), 325 nm (He-Cd) and 785 nm (GaAs) lasers. Raman scattering is proportional to v^4 , where v is the frequency and hence would appear that using shorter wavelengths is ideal. However, in order to limit fluorescence and prevent sample damage, it is not ideal to use short wavelengths always. While choosing a wavelength, it is advantageous to choose a wavelength close to the resonance of the metal NSs or the probe molecule in order to enhance the signal further through resonance effects [23]. The choice of the wavelength is made through the software LabSpec and there are notch and edge filters which are automatically adjusted after the wavelength selection in order to reject Rayleigh frequencies (F₄ and F₅) (Refer figure 2.15). It also consists of nine positions which will allow to change the laser power though selection from the software by rotating the filter wheel F3. The sample is mounted on an XY stage controlled by a joy stick. The system is also equipped with a microscope with white light illumination by transmission and objectives of magnification 10×, 20×, 50×, 40× and 100× mounted on a rotating turret. It consists of a grating with 1800 grooves/mm. It consists of a multichannel CCD detector cooled to -60°C covering UV-Vis-IR regions. It has a spectral resolution of 0.35 cm⁻¹. The beam enters the system through the mirrors M1 and M2 and passes through a polarizer P1. It has a spectrometer in Czerny-Turner alignment with a CCD detector.

The portable Raman spectrometer has a laser source with an excitation wavelength of 785 nm. It offers best balance between fluorescence and the Raman signal and is known to have less damage threshold for many materials making it a popular choice for SERS. The

beam size is nearly 90 μ s and is extremely useful for collecting signal from large area averaging the SERS signal fluctuations. The power can be adjusted through the software from 1mW to nearly 350 mW. It consists of a high band pass filter to filter Rayleigh and anti-Stokes lines.

2.5. Characterization Techniques

2.5.1. FESEM and TEM

Electron microscopes offer higher resolution than the light microscopes and has hence revolutionized many areas of science [71]. Field emission scanning electron microscope (FESEM) and Tunnelling Electron Microscope (TEM) are the two frontline electron imaging techniques that are being extensively used for characterization of SERS substrates. Electrons in these techniques are accelerated through a potential gradient and the interaction of these electrons with the sample leads to different events that are imaged consequently. Electrons from the source, referred as primary electrons, are generated and passed in high vacuum environment in order to increase their mean free path. These electrons are focused on the sample though different electromagnetic lenses. The electron interaction with the sample leads to the formation of secondary electrons which are used for imaging. The properties of emitted electrons from the sample like angle and energy reflect the topography of the sample. These electrons are detected using a detector and are amplified to achieve a final digital image of the sample. A sharp tungsten tip is an electron source and functions as a cathode where the anode is placed just after the tip.

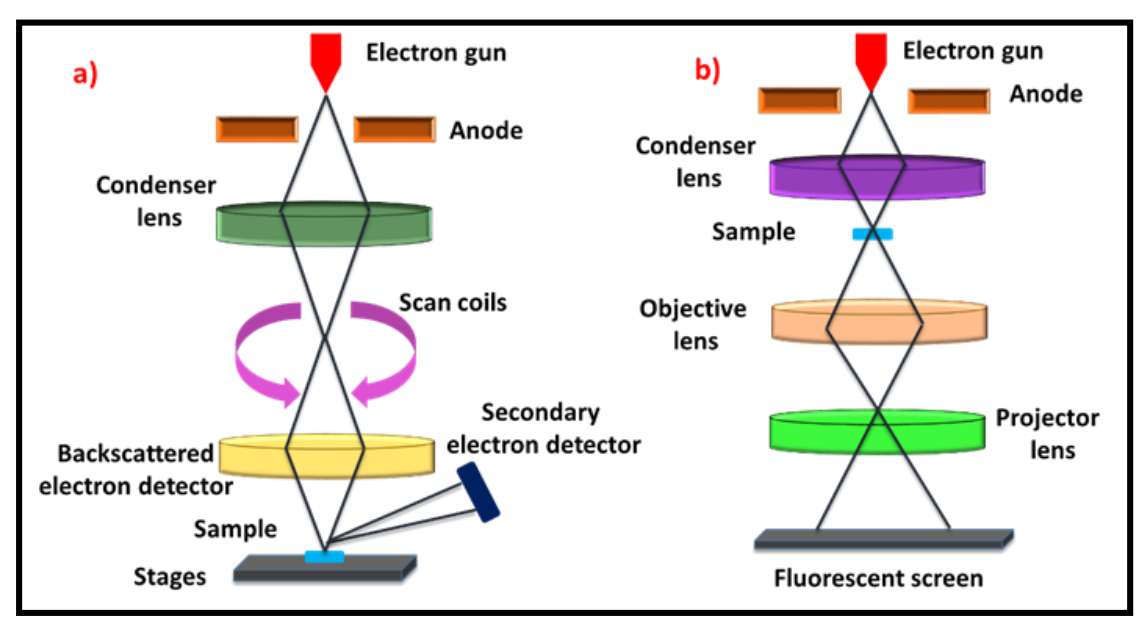


Figure 2.16: Schematic to illustrate the working principle of a) SEM and b) TEM for imaging.

Different electromagnetic lenses like the condenser lens, scanning coil, and objective lens focus the electron beam to a sharp point on the sample. In FESEM, scattered electrons are imaged and whereas in TEM, transmitted electrons are imaged as shown in figure 2.16. The current in the condenser lens is inversely proportional to the beam size. The electron beam scans the surface of the sample in a raster pattern. In a TEM system, the primary electrons pass through the sample providing information about the internal structure of it and hence offers better resolution (0.1nm) while FESEM offers a resolution a few nanometres. In FESEM images are formed by scattered electrons resulting in 3-D images whereas in TEM transmitted electrons resulting in 2-D images. In TEM, high resolution TEM images (HR-TEM) images that are formed by both scattered and transmitting electrons are useful in analysing the crystal structure. TEM also facilitates electron diffraction studies that give detailed information about the lattice parameters of the crystal using selected area electron diffraction (SAED).

2.5.2. UV-Visible Spectroscopy

Understanding LSPR resonances is essential to utilise the nanomaterials for SERS based applications. UV-Visible spectroscopy measures attenuation of light as it passes through the sample either in reflection or transmission geometry covering UV and Visible spectrum of the electromagnetic radiation. It provides valuable information regarding the electronic states of the sample through absorption of the incident radiation. A beam of light emitted from a visible and/or UV light source is directed towards a prism or diffraction grating. These optical elements separate the beam of light into its constituent wavelengths, creating a spectrum. Each individual wavelength, also known as a monochromatic beam, is then split into two beams of equal intensity using a half-mirrored device. One of these beams, called the sample beam, passes through a small transparent container called a cuvette. Inside the cuvette, there is a solution of the compound that is being investigated, dissolved in a transparent solvent. This sample beam interacts with the compound in the solution. The other beam, known as the reference beam, passes through an identical cuvette that contains only the solvent without the compound. This reference beam serves as a baseline for comparison. Both the sample beam and the reference beam continue their paths and are directed towards electronic detectors. These detectors measure the intensities of the light beams. The intensities of the sample beam and the reference beam are then compared. By analysing the differences in intensities between the two beams, one can gain valuable

information about the compound under investigation. This information can include characteristics such as the absorption, emission, or scattering of light by the compound, which can provide insights into its properties and behaviour. In UV-Visible spectroscopy absorption is indirectly measured through transmittance which is a measure of what is not absorbed. This is reinforced by the fact that photons that are absorbed by the sample will be extinguished and reflects in the intensity of transmitted light, the transmitted light reflecting in the intensity. The power extinguished, P_{Ext} is given as,

$$P_{Ext} = \sigma_{Ext} S_{Inc} \tag{2.13}$$

Here, S_{Inc} is a measure of incident power density of the light source and σ_{Ext} is the proportionality constant known as the extinction cross section, an attribute of the molecule. To extrapolate this to an ensemble of molecules in a solvent, consider a solution of these molecules adding to a concentration of c_m [M], in an elementary volume of length dL [m] along the beam, and a surface area A [m²] across. Therefore, $P = S_{Inc}A$ [W] is the power entering this box. The volume comprises molecules with a mass $dN = Nc_mAdL$, each of which contributes to extinction with a cross-section σ_{Ext} , producing an extinguished power $dP_{Ext} = N_{Ext}S_{Inc}c_mAdL$ using Avogadro's number N. The incident beam's power as it leaves the box is consequently given as the differential equation,

$$\frac{dP}{P} = -N\sigma_{Ext}c_m dL \tag{2.14}$$

The power transmitted over a length L is then obtained by integrating equation (2.14),

$$P_{tran} = P_{Inc}e^{-(N\sigma_{Ext}c_mL)}$$
 (2.15)

Transmittance is often defined as the ration of transmitted power and the incident power whereas absorbance (A) is defined as negative logarithm of transmittance.

$$A = -\log(T) = -\log\left(\frac{P_{tran}}{P_{Inc}}\right) = \frac{N\sigma_{Ext}c_mL}{\ln(10)}$$
 (2.16)

The molar absorption coefficient (ε) is defined as,

$$\varepsilon = \frac{N\sigma_{Ext}}{\ln(10)} \tag{2.17}$$

From equation (2.16) and (2.17), we have absorbance as,

$$A = \varepsilon c_m L \tag{2.18}$$

The above equation is known as the Beer-Lambert's law.

UV-Visible spectroscopy provides useful insights into shape, size, and density of the nanoparticles. The absorption information provides a flexibility to choose an excitation for the specific nanomaterial in order to exploit resonance. UV-Visible absorption of the probe molecules is also important in accessing the resonance enhancement. Anisotropic or asymmetric nanostructures often have a longitudinal and transverse absorption peaks in the absorption spectrum [72]. Aggregation of NPs, as is the case during the addition of salts reflects as increase in the value of absorbance [73]. The LSPR resonance is known to red shift with increase in the size of the NPs [74].

2.5.3. Energy Dispersive X-Ray Spectroscopy

FESEM instruments in addition to imaging also facilitate energy dispersive X-Ray spectroscopy (EDX) for the identification of elements in the selected region. It will help in both qualitative and quantitative identification (relative abundance) of elements on the surface of the sample. It is based on the principle that each element has a characteristic X-ray peak. In order to generate X-rays, high intensity electron beam is focused on the sample. This results in the emission of electron from the inner shell of the atomic structure leading to the formation of an electron hole at the site. An electron at a higher shell occupies this vacancy by emitting a characteristic X-ray. The quantity and intensity of the emitted electrons is measured using an energy dispersive spectrometer (EDS). EDS enables the measurement of the specimen's elemental composition since the energies of the X-rays are indicative of the energy difference between the two shells and of the atomic structure of the emitting element. We have used EDX to confirm and identify the elements on the surface of nanostructures and nanoparticles synthesised by both chemical and laser ablation in this study.

2.5.4. SERS Measurements

Different SERS substrates were used to full fill different performance metrics of SERS efficiency. All the substrates in this study are planar. In all the cases we have used simple drop-casting of the colloid NPs for SERS studies. The samples were cleaned right after their respective preparation techniques using acetone and ultra-sonication. SERS studies were performed on different molecules summarised in table 2.1. Different concentrations of each analyte molecules were prepared using serial dilution methods and stored in sealed

glass vials. Upon the plasmonic substrate, 2-20 µl of the probe molecule of given concentration was drop casted on the substrate and waited to dry. In this thesis, both portable and micro-Raman systems were used for measurements. Fresh sample was used for each study. For the AuNPs@AgNDs work and laser ablated Ag, we have used 532 nm laser excitation in the Horiba system. In a different study involving laser ablated Ag-Au, extensive UV-Visible absorption studies of the analyte molecule were carried out before choosing an excitation wavelength in order to be close to the resonance. Measurements were performed after focusing the sample using inbuilt microscope in micro Raman system assisted by the software [75]. For mapping studies, random large area was chosen on the surface and a peak window has been selected to map the intensity. The acquisition time and laser power were chosen carefully to prevent sample damage and at the same time get maximum SERS signal. In order to take into account spatial signal fluctuations in SERS, we have performed different at least 10 random measurements on the sample surface and considered the average spectrum as the representation at a particular concentration. For studying the aging of the substrates, the samples were sealed and stored in desiccator and measurements were carried at regular intervals of time. Detailed protocol for the end-toend measurements carried out in the thesis work have been published step wise [75].

References

- [1] V.M. Arole, S. V Munde, Fabrication of Nanomaterials By Top-Down and Bottom-Up Approaches-an Overview, JAAST:Material Science (Special issue) 1 (2014) 89-93.
- [2] N. Abid, A.M. Khan, S. Shujait, K. Chaudhary, M. Ikram, M. Imran, J. Haider, M. Khan, Q. Khan, M. Maqbool, Synthesis of nanomaterials using various top-down and bottom-up approaches, influencing factors, advantages, and disadvantages: A review, Adv. Colloid Interface Sci. 300 (2022) 102597. https://doi.org/10.1016/j.cis.2021.102597.
- [3] P. Iqbal, J.A. Preece, P.M. Mendes, Nanotechnology: The "Top-Down" and "Bottom-Up" Approaches, Supramolecular chemistry: from molecules to nanomaterials, Supramolecular chemistry: from Molecules to Nanomaterials, John Wiley & Sons, Ltd. (2012) 1–14. https://doi.org/10.1002/9780470661345.smc195.
- [4] V.K.G. Neha Srivastava, M. Srivastava, P. K. Mishra, Green Synthesis of Nanomaterials for Bioenergy Applications, John Wiley & Sons, 2020.
- [5] A.M. Ealias, M.P. Saravanakumar, A review on the classification, characterisation, synthesis of nanoparticles and their application, IOP Conf. Ser. Mater. Sci. Eng. 263 (2017). https://doi.org/10.1088/1757-899X/263/3/032019.
- [6] S.V. Rao, G.K. Podagatlapalli, S. Hamad, Ultrafast laser ablation in liquids for nanomaterials and applications, J. Nanosci. Nanotechnol. 14 (2014) 1364–1388. https://doi.org/10.1166/jnn.2014.9138.
- [7] J. Reguera, J. Langer, D. Jiménez De Aberasturi, L.M. Liz-Marzán, Anisotropic metal nanoparticles for surface enhanced Raman scattering, Chem. Soc. Rev. 46 (2017) 3866–3885. https://doi.org/10.1039/c7cs00158d.
- [8] K. Rhee, A. Tukova, M. Tavakkoli Yaraki, Y. Wang, Nanosupernova: a new anisotropic nanostructure for SERS, Nanoscale. 15 (2023) 2087–2095. https://doi.org/10.1039/d2nr05287c.
- [9] H. Maiman Theodore, Stimulated optical radiation in ruby, *Nature*, 4736 (1960), 493-494. https://doi.org/10.1038/187493a0.
- [10] A. Fojtik, M. Giersig, and A. Henglein, Formation of Nanometer-Size Silicon Particles, Berichte der Bunsengesellschaft für physikalische Chemie, 97 (1993), 1493–1496. https://doi.org/10.1002/bbpc.19930971112.
- [11] S. Preuss, M. Stuke, Subpicosecond ultraviolet laser ablation of diamond: Nonlinear

- properties at 248 nm and time-resolved characterization of ablation dynamics, Appl. Phys. Lett. 67 (1995) 338. https://doi.org/10.1063/1.115437.
- [12] B.N. Chicbkov, C. Momma, S. Nolte, F. yon Alvensleben, A. Tunnermann,
 Femtosecond, picosecond and nanosecond laser ablation of solids, Appl. Phys. A.
 63 (1996) 109–115. https://doi.org/10.54870/1551-3440.1147.
- [13] B. Barcikowski, S., Amendola, V., Lau, M., Marzun, G., Rehbock, C., Reichenberger, S., Zhang, D., Gökce, Handbook of & Processing of Colloids, Universität Duisburg-Essen. (2019).
- [14] V. Amendola, M. Meneghetti, What controls the composition and the structure of nanomaterials generated by laser ablation in liquid solution?, Phys. Chem. Chem. Phys. 15 (2013) 3027–3046. https://doi.org/10.1039/c2cp42895d.
- [15] C. Byram, S. Satya, B. Moram, D. Banerjee, R Beeram Review of ultrafast laser ablation for sensing and photonic applications, Journal of Optics (2023). 10.1088/2040-8986/acbc31.
- [16] K.R. Kumar, D. Banerjee, A. Mangababu, R.S. Prasad Goud, A.P. Pathak, V.R. Soma, S.V.S. Nageswara Rao, Resistivity dependence on nanostructure formation in picosecond ablation of silicon and SERS-based sensing applications, J. Phys. D. Appl. Phys. 55 (2022). https://doi.org/10.1088/1361-6463/ac818b.
- [17] E. Fazio, B. Gökce, A. De Giacomo, M. Meneghetti, G. Compagnini, et al., Nanoparticles engineering by pulsed laser ablation in liquids: Concepts and applications, Nanomaterials. 10 (2020) 2317. https://doi.org/10.3390/nano10112317.
- [18] J. Xiao, P. Liu, C.X. Wang, G.W. Yang, External field-assisted laser ablation in liquid: An efficient strategy for nanocrystal synthesis and nanostructure assembly, Prog. Mater. Sci. 87 (2017) 140–220. https://doi.org/10.1016/j.pmatsci.2017.02.004.
- [19] A.A. Serkov, E. V. Barmina, G.A. Shafeev, V. V. Voronov, Laser ablation of titanium in liquid in external electric field, Appl. Surf. Sci. 348 (2015) 16–21. https://doi.org/10.1016/j.apsusc.2014.12.139.
- [20] P. Liu, C.X. Wang, X.Y. Chen, G.W. Yang, Controllable fabrication and cathodoluminescence performance of high-index facets GeO₂ micro- and nanocubes and spindles upon electrical-field-assisted laser ablation in liquid, J. Phys. Chem. C. 112 (2008) 13450–13456. https://doi.org/10.1021/jp802529r.
- [21] H. Marrapu, R. Avasarala, V.R. Soma, S.K. Balivada, G.K. Podagatlapalli, Silver

- nanoribbons achieved by picosecond ablation using cylindrical focusing and SERS-based trace detection of TNT, RSC Adv. 10 (2020) 41217–41228. https://doi.org/10.1039/d0ra05942k.
- [22] V.R.S. Dipanjan Banerjee, Mangababu Akkanaboina, Subhasree Ghosh, Picosecond Bessel Beam Fabricated Pure, Gold-Coated Silver Nanostructures for Trace-Level Sensing of Multiple Explosives and Hazardous Molecules, Materials. 15 (2022) 4155. https://doi.org/https://doi.org/10.3390/ma15124155.
- [23] R. Beeram, V.R. Soma, Ultra-trace detection of diverse analyte molecules using femtosecond laser structured Ag Au alloy substrates and SERRS, Opt. Mater. 137 (2023) 113615. https://doi.org/10.1016/j.optmat.2023.113615.
- [24] E. Solati, D. Dorranian, Effect of temperature on the characteristics of ZnO nanoparticles produced by laser ablation in water, Bull. Mater. Sci. 39 (2016) 1677–1684. https://doi.org/10.1007/s12034-016-1315-7.
- [25] N.N. Nedialkov, S.E. Imamova, P.A. Atanasov, Ablation of metals by ultrashort laser pulses, J. Phys. D. Appl. Phys. 14 (1997) 638–643. https://doi.org/10.1088/0022-3727/37/4/016.
- [26] A. Kanavin, I. Smetanin, V. Isakov, Y. V. Afanasiev, B. Chichkov, B. Wellegehausen, Heat transport in metals irradiated by ultrashort laser pulses, Phys. Rev. B Condens. Matter Mater. Phys. 57 (1998) 14698–14703. https://doi.org/10.1103/PhysRevB.57.14698.
- [27] G.W. Yang, Laser ablation in liquids: Applications in the synthesis of nanocrystals, Prog. Mater. Sci. 52 (2007) 648–698. https://doi.org/10.1016/j.pmatsci.2006.10.016.
- [28] A. You, M. Be, I. In, Initiation of an early-stage plasma during picosecond laser ablation of solids, 2466 (2001) 2464–2466. https://doi.org/10.1063/1.1318239.
- [29] H.D. Vora, S. Santhanakrishnan, S.P. Harimkar et al. One-dimensional multipulse laser machining of structural alumina: evolution of surface topography. Int J Adv Manuf Technol 68(2013), 69–83. https://doi.org/10.1007/s00170-012-4709-8.
- [30] D. Zhang, B. Go, S. Barcikowski, Laser Synthesis and Processing of Colloids: Fundamentals and Applications, Chemical reviews 117(2017) 3990-4103. https://doi.org/10.1021/acs.chemrev.6b00468.
- [31] G. Kumar, Y. Shivam, S.D. Sastikumar, P. Koinkar, Progress in pulsed laser ablation in liquid (PLAL) technique for the synthesis of carbon nanomaterials: a review, Applied Physics A 127 (2021)1-40. https://doi.org/10.1007/s00339-021-

- 04951-6.
- [32] C.Y. Shih, M. V. Shugaev, C. Wu, L. V. Zhigilei, The effect of pulse duration on nanoparticle generation in pulsed laser ablation in liquids: Insights from large-scale atomistic simulations, Phys. Chem. Chem. Phys. 22 (2020) 7077–7099. https://doi.org/10.1039/d0cp00608d.
- [33] B. Lim, M. Jiang, P.H.C. Camargo, E.C. Cho, J. Tao, X. Lu, Y. Zhu, Y. Xia, Pd-Pt bimetallic nanodendrites with high activity for oxygen reduction, Science 324 (2009) 1302–1305. https://doi.org/10.1126/science.1170377.
- [34] B.D. Adams, G. Wu, S. Nlgro, A. Chen, Facile synthesis of Pd-Cd nanostructures with high capacity for hydrogen storage, J. Am. Chem. Soc. 131 (2009) 6930–6931. https://doi.org/10.1021/ja901798u.
- [35] A.Y. Li Fu, Tasnuva Tamanna, Wen-Jing Hu, Chemical preparation and applications of silver dendrites, Chem. Pap. 68 (2014) 1283–1297. https://doi.org/10.2478/s11696-014-0582-2.
- [36] A. Taleb, C. Mangeney, V. Ivanova, Electrochemical synthesis using a self-assembled Au nanoparticle template of dendritic films with unusual wetting properties, Nanotechnology. 22 (2011) 205301. https://doi.org/10.1088/0957-4484/22/20/205301.
- [37] S. Kaniyankandy, J. Nuwad, C. Thinaharan, G.K. Dey, C.G.S. Pillai, Electrodeposition of silver nanodendrites, Nanotechnology. 18 (2007) 125610. https://doi.org/10.1088/0957-4484/18/12/125610.
- [38] M. Matsushita, M. Sano, Y. Hayakawa, H. Honjo, Y. Sawada, Fractal structures of zinc metal leaves grown by electrodeposition, Phys. Rev. Lett. 53 (1984) 286–289. https://doi.org/10.1103/PhysRevLett.53.286.
- [39] D. Li, Z. Zheng, Y. Lei, S. Ge, Y. Zhang, Y. Zhang, K.W. Wong, F. Yang, W.M. Lau, Design and growth of dendritic Cu2-xSe and bunchy CuSe hierarchical crystalline aggregations, Cryst. Eng. Comm. 12 (2010) 1856–1861. https://doi.org/10.1039/b919087m.
- [40] T. Qiu, X.L. Wu, Y.F. Mei, P.K. Chu, G.G. Siu, Self-organized synthesis of silver dendritic nanostructures via an electroless metal deposition method, Appl. Phys. A Mater. Sci. Process.81(2005) 669–671.https://doi.org/10.1007/s00339-005-3263-8.
- [41] T.A. Witten, L.M. Sander, Diffusion-limited aggregation, Phys. Rev. B. 27 (1983) 5686–5697. https://doi.org/10.1103/PhysRevB.27.5686.
- [42] M. V Mandke, S.H. Han, H.M. Pathan, Growth of silver dendritic nanostructures

- via electrochemical route, CrystEngComm. 14 (2012) 86–89. https://doi.org/10.1039/c1ce05791j.
- [43] V.S. Vendamani, S.V.S. Nageswara Rao, S. Venugopal Rao, D. Kanjilal, A.P. Pathak, Three-dimensional hybrid silicon nanostructures for surface enhanced Raman spectroscopy based molecular detection, J. Appl. Phys. 123 (2018). https://doi.org/10.1063/1.5000994.
- [44] V.S. Vendamani, R. Beeram, M.M. Neethish, S.V.S.N. Rao, S.V. Rao, Wafer-scale silver nanodendrites with homogeneous distribution of gold nanoparticles for biomolecules detection, IScience. 25 (2022) 104849. https://doi.org/10.1016/j.isci.2022.104849.
- [45] W. Ye, C. Shen, J. Tian, C. Wang, C. Hui, H. Gao, Controllable growth of silver nanostructures by a simple replacement reaction and their SERS studies, Solid State Sci.11 (2009) 1088–1093. https://doi.org/10.1016/j.solidstatesciences.2009.03.001.
- [46] P.F. Liao, A. Wokaun, Lightning rod effect in surface enhanced Raman scattering, J. Chem. Phys. 76 (1982) 751–752. https://doi.org/10.1063/1.442690.
- [47] M.J. Lo Faro, C. D'andrea, A.A. Leonardi, D. Morganti, A. Irrera, B. Fazio, Fractal silver dendrites as 3D SERS platform for highly sensitive detection of biomolecules in hydration conditions, Nanomaterials. 9 (2019) 1630. https://doi.org/10.3390/nano9111630.
- [48] V.S. Vendamani, S.V.S.N. Rao, A.P. Pathak, V.R. Soma, Silicon Nanostructures for Molecular Sensing: A Review, ACS Appl. Nano Mater. 5 (2022) 4550–4582. https://doi.org/10.1021/acsanm.1c04569.
- [49] X. Li, P.W. Bonn, Metal-assisted chemical etching in HF/H2O2 produces porous silicon, Appl. Phys. Lett. 77 (2000) 2572–2574. https://doi.org/10.1063/1.1319191.
- [50] V.S. Vendamani, R. Beeram, S.V.S. Nageswara Rao, A.P. Pathak, V.R. Soma, Trace level detection of explosives and pesticides using robust, low-cost, free-standing silver nanoparticles decorated porous silicon, Opt. Express. 29 (2021) 30045. https://doi.org/10.1364/oe.434275.
- [51] A. Wang, L. Jiang, X. Li, Q. Xie, B. Li, Z. Wang, K. Du, Y. Lu, Low-adhesive superhydrophobic surface-enhanced Raman spectroscopy substrate fabricated by femtosecond laser ablation for ultratrace molecular detection, J. Mater. Chem. B. 5 (2017) 777–784. https://doi.org/10.1039/c6tb02629j.
- [52] M. Lee, K. Oh, H.K. Choi, S.G. Lee, H.J. Youn, H.L. Lee, D.H. Jeong, Subnanomolar Sensitivity of Filter Paper-Based SERS Sensor for Pesticide

- Detection by Hydrophobicity Change of Paper Surface, ACS Sensors. 3 (2018) 151–159. https://doi.org/10.1021/acssensors.7b00782.
- [53] F. De Angelis, F. Gentile, F. Mecarini, G. Das, M. Moretti, et al., Breaking the diffusion limit with super-hydrophobic delivery of molecules to plasmonic nanofocusing SERS structures, Nat. Photonics. 5 (2011) 682–687. https://doi.org/10.1038/nphoton.2011.222.
- [54] N. V. Godoy, D. García-Lojo, F.A. Sigoli, J. Pérez-Juste, I. Pastoriza-Santos, I.O. Mazali, Ultrasensitive inkjet-printed based SERS sensor combining a high-performance gold nanosphere ink and hydrophobic paper, Sensors Actuators, B Chem. 320 (2020) 128412. https://doi.org/10.1016/j.snb.2020.128412.
- [55] A. Raza, B. Saha, In situ silver nanoparticles synthesis in agarose film supported on filter paper and its application as highly efficient SERS test stripes, Forensic Sci. Int. 237 (2014) 42–46. https://doi.org/10.1016/j.forsciint.2014.01.019.
- [56] D.J. Lee, D.Y. Kim, Hydrophobic paper-based SERS sensor using gold nanoparticles arranged on graphene oxide flakes, Sensors. 19 (2019) 8–14. https://doi.org/10.3390/s19245471.
- [57] C. Zhang, T. You, N. Yang, Y. Gao, L. Jiang, P. Yin, Hydrophobic paper-based SERS platform for direct-droplet quantitative determination of melamine, Food Chem. 287 (2019) 363–368. https://doi.org/10.1016/j.foodchem.2019.02.094.
- [58] D.Z. and W.S. Ruoyang Chen, Liyuan Zhang, Wetting and Drying of Colloidal Droplets: Physics and Pattern Formation, Advances in Colloid Science (2016) 3-25.
- [59] A. Nilghaz, L. Zhang, W. Shen, Coffee stains on paper, Chem. Eng. Sci. 129 (2015)34–41. https://doi.org/10.1016/j.ces.2015.02.017.
- [60] R. Beeram, D. Banerjee, L.M. Narlagiri, V.R. Soma, Machine learning for rapid quantification of trace analyte molecules using SERS and flexible plasmonic paper substrates, Anal. Methods. 14 (2022) 1788–1796. https://doi.org/10.1039/d2ay00408a.
- [61] P.F. Moulton, Spectroscopic and laser characteristics of Ti:Al₂O₃, J. Opt. Soc. Am.
 B. 3 (1986) 125. https://doi.org/10.1364/josab.3.000125.
- [62] D.E. Spence, P.N. Kean, W. Sibbett, 60-fsec pulse generation from a self-mode-locked Ti: sapphire laser, Opt. Soc. Am. 16 (1991) 42–44. https://doi.org/10.1364/OL.16.000042
- [63] S. Pandit, Fundamentals of Femtosecond LASER, A Project Report (2015) TIFR. https://doi.org/10.13140/RG.2.1.1885.1680.

- [64] Coherent, Operator's manual for Chameleon Ultra and Chameleon Vision Diode-Laser systems.
- [65] P. Maine, D. Strickland, P. Bado, M. Pessot, G. Mourou, Generation of Ultrahigh Peak Power Pulses by Chirped Pulse Amplification, IEEE J. Quantum Electron. 24 (1988) 398–403. https://doi.org/10.1109/3.137.
- [66] Coherent, Operator's manual for Libra Ultrafast amplifier laser System.
- [67] Swamp Optics Tutorial on Interferometric Autocorrelation, (2008) 1–5. https://www.swampoptics.com/assets/tutorials_interferometric_autocorrelation.pd
 f; https://www.swampoptics.com/autocorrelation.html
- [68] S.S.B. Moram, A.K. Shaik, C. Byram, S. Hamad, V.R. Soma, Instantaneous tracedetection of nitro-explosives and mixtures with nanotextured silicon decorated with Ag–Au alloy nanoparticles using the SERS technique, Anal. Chim. Acta. 1101 (2020) 157–168. https://doi.org/10.1016/j.aca.2019.12.026.
- [69] C. V. Raman, K.S. Krishnan, A new type of secondary radiation, Nature. 121 (1928) 501–502. https://doi.org/10.1038/121501c0.
- [70] Horiba Scientific, LabRam HR evolution user manual.
- [71] E. Ruska, The Development of the Electron Microscope and of Electron Microscopy (Nobel Lecture), Angew. Chemie Int. Ed. English. 26 (1987) 595–605. https://doi.org/10.1002/anie.198705953.
- [72] L. Bi, X. Wang, X. Cao, L. Liu, C. Bai, Q. Zheng, J. Choo, L. Chen, SERS-active Au@Ag core-shell nanorod (Au@AgNR) tags for ultrasensitive bacteria detection and antibiotic-susceptibility testing, Talanta. 220 (2020) 121397. https://doi.org/10.1016/j.talanta.2020.121397.
- [73] S.S.B. Moram, C. Byram, V.R. Soma, Gold-nanoparticle- and nanostar-loaded paper-based SERS substrates for sensing nanogram-level Picric acid with a portable Raman spectrometer, Bull. Mater. Sci. 43 (2020) 1–8. https://doi.org/10.1007/s12034-019-2017-8.
- [74] G. Barbillon, Plasmonics and its applications, Materials. 12 (2019) 10–13. https://doi.org/10.3390/ma12091502.
- [75] V.S. Vendamani, R. Beeram, S.V.S.N. Rao, S.V. Rao, Protocol for designing AuNP-capped Ag dendrites as surface-enhanced Raman scattering sensors for trace molecular detection, STAR Protoc. 4 (2023) 102068. https://doi.org/10.1016/j.xpro.2023.102068.

Intentional Blank Page

Chapter 3

Ultrafast Laser Ablated Plasmonic NSs for SERS

Abstract

This chapter exclusively focuses on ultrafast laser ablated nanostructures and their application as highly reproducible SERS substrates. Different nanostructures were prepared using laser ablation of Si, Ag, Ag-Au, and Cu using both femtosecond laser amplifier and oscillator pulses. In **Chapter 3.1.** using a femtosecond laser oscillator (140 fs, 800 nm, 80 MHz), web-like structures were fabricated on Si via laser ablation in the air. The nanostructures formed on Si exhibited unique web-like structures where the nanoparticles self-assembled into nanochains, interweaving closely. The effects of different laser parameters like fluence and scan speed on the formation of these structures were studied in detail. These structures were coated with a thin layer of Au (~10 nm) and used as SERS substrate with methylene blue as the probe molecule. Chapter 3.2. describes the SERS substrates fabricated using femtosecond laser (800 nm, 50 fs, 1kHz) ablation of Ag-Au (1:1) in air. The effect of the angle of incidence on the formation of the nanostructures has been studied. In this study, an explosive molecule (picric acid), two dye molecules (Rhodamine 6G and crystal violet), and an amino acid (cysteine) are all investigated using SERRS. We have looked at the much-contested link between enhancement and repeatability, with the benefit of having randomly stacked nanoparticles in debris and periodic substrates without debris. Rhodamine 6G, crystal violet, picric acid, and cysteine were shown to have substrate sensitivity values of 10 fM, 100 fM, 100 nM, and 100 nM, respectively, with high repeatability. Chapter 3.3 presents studies on ultrafast laser ablation, using an amplifier system, of Ag and Cu in the air using cylindrical focusing conditions. These structures were further utilized for SERS-based detection of different explosives and biomolecules. Using chemometrics in conjugation with SERS, different bacteria species have been classified using the SERS spectra.

3.1. Introduction

Fabrication of precise, ligand-free, and controllable nanostructures is requisite for many plasmonic-based applications. Ultrafast laser ablation is a go-to technique that allows the fabrication of diverse nanostructures in a single step by controlling the experimental parameters. The detailed mechanism of laser ablation has been discussed in Chapter 2. In this thesis work, we have limited ourselves to working with femtosecond lasers as they are known to result in minimum heat affected zone (HAZ) and, consequently, a precise structure, as shown in figure 3.1 [1].

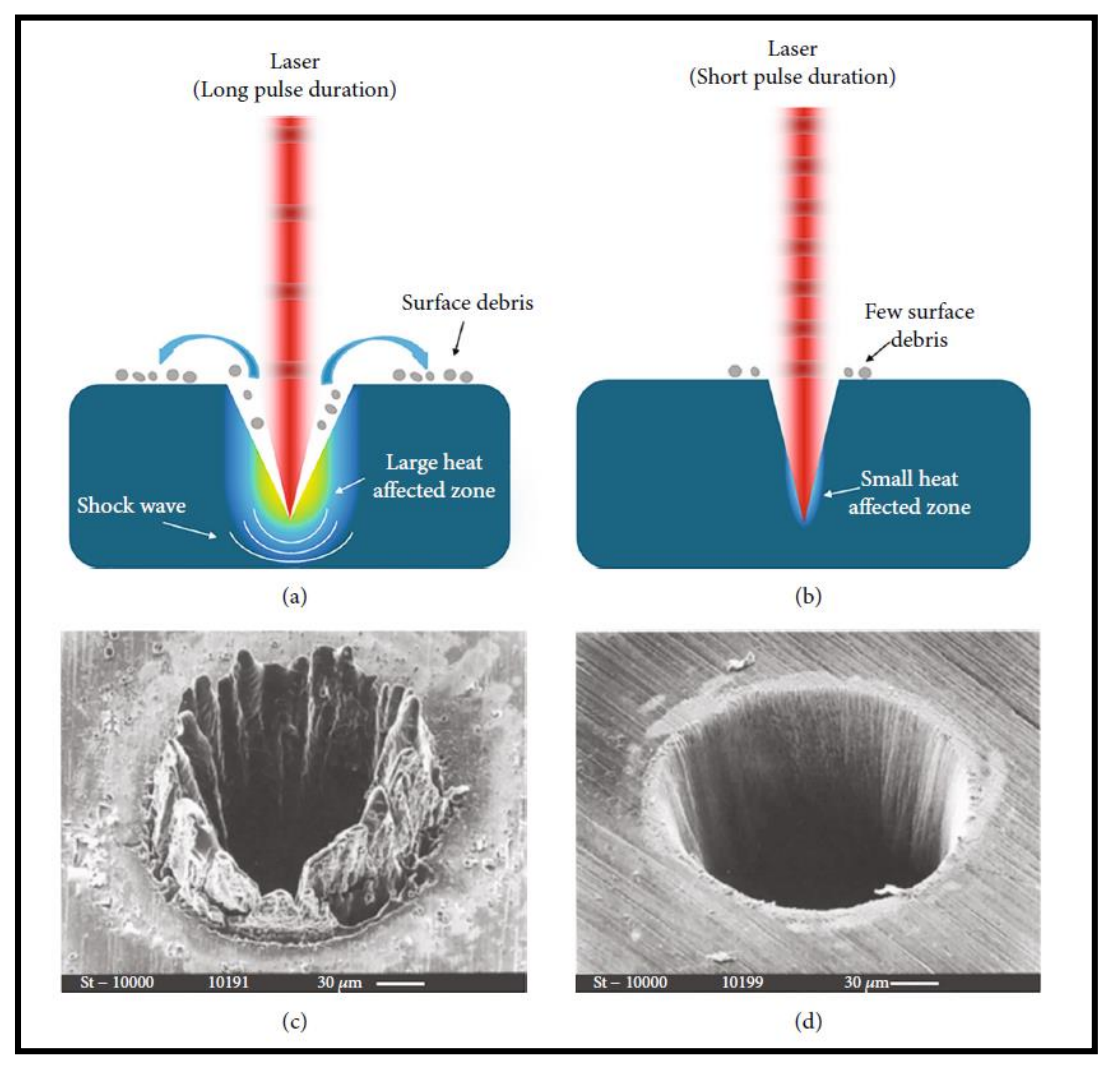


Figure 3.1: Schematic of laser ablation by a) nanosecond pulses, b) femtosecond pulses and SEM images of laser ablated steel foil with c) nanosecond and d) femtosecond laser of same wavelength. Figure reproduced from [2].

In the fs regime, ultrashort [femtosecond (fs)] pulses primarily interact with electrons, whereas longer pulse durations as the case of nanosecond pulses engage with the lattice

structure. Therefore, when a fs pulse interacts with a material heat conduction is limited [2]. Consequently, the material undergoes ablation within a confined and well-defined spatial region, minimizing the mechanical and thermal damage inflicted on the target area. Conversely, irradiating materials with longer [nanosecond (ns)] pulse durations lead to continuous heating of the target material. Heat conduction then disperses the laser pulse energy beyond the size of the laser spot, resulting in the boiling and evaporation of the irradiated target material. This uncontrolled boiling and evaporation process generates an uncontrollable melt layer as indicated by figure 3.1. For these reasons, fs laser was preferred for ablation with focus on both amplifier and oscillator systems for metals and semiconductors.

3.2. Structures Prepared using Femtosecond Laser Oscillator

Conventional laser ablation is often performed using a femtosecond amplifier system for its high energy per pulse (typically mJ). However, the complexity and cost of the system limits its application for material processing. In this study we have used an oscillator system with high repetition rate in order to study the effects of different experimental conditions on the laser ablation of Si in air. The mechanism of ablation is different for the case of high repetition rate pulses resulting in structures that are unconventional and have found far reaching applications in solar cells and cancer therapy [3] [4]. Often controlled environments like a furnace with tunable temperature or presence of noble gas atmosphere is required in order to fabricate anisotropic structures like wires or rods through laser ablation. However, owing to their unique mechanism, nanoparticles that self-assemble into chains which intertwine into webs is possible to achieve using MHz pulses [5]. In the case of repetition rates in the kHz regime, the nanoparticles are known to aggregate by random stacking. But for the case of MHz pulses, particles were seen to be fused into nanochains. 3D web-like structures were also reported for high repetition rate laser ablation of egg shells constituting of calcium carbonate [6]. They have also studied the effects of repetition rate on the density of the nanofibers formed during ablation. Similar web-like nanostructures were reported with Si coated with Au during MHz ablation and the structures have demonstrated suitable properties for the application in solar cells owing to their properties of high surface area and anisotropy [7]. Sivakumar et al. have systematically studied the effects of different laser parameters and composition on these

structures [8]. Using laser vaporization-condensation technique (LVC), web-like nanostructures were reported on Si under controlled experimental conditions like temperature, pressure and background gas [9]. The similarity of nanostructures formed during MHz ablation and LVC indicates that the web-like structures are formed during nucleation and growth of the nanoparticles [5]. For their ability to mimic extracellular matrix, these Si nanostructures have also found applications in biology for cell proliferation, tissue engineering and regeneration [10]. These Si structures were also studied as a potential for cancer therapy and diagnosis for their selective binding capacity without the need of any additives or catalysts [4] [11].

Web-like Si nanostructures were fabricated by laser ablation of Si in air with a fs laser oscillator (Coherent Chameleon). The laser system has been elaborately discussed in chapter 2 including the experimental setup. After gold coating, these nanostructures were used for SERS studies with methylene blue as a probe molecule. Femtosecond laser ablation is a simple and green technique for precise surface processing of different materials including dielectrics, metals, and semiconductors. The simplicity of the experimental setup and diversity of the material processing capabilities have expanded new horizons for this field. The formed structures are highly dependent on the input laser parameters such as pulse duration, repetition rate, fluence and wavelength. Conventionally, fs laser processing is performed with amplified systems which are expensive. Such laser processed materials have found diverse applications in many areas, SERS being one [12]. SERS is both a quantitative and qualitative technique for unique identification of molecule under study. Very little work has been done on using femtosecond oscillator structured substrates for SERS. We have extensively studied the effects of number of pulses per spot and fluence on the web-like structures formed and characterized them using FESEM. These structures exhibited interesting morphology with Si nanoparticles aggregating into nano-chains which further self-assembled into web-like structures. The mechanism of formation of these web-like structures is understood and the effects of different experimental conditions on these structures were investigated. The web-like structures demonstrated better enhancements than plain Au coated Si substrates owing to the chemical enhancement from the Si nanostructures and resulted in 1 µM sensitivity. As opposed to conventional laser ablation using amplifier systems, this is lowcost alternative for plasmonic SERS substrates.

3.2.1. Experimental Setup

We have used a tunable Ti-Sapphire laser (Chameleon Ultra, M/s Coherent) with pulse duration of ~140 fs (wavelength of 800 nm; average power of ~2.5 W and repetition rate 80 MHz) for our studies. The laser was aligned using different reflective mirrors and was focused on the sample using long working distance objectives (50X and 100X). The sample was moved on a computer controlled translational stages to make patterns on the Si substrate. We have studied the effects of different experimental parameters and characterized the resulting structures by FESEM. A square pattern was used for SERS studies as it was proven to be advantageous in our previous study using a femtosecond amplifier [13]. Laser ablated Si structures with 50X, 1.5 mm/s, a laser power of 2.5 W, and fluence of 1 J/cm² were used for SERS after coating it with thin layer of Au (~10 nm) by thermal evaporation method.

3.2.2. Effects of Scan Speed

The speed of the translational stages determines the number of pulses per spot and the time a pulse dwells on the target surface. We have systematically studied the effects of scan speed on the formation of the web-like structures. The resulting structures were characterized using FESEM. The results as shown in figure 3.2 indicate low scan speed (0.05 mm/s) yielded a dense network of the nanofibers with smaller nanoparticles whereas relatively high scan speed (2 mm/s) yielded in less dense nanofibers with larger nanoparticles. This happened because for the case of low scan speed, we have a greater number of pulses per spot and hence ablating more material, resulting in greater yield and also further fragmentation of the nanoparticles formed during the initial stages. Results with the intermediate scan speeds are summarized in the figure 3.3 and are consistent with the explanation.

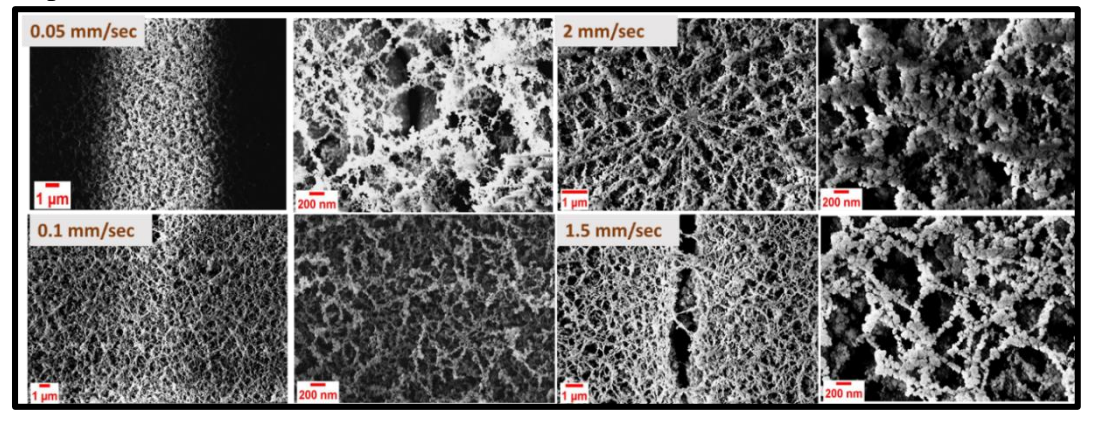


Figure 3.2: FESEM images of laser ablated Si for different scan speeds as indicated in the figure. Left side images are in low-resolution while the right ones are in high-resolution.

The nanoparticle size for all the scan speeds can be seen to be uniform for each scan speed indicating homogeneous nucleation. The results are also in agreement with equation (11) where scan speed is correlated to the dwelling time (D_t). The number of evaporated species which determine the density of the nanoparticles can be seen to proportionate to the dwelling time of the laser pulse at a spot as suggested by the equation.

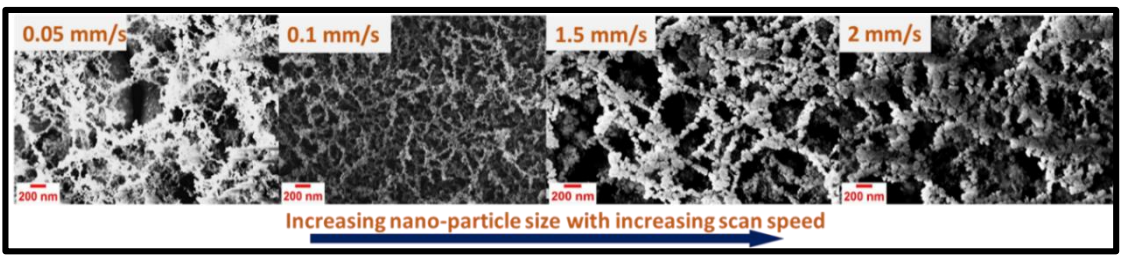


Figure 3.3: Summary of results on studying the effects of scan speed on the density and size of the Si nanoparticles comprising the web-like nanostructures.

Previous studied by Bo Tan et al. have indicated that there is a threshold number of pulses for the formation of these web-like structures [5]. The number of pulses at which the web-like structures form was found to be matching with the time taken for the formation of the nanoparticles [5].

3.2.3. Effects of Fluence

Laser fluence is a critical parameter determining the resulting nanostructures in laser ablation. Previous studies have studied effects of laser fluence as a consequence of change in pulse repetition rate and analysed the results [5]. In our case we have changed the laser fluence by changing the working objective from $50 \times \text{to } 100 \times \text{consequently changing the}$ spot size from 2.6 µm to 1.6 µm at a constant power. The input power and scan speed were kept constant at a value of 2.5 W and 1.5 mm/s. The results are presented in figure 3.4 and indicate that as the fluence is increased the web-like structures disappeared and heat induced agglomeration into cauliflower like nanostructures. In order to understand if there is a threshold fluence for the formation of these web-like structures, we have lowered the laser power to 1.5 W accounting for 7.5 J/cm² and the results indicate that there is indeed a threshold fluence for the formation of the web-like structures. The results for different fluences, as shown in figure 3.5 indicate that there is an increase in aggregation of nanoparticles with increasing fluence of the laser. Perriere et al. have discussed the effects of laser fluence on the ablation outcomes for the case of femtosecond laser with different targets [14]. It was found that different ablation species are emitted at different ablation fluences depending on the material and the energy.

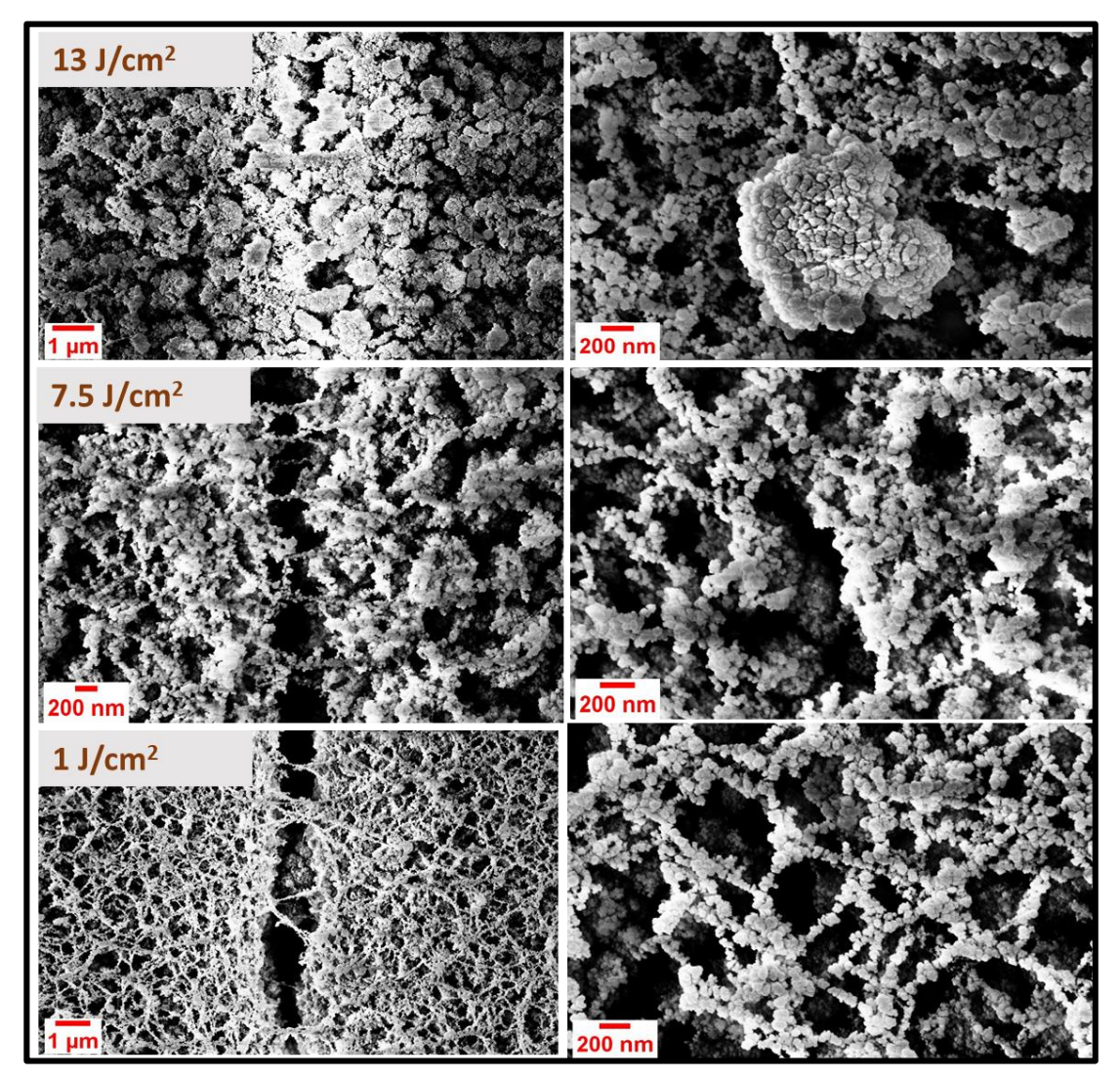


Figure 3.4: FESEM images of femtosecond laser ablated Si nanostructures for different laser fluencies as indicated in the image.

The order of fluence for the emission of droplets (E_d) , atomic species (E_a) and clusters (E_c) is given as,

$$E_c \approx E_a < E_d$$

This indicates that ablation at higher fluence is dominated by droplet emission resulting in aggregates as shown in the figure 3.5 deviating from the web-like structures. Using the same objective of 100×, laser power has been decreased to 1.5 W in order to reduce the fluence and understand if there is threshold fluence for the formation of the web-like nanostructures.

Figure 4 image corresponding to 7.5 J/cm² with web-like structures confirms that there is indeed a threshold fluence for the same. However, at this fluence, the size of the nanoparticles within the nano-chains is inhomogeneous unlike the case for ablation at 1

J/cm². It has to be noted that the geometric effect of changing spot size even at constant fluence itself has consequences in the mechanism of laser ablation [14]. Smaller spot sizes were known to favour nanoparticle formation whereas larger spot sizes lead to the formation of droplets analogous to the mechanism of supersonic jet formation as shown in the figure 3.5. Figure 3.6 summarizes the effects of laser fluence on the formation of nanoparticle aggregates for the case of high repetation rate fs ablation of Si in air.

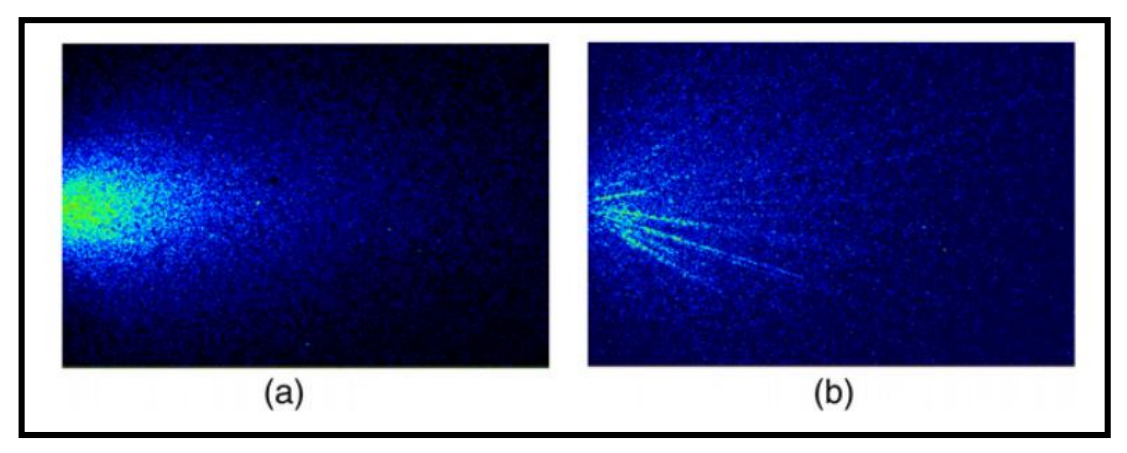


Figure 3.5: CCD images of emissions during fs laser abaltion of Ti with nearly same fluence but different spot sizes of a) 1×10^{-3} cm² and b) 2.4×10^{-4} cm². Figure reproduced from the reference [14].

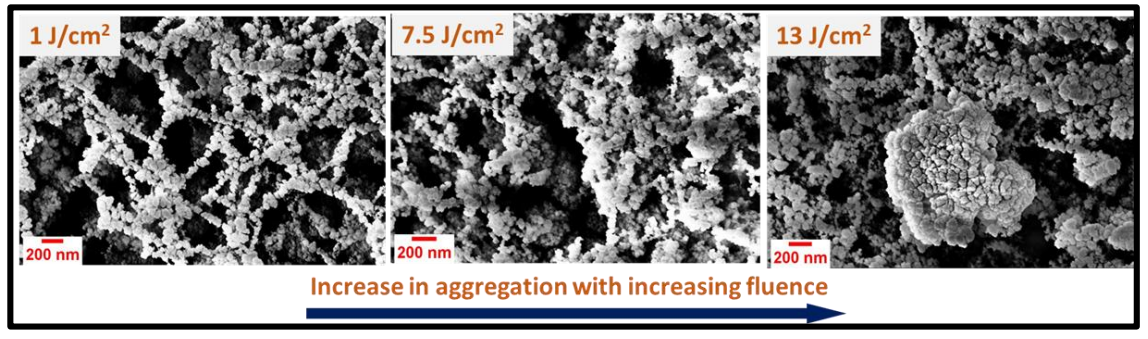


Figure 3.6: Summary of effects of fluence on laser ablation of Si showing increase in aggregation with increasing fluence.

3.2.4. Mechanism of Laser Ablation

Nanoparticles during laser ablation are generated by nucleation and growth of laser ablated species. When laser beam is focused on the solid target the temperature of the spot is increased rapidly leading to vaporization of the target. The collisions between the evaporated species leads to the formation of laser induced plasma plume the properties of which depend on the ambient gas, material and pressure [15]. The expansion of plasma plume leads to rapid quenching in the temperature of the vaporized materials facilitating the formation of nanoparticles by nucleation [16]. Nanoparticles are formed during the cooling stage of plasma plume through nucleation. The size and shape of the nanoparticles

is largely determined by the wavelength, fluence of the laser and the surrounding environment of the plasma plume [17]. The nanoparticle formation will come to halt when the density reaches an equilibrium concentration or if the particle temperature reaches to equilibrium. In the case of MHz pulses, you have constant flux of new particles leading to steady growth of NPs and their agglomeration as shown in figure 3.7. This is explained by equation (3.11) derived for the case of titanium NPs by Bo Tan et al. [18]. The equation gives the number of evaporated atoms (N), during laser ablation as a function of both material and laser properties. The first terms in the bracket are the parameters related to the properties of the material and the second term refers to the laser parameters like power (P_{avg}), repetition rate (R_{rep}) and beam size at the focus (A_{foc}) [19]. The number of particles ejected from an ablation area is also proportional to the amount of time a pulse spends on a particular spot (D_t) [18]. This is determined by the scanning speed of the laser.

The thermal evaporation as derived from equilibrium conditions, for a single pulse, elsewhere is given as [19],

$$R_{evp} \approx n_{air} \left(\frac{k_B T_{max}}{2\pi M_a}\right)^{\frac{1}{2}} \left(t_p t_{eq}\right)^{\frac{1}{2}} \left[\frac{atoms}{cm^2}\right]$$
 (3.1)

Here T_{max} is the maximum temperature of the sample surface at the end of the laser pulse, t_p is the pulse duration and t_{eq} is the time taken to reach the equilibrium distribution.

The average temperature can be modelled using 1 D heat conduction equation as derived elsewhere by Gamalay et al. as [20],

$$T_{avg} = \left(\frac{2}{\pi}\right)^{1/2} \frac{I_a(at_p)^{1/2}}{k_h} = \frac{1}{2^{1/2}} T(0, t_p)$$
 (3.2)

 I_a here is the intensity of the laser absorbed by the material and 'a' is the area of scanning on the sample. For pulsed laser ablation the maximum temperature, T_{max} occurs at the end of the laser pulse and hence it follows that,

$$T_{max} = T(0, t_p) \tag{3.3}$$

So from equation (3.2) and (3.3), it can be written that,

$$T_{max} = \frac{2I_a(at_p)^{1/2}}{k_h(\pi)^{1/2}}$$
 (3.4)

The intensity absorbed by the sample for a laser intensity of I_0 , depends on the absorption coefficient of the material, ϵ , and is hence given as,

$$I_a = \varepsilon I_0 \tag{3.5}$$

The intensity of the incident laser pulse, I₀ is known to be,

$$I_0 = \frac{P_{avg}}{R_{rep}t_p A_{foc}} \tag{3.6}$$

From equation (3.4), (3.5) and (3.6), the maximum temperature and hence the thermal evaporation of the surface can be written as,

$$T_{max} = \frac{2 \varepsilon P_{avg} a^{1/2}}{k_h R_{rep} A_{foc} (\pi t_p)^{1/2}}$$
(3.7)

$$R_{evp} \approx n_{air} \left(\frac{k_B a \varepsilon t_{eq}^{3/2}}{\pi^{3/2} M_a k_h} \frac{P_{avg}}{R_{rep} A_{foc}} \right)^{\frac{1}{2}} \left[\frac{atoms}{cm^2} \right]$$
 (3.8)

For a single pulse, the number of evaporated species, N_p is given as,

$$N_p = R_{evp} A_{foc} (3.9)$$

For estimating the number of species evaporated for the case of multiple pulses (N_{MP}), it is crucial to consider the time a pulse spends at a particular spot known as dwell time, D_t and is given as,

$$N_{MP} = R_{evp} A_{foc} R_{rep} D_t (3.10)$$

Hence, the total number of evaporated species from equation (3.8) and (3.10) can be written as,

$$N_{MP} = n_{air} \left(\frac{k_B a \varepsilon t_{eq}^{3/2}}{M_a k_h \pi^{3/2}} \right)^{1/2} \left(P_{avg} R_{rep} A_{foc} \right)^{1/2} D_t$$
 (3.11)

The equation indicates that the laser parameters like pulse duration, repetition rate and energy strongly influence the outcomes of the laser ablation. Specifically, it says that the repetition rate of the laser influences the number of evaporated species through a factor of square root.

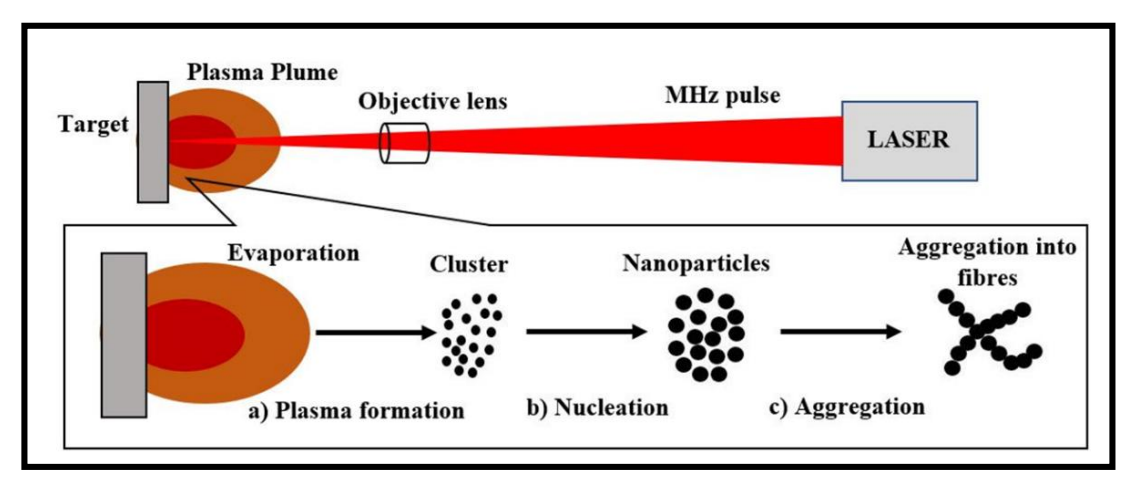


Figure 3.7: Schematic of mechanism of formation of nanochains during high repetition rate fs ablation of Si.

3.2.5. SERS Measurements

In order to fabricate a SERS substrate, the Si sample was moved in a raster pattern using two stages to achieve square arrays as shown in figure 3.8 a). Such square arrays were proven to be advantageous for signal enhancement in SERS in our previous studies [13]. Detailed experimental setup has been discussed in chapter 2. We have used a 50 \times objective with laser power of 2.5 W and scan speed of 1.5 mm/cm² for SERS studies. The spacing between the lines was kept to 20 μ m. The sample (LS-Si) was subsequently coated with a thin layer of Au (~10 nm) using thermal evaporation technique and was then characterized using FESEM as shown in figure 3.8. EDX data indicate the presence of both Au and Si on the sample surface.

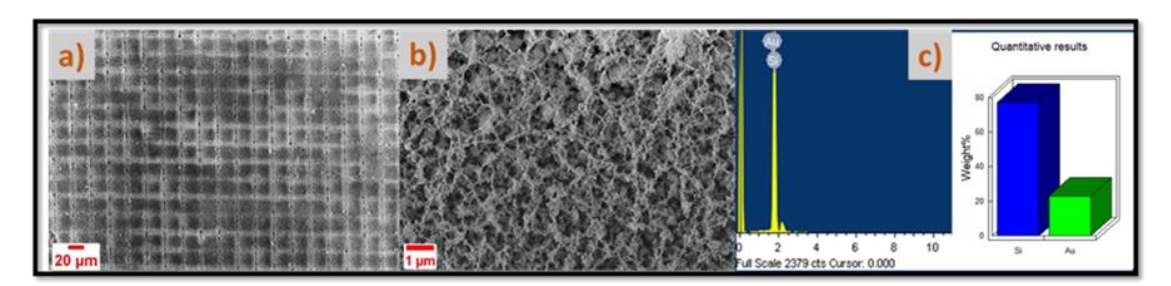


Figure 3.8: a, b) FESEM imaging of web-like Si nanostructures as SERS substrate FESEM micrographs of LS-Si used for SERS studies at different magnifications and c) EDX spectrum with quantitative results for the gold coated Si used for SERS.

Methylene blue (MB) was chosen as the probe molecule and different concentrations of the analyte were prepared as discussed in chapter 2. 5 µl of the selected concentration of the sample was drop-casted on the substrate and was waited to dry. Portable Raman

Spectrometer (BWTek) with laser excitation 785 nm was used for SERS. Each spectrum is an average of 20 spectra collected at random sites on the sample.

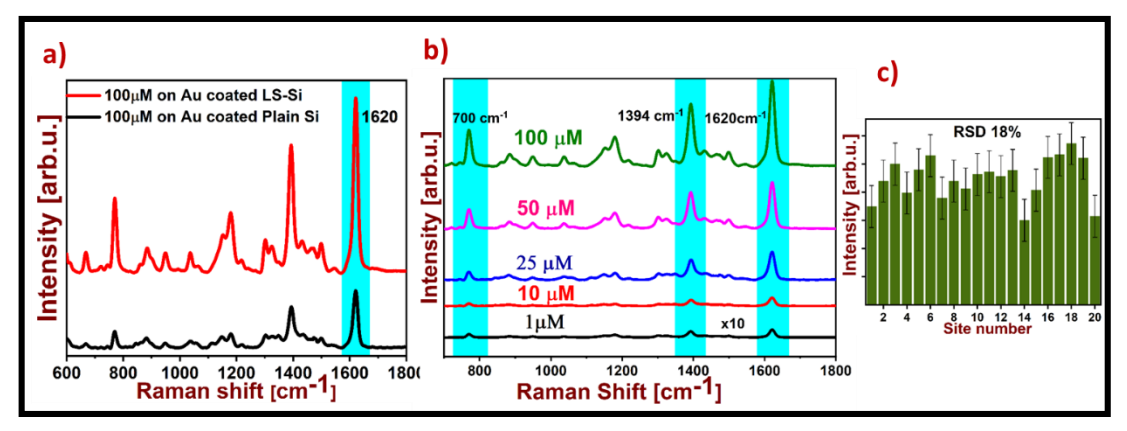


Figure 3.9: a) SERS spectra of MB with 785 nm excitation, 10s acquisition time and 20 mW laser power a) on LS-Si and plain Au coated Si for 100 μ M concentration b) SERS spectra of MB on LS-Si for different concentrations. The spectrum of 1 μ M concentration was multiplied by 10 for better visibility c) Intensity variation of 1621 cm⁻¹ peak of MB at 20 random spots on the substrate.

The data as shown in figure 3.9 indicates that the LS-Si enhances the signal nearly two-fold relative to the plain Si coated with Au. It was reported that the combination of plasmonic metals and dielectrics would enhance the plasmonic response of the ensemble [21]. Recently, dielectrics are being explored as alternatives to metal plasmonics as they are known to enhance the signal through charge transfer mechanisms [22]. Si based materials have been used as SERS substrates and established to enhance the signal [23].

3.3. Metal Nanostructures Using Femtosecond Amplifier

Metals have a higher ablation threshold relative to semiconductors and need higher energy per pulse in order to achieve ablation. Using femtosecond amplifier system that is described in detail in chapter 2, laser ablation of Ag, Ag-Au and Cu has been studied and their application as SERS substrates for detection of different analytes has been explored.

3.3.1. Femtosecond Laser Ablation of Ag:Au Alloy and Application in SERS

Using femtosecond laser (800 nm, 50 fs, 1kHz) ablation of Ag-Au (1:1) in air, diverse nanostructures have been fabricated. The effects of angle of incidence on the formation of the nanostructures for 0°, 10°, 20°, and 30° has been studied. focuses on surface enhanced resonance Raman spectroscopy (SERRS) for the study of an explosive molecule (picric acid), two dye molecules (rhodamine 6G, crystal violet), and an amino acid (cysteine). These molecules were first analysed using UV-Visible spectroscopy to understand the

absorption regions. Accordingly, laser excitation close to the resonance were chosen in order to achieve ultra-trace detection limits. The effects of angle of incidence on the formation of NSs and the consequence of it on the SERRS performance has been studied. The optimum structure was used for further studies. Surface debris is inevitable in laser ablation in the air and is eliminated before employing them for the application. But here, we have looked at the hotly contested link between enhancement and repeatability, with the benefit of having randomly stacked nanoparticles in debris and periodic substrates without debris. With statistically significant data (~5000 spectra for each), an inverse relationship has been found between enhancement and reproducibility in SERS using the advantage of two substrates from single experiment. The SERRS has clearly proved to be advantageous for the trace detection of R6G, crystal violet, picric acid, and cysteine with sensitivities of 10 fM, 100 fM, 100 nM, and 100 nM, respectively, with good reproducibility [24].

3.3.1.1. Experimental Setup

The experimental investigation involved the utilization of a fs laser ablation technique, employing a Ti-Sapphire laser system (M/s Coherent; Libra) emitting light pulses with a central wavelength of 800 nm and a pulse duration of 50 fs as described in chapter 2. A comprehensive account of the intricate setup can be found elsewhere [25]. In summary, the laser beam was directed towards the target specimen through a series of reflective mirrors, while the sample itself was strategically positioned on programmable translation stages, enabling controlled movement in a raster pattern to facilitate the creation of intricate structures within a defined area of 4x4 mm². To focus the beam onto the sample with precision, a 15 cm plano-convex lens was employed. For attenuation purposes, a combination of a Brewster window and a half wave plate was utilized, effectively reducing the laser energy. Specifically, an energy level of 20 mJ was chosen for the ablation process. To enable adjustments in the angle of incidence on the sample, a mirror positioned above the sample was mounted on a rotational platform, allowing for accurate readings and alterations. Prior to the commencement of the ablation process, the Ag-Au sample underwent a meticulous cleansing procedure involving the application of acetone, followed by ultra-sonication to meticulously eliminate any traces of surface contamination. Subsequently, the ablation procedure was carried out at four distinct angles: 0^0 , 10^0 , 20^0 , and 30^0 . To facilitate easy identification and categorization of the resulting debris substrates, the samples were designated as D-S0, D-S10, D-S20, and D-

S30, respectively, based on the corresponding angles and 'D' representing debris. Moreover, for the samples that underwent sonication treatment to remove surface debris before ablation, an additional label of ND-S0, ND-S10, ND-S20, and ND-S30 was affixed, where "ND" denoted the absence of debris.

3.3.1.2. Characterization of fs Laser Structured Ag-Au Nanostructures

The nanostructures as fabricated by laser ablation for different angles of incidence were characterized by FESEM imaging. The micrographs captured by FESEM in Figure 3.10 depict the laser-ablated structures alongside the associated debris, showcasing the impact of varying ablation angles. It is noteworthy that all images were captured at an identical magnification of 10 KX, ensuring consistent visual representation. The findings of the study reveal a notable trend in the production of nanoparticles, which manifest as debris, as the ablation angle changes. Specifically, the yield of nanoparticles exhibited an increase from the incidence angle of 0^0 , followed by a subsequent decrease with further increments in the angle. This observation aligns with the results obtained from the work conducted by Gopala Krishna et al., who performed similar experiments in a water-based medium utilizing Ag nanoparticles [26]. Their study reported that, at a specific angle of incidence, the absorption of laser energy was comparatively higher, indicating a greater concentration of nanoparticles at that particular angle as the ablation was carried out in liquid [26]. Furthermore, Gopala Krishna et al. also observed distinct variations in the particle size distribution as a consequence of different angles of incidence, as outlined in their comprehensive investigation. To comprehend the underlying mechanism governing these phenomena, an analogy can be drawn to the process of tilling soil with a sharp-pointed tool. In this analogy, the amount of soil removed is contingent upon the angle at which the tool is positioned relative to the ground. Similarly, the angle of incidence during laser ablation plays a pivotal role in the magnitude of debris production and subsequent nanoparticle concentration, thus influencing the particle size distribution. Overall, the utilization of FESEM micrographs, combined with the findings from Gopala Krishna et al.'s research, contributes to a deeper understanding of the intricate dynamics at play in laser ablation processes and sheds light on the importance of ablation angles in nanoparticle yield and distribution. To eliminate any surface debris, present on the samples, a meticulous cleaning procedure was conducted by subjecting the specimens to ultrasonic treatment in water for ~15 minutes, followed by thorough rinsing. Subsequently, the cleaned structures underwent further characterization through FESEM imaging.

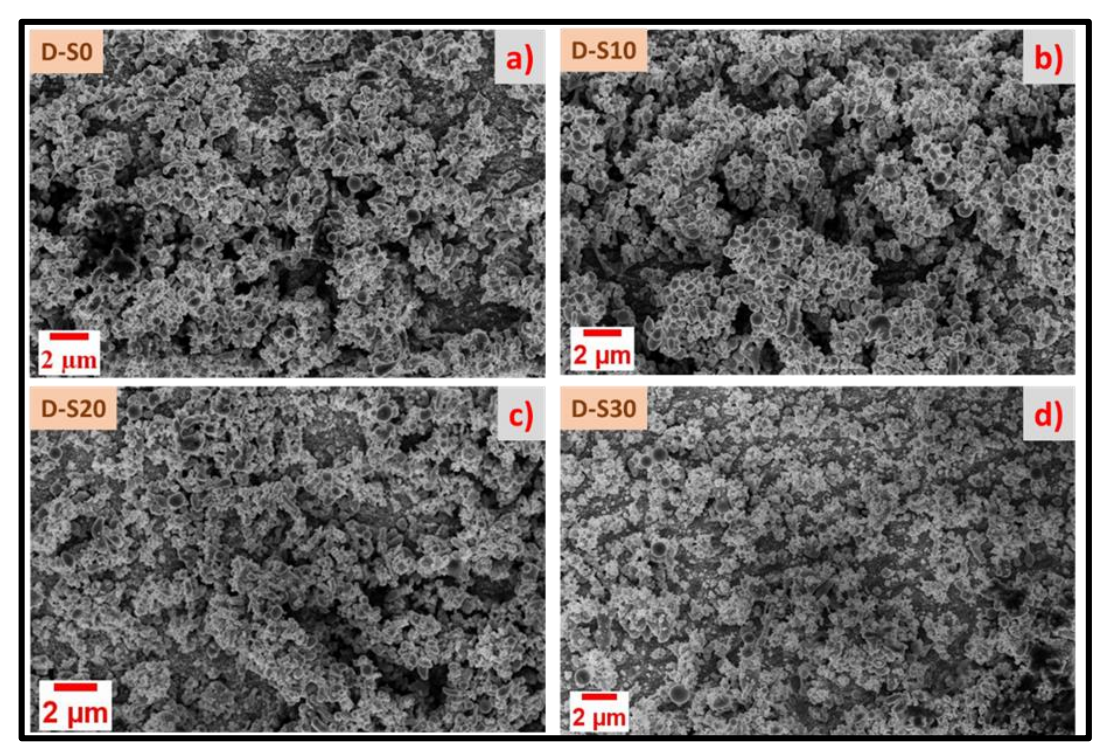


Figure 3.10: FESEM images of laser ablated Ag-Au nanostructures with debris for different angles of incidence a) 0^0 , b) 10^0 , c) 20^0 and d) 30^0 as indicated in the figure. The images indicate that the number of nanoparticles ablated is different for different angles of incidence.

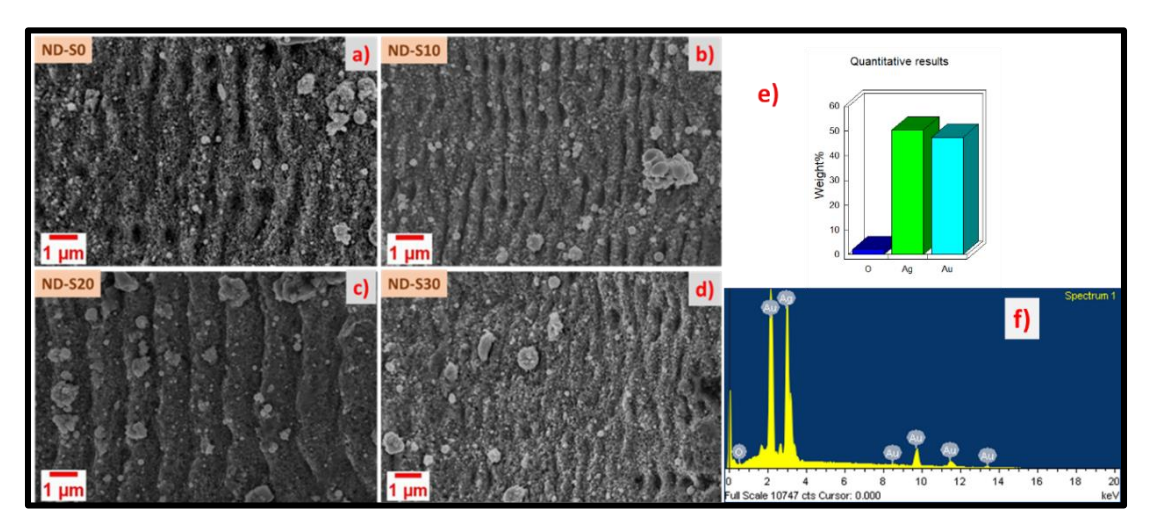


Figure 3.11: FESEM images of laser ablated Ag-Au nanostructures without debris for different angles of incidence a) 0^0 , b) 10^0 , c) 20^0 and d) 30^0 as indicated in the figure. The images indicate the formation of ripples on Ag-Au surface for all angles of incidence but with varying periodicity. e) and f) Represent EDX data showing the presence of both Ag and Au.

The outcomes of this analysis are graphically presented in Figure 3.11, where it is important to note that all the captured images were taken at an identical magnification of 25 KX. The results indicate the formation of ripple like structures for all energies which

have proven to have advantage in the SERS in our previous studies [27]. The results obtained from the FESEM imaging reveal the formation of distinctive ripple-like structures across all energy levels investigated. It is worth highlighting that these specific ripple formations have demonstrated advantageous characteristics in SERS, as previously established in our own research endeavors.

3.3.1.3. UV-Visible Spectroscopy of the Analyte Molecules

To gain insight into the absorption characteristics of the analyte molecules and subsequently determine the most appropriate excitation wavelength, UV-Visible spectroscopy was conducted for each of the chosen analyte molecules intended for SERS. The absorption spectra of the various analytes are presented in Figure 3.12 (a), providing a visual representation of their absorption properties.

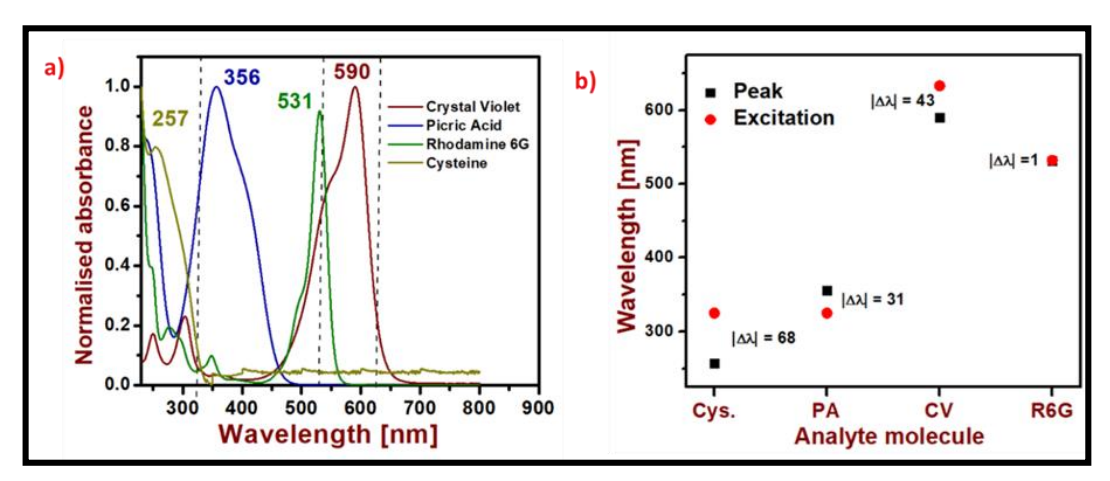


Figure 3.12: a) UV-Visible absorption spectrum of different probe molecules used in SERS studies for this work. The dotted line indicates the laser excitation wavelengths. b) Scatter plot of the absorption peak and excitation wavelength for each probe molecule where $|\Delta\lambda|$ is indicating the absolute difference between the two.

From the graph, it is evident that both dye molecules exhibit absorption peaks within the visible region while on the other hand, the explosive compound and the biomolecule display absorption primarily within the UV region, signifying their preferential absorption of light at shorter wavelengths. Based on the absorption characteristics obtained from UV-Visible spectroscopy, the laser excitation wavelength was carefully selected to match the absorption peaks of the respective analyte molecules. This chosen excitation wavelength is visually represented as a dotted line in Figure 3.12 a). To provide a comprehensive understanding of the relationship between the absorption peaks and the excitation wavelength, Figure 3.12 b) presents a scatter plot illustrating the absorption peak values plotted against the corresponding excitation wavelengths for each analyte molecule.

Furthermore, it is worth noting that the plasmonic resonance exhibited by the Ag-Au material occurs within the visible region, as clearly indicated in Figure 3.13. This plasmonic resonance characteristic presents a significant advantage, particularly for the dye molecules that overlap with the absorption range. The overlapping of the dye molecules' absorption peaks with the plasmonic resonance enhances the SERS signals and ultimately contributes to improved detection sensitivity and signal enhancement [28,29].

3.3.1.4. Surface Enhanced Resonance Raman Spectroscopy (SERRS)

Surface-enhanced Raman spectroscopy (SERS) benefits not only from the plasmonic nanostructures and chemical enhancement mechanisms but also from an additional enhancement when the incident laser excitation closely aligns with the electronic transitions of the molecules and the resonance of the plasmonic material under investigation. These resonance conditions are known to amplify the standard SERS signal by up to 10⁶ times [30]. This phenomenon is commonly referred to as Surface Enhanced Resonance Raman Spectroscopy (SERRS). With advancements in laser technology and instrumentation, rendering them portable and cost-effective, there is an increasing opportunity to select excitation wavelengths that precisely match the characteristics of the sample and the specific field of study. It is well established that different classes of materials exhibit absorption within distinct spectral domains. For instance, explosives and biomolecules typically absorb light within the ultraviolet (UV) spectral region, while dyes tend to absorb within the visible region [31]. By aligning the excitation wavelength with the absorption characteristics of the analyte molecules and the plasmonic resonance of the substrate material, researchers can exploit the resonance effects to optimize the SERS signal and achieve heightened sensitivity and enhanced analytical capabilities [32].

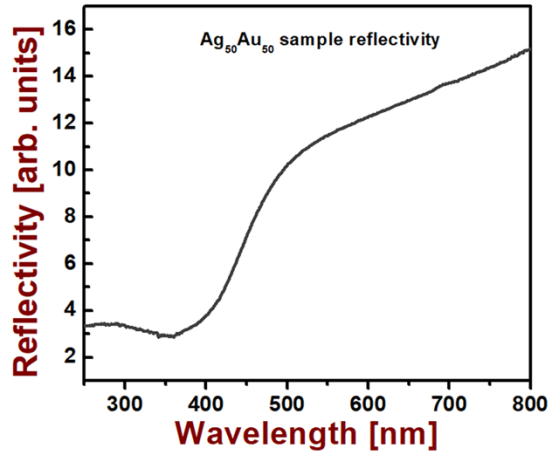


Figure 3.13: UV-Visible reflectance data of Ag-Au sample used in this study indicating plasmonics resonance in the visible range.

3.3.1.5. SERRS Data Analysis

The resonance Raman spectra of Rhodamine 6G (R6G) have been extensively studied and established as a suitable analyte molecule due to the availability of 532 nm laser excitation, which closely aligns with its absorption peak. Additionally, R6G has demonstrated a remarkable affinity for metals, particularly silver nanostructures [33]. This advantageous combination of factors has allowed for comprehensive investigations into R6G, extending to the study of single molecules and fundamental aspects [34]. In the initial stages of our studies, we assessed the performance of each substrate with debris using a concentration of 1 μ M R6G. The results revealed that the substrate ablated at an angle of 100 outperformed the other substrates, as illustrated in Figure 3.14. This superior performance can be attributed to the higher yield of nanoparticles produced at this specific angle, consequently providing an increased number of hotspots for the adsorption of R6G molecules.

Figure 3.14 showcases the SERRS spectra obtained from different substrates, with the data averaged over ten random spots on each sample. The accompanying bar graph highlights the enhanced performance of the D-S10 sample. It is worth noting that the observed deviation in performance, although notable, is not statistically significant when compared to the RSD within a single sample at different spots (22%) or the RSD between different samples (26%). Based on these findings, we selected the sample ablated at an angle of 10⁰ as the preferred substrate for subsequent studies involving various analyte molecules and fundamental investigations.

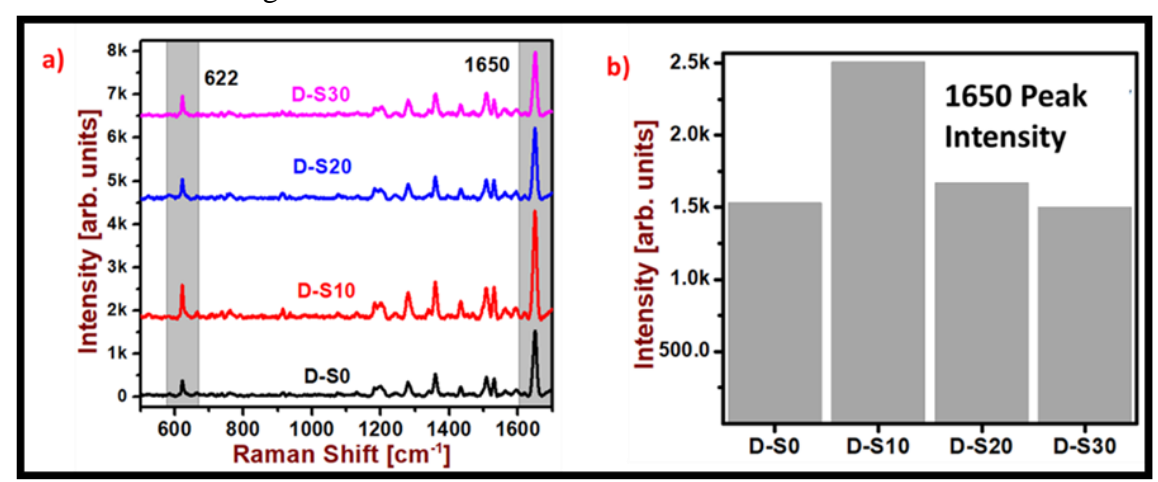


Figure 3.14: a) SERRS spectra of femtosecond laser ablated Ag-Au samples for different angles of incidence for 1 μ M of R6G with 532 nm laser excitation. Each spectrum is an average of 10 spectra collected at different spots on each sample. b) Bar graph for 1650 cm⁻¹ peak intensity of R6G indicating better performance of D-S10 sample.

SERS is often characterized by two key aspects: enhancement factor and reproducibility. The relationship between these two factors is a subject of ongoing debate and is often described as an uncertainty relation, where an increase in EF comes at the expense of reproducibility, and vice versa [30]. This trade-off can be attributed to the localized nature of the hotspots responsible for high enhancement, which can also lead to poor reproducibility [35]. To delve deeper into this relationship, it is instructive to examine the SERS behavior on two different types of substrates: densely packed, randomly stacked nanoparticles and periodic nanostructures. In this context, we utilized debris (D-S10) and no debris (ND-S10) structures to explore this advantage. A concentration of 5 μM R6G was employed, and SERRS mapping was performed on both substrates, specifically focusing on the 612 cm⁻¹ peak of R6G, within an area of 100 µm². Figure 3.15 illustrates the SERRS mapping data, with false colors representing the intensity of the 612 cm⁻¹ peak of R6G on a) the ND-S10 substrate and e) the D-S10 substrate. Figures 3.15 b) and 3.15 f) display the corresponding spectra, while Figures 3.15 c) and figure 3.15 g) depict contour maps of the intensity distribution. Figures 3.15 d) and 3.15 h) present statistical analyses of approximately ~5000 spectra for each sample, clearly indicating the RSD, mean, standard deviation (SD), and range (maximum-minimum intensity). The data clearly reveal that the ND-S10 substrate exhibits higher reproducibility, with an RSD of 10%, albeit with a compromise on enhancement, as indicated by the maximum intensity of 2403 counts. On the other hand, the D-S10 substrate demonstrates superior enhancement, with a maximum intensity of 4671 counts, but at the cost of higher RSD of 31%. These trends are further supported by the statistical parameters presented in the figures. Based on this statistically significant data, it is evident that an inverse relationship exists between reproducibility and enhancement in SERS. This study emphasizes that for applications focused on trace detection, such as forensics or explosive detection, SERS substrates with a high density of hotspots are preferable. We have also performed mapping studies at low concentration (10p pM) of R6G with the ND-S10 substrate and still found good reproducibility as shown in Figure 3.16.

To evaluate the efficiency of the substrate, we conducted a study on R6G at different concentrations using the ND-S10 substrate. For ultra-trace detection, we utilized the D-S10 substrate based on the insights gained from the mapping studies, and successfully detected concentrations as low as 10 fM, as depicted in Figure 3.17 a). For better readability, the complete spectrum is presented in Figure 3.17 b). Notable peaks observed

in the spectrum correspond to R6G's C-C-C ring bending at 614 cm⁻¹, as well as the aromatic C-C stretching at 1363 cm⁻¹ and 1650 cm⁻¹ [33]. The relationship between concentration and intensity was found to be nonlinear, with the intensity saturating at higher concentrations. To quantify the data and enable quantitative detection, we have

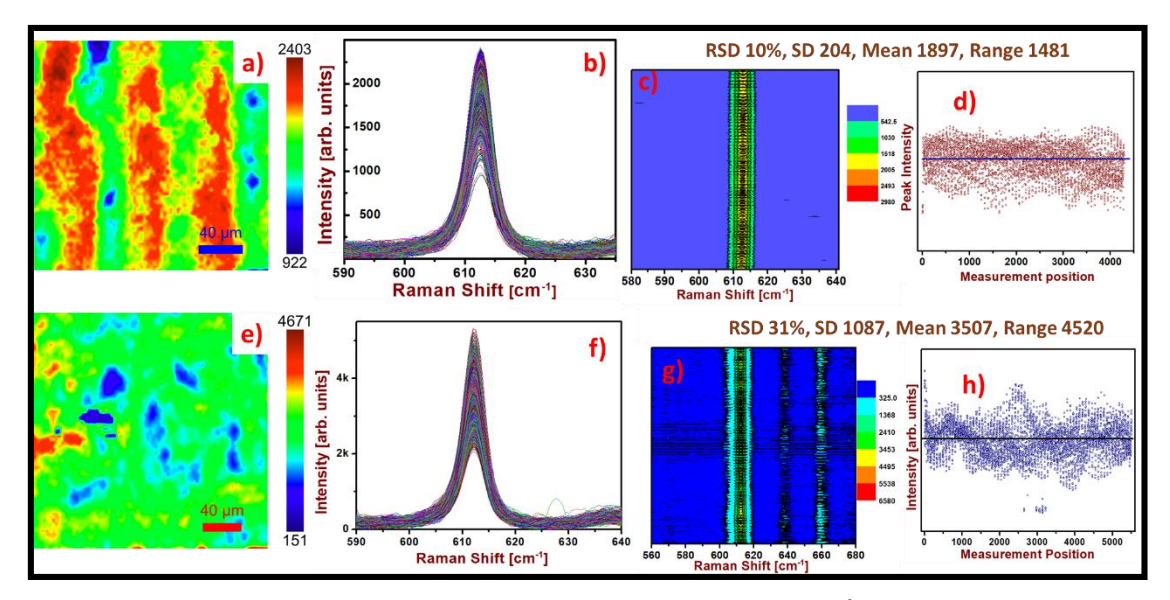


Figure 3.15: SERRS mapping studies performed in an area of $100 \ \mu m^2$ with $5 \ \mu M$ of R6G for D-S10 and ND-S10 substrate with $612 \ cm^{-1}$ peak as reference. a,e) SERRS false color image generated for the peak intensity for a) ND-S10, e) D-S10 substrate. b and f represent corresponding spectra while c,g) show the contour maps of the peak intensity distribution. d,h) Scatterplot of peak intensity for d) ND-S10 and h) D-S10 sample with statistical parameters summarized in the figure. The line in the graphs indicate the mean value.

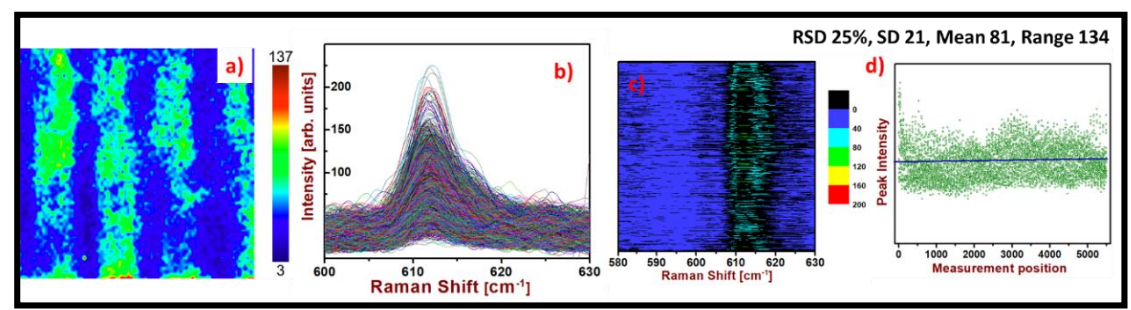


Figure 3.16: SERRS mapping studies performed in an area of $100 \, \mu m^2$ with $10 \, pM$ of R6G on ND-S10 substrate with $612 \, cm^{-1}$ peak as reference. a) SERRS false color image generated for the peak intensity. b) corresponding spectra while c) show the contour map of the peak intensity distribution. d) Scatterplot of peak intensity for d) with statistical parameters summarized in the figure. The line in the graphs indicate the mean value.

fitted the experimental data to a polynomial equation with an R^2 value of 0.98, indicating a good fit for prediction purposes. This fitting equation can be employed to facilitate quantitative analysis of R6G concentrations. To assess reproducibility, we examined 5 μ M R6G within each ND-S10 substrate (represented in the figure 3.17 d) by

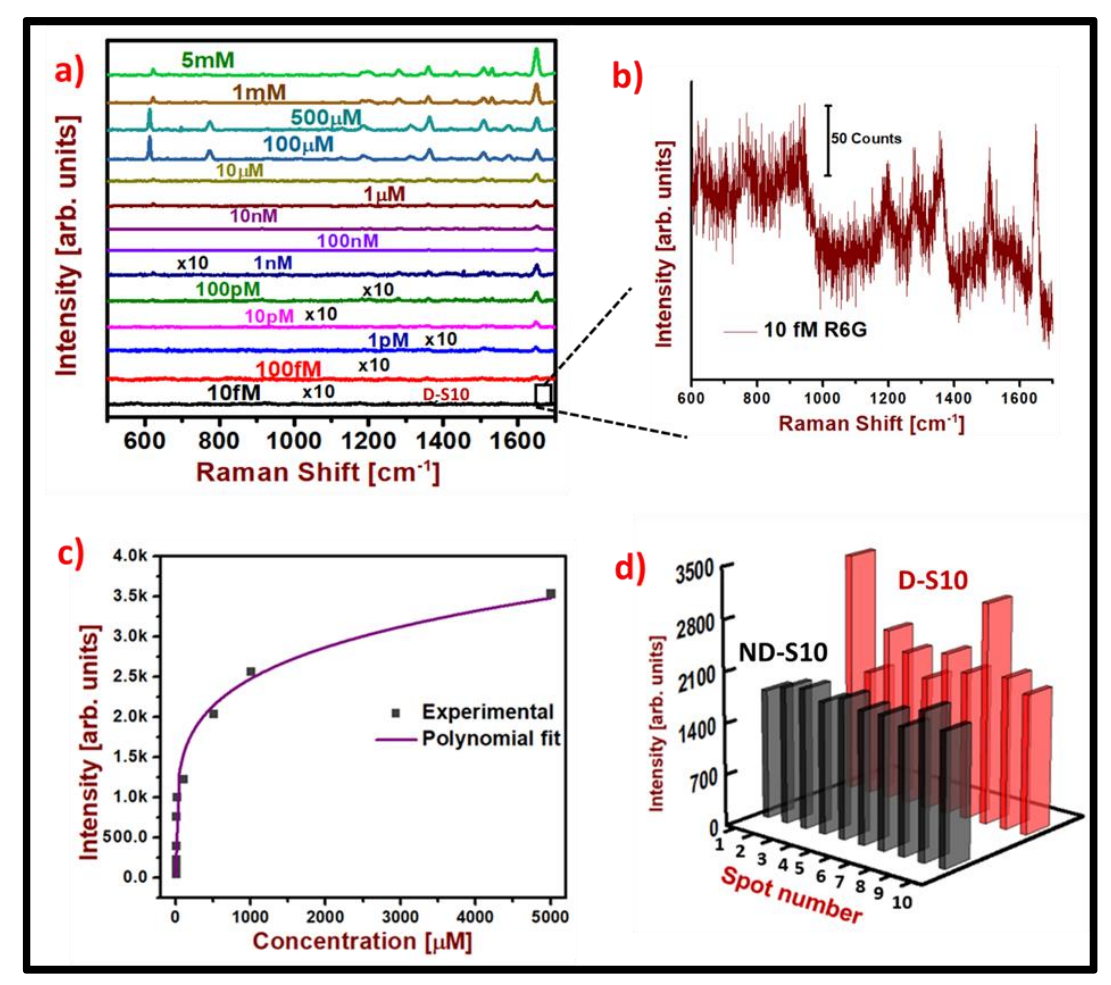


Figure 3.17: a) SERRS spectra of R6G for different concentrations collected on ND-S10 substrate with 532 nm laser excitation and 1mW laser power. The spectrum at 10 fM is collected with D-S10 sample and is multiplied by 10 for better readability. b) The full spectrum of the 10fM of R6G presented for readability. c) SERRS intensity and concentration relation for 1650 cm⁻¹ peak intensity of R6G fitted to a polynomial with an R^2 value of 0.98. d) Reproducibility of the signal at 10 random spots on the substrate for ND-S10 (black) and D-S10 (red) samples with 5 μ M R6G.

the grey curve) and D-S10 substrate [represented by the red curve in Figure 3.17 d)]. We collected ten random spectra on each sample for analysis. The results revealed that the D-S10 substrate exhibited a higher RSD of 22%, while the ND-S10 substrate demonstrated a lower RSD of 5%, consistent with the findings discussed in the mapping section. This reinforces the inverse relationship between reproducibility and enhancement in SERS, as established earlier. The EF was calculated for lowest detected value of R6G (10fM) using the method described elsewhere [36] and was found to be 8×10^9 .

In addition to R6G, we also investigated CV, a dye with absorption at 592 cm⁻¹. To maximize the excitation efficiency, we employed a 633 nm laser, which closely matches

the absorption peak of CV. SERRS spectra of CV at various concentrations were collected using the ND-S10 substrate, with the exception of the lowest concentration (100 fM),

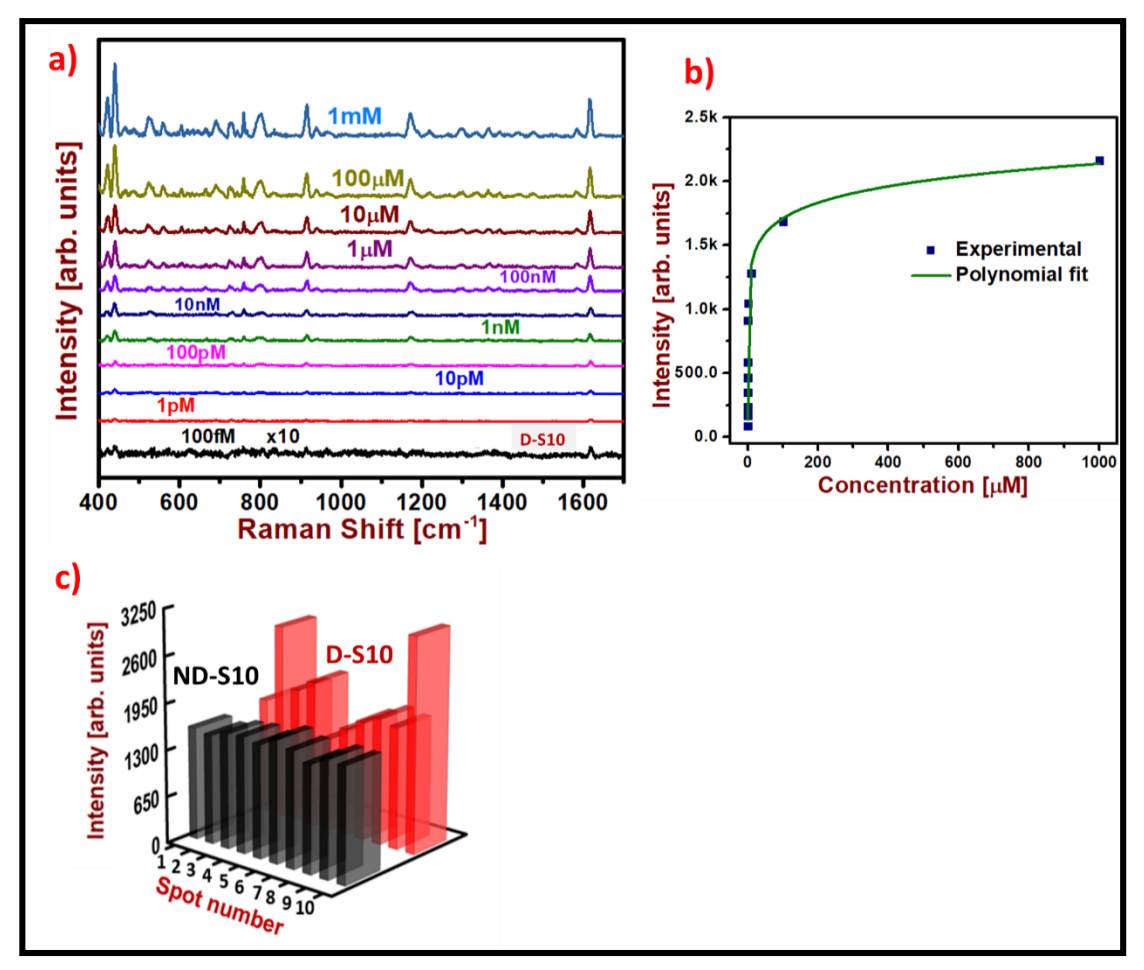


Figure 3.18: a) SERRS spectra of CV for different concentrations collected on ND-S10 substrate with 633 nm laser excitation and 1mW laser power. The spectrum at 100 fM is collected with D-S10 sample and is multiplied by 10 for better readability. b) SERRS intensity and concentration relation for 1618 cm⁻¹ peak intensity of CV fitted to a polynomial with an R^2 value of 0.98. c) Reproducibility of the signal at 10 random spots on the substrate for ND-S10 (black) and D-S10 (red) samples with 1 μ M of CV.

which was measured using the D-S10 sample, as illustrated in Figure 3.18 a). The SERRS spectra of crystal violet exhibited distinct peaks at 1618 cm⁻¹, 1179 cm⁻¹, 912 cm⁻¹, and 723 cm⁻¹, corresponding to C-C stretching, C-H in-plane bending, ring skeletal vibrations, and C-H out-of-plane bending modes, respectively [37]. Figure 3.18 b) demonstrates the relationship between intensity and concentration for the 1618 cm⁻¹ peak of CV. The data points were fitted to a polynomial equation with an R² value of 0.98, indicating a robust non-linear relationship. To assess reproducibility, we collected ten random spectra on both the ND-S10 (represented by the black curve) and D-S10 (represented by the red curve) substrates, as depicted in Figure 3.18 c). The ND-S10 substrate exhibited a low Relative Standard Deviation (RSD) of 4%, signifying high reproducibility. On the other hand, the

D-S10 substrate demonstrated a higher RSD of 28%, indicating slightly reduced reproducibility compared to the ND-S10 substrate.

Explosives and biomolecules have absorption in the UV region as is also demonstrated in figure 12. The resonance excitation of explosives using UV-SERS has been extensively studied and recognized as advantageous[38,39]. However, it is important to note that UV lasers can potentially damage the analyte molecules, necessitating the use of extremely low laser powers to avoid such damage and enable ultra-trace detection[40–45]. In this study, we employed a 325 nm He-Cd laser with a power of 1 mW to investigate the SERS behavior of an explosive molecule, picric acid (PA), and an amino acid called cysteine. Figure 3.19 a) presents the SERRS spectra of PA at various concentrations, with the lowest detected concentration being 100 nM, even at the low power of 1 mW. The distinct peaks observed at 1343 cm⁻¹ and 826 cm⁻¹ correspond to the symmetric stretching mode of the NO₂ group and the bending mode of the C-H bond, respectively [46]. Similarly, Figure 3.20 a) displays the SERRS data for cysteine at different concentrations, with the lowest detected concentration also being 100 nM.

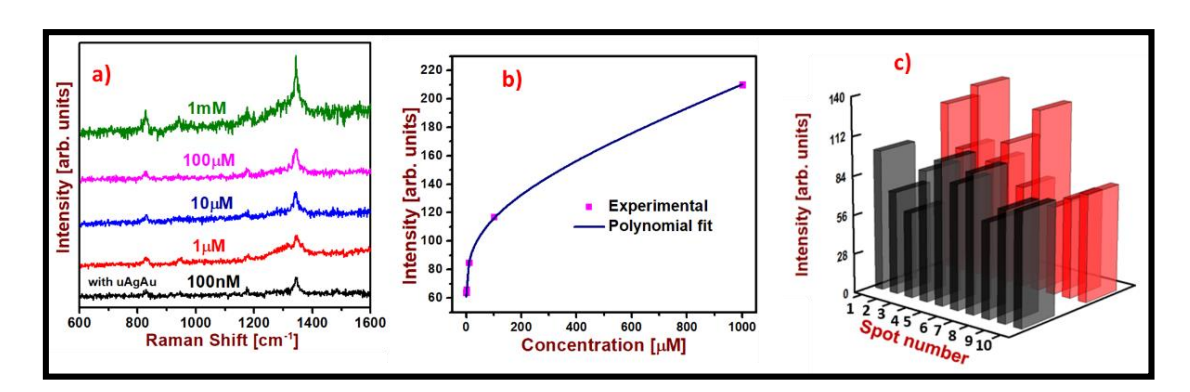


Figure 3.19: SERRS spectra of for different concentrations for a) PA studied with 325 nm laser excitation and 1.3 mW laser power on ND-S10 substrate. The 100 nM spectrum for PA is multiplied by 5 to increase visibility. c) Reproducibility of 1343 cm⁻¹ of PA collected at 10 random spots on the same with RSDs of 16%.

The peaks observed at 2944 cm⁻¹, 2564 cm⁻¹, and 677 cm⁻¹ correspond to specific vibrational modes of cysteine, as confirmed by the existing literature [47]. Reproducibility is a critical aspect of SERS measurements. Figure 3.19 c) and Figure 3.20 c) depict the reproducibility of the ND-S10 substrate for both picric acid and cysteine, respectively. Ten spectra were collected for each analyte, and the RSD was calculated. The RSD for picric acid was found to be 16% (for ND-S10), while for cysteine, it was 18%.

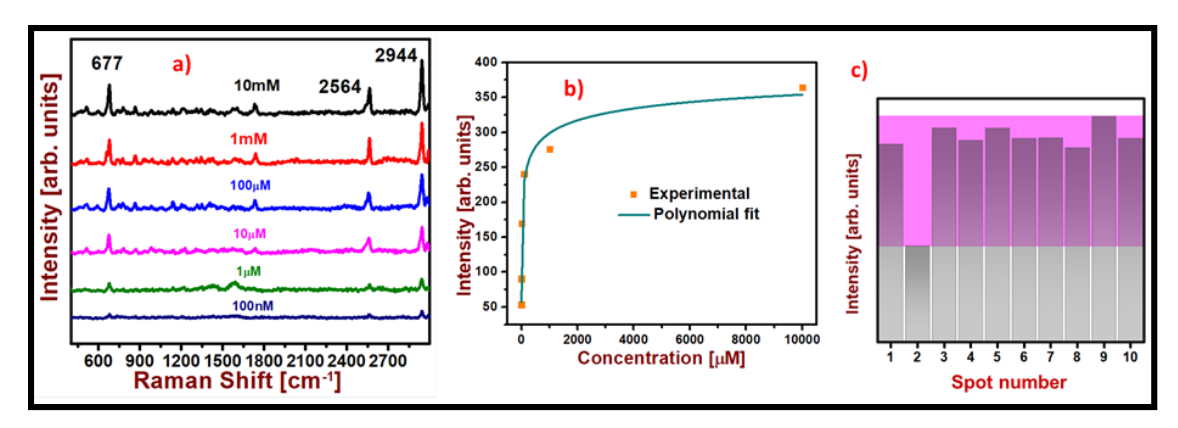


Figure 3.20: SERRS spectra of for different concentrations for a) Cysteine studied with 325 nm laser excitation and 1.3 mW laser power on ND-S10 substrate. b) Intensity and concentration fit c) Reproducibility of 2944 cm⁻¹ peak of Cysteine collected at 10 random spots on the same with RSDs of 18%.

Table 3.1 provides a comprehensive summary of the reproducibility and EFs obtained for the various analytes investigated in this study. The data clearly demonstrates an inverse relationship between reproducibility and EF, as exemplified by the results obtained using the D-S10 and ND-S10 substrates. It is important to note that despite the lower reproducibility, the EFs achieved for the dye molecules remain promising due to the advantage of resonance excitation, which effectively compensates for some of the inherent limitations of SERS. However, it is worth mentioning that the EFs observed for the explosive and dye molecules are relatively modest. This is primarily attributed to the experimental conditions, wherein the laser power was deliberately kept very low at 1.3 mW to prevent potential sample damage caused by the UV laser. By prioritizing the preservation of the sample integrity, the EFs for these particular analytes were compromised. Nevertheless, the obtained EFs still exhibit considerable potential, particularly in the context of resonance excitation, which effectively addresses some of the challenges associated with SERS analysis.

Table 3.1: Summary of analytes and SERS parameters for this study.

Substrate	Analyte	RSD	Enhancement
			Factor
ND-S10	R6G	10% (~5000 spectra)	1×10 ⁹
D-S10	R6G	31% (~5000 spectra)	8×10 ¹⁰
ND-S10	CV	4% (10 spectra)	3×10 ⁹
D-S10	CV	28% (10 spectra)	2×10 ¹⁰
ND-S10	PA	16%	6×10 ⁵
ND-S10	Cysteine	18%	4×10 ⁵

3.3.2. Femtosecond Ablation with Cylindrical Focusing

Femtosecond laser pulses (~70 fs) at a central wavelength of 800 nm and a repetition rate of 1 kHz were used for our cylindrical focusing studies. The detailed experimental setup is discussed in chapter 2. We have used a cylindrical lens to focus the laser on the substrate. The line focus has significantly increased the rate of ablation and hence reduced the time. It also resulted in novel sand dune-like nanoripples that were later shown to have an advantage in our SERS studies. The sample was moved in a raster pattern in an area of 4x4 mm² using programmable linear translational stages. Prior to SERS studies, the formation of these nanoripples as a function of laser energy was studied and characterized using FESEM imaging. A structure with regular and uniform nanoripples was chosen for SERS studies keeping in view the reproducibility of the signal. These laser-induced periodic surface structures (LIPSS) are known to form by the interference of incident electromagnetic waves with surface plasmon polaritons [48]. The other theory proposes that they are a consequence of non-uniform energy absorption by the surface [49]. These LIPSS were proven to have an advantage in SERS in our previous studies [50] [51].

3.3.2.1. Results on Ag

Effects of laser power on the resulting nanostructures has been studied thoroughly by changing the laser power using a combination of half wave plate and Brewster window as discussed in chapter 2. The resulting nanostructures were characterized by FESEM and the results are presented in figure 3.21.

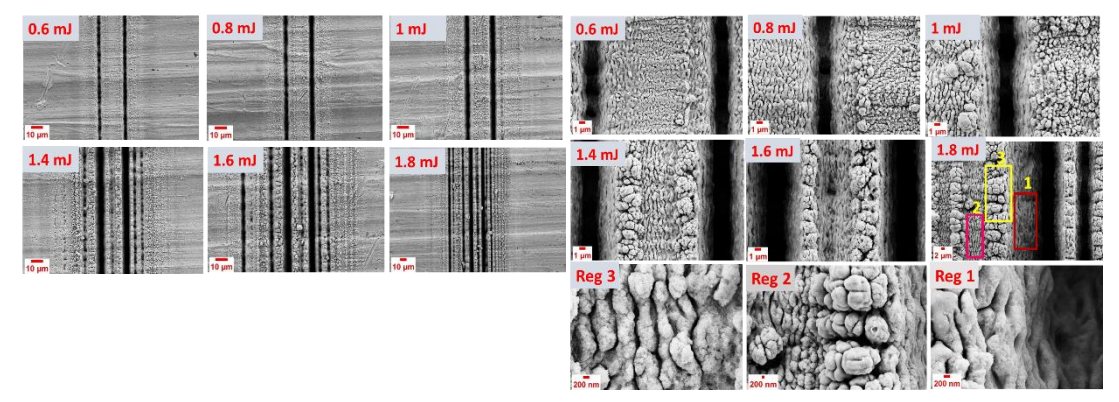


Figure 3.21: FESEM images of laser structured Ag with different energies as indicated in the figure for different magnifications.

The formation of LIPS on the sample surface depends on the beam profile of the incident beam [52]. Accordingly, different structures were observed for Gaussian and Bessel beam ablation [53].

3.3.2.2. SERS Studies

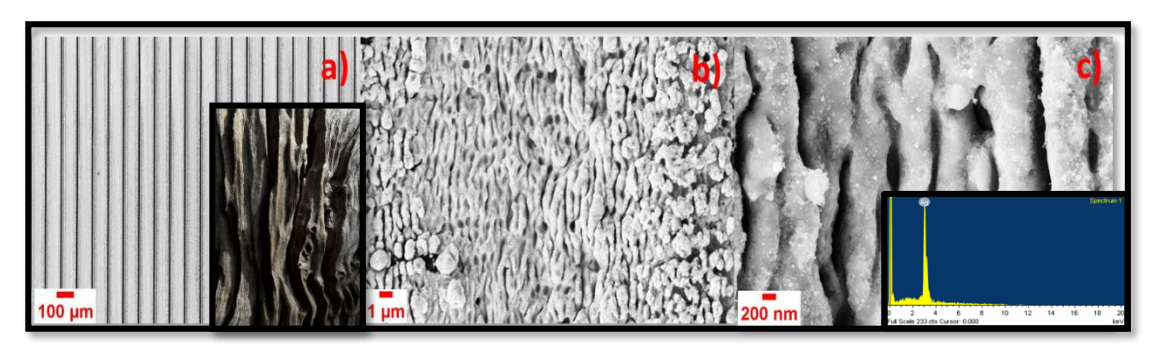


Figure 3.22: FESEM images of laser structured Ag that was used as SERS substrate for different magnifications as indicated in the figure. The inset image shows a tree bark with ripples resembling the nano-ripples on Ag. Inset show EDX spectrum with Ag peak.

In order to carry out SERS measurements, the sample was ablated in an area of 4x4 cm² with lines of spacing 80 µm and characterised using FESEM as shown in figure 3.22. The area between the lines was covered with nano-ripples. The inset image shows uncanny resemblance of these nano-ripples with wavy patterns on a tree bark. The samples were then utilised for the trace detection of two explosive molecules, tetryl and RDX along with a biomolecule, cytosine. A portable Raman spectrometer with 10 mW laser power and 10s of acquisition time has been used for the measurements. The data for each concentration of the analyte molecule is presented in figure 3.23. The lowest detected concentration of the analyte molecules tetryl, RDX and cytosine was found to be 50 nM, 100 µM and 100 nM, respectively. The prominent peak of tetryl, RDX and cytosine at 1357 cm⁻¹, 857 cm⁻¹ and 791 cm⁻¹ correspond to NO₂ symmetric stretching [54], N–N stretching and NO₂ axial scissoring [55] and ring breathing [56], respectively. The intensity and concentration relation for these prominent peaks of the three molecules has found to be non-linear as shown in the figure 3.23 d). The EF calculated using the method described elsewhere [56][57] was found to be 1.7×10^8 , 3.1×10^4 and 5.6×10^7 for Tetryl, RDX and cytosine, respectively.

Using cylindrical focusing, large area LIPS have been achieved in between the spacing between two lines. In order to understand the distribution of hotspots and SERS intensity in this region, we have performed Raman mapping using 532 nm laser excitation and 50

 \times objective for 5 μ M concentration of Tetryl with Horiba Raman spectrometer. A random area of 65 μ m² has been chosen on the sample and was focused using the objective.

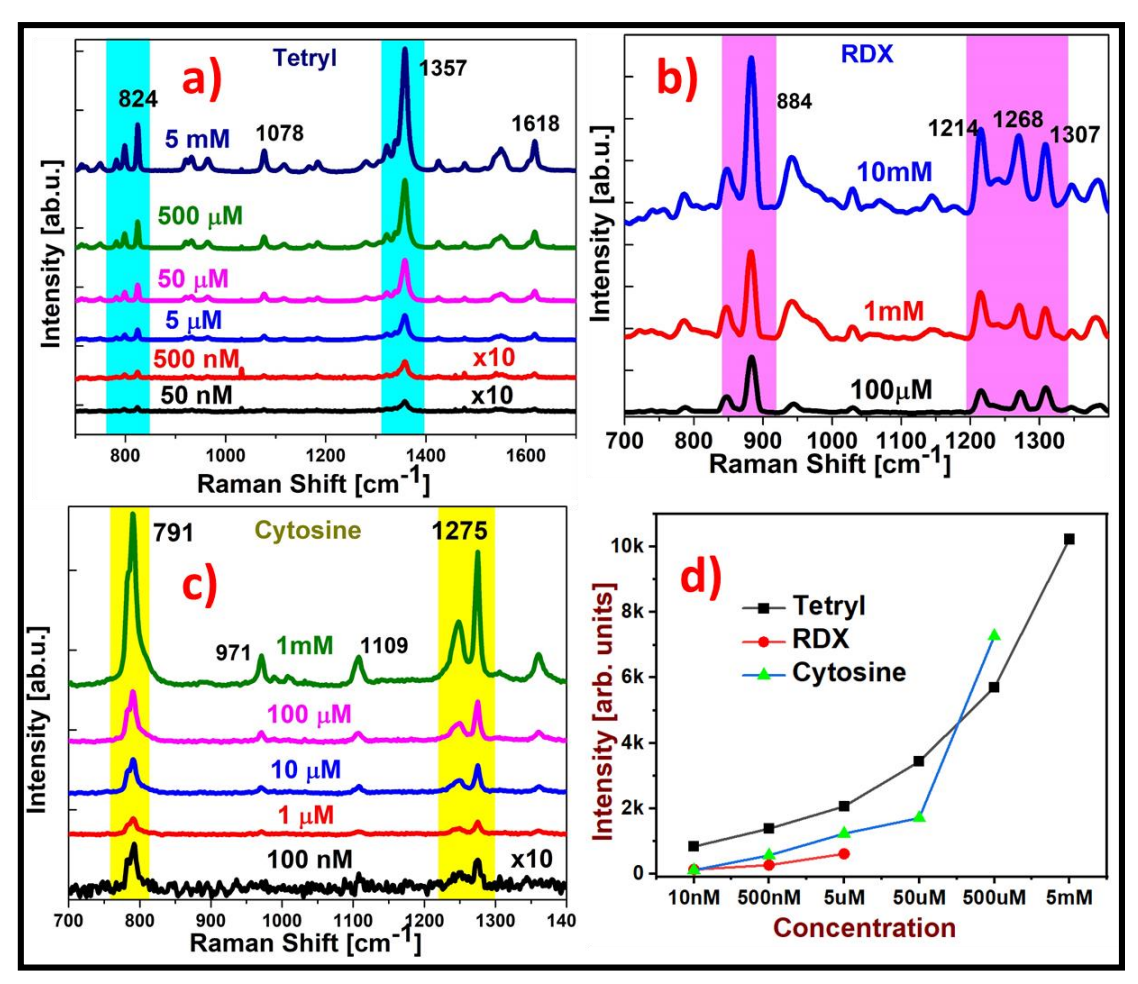


Figure 3.23: SERS spectra of a) Tetryl, b) RDX and, c) Cytosine for different concentrations collected using portable Raman spectrometer with laser power of 10mW and acquisition time of 10s. d) Intensity and concentration relation for prominent peaks of the three analyte molecules.

The laser power was set to 10 mW and the acquisition time was kept at 2s. For intensity mapping, 1358 cm⁻¹ peak of Tetryl corresponding to NO₂ symmetric stretching has been chosen and false colours as shown in figure 3.24 a) indicate the intensity scale for different ranges. The intensity distribution indicates that the signal distribution is uniform for large areas but is specifically high at certain regions corresponding to hotspots. The distribution of signal intensity is guided by different conditions in SERS like the orientation of the molecule and the adsorption at a particular site [58] [25].

SERS recently is being extensively used for detection of microorganisms including covid-19 [59]. The promise of SERS to perform label-free, rapid and bio-compatible measurements has been the reason for its popular choice. However, unlike molecules, microorganisms do not have a fingerprint spectrum for identification as they are composed of many biomolecules like lipids, proteins, and nucleic acids all of which are Raman active [60] [61]. Often machine learning algorithms are used in conjugation with SERS data in order to specifically identify the organism under study [62] [63].E. coli, short for Escherichia coli, is a type of bacteria commonly found in the lower intestines of warmblooded organisms, including humans. While most strains of E. coli are harmless, some can cause severe illness and even be life-threatening. Therefore, the detection and identification of E. coli bacteria are of significant importance for several reasons. E. coli can cause various infections, including urinary tract infections, respiratory illnesses, and gastrointestinal diseases. Certain strains, such as E. coli O157:H7, are known to produce toxins that can lead to severe foodborne illnesses, such as diarrhoea, abdominal cramps, and even kidney failure. Rapid and accurate detection of E. coli is crucial to prevent the spread of these infections and promptly treat affected individuals, minimizing the risk to public health. E. coli contamination is often associated with foodborne outbreaks, particularly in undercooked or improperly handled meat, raw vegetables, and contaminated water. The presence of E. coli in food products can lead to widespread

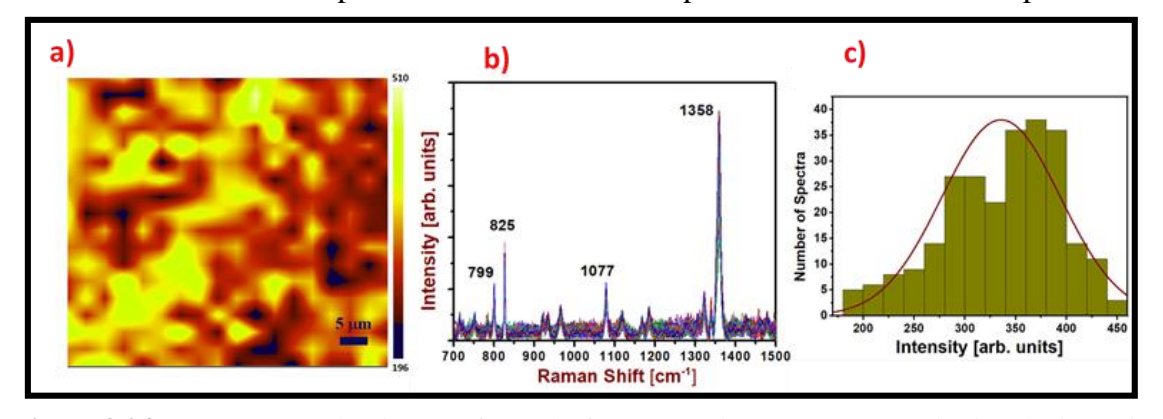


Figure 3.24: a) SERS mapping image of Tetryl of concentration $5\mu M$ generated using the intensity of 1358 cm⁻¹ peak of Tetryl in an area of 65 μm^2 . b) Corresponding SERS spectra of the mapping region and, c) Intensity distribution of the mapping area.

illnesses and has the potential for significant economic impact due to product recalls, hospitalizations, and potential lawsuits. Detecting E. coli in food processing plants, farms, and water sources allows for timely intervention, ensuring the safety of food supplies and preventing outbreaks. E. coli is used as an indicator organism to assess water quality and detect faecal contamination in natural water bodies, recreational waters, and wastewater treatment facilities. Monitoring E. coli levels helps identify potential sources of contamination, assess the effectiveness of sanitation measures, and safeguard the environment. High levels of E. coli can indicate the presence of other harmful pathogens,

making its detection crucial for maintaining ecological balance and protecting human and animal populations. Detecting and monitoring E. coli strains are essential for scientific research and epidemiological surveillance. By understanding the distribution, prevalence, and characteristics of different E. coli strains, researchers can study their virulence factors, antibiotic resistance patterns, and evolutionary traits. This information is critical for developing effective treatments, vaccines, and public health strategies to combat E. colirelated infections.

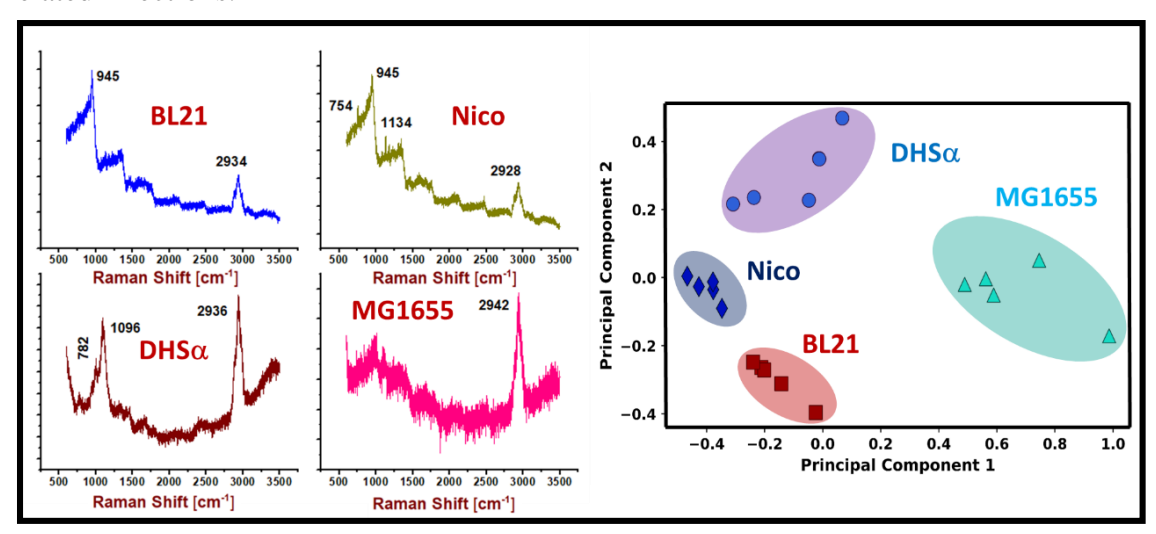


Figure 3.25: a) SERS spectra of different E. coli species as indicated in the image, b) PCA for classification and identification of the species using SERS data.

Using the laser structured Ag as the substrate, different species of E. coli have been detected using SERS. E. coli samples were prepared using a standard protocol in a biology lab and were allowed to grow overnight. To remove the effects of growth medium, the samples were centrifuged and the pellet was collected, transferred to 6 μl of water. SERS spectra was collected using the Horiba Raman spectrometer with 532 nm and 1 mW laser power, 2s of acquisition time. Five E. coli species labelled as BL21, Nico, DHSα, ML1655, and BL21 DE3 were taken for the studies. These variants have a slightest difference in their genetic makeup which reflects in their composition and in turn in the SERS spectra. The unprocessed SERS spectra for each species are plotted and presented in figure 3.25 a) indicating that there is no significant feature difference between the species especially for BL21 and Nico. In order to classify and identify the spectra, the data was processed using principal component analysis (PCA) collecting 5 spectra for each species. The resulting data as shown in figure 3.25 b) indicates that the species can indeed be distinguished using machine learning techniques.

3.3.2.3. Sand dune like Cu NSs for SERS

Most often than not, SERS substrates are made of Au or Ag, which are usually expensive. Here we present femtosecond laser processed Cu substrate as SERS substrate for the detection of two explosive molecules, ammonium nitrate and Tetryl (2, 4, 6-trinitro phenylmethyl nitramine), and a dye molecule, methylene blue. Ammonium Nitrate is the most commonly used explosive molecule in recent mishaps. Effects of laser energy on the formation of these nanostructures has been studied and characterised using FESEM. Laser structures fabricated at 0.8 mJ were used for the SERS studies as shown in the figure 3.26. Laser Induced Periodic Structures (LIPS) are formed upon irradiation of solids with linearly polarized Ti:sapphire fs laser pulses in air under normal incidence. These LIPS are generated by interference of the incident laser beam with a surface electromagnetic wave (SEW) generated at the rough surface which might include the excitation of surface plasmon polaritons (SPPs). LIPSSs are important for modification of materials so that enhancement in their performance can be achieved with respect to properties such as coefficient of friction, wear, wettability adhesion, fracture and impact strengths just to name a few.

The SERS studies were carried out with a portable Raman spectrometer with 785 nm laser excitation, 30 mW laser energy, and 3s acquisition time. Our preliminary studies have promised that these substrates can be used for the detection of two explosive molecules ammonium nitrate and tetryl with concentrations of 50 μM and 100 μM, respectively. Figures 3.26 a)-c) show the FESEM micrographs of laser-ablated Cu at different magnifications. The images at higher magnification clearly indicate the formation of sand dune-like LIPSS on Cu. Figures 3.26 d) shows the EDX quantitative data of the selected area on laser structured Cu. Figure 3.29 shows SERS spectra of Tetryl, Methylene Blue, and Ammonium Nitrate at concentrations of 100 μM, 5 μM, and 50 μM on the Cu substrate, respectively. The prominent modes of MB were identified at 1284 cm⁻¹, 1435 cm⁻¹, and 1626 cm⁻¹, which correspond to the C-H in-plane bending, C-C asymmetric, and C-N ring stretching, modes, respectively [6]. The observed 1042 cm⁻¹ Raman mode for AN corresponds to symmetric NO₃- stretching [6]. The 1357 cm⁻¹ Raman mode of Tetryl corresponds to symmetric stretching of nitro group [7].

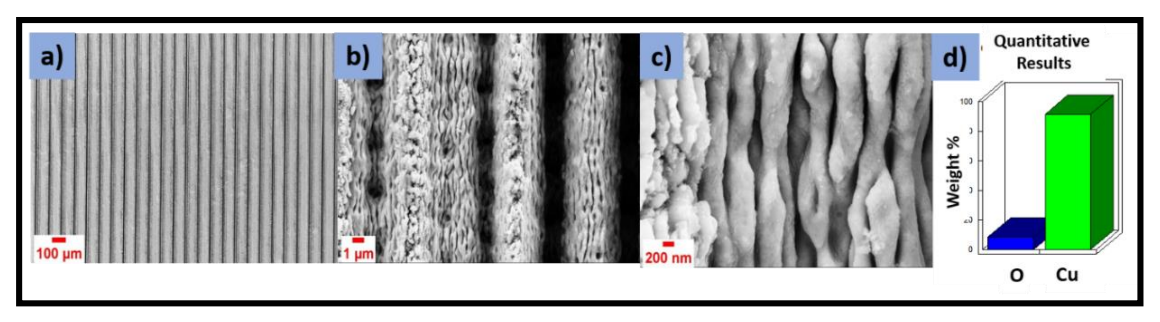


Figure 3.26: a)-c) FESEM micrographs of laser ablated Cu nanostructures at different magnifications indicate the presence of sand dune-like laser-induced periodic structures. d) Quantitative results of the EDX spectrum of a selected area on laser structured Cu.

The SERS studies were performed with a portable Raman Spectrometer with 785 nm laser excitation, 30 mW laser energy, and 3s acquisition time. A structure with regular and uniform nanoripples obtained for 0.8mJ was chosen for SERS studies keeping in view the reproducibility of the signal as shown in Figure 3.27. 10 μl of the analyte was drop-casted on the substrate and waited to dry. Figure 3.27 a) shows the SERS spectrum of tetryl at a concentration of 100 μM on the LS-Cu (black line) and plain Cu (red line), respectively. The laser structured Cu (LS-Cu) has clearly performed better than plain Cu by nearly ~12 times. Similar studies were performed with MB and AN as shown in Figure 3.27 c). Reproducibility is an important factor determining the performance of a SERS substrate. We have collected the SERS signal at 10 random spots on the substrate and estimated the relative standard deviation (RSD) to be ~5% as shown in figure 3.27 b).

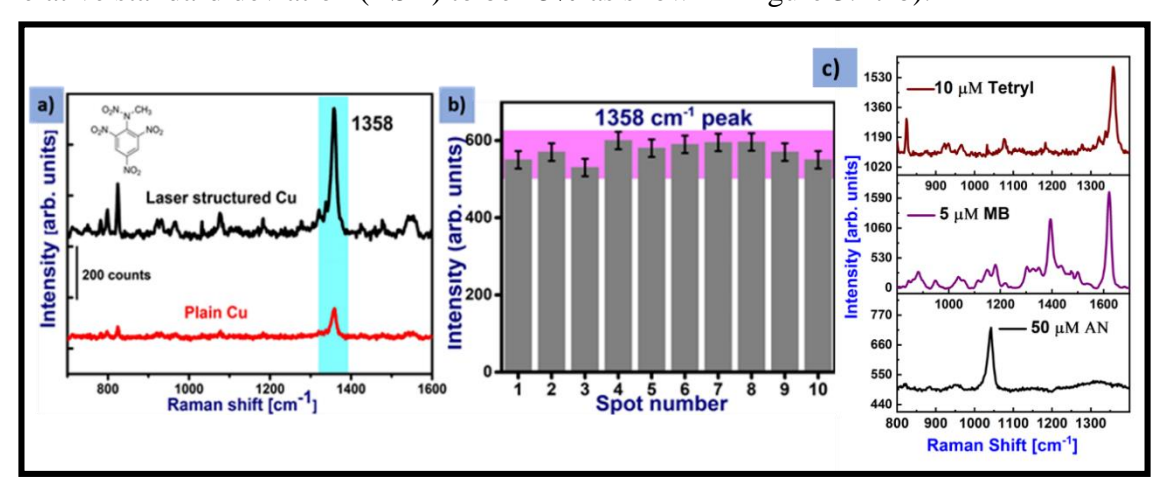


Figure 3.27: a) SERS spectra of Tetryl for a concentration at 100 μ M on laser structured Cu (LS-Cu) (black line, top) and plain Cu (red line, bottom) (multiplied by 3 to enhance the readability) b) Intensity of the 1358 cm⁻¹ peak collected at 10 random spots on the substrate demonstrating an RSD of 5%. c) SERS spectra of Tetryl, MB and AN for concentrations 10 μ M, 5 μ M and 50 μ M, respectively, collected with portable Raman spectrometer with 785 nm laser excitation and 30 mW laser power.

3.4. Conclusions

This chapter focused on fabrication of diverse nanostructures on Ag, Ag-Au (1:1), Si and Cu using femtosecond laser ablation in air. In chapter 3.1, fs laser oscillator has also been employed to achieve web-like nanostructures on Si. Effects of different experimental parameters like laser fluence, and scan speed on all the resulting nanostructures have been studied. The mechanism of formation of the web-like structures is thoroughly understood and the results were correlated with the theory. Subsequently, after coating with Au, these nanostructures were utilised as SERS substrates for detection of MB with a sensitivity of 1 μ M. In chapter 3.2., effects of changing incident angle on fs laser amplifier-based ablation of Ag-Au alloy have been studied for four different angles of 0°, 10°, 20° and 30°. These structures were utilised for SERS measurements with two different motives.

- a) With the use of contrast in nanostructures between debris and no-debris substrates, the fundamental relationship between SERS enhancement and reproducibility has been studied. An uncertainty product like relationship has been found between the two parameters communicating that a high enhancement comes at a trade-off of reproducibility owing to the localization of the hotspots.
- b) Using resonant excitation and through SERRS, ultra-trace detection of four molecules, R6G, PA, CV and Cysteine has been studied achieving sensitivity of 10 fM, 100 nM, 100 fM, and 100 nM, respectively with good reproducibility.
- c) Using cylindrical focusing, ripple like nanostructures have been obtained on Ag and Cu and effects of laser energy on these parameters have been studied. Ag structures were utilised for the detection of tetryl, RDX and cytosine with sensitivity of 50 nM, 100 μ M and 100 nM, respectively. The EF was found to be 1.7×10^8 , 3.1×10^4 and 5.6×10^7 for tetryl, RDX and cytosine, respectively. Sanddune like Cu NSs were utilised for the detection of tetryl, methylene blue and ammonium nitrate achieving a remarkable RSD of 5% with sensitivity of 10 μ M, 5 μ M and 50 μ M, respectively.

The performance of the Si nanostructures could be significantly improved by changing the thickness of the gold coating. In-situ synthesis of Au-Si nanostructures by ablating after gold coating has been explored elsewhere and also resulted in similar structures [8]. There is scope to use silver instead of gold which could have resulted in higher enhancement. SERRS measurement in section 3.1.5. have been performed under extremely low power

of nearly ~1 mW to suppress fluorescence and prevent damage to the sample under resonance conditions. The unusually low power has clearly reflected in the detection sensitivity of explosive molecule PA. Studies carried out for identification and classification of bacteria species can be extended to identifying covid-variants through SERS spectra.

References

- [1] A.H. Hamad, Effects of Different Laser Pulse Regimes (Nanosecond, Picosecond and Femtosecond) on the Ablation of Materials for Production of Nanoparticles in Liquid Solution, in: R. Viskup (Ed.), High Energy Short Pulse Lasers, IntechOpen, Rijeka, 2016. https://doi.org/10.5772/63892.
- [2] Z. Lin, M. Hong, Femtosecond Laser Precision Engineering: From Micron, Submicron, to Nanoscale, Ultrafast Sci. (2021). https://doi.org/10.34133/2021/9783514.
- [3] F. Fraggelakis, G. Mincuzzi, J. Lopez, I. Manek-Hönninger, R. Kling, Texturing metal surface with MHz ultra-short laser pulses, Opt. Express. 25 (2017) 18131. https://doi.org/10.1364/oe.25.018131.
- [4] P. Premnath, K. Venkatakrishnan, B. Tan, Programming cancer through phase-functionalized silicon based biomaterials, Sci. Rep. 5 (2015) 10826. https://doi.org/10.1038/srep10826.
- [5] B. Tan, K. Venkatakrishnan, Synthesis of fibrous nanoparticle aggregates by femtosecond laser ablation in air, Opt. Express. 17 (2009) 1064. https://doi.org/10.1364/oe.17.001064.
- [6] A. Tavangar, B. Tan, K. Venkatakrishnan, Synthesis of bio-functionalized three-dimensional titania nanofibrous structures using femtosecond laser ablation, Acta Biomater. 7 (2011) 2726–2732. https://doi.org/10.1016/j.actbio.2011.02.020.
- [7] A.S. Mahmood, K. Venkatakrishnan, B. Tan, Gold-silicon nanofiber synthesized by femtosecond laser radiation for enhanced light absorptance, Nanoscale Res. Lett. 9 (2014) 1–7. https://doi.org/10.1186/1556-276X-9-255.
- [8] M. Sivakumar, K. Venkatakrishnan, B. Tan, Characterization of mhz pulse repetition rate femtosecond laser-irradiated gold-coated silicon surfaces, Nanoscale Res. Lett. 6 (2011) 1-5. https://doi.org/10.1186/1556-276X-6-78.
- [9] S. Li, S.J. Silvers, M.S. El-Shall, Surface oxidation and luminescence properties of weblike agglomeration of silicon nanocrystals produced by a laser vaporizationcontrolled condensation technique, J. Phys. Chem. B. 101 (1997) 1794–1802. https://doi.org/10.1021/jp963192m.
- [10] P. Premnath, B. Tan, K. Venkatakrishnan, Bioactive interlinked extracellular matrix-like silicon nano-network fabricated by femtosecond laser synthesis, Biores. Open Access. 1 (2012) 231–238. https://doi.org/10.1089/biores.2012.0254.

- [11] P. Premnath, B. Tan, K. Venkatakrishnan, Engineering functionalized multi-phased silicon/silicon oxide nano-biomaterials to passivate the aggressive proliferation of cancer, Sci. Rep. 5 (2015) 1–12. https://doi.org/10.1038/srep12141.
- [12] S.V. Rao, G.K. Podagatlapalli, S. Hamad, Ultrafast laser ablation in liquids for nanomaterials and applications, J. Nanosci. Nanotechnol. 14 (2014) 1364–1388. https://doi.org/10.1166/jnn.2014.9138.
- [13] S.S.B. Moram, A.K. Shaik, C. Byram, S. Hamad, V.R. Soma, Instantaneous trace detection of nitro-explosives and mixtures with nanotextured silicon decorated with Ag–Au alloy nanoparticles using the SERS technique, Anal. Chim. Acta. 1101 (2020) 157–168. https://doi.org/10.1016/j.aca.2019.12.026.
- [14] J. Perrière, C. Boulmer-Leborgne, R. Benzerga, S. Tricot, Nanoparticle formation by femtosecond laser ablation, J. Phys. D. Appl. Phys. 40 (2007) 7069–7076. https://doi.org/10.1088/0022-3727/40/22/031.
- [15] B.R. Tull, J.E. Carey, M.A. Sheehy, C. Friend, E. Mazur, Formation of silicon nanoparticles and web-like aggregates by femtosecond laser ablation in a background gas, Appl. Phys. A. 83 (2006) 341–346. https://doi.org/10.1007/s00339-006-3502-7.
- [16] M. Kim, S. Osone, T. Kim, H. Higashi, T. Seto, Synthesis of nanoparticles by laser ablation: A review, KONA Powder Part. J. 2017 (2017) 80–90. https://doi.org/10.14356/kona.2017009.
- [17] S.-B. Wen, X. Mao, R. Greif, R.E. Russo, Experimental and theoretical studies of particle generation after laser ablation of copper with a background gas at atmospheric pressure, J. Appl. Phys. 101 (2007). https://doi.org/10.1063/1.2748635.
- [18] A. Tavangar, B. Tan, K. Venkatakrishnan, Study of the formation of 3-D titania nanofibrous structure by MHz femtosecond laser in ambient air, J. Appl. Phys. 113 (2013). https://doi.org/10.1063/1.4771667.
- [19] E.G. Gamaly, The physics of ultra-short laser interaction with solids at non-relativistic intensities, Phys. Rep. 508 (2011) 91–243. https://doi.org/https://doi.org/10.1016/j.physrep.2011.07.002.
- [20] E.G. Gamaly, A. V. Rode, B. Luther-Davies, Ultrafast ablation with high-pulse-rate lasers. Part I: Theoretical considerations, J. Appl. Phys. 85 (1999) 4213–4221. https://doi.org/10.1063/1.370333.
- [21] F. Floris, C. Figus, L. Fornasari, M. Patrini, P. Pellacani, G. Marchesini, A.

- Valsesia, F. Artizzu, D. Marongiu, M. Saba, A. Mura, G. Bongiovanni, F. Marabelli, F. Quochi, Optical sensitivity gain in silica-coated plasmonic nanostructures, J. Phys. Chem. Lett. 5 (2014) 2935–2940. https://doi.org/10.1021/jz501443c.
- [22] I. Alessandri, J.R. Lombardi, Enhanced Raman Scattering with Dielectrics, Chem. Rev. 116 (2016) 14921–14981. https://doi.org/10.1021/acs.chemrev.6b00365.
- [23] P. Pellacani, V. Torres-Costa, F. Agulló-Rueda, R. Vanna, C. Morasso, M. Manso Silván, Laser writing of nanostructured silicon arrays for the SERS detection of biomolecules with inhibited oxidation, Colloids Surfaces B Biointerfaces. 174 (2019) 174–180. https://doi.org/10.1016/j.colsurfb.2018.11.010.
- [24] R. Beeram, V.R. Soma, Ultra-trace detection of diverse analyte molecules using femtosecond laser structured Ag Au alloy substrates and SERRS, Opt. Mater. 137 (2023) 113615. https://doi.org/10.1016/j.optmat.2023.113615.
- [25] R. Beeram, D. Banerjee, L.M. Narlagiri, V.R. Soma, Machine learning for rapid quantification of trace analyte molecules using SERS and flexible plasmonic paper substrates, Anal. Methods. 14 (2022) 1788–1796. https://doi.org/10.1039/d2ay00408a.
- [26] G. Krishna Podagatlapalli, S. Hamad, M. Ahamad Mohiddon, S. Venugopal Rao, Effect of oblique incidence on silver nanomaterials fabricated in water via ultrafast laser ablation for photonics and explosives detection, Appl. Surf. Sci. 303 (2014) 217–232. https://doi.org/10.1016/j.apsusc.2014.02.152.
- [27] C. Byram, S.S.B. Moram, V.R. Soma, Surface-enhanced Raman scattering studies of gold-coated ripple-like nanostructures on iron substrate achieved by femtosecond laser irradiation in water, J. Raman Spectrosc. 50 (2019) 1103–1113. https://doi.org/10.1002/jrs.5617.
- [28] I. Ros, T. Placido, V. Amendola, C. Marinzi, N. Manfredi, R. Comparelli, M. Striccoli, A. Agostiano, A. Abbotto, D. Pedron, R. Pilot, R. Bozio, SERS Properties of Gold Nanorods at Resonance with Molecular, Transverse, and Longitudinal Plasmon Excitations, Plasmonics. 9 (2014) 581–593. https://doi.org/10.1007/s11468-014-9669-4.
- [29] D. Cunningham, R.E. Littleford, W.E. Smith, P.J. Lundahl, I. Khan, D.W. McComb, D. Graham, N. Laforest, Practical control of SERRS enhancement, Faraday Discuss. 132 (2006) 135–145. https://doi.org/10.1039/b506241a.
- [30] E.C.L. Ru, Principles of Surface Enhanced Raman Spectroscopy and Related

- Plasmonic effects, Elsevier, 2008.
- [31] A. Hakonen, P.O. Andersson, M. Stenbæk Schmidt, T. Rindzevicius, M. Käll, Explosive and chemical threat detection by surface-enhanced Raman scattering: A review, Anal. Chim. Acta. 893 (2015) 1–13. https://doi.org/10.1016/j.aca.2015.04.010.
- [32] G. McNay, D. Eustace, W.E. Smith, K. Faulds, D. Graham, Surface-enhanced Raman scattering (SERS) and surface-enhanced resonance raman scattering (SERRS): A review of applications, Appl. Spectrosc. 65 (2011) 825–837. https://doi.org/10.1366/11-06365.
- [33] P. Hildebrandt, M. Stockhurger, Surface-Enhanced Resonance Raman Spectroscopy of Rhodamine 6G adsorbed on colloidal silver, J. Phys. Chem. 88 (1984) 5935–5944. https://doi.org/10.1021/j150668a038.
- [34] K. Kneipp, Y. Wang, R.R. Dasari, M.S. Feld, Approach to Single Molecule Detection Using Surface-Enhanced Resonance Raman Scattering (SERRS): A Study Using Rhodamine 6G on Colloidal Silver, Appl. Spectrosc. 49 (1995) 780– 784. https://doi.org/10.1366/0003702953964480.
- [35] A.I. Pérez-Jiménez, D. Lyu, Z. Lu, G. Liu, B. Ren, Surface-enhanced Raman spectroscopy: benefits, trade-offs and future developments, Chem. Sci. 11(2020) 4563-4577. https://doi.org/10.1039/d0sc00809e.
- [36] V.S. Vendamani, R. Beeram, S.V.S. Nageswara Rao, A.P. Pathak, V.R. Soma, Trace level detection of explosives and pesticides using robust, low-cost, free-standing silver nanoparticles decorated porous silicon, Opt. Express. 29 (2021) 30045. https://doi.org/10.1364/oe.434275.
- [37] S.L. Kleinman, E. Ringe, N. Valley, K.L. Wustholz, E. Phillips, K.A. Scheidt, G.C. Schatz, R.P. Van Duyne, Single-molecule surface-enhanced raman spectroscopy of crystal violet isotopologues: Theory and experiment, J. Am. Chem. Soc. 133 (2011) 4115–4122. https://doi.org/10.1021/ja110964d.
- [38] D.O. Sigle, E. Perkins, J.J. Baumberg, S. Mahajan, Reproducible deep-UV SERRS on aluminum nanovoids, J. Phys. Chem. Lett. 4 (2013) 1449–1452. https://doi.org/10.1021/jz4004813.
- [39] S.K. Jha, Y. Ekinci, M. Agio, J.F. Löffler, Towards deep-UV surface-enhanced resonance Raman spectroscopy of explosives: Ultrasensitive, real-time and reproducible detection of TNT, Analyst. 140 (2015) 5671–5677. https://doi.org/10.1039/c4an01719f.

- [40] K. Faulds, W.E. Smith, D. Graham, DNA detection by surface enhanced resonance Raman scattering (SERRS), Analyst. 130 (2005) 1125–1131. https://doi.org/10.1039/b500248f.
- [41] F. Nicolson, L.E. Jamieson, S. Mabbott, K. Plakas, N.C. Shand, M.R. Detty, D. Graham, K. Faulds, Surface enhanced resonance Raman spectroscopy (SERRS) for probing through plastic and tissue barriers using a handheld spectrometer, Analyst. 143 (2018) 5965–5973. https://doi.org/10.1039/c8an01249k.
- [42] I.R. Lewis, N.W. Daniel, P.R. Griffiths, Interpretation of Raman spectra of nitro-containing explosive materials. Part I: Group frequency and structural class membership, Appl. Spectrosc. 51 (1997) 1854–1867. https://doi.org/10.1366/0003702971939686.
- [43] H. Liu, D. Lin, Y. Sun, L. Yang, J. Liu, Cetylpyridinium chloride activated trinitrotoluene explosive lights up robust and ultrahigh surface-enhanced resonance raman scattering in a silver sol, Chem. A Eur. J. 19 (2013) 8789–8796. https://doi.org/10.1002/chem.201300815.
- [44] Kumar G, Soni RK. Rhodium concave nanocubes and nanoplates as deep-UV resonant SERS platform. Journal of Raman Spectroscopy. 53(2022) 1890-903. https://doi.org/10.1002/jrs.6427.
- [45] N. Feliu, M. Hassan, E. Garcia Rico, D. Cui, W. Parak, R. Alvarez-Puebla, SERS Quantification and Characterization of Proteins and Other Biomolecules, Langmuir. 33 (2017) 9711–9730. https://doi.org/10.1021/acs.langmuir.7b01567.
- [46] S.S.B. Moram, C. Byram, S.N. Shibu, B.M. Chilukamarri, V.R. Soma, Ag/Au Nanoparticle-Loaded Paper-Based Versatile Surface-Enhanced Raman Spectroscopy Substrates for Multiple Explosives Detection, ACS Omega. 3 (2018) 8190–8201. https://doi.org/10.1021/acsomega.8b01318.
- [47] C. Jing, Y. Fang, Experimental (SERS) and theoretical (DFT) studies on the adsorption behaviors of 1-cysteine on gold/silver nanoparticles, Chem. Phys. 332 (2007) 27–32. https://doi.org/10.1016/j.chemphys.2006.11.019.
- [48] F. Keilmann, Y.H. Bai, Periodic surface structures frozen into CO2 laser-melted quartz, Appl. Phys. A. 29 (1982) 9–18. https://doi.org/10.1007/BF00618110.
- [49] J.E. Sipe, J.F. Young, J.S. Preston, H.M. van Driel, Laser-induced periodic surface structure. I. Theory, Phys. Rev. B. 27 (1983) 1141–1154. https://doi.org/10.1103/PhysRevB.27.1141.
- [50] S. Hamad, S. Satya, B. Moram, B. Yendeti, G.K. Podagatlapalli, S.V.S.N. Rao, A.P.

- Pathak, M.A. Mohiddon, V.R. Soma, Femtosecond Laser-Induced, Nanoparticle-Embedded Periodic Surface Structures on Crystalline Silicon for Reproducible and Multi-utility SERS Platforms, ACS Omega. 3 (2018) 18420–18432. https://doi.org/10.1021/acsomega.8b02629.
- [51] C. Byram, S. Satya, B. Moram, V. Rao, Surface enhanced Raman scattering studies of gold coated ripple like nanostructures on iron substrate achieved by femtosecond laser irradiation in water, J. of Raman spec., 50 (2019), 1103–1113. https://doi.org/10.1002/jrs.5617.
- [52] J.K. Jörn Bonse, Sabrina V. Kirner, Laser-induced Periodic Surface Structures, IEEE Journal of selected topics in quantum electronics, 23(2021). https://doi.org/10.1515/zwf-2021-0169.
- [53] D. Banerjee, M. Akkanaboina, R. Kumar Kanaka, V. Rao Soma, Femtosecond Bessel beam induced ladder-like LIPSS on trimetallic surface for SERS-based sensing of Tetryl and PETN, Appl. Surf. Sci. 616 (2023) 156561. https://doi.org/10.1016/j.apsusc.2023.156561.
- [54] K. Milligan, N.C. Shand, D. Graham, K. Faulds, Detection of Multiple Nitroaromatic Explosives via Formation of a Janowsky Complex and SERS, Anal. Chem. 92 (2020) 3253–3261. https://doi.org/10.1021/acs.analchem.9b05062.
- [55] M. Ghosh, L. Wang, S.A. Asher, Deep-ultraviolet resonance raman excitation profiles of NH 4NO 3, PETN, TNT, HMX, and RDX, Appl. Spectrosc. 66 (2012) 1013–1021. https://doi.org/10.1366/12-06626.
- [56] V.S. Vendamani, R. Beeram, M.M. Neethish, S.V.S.N. Rao, S.V. Rao, Wafer-scale silver nanodendrites with homogeneous distribution of gold nanoparticles for biomolecules detection, IScience. 25 (2022) 104849. https://doi.org/10.1016/j.isci.2022.104849.
- [57] S. Hamad, G.K. Podagatlapalli, M.A. Mohiddon, V.R. Soma, Cost effective nanostructured copper substrates prepared with ultrafast laser pulses for explosives detection using surface enhanced Raman scattering, Appl. Phys. Lett. 104 (2014). https://doi.org/10.1063/1.4885763.
- [58] R. Beeram, V.S. Vendamani, V.R. Soma, Deep learning approach to overcome signal fluctuations in SERS for efficient On-Site trace explosives detection, Spectrochim. Acta Part A Mol. Biomol. Spectrosc. 289 (2023) 122218. https://doi.org/10.1016/j.saa.2022.122218.
- [59] R. Beeram, K.R. Vepa, V.R. Soma, Recent Trends in SERS-Based Plasmonic

- Sensors for Disease Diagnostics, Biomolecules Detection, and Machine Learning, 5 (2023) 328. https://doi.org/10.3390/bios13030328.
- [60] S. Stöckel, J. Kirchhoff, U. Neugebauer, P. Rösch, J. Popp, The application of Raman spectroscopy for the detection and identification of microorganisms, J. Raman Spectrosc. 47 (2016) 89–109. https://doi.org/10.1002/jrs.4844.
- [61] S. Efrima, L. Zeiri, Understanding SERS of bacteria, J. Raman Spectrosc. 40 (2009) 277–288. https://doi.org/10.1002/jrs.2121.
- [62] R.M. Jarvis, R. Goodacre, Characterisation and identification of bacteria using SERS, Chem. Soc. Rev. 37 (2008) 931–936. https://doi.org/10.1039/b705973f.
- [63] J. Xia, W. Li, M. Sun, H. Wang, Application of SERS in the Detection of Fungi, Bacteria and Viruses, Nanomaterials. 12 (2022) 1–24. https://doi.org/10.3390/nano12203572.

Intentional Blank Page

Chapter 4

Novel Flexible, Hydrophobic, Hybrid and Low-cost SERS Substrates

Abstract

The work presented in this chapter focused on low-cost and durable SERS substrates that were synthesised by simple chemical and physical methods. First section discusses hybrid and low-cost rigid substrates with anisotropic Ag and Ag-Au nanostructures that were fabricated by etching the Si in the presence of metal salts. Effects of salt concentrations, duration of etching on the formation of highly anisotropic nanostructures were studied. Extensive SERS mapping studies along with trace detection of different hazardous and bio molecules like crystal violet, adenine, cytosine, penicillin G, kanamycin, ampicillin, AN, and thiram will be presented. Further, application of Si nanostructures decorated with 2-D laser ablated MoS₂ as SERS substrates will be presented. Novel MoS₂ morphologies were generated by femtosecond laser ablation of commercial MoS₂ powder in water, ethanol and methanol. Si nanowires decorated with bimetallic Ag-Au nanoparticles after coating with MoS₂ they were utilised for trace detection of diverse analyte molecules like MG (0.5 nM), melamine (100 nM), naphthalene (300 nM), L-Cysteine (100 nM), tetryl (50 nM) and E. coli. The results indicate that the MoS₂ has offered dual benefit of signal enhancement and increasing the durability of the substrates. The second part of the chapter focuses on flexible SERS substrates highlighting the novel hydrophobic plasmonic substrate that has been fabricated by a simple method of spin coating filter paper with Si oil. We have observed that this has been by far the cheapest and single step method to modify the filter paper wettability. Using nonlinear machine learning models such as principal component analysis (PCA) and support vector regression (SVR), these substrates have been used for rapid quantification using the SERS data. Towards the end, this chapter presents free standing porous Si decorated with Ag nanoparticles synthesised by wet etching method for trace detection of methylene blue, picric acid, ammonium nitrate, and thiram with sensitivities of 50 nM, 1 μ M, 2 μ M, and 1 μ M.

4.1. Introduction

To translate the SERS technique for real world applications, cost and ease of sample collection are two important constraints. Bottom-up chemical methods offer flexibility to synthesise highly anisotropic nanostructures that promise higher enhancement and limit of detection in trace sensing [1][2]. Silver dendrites have garnered significant attention since the 1990s due to their distinctive structure and their applications in catalysis, fuel cells, and storage devices [3] [4]. These dendrites offer a large surface area and desirable optical properties, making them suitable for signal enhancement in various applications, including SERS. The fabrication of Ag dendrites can be achieved through different methods, broadly categorized as electrochemical or chemical routes [5]. Electrochemical processes involve the utilization of potential or current to facilitate the reduction of Ag ions. The formation of dendrites is influenced by factors such as the applied field/current, presence of surfactants, and reaction time [6] [7]. On the other hand, electroless deposition processes involve simultaneous reduction and oxidation reactions on the surface of a template material. This method can be extended to various metals; for instance, Matsushita et al. reported the formation of Zinc and CuSe nano-dendrites using this technique [8] [9]. In 2005, Qiu et al. introduced the use of silicon (Si) wafers as templates for fabricating Ag dendrites, employing hydrofluoric acid (HF) as an etching agent [10]. The formation of these dendritic structures can be better explained by the diffusion-limited aggregation theory (DLA) [11]. According to DLA, particles undergo random walks and eventually settle at specific sites, contributing to the growth of the structure. The fractal structures are initiated by the formation of a seed particle from the metal salt. Particles formed at different locations diffuse randomly and attach to low energy sites near the seed particle. During this time, Ag2+ nuclei released from random sites move freely throughout the substrate until they reach designated low energy sites and deposit there. The cluster is formed by the sequential aggregation of these nuclei [12]. To initiate the formation of Ag dendrites, the Si surface is initially etched in the presence of HF, resulting in the formation of Si nanowires. Simultaneously, Ag nuclei are formed through a redox reaction and assemble on the Si nanowires, leading to cluster formation. The Ag ions in the solution are continually reduced by Si atoms through electron transfer, and the reduced Ag atoms are subsequently deposited on the Si surface. Si etching in the presence of an electric field induces diverse structural formations and introduces porosity in the material [13].

Furthermore, the utilization of an etch cell along with the application of current density in the presence of HF has enabled the fabrication of freestanding porous Si [14] [15]. Subsequently, this porous Si has been decorated with Ag nanoparticles through electroless etching [16]. Recently, there has been significant interest in hydrophobic and superhydrophobic substrates due to their capacity to concentrate analytes and nanoparticles in a confined area, thereby facilitating a higher density of hotspots and lower detection limits [17] [18] [19]. However, conventional filter paper, due to its porosity, tends to disperse the analyte and nanoparticles, leading to poor enhancement. To address this limitation, various techniques have been employed to fabricate hydrophobic filter paper (HFP), such as coating with alkyl ketene dimer [18], (2-dodecen-1-yl)-succinic anhydride [20], agar [21], spin-coating diluted polydimethylsiloxane (PDMS) [22], and perfluoroalkyltriethoxysilanes [23]. These methods often require extensive pre-treatment, may interfere with SERS probes, and are not cost-efficient. The difference in drying mechanism of a colloidal nanoparticles on the hydrophobic surface is also known to minimise the undesirable coffee ring effects [24] [25].

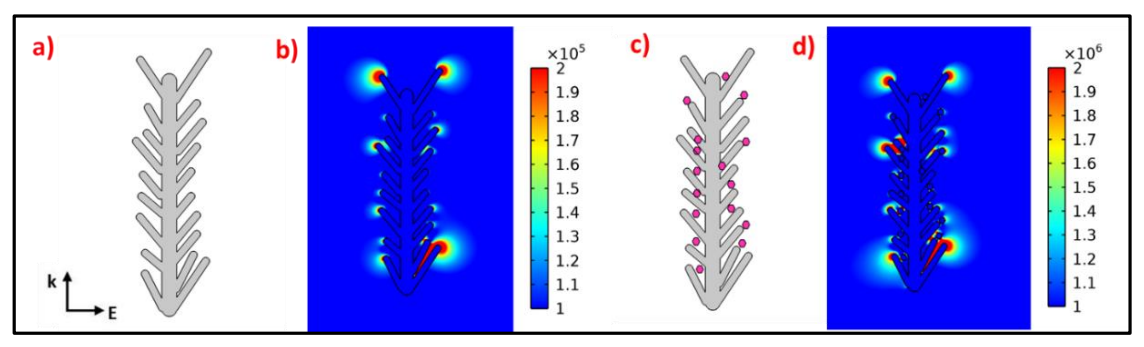


Figure 4.1: Results of COMSOL simulation showing a) Geometry of Ag dendrites constructed b) Near field simulation of the Ag dendrites showing enhancement at the tips. c) Geometry of Au@Ag nano-dendrites constructed. d) Near field simulation of Au@Ag nano-dendrites clearly showing additional enhancement relative to the plain Ag dendrites. Image taken from [26].

4.2. Anisotropic and Hybrid SERS Substrates

4.2.1. Highly Anisotropic Ag Dendrites for SERS

High density of hotspots is a prerequisite for SERS based trace detection to facilitate electromagnetic enhancement. Ag dendrites not only have the advantage of concentrated field at the tips but also offer high surface area for the adsorption of the probe molecules. Combining the Ag nanostructures with Au is known to offer the dual benefit of enhancing the field further and also to prevent rapid oxidation of the Ag nanostructures. COMSOL simulations have been carried out in order to visualise and understand the field enhancement around these structures as shown in figure 4.1. The images indicate higher

field enhancement around the tips of the fractals shown by false colour map. The near field enhancement is higher for the case of AuNPs@Ag nanodendrites relative to the case of only Ag nanodendrites as anticipated. In a different study, these dendrites were transferred to a filter paper and used as flexible substrate for SERS based detection [27].

4.2.2. Sample Preparation

Silver dendrites were prepared by a technique that was first proposed by Qiu et al. and was also carried forward by our group previously [10]. The protocol was scaled to produce dendrites in large scale on a 3-inch Si wafer. Briefly, Si wafer was cleansed with acetone and diluted HF to eliminate chemical residues and native oxide, respectively. Subsequently, the clean Si wafer was immersed in an electrolytic solution containing AgNO₃ and HF with concentration of 30 mM, 4.6 M, respectively, to induce dendrite formation at a temperature of 30°C through the mechanism that is best described in chapter 2. Following the dendrite growth, the samples were rinsed with deionized water and dried in the surrounding atmosphere. In order to decorate the Ag dendrites with Au NPs, the samples the wafer was immersed in gold salt of 1mM concentration for 30 min, 1 h, 2 h, and 3 h and labelled as AuNPs@AgNDs-0.5, AuNPs@AgNDs-1, AuNPs@AgNDs-2, AuNPs@AgNDs-3, respectively. The optical images of the final samples are presented in figure 4.2.

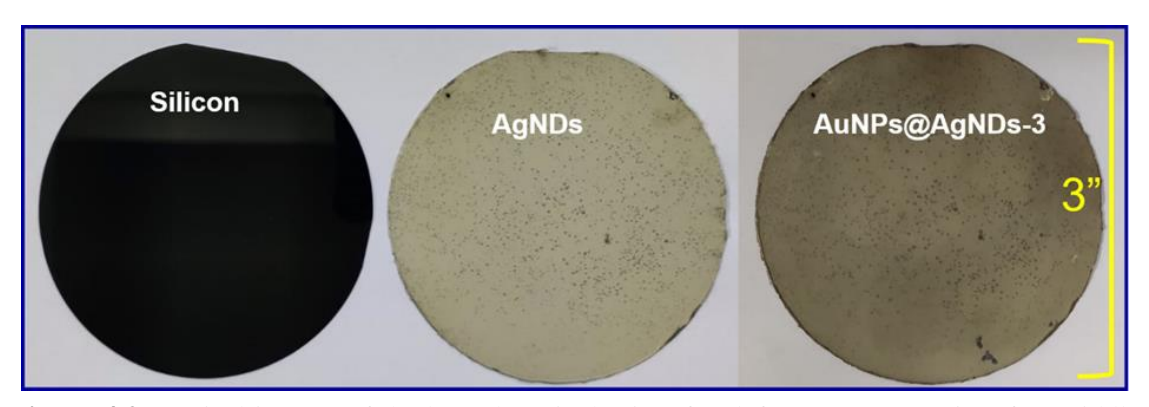


Figure 4.2: Optical images of the bare three-inch Si wafer (left), AgNDs on Si wafer (middle), and AuNPs@AgNDs on Si wafer (right). The AuNPs were decorated in ~3 hours (i.e., AuNPs@AgNDs-3).

The formation of Ag dendrites in an electroless etching method depends hugely on the concentration of the metal salt, duration of the etching and the ambient temperature. Effects of these parameters on the dendrites were studied systematically for the case of pure Ag dendrites [28]. In the present study we have studied the effects of concentration

of Au salt on the coverage of Ag dendrites for different concentration of HAuCl₄.3H₂O as presented in figure 4.3.

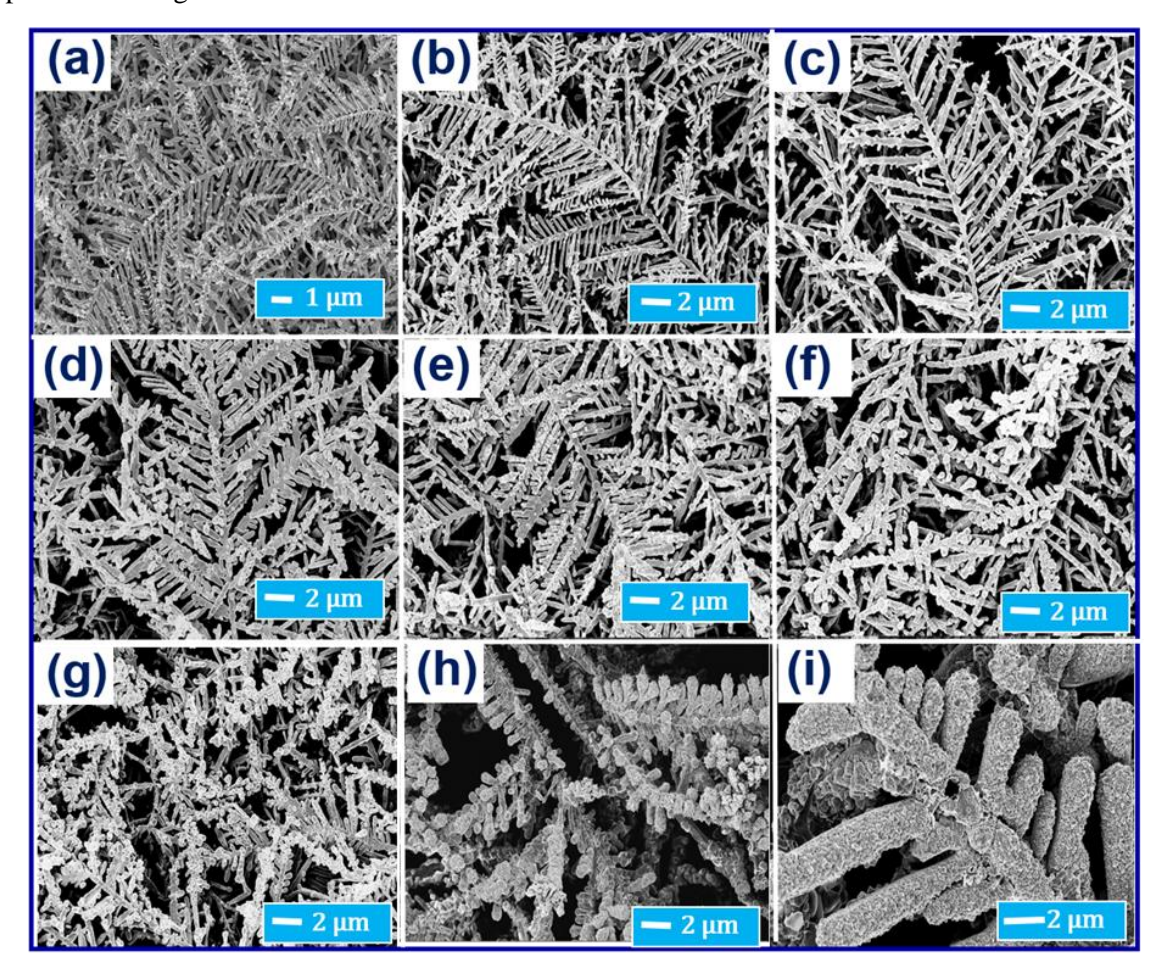


Figure 4.3: FESEM images of (a) as prepared AgNDs and AuNPs decorated AgNDs at various molar concentrations of Au seed solutions at b) 0.05 mM, c) 0.1 mM, d) 0.5 mM, e) 1 mM, f) 1.5 mM (g) 3 mM, h) 5 mM, i) 7 mM at room temperature.

The presented data clearly indicates that an increase in the concentration of the gold solution led to a noticeable enhancement in the decoration of AuNPs on the surfaces of AgNDs. At lower concentrations of the Au seed of 0.05 mM to 1mM, a sparsely populated layer of AuNPs was observed on the AgNDs. However, as the concentration of the gold solution increased, particularly at 1.5 mM, significant changes in the density of AuNPs decoration became apparent, as depicted in figure 4.3 f). Notably, at 3 mM concentration, a higher density of AuNPs grew, covering almost the entire dendritic structure, as illustrated in figure 4.3 g). As we proceeded to even higher concentrations, the AuNPs completely obscured the dendrite structure. This excessive coverage of AuNPs may not be suitable for SERS measurements, as it conceals the desired dendritic nature of the substrate. After carefully examining all the concentrations of AuNPs, we intentionally selected the favourable deposition condition of 1 mM concentration, which exhibited

isolated AuNPs with a uniform distribution along with prominent Ag dendrite structure. The duration of growth of Au NPs at this concentration is also optimised and the results are depicted in figure 4.4 for 0.5, 1, 2 and 3 hours. It can be seen that distinct and homogenously distributed Au NPs were formed at the duration of 3 hours which is presented in detail in figure 4.5 and hence was used for SERS studies.

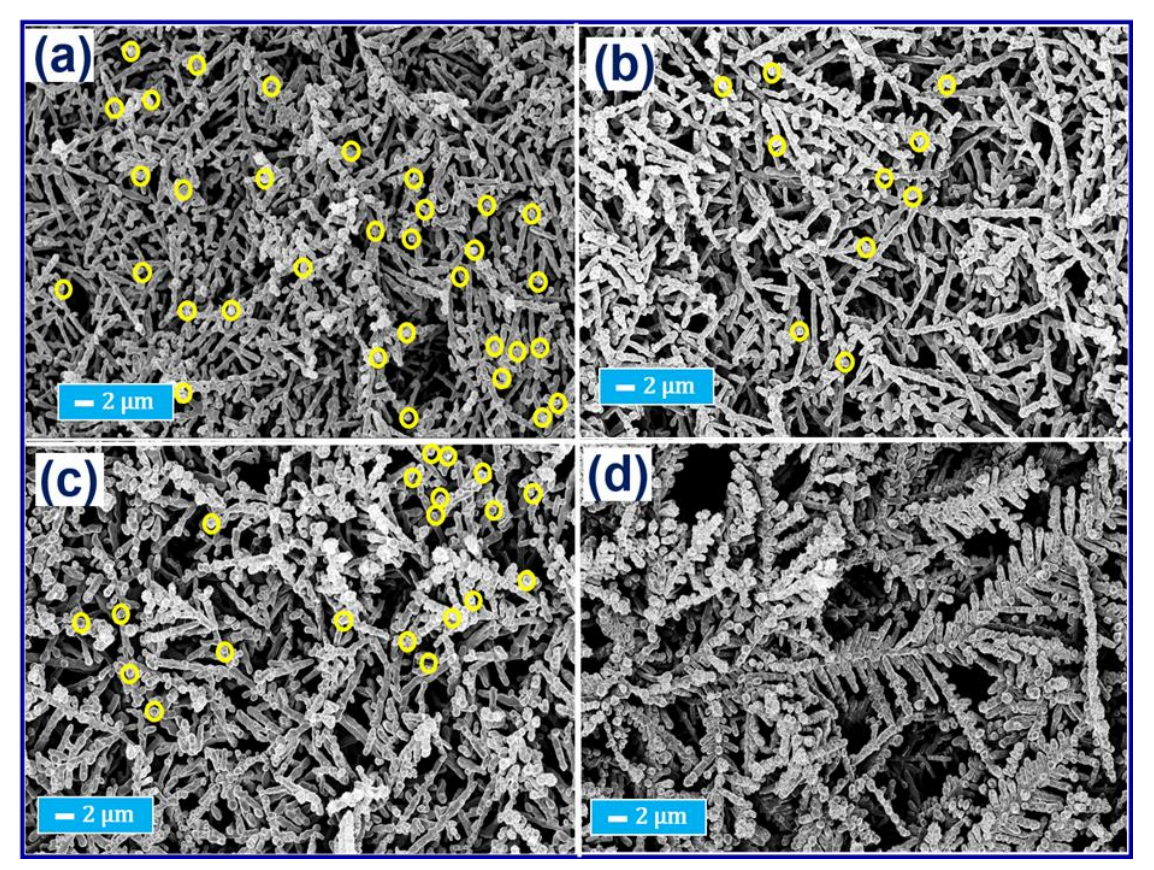


Figure 4.4: SEM images displaying morphology of the AgNDs decorated with 1 mM AuNPs at various times of deposition, a) 30 minutes (i.e., AuNPs@AgNDs-0.5), b) 1 hour (i.e., AuNPs@AgNDs-1), c) 2 hours (i.e., AuNPs@AgNDs-2) and, d) 3 hours (i.e., AuNPs@AgNDs-3) (highlighted yellow-coloured circles represent the AuNPs decoration on AgNDs at a few places for clarity).

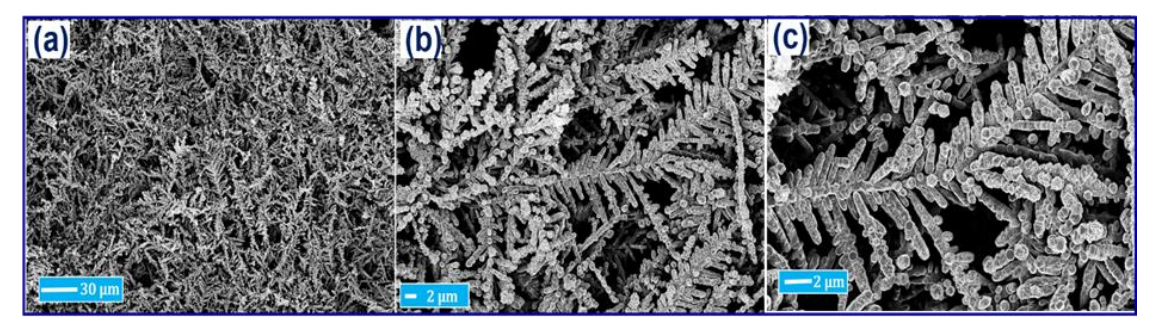


Figure 4.5: SEM images of the AuNPs (on AgNDs) decorated at 3 hours' reaction time (AuNPs deposited at 1 mM concentration) (i.e., AuNPs@AgNDs-3) viewed at different magnifications.

EDX mapping for the AuNPs@AgNDs-3 has been carried out in order to assess the distribution of nanostructures and their composition and is presented in figure 4.6.

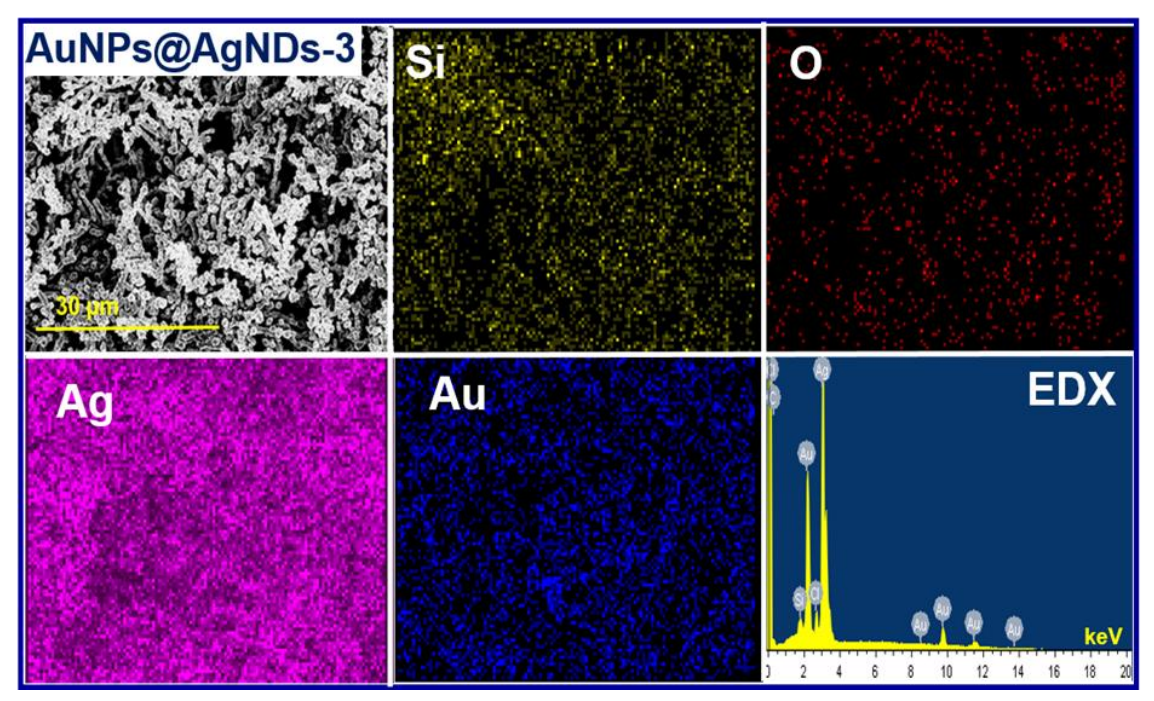


Figure 4.6: EDX mapping presents the elemental composition of the AuNPs@AgNDs-3 sample, which depicts a high concentration of Ag, Au, and Si, and a lower concentration of O as expected.

Figure 4.7 displays the reflection properties of silver nano-dendrites (AgNDs) and AgNDs coated with gold nanoparticles (AuNPs). It is evident that the reflection decreases as the deposition time of AuNPs on AgNDs increases, indicating a change in surface roughness. Through meticulous analysis of the reflection data, we have determined that the AuNPs@AgNDs-3 sample exhibits lower reflection properties at shorter wavelengths. In the case of anisotropic structures like AgNDs, both longitudinal and transverse surface plasmon resonance (SPR) bands are observed. The longitudinal band is typically at higher wavelengths compared to the transverse band in elongated structures. Specifically, in our study, the transverse mode corresponds to a wavelength of 426 nm, while the longitudinal mode corresponds to 696 nm in AgNDs [29] [30] [31]. The dip in the reflection spectrum is more pronounced for the longitudinal mode, indicating a higher degree of anisotropy. However, the dip at 464 nm is relatively weak and requires further investigation for accurate assignment. This peak could be attributed to variations in the sizes, shapes, and configurations of the AuNPs on AgNDs, which themselves exhibit diverse sizes and shapes. In previous studies, multiple resonance peaks were reported for silver-based fractal structures such as dendrites [32]. Similarly, the characteristics of AgNDs, dominated by branches with high aspect ratios, contribute to the observed longitudinal bands in the higher wavelength regions. The positions of the SPR bands correlate with the maximum electric field strength, which aids in selecting an appropriate excitation wavelength that provides better resonant conditions for SERS measurements on these active AgNDs-based substrates. In this study, an excitation wavelength of 532 nm was chosen based on these considerations.

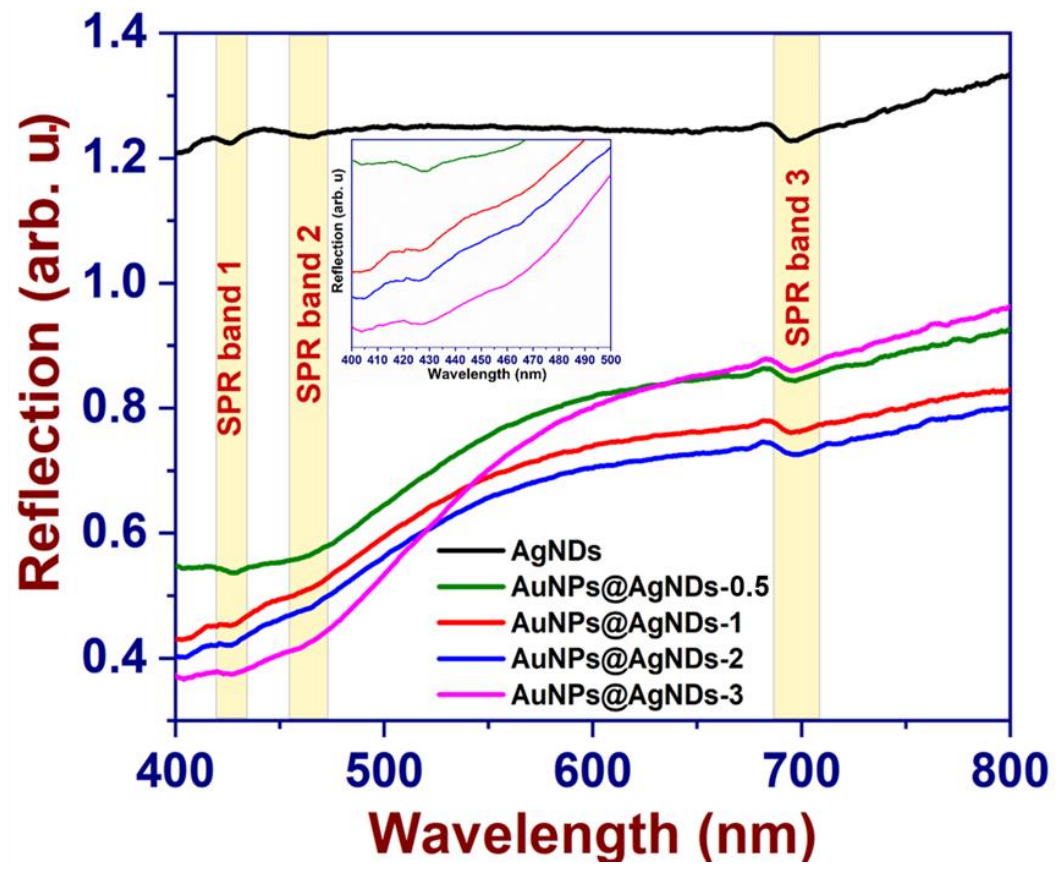


Figure 4.7: Reflectance spectra of AgNDs and AuNPs decorated AgNDs at various deposition times (inset shows the magnified SPR band 1 in 400-500 nm).

4.2.3. Application for Detection of Diverse Analytes

SERS activity serves as a crucial parameter for assessing the efficacy of SERS substrates. Consequently, we conducted a comprehensive evaluation of the SERS activity of AuNPs@AgNDs-3 substrates by utilizing various probing molecules such as dyes, explosives, DNA bases, and antibiotics. In the initial stage, to gauge the sensitivity and capability of the substrate, we employed a basic cationic dye molecule, namely crystal violet (CV). CV was chosen due to its strong absorption characteristics in the visible region under 532 nm laser excitation. Figure 4.8 a) illustrates the concentration-dependent plot (ranging from 10 μM to 1 nM) obtained on the active substrate, where the vibrational modes of CV were identified at 918 cm⁻¹ and 1181 cm⁻¹, following the literature [33]. A notable change in intensity was observed in the primary characteristic peak at 918 cm⁻¹, which demonstrated a gradual decrease with decreasing concentration, as expected. The

logarithm of intensity versus analyte concentration for the Raman mode at 918 cm⁻¹ exhibited a linear relationship with an R^2 value of 0.99, as depicted in figure 4.8 b). In addition to assessing the SERS activity of the substrate, it is essential to evaluate the degree of sensitivity by determining the analytical enhancement factor (AEF). The AEF is derived by incorporating the adsorption factor η , obtained from the intensity versus concentration plot, into the standard formula described in our earlier publications [34] [28]. For a concentration of 1 nM CV, the calculated AEF was approximately 3.2×10^7 , as shown in table 4.1.

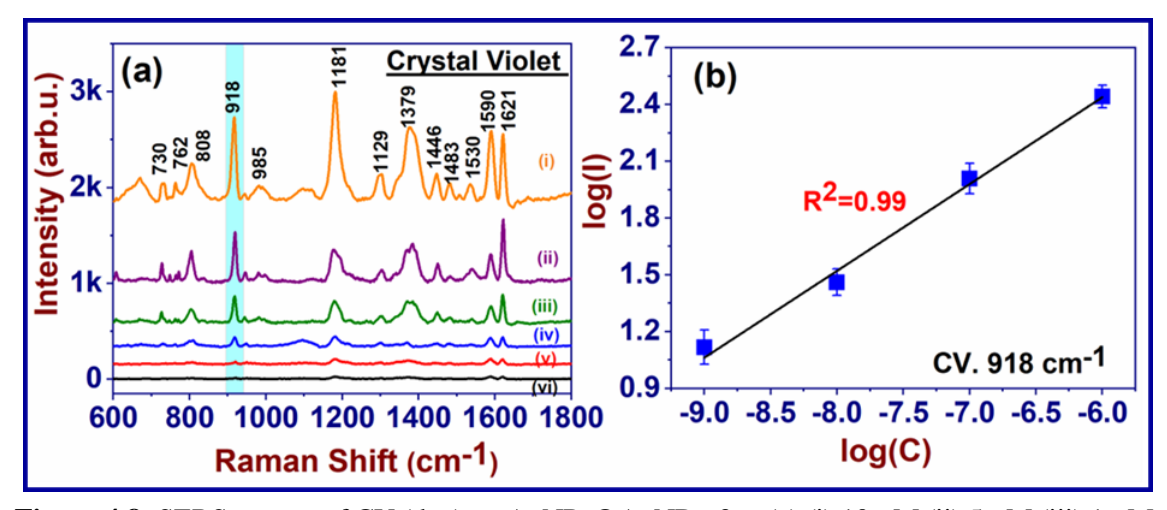


Figure 4.8: SERS spectra of CV (dye) on AuNPs@AgNDs-3 at (a) (i) $10 \,\mu\text{M}$ (ii) $5 \,\mu\text{M}$ (iii) $1 \,\mu\text{M}$, and (iv) $100 \,\text{nM}$ (v) $10 \,\text{nM}$ and (vi) $1 \,\text{nM}$ concentrations and (b) corresponding linear fit of log (intensity) versus log (lower concentration) of the $918 \,\text{cm}^{-1}$ Raman peak.

DNA bases play a fundamental role in the structure and function of DNA, which is the hereditary material in living organisms. The four DNA bases, adenine (A), thymine (T), cytosine (C), and guanine (G), are responsible for encoding genetic information. Detecting and analyzing DNA bases are of significant importance in various fields such as biomedical research, clinical diagnostics, forensic science, and environmental monitoring. The detection of DNA bases provides valuable insights into numerous biological processes and can aid in the identification of genetic mutations, disease markers, genetic relationships, and biodiversity. By understanding the variations and interactions of DNA bases, researchers can unravel genetic predispositions to diseases, develop personalized medicine approaches, and design targeted therapeutic interventions. DNA base detection also plays a crucial role in forensic investigations, enabling the identification of individuals and establishing relationships between individuals based on their genetic profiles. In recent years, SERS have emerged as powerful tools for DNA base detection. SERS offers several advantages, including high sensitivity, label-free detection, and multiplexing capabilities.

It allows for the detection of minute quantities of DNA bases, facilitating rapid and accurate analysis. Furthermore, SERS-based detection methods can be integrated with microfluidic systems, enabling high-throughput screening and miniaturization of analytical platforms. It opens doors to advancements in personalized medicine, genetic diagnostics, and forensic investigations. In this study we have detected two DNA bases, adenine and cytosine to demonstrate the potential of the AuNPs@AgNDs-3 substrates.

The SERS spectra of adenine were obtained with concentration ranging from 1 mM to 100 nM, as depicted in Figure 4.9 a). It is evident that the intensity values decrease as the concentration approaches trace levels. The Raman modes associated with adenine were identified at 534 cm⁻¹, 621 cm⁻¹, 722 cm⁻¹, 1125 cm⁻¹, 1246 cm⁻¹, 1330 cm⁻¹, and 1481 cm⁻¹ ¹, corresponding to adenine as identified with an earlier report [35]. Notably, the intensity of the characteristic peak at 722 cm⁻¹ remained observable even at lower concentrations. The relationship between the log intensity and analyte concentration for the specific Raman mode at 722 cm⁻¹ exhibited a linear dependence, with an R² value of 0.99, as illustrated in Figure 4.9 b). Furthermore, cytosine, another DNA base, was detected using the AgNDs@AuNPs-3 substrate. SERS spectra of cytosine were acquired with different solutions, ranging from 1 mM to 10 nM, as shown in Figure 4.9 c). The characteristic vibrational peaks of cytosine were identified at 604 cm⁻¹, 792 cm⁻¹, 1115 cm⁻¹, 1251 cm⁻¹, 1368 cm⁻¹, 1524 cm⁻¹, and 1641 cm⁻¹ as identified with the reference [36]. The specific mode at 792 cm⁻¹ exhibited a distinct peak even at lower detection levels, indicating the significant role of AuNPs-coated AgNDs in biomarker detection. The plot of log intensity versus analyte concentration for cytosine displayed linearity with an effective R² value of 0.99, as demonstrated in Figure 4.9 d). The calculated AEF for different concentrations of adenine and cytosine are listed in table 4.1. Specifically, the AEF for 100 nM adenine and 10 nM cytosine were estimated to be 1.7×10^6 and 8.1×10^6 , respectively.

The detection of antibiotics holds immense significance in various fields, including medicine, public health, and environmental monitoring. Antibiotics are crucial medications used to treat bacterial infections and have greatly improved human health by saving countless lives. However, the emergence of antibiotic resistance poses a significant challenge to effective treatment and necessitates the development of robust detection methods. The detection of antibiotics plays a vital role in clinical settings, enabling healthcare professionals to identify the presence of specific antibiotics in patient samples. This information helps guide appropriate treatment decisions, ensuring that patients

receive the most effective and targeted therapy. Timely and accurate detection of antibiotics can assist in determining the appropriate dosage and duration of treatment, minimizing the risk of adverse effects and optimizing patient outcomes.

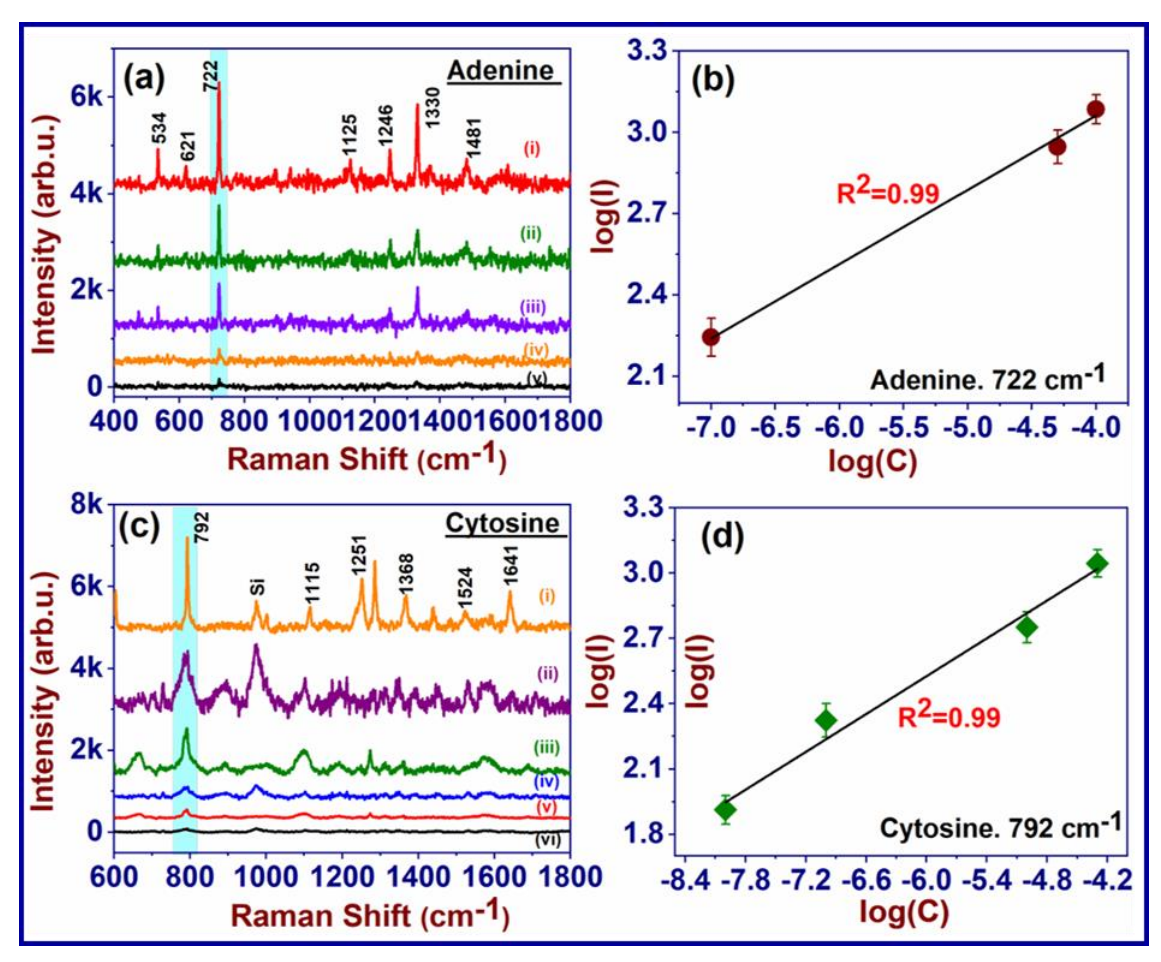


Figure 4.9: SERS spectra of adenine (DNA bases) on AuNPs@AgNDs-3 at (a) (i) 1 mM (ii) 100 μ M (iii) 50 μ M, and (iv)10 μ M, and (v) 100 nM concentrations, (b) corresponding linear fit of log (intensity) Versus log (lower concentration) of the 722 cm⁻¹ Raman peak, (c) Cytosine (i) 1 mM (ii) 100 μ M (iii) 50 μ M, and (iv) 10 μ M M, (v) 100 nM, and (vi) 10 nM concentrations, and (d) corresponding linear fit of log (intensity) versus log (lower concentration) of the 792 cm⁻¹ Raman peak.

Furthermore, the detection of antibiotics is essential in monitoring and controlling the spread of antibiotic resistance. Antibiotic-resistant bacteria pose a serious threat to public health, as they can cause infections that are difficult to treat and may lead to increased morbidity and mortality. By detecting antibiotics in environmental samples, such as water sources and agricultural systems, scientists can assess the extent of antibiotic pollution and its impact on the development of antibiotic resistance in bacteria. This information is crucial for implementing strategies to mitigate the spread of resistance and preserve the effectiveness of antibiotics. Detection of antibiotics also plays a pivotal role in food safety and quality control. Antibiotics are commonly used in animal husbandry and aquaculture

to prevent and treat bacterial infections. However, the presence of antibiotics in food products beyond acceptable levels can have adverse effects on consumer health. Detecting antibiotics in food samples helps ensure compliance with regulatory standards, protects consumers from potential health risks, and maintains the integrity of the food supply chain. Here, we have detected three antibiotics, namely penicillin, kanamycin and ampicillin as a proof of the concept, in order to establish the capability of our substrates in antibiotic detection. The substrates have demonstrated as sensitivity of 10 nM, 100 nM and 10 nM for the three analyte molecules, respectively, as shown in the figure 4.10 demonstrating trace detection. The prominent peaks of each of the molecule were identified using the references [37] [38] [39].

Further, these substrates also demonstrated promising performance for the detection of trace explosives and pesticides. Ammonium nitrate and thiram were chosen as model molecules for demonstrating because they are the commonly used explosive and pesticide molecules. Based on our previous analysis of SERS data on AN [28], we have determined that the AuNPs@AgNDs-3 substrate exhibits approximately a 40% increase in Raman intensity compared to simple AgNDs at a concentration of 10 μ M as shown in figure 4.11. This enhancement in intensity is primarily attributed to the improved stability of AgNDs after the deposition of AuNPs, which reduces natural oxidation effects. Additionally, the cooperative effect of both AuNDs and AuNPs contributes to the observed enhancement. Furthermore, our investigations have extended to the detection of trace amounts of thiram, a common pesticide in food safety [40].

Table 4.1: Summary of analytes detected and SERS parameter for AuNPs@AgNDs.

Analyte	Peak [cm ⁻¹]	Lowest	AEF	LOD
		Detected		
Thiram	1384	10 nM	1.1×10^6	2 nM
AN	1045	100 nM	5.0×10^5	5 nM
Ampicillin	988	10 nM	7.2×10^6	4 nM
Kanamycin	975	100 nM	2.8×10^5	56 nM
Penicillin-G	985	10 nM	5.4×10^6	2 nM
Cytosine	792	10 nM	8.1×10^6	28 nM
Adenine	722	100 nM	1.7×10^6	2 nM
Crystal violet	918	1 nM	3.2×10^7	348 pM

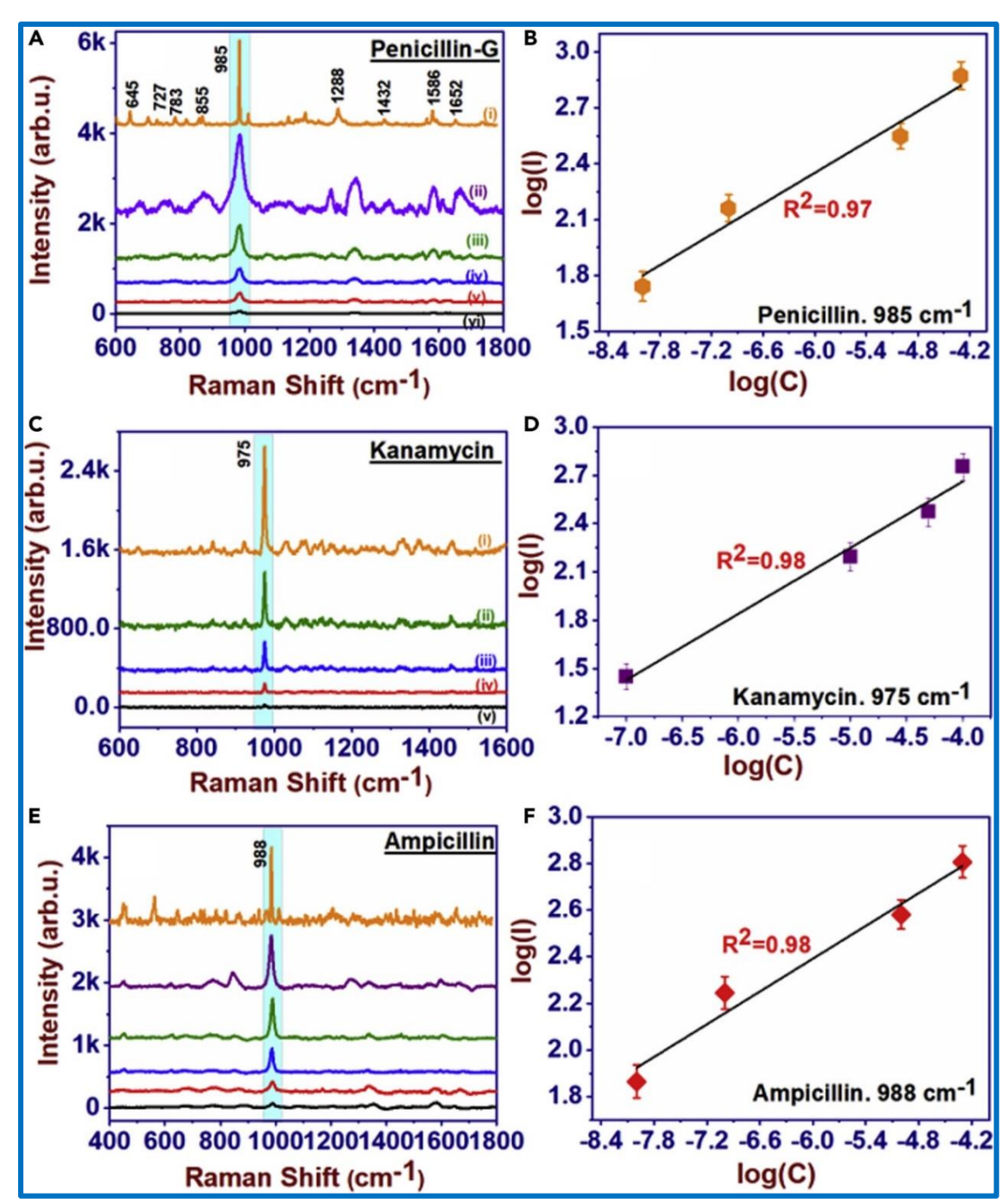


Figure 4.10: SERS spectra of penicillin G on AuNPs@AgNDs-3 at (a) (i) 1 mM (ii) 100 μM (iii) 50 μM, and (iv) 10 μM M, (v) 100 nM, and (vi) 10 nM concentrations, and (b) corresponding linear fit of log (intensity) vs log (lower concentration) of the 985 cm⁻¹ Raman peak (c) Kanamycin (i) 1 mM (ii) 100 μM (iii) 50 μM, and (iv)10 μM, and (v) 100 nM concentrations, and (d) corresponding linear fit of log (intensity) vs log (lower concentration) of the 975 cm⁻¹ peak, (e) Ampicillin (i) 1mM (ii) 100 μM (iii) 50 μM, and (iv)10 μM, (v) 100 nM, and (vi) 10 nM concentrations, and (f) corresponding linear fit of log (intensity) versus log (lower concentration) of the 988 cm⁻¹ peak.

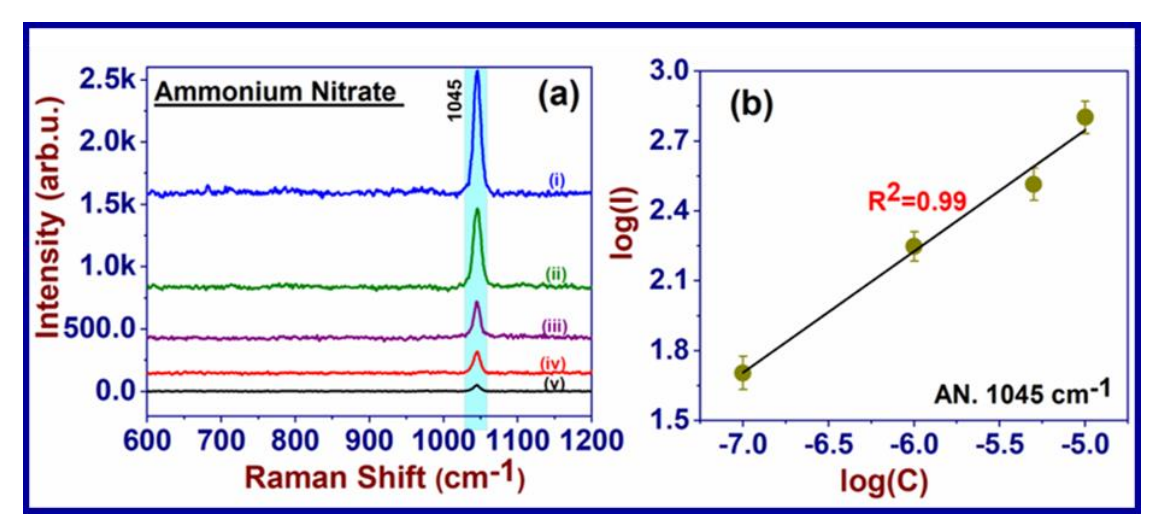


Figure 4.11: SERS spectra of AN (explosive) on AuNPs@AgNDs-3 at (a) (i) 50 μ M (ii) 10 μ M (iii) 5 μ M, and (iv) 1 μ M, and (v) 100 nM concentrations, and (b) corresponding linear fit of log (intensity) versus log (lower concentration) of the 1045 cm⁻¹ Raman peak.

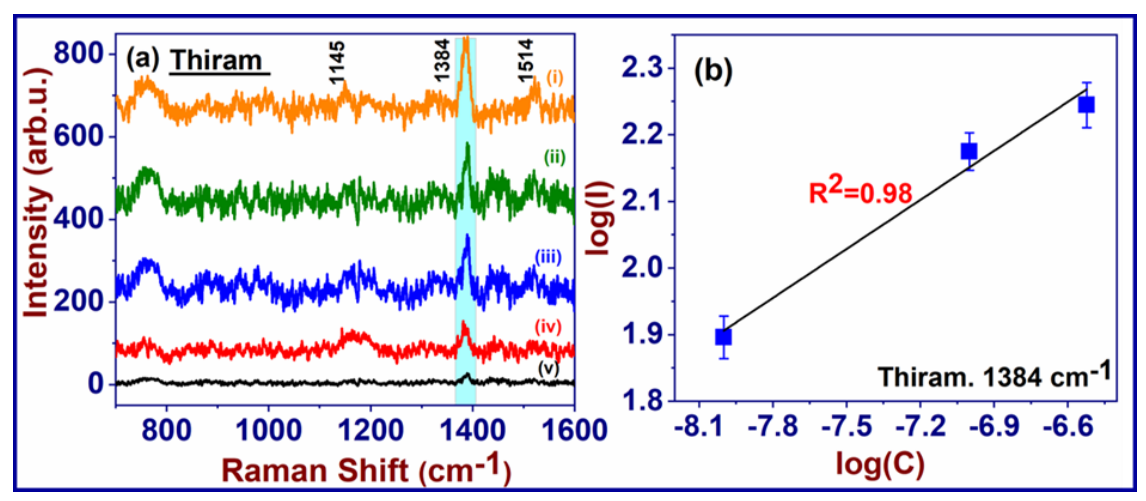


Figure 4.12. SERS spectra of thiram (pesticide) on AuNPs@AgNDs-3 at (a) (i) $10 \mu M$, (ii) $5 \mu M$, (iii) 300 nM, (iv)100 nM, and (v) 10 nM concentrations, and (b) corresponding linear fit of log (intensity) versus log (lower concentration) of the 1384 cm^{-1} Raman peak.

Figure 4.12 represents SERS spectra for thiram of different concentrations collected using the AuNPs@AgNDs-3 showing a sensitivity of 10 nM and AEF for the same was estimated to be 1.1×10^6 for 10 nM concentration. The durability and reproducibility of the substrates has been studied using CV and cytosine as the probe molecules. The results as indicated in figure 4.13 communicates that the substrates offer a decent reproducibility with RSD less than 9% for both the molecules indicating practical usage. The durability of the substrates measured at regular intervals for CV of 5 μ M is presented in figure 4.13. The intensity of the 918 cm⁻¹ peak indicates that the samples have a shelf life of nearly 120

days in ambient conditions. The durability can further be improved by storing them in vacuum conditions.

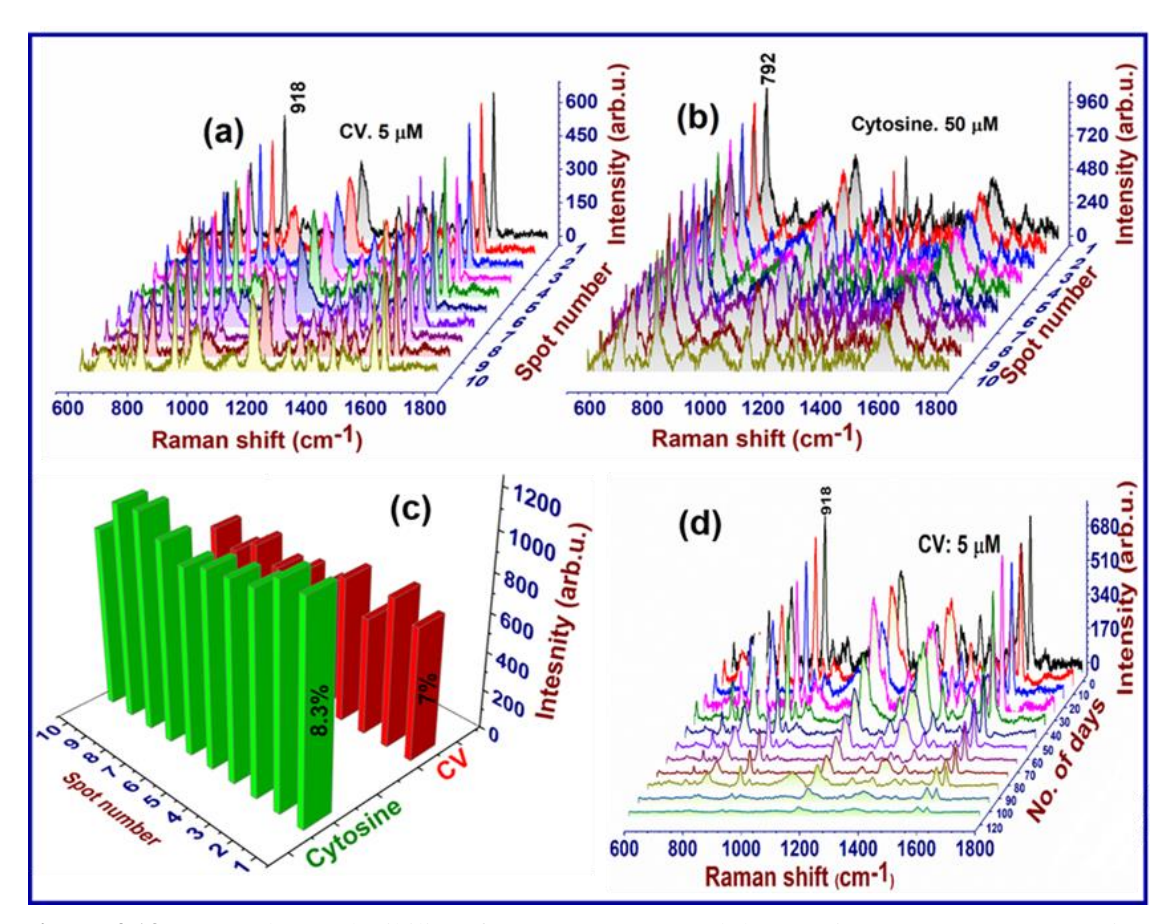


Figure 4.13: Spectral reproducibility of (a) CV at 5 μ M, and (b) cytosine at 50 μ M concentrations, (c) corresponding histogram with RSD values, (d) Stability estimation of AuNPs@AgNDs-3 substrate at 5 μ M CV over 120 days.

Raman mapping was conducted on CV at a selected area of 45×45 μm² with 4 μm spacing using a 10X microscope objective. Approximately 120 SERS spectra were collected from the sample for mapping, as shown in figures 4.14 a)-c). The relative standard deviation (RSD) of the 80 selected spectra from the mapping data in figure 4.14 b) was found to be <5%, while for the 170 selected spectra, the RSD was <7%, as depicted in figure 4.14 c). The acquisition time was set to 3 seconds with 3 spectra averaged at each point. Furthermore, a smaller area Raman mapping was performed within a 20×20 μm² region with a spacing of approximately 1.5 μm, resulting in the collection of around 200 spectra. Color maps were generated to represent the SERS intensities across the mapping area for the CV mode at 918 cm⁻¹, corresponding to ring skeletal vibrations [41]. The color scale reflects the intensity counts for each mode. The color maps generally displayed a uniform distribution across the majority of the mapping area, except for small regions resembling islands. This variation can be attributed to the presence of high-density hotspots in certain

parts of the sample, influenced by the distribution of AgNPs on AgNDs and the overlapping of AgNDs observed in the FESEM images. Signal variations will also arise from non-uniform adsorption of the analyte on the substrate, molecular orientation, coupling with nanoparticles and the laser, as well as the distance between molecules and hotspots. It is pertinent to note that the signal collection during mapping was performed on a single plane and not from the highest signal plane of the substrate. These three-dimensional anisotropic dendrites, along with the positioning of AgNDs and AuNPs, contribute to the overall Raman signal.

Improvements can be made by implementing automated Z-axis scanning for autofocus and collecting the best Raman signal from each point. Although this approach would reduce the RSD value, it would increase the scanning time. Another consideration is to enhance the enhancement factors by 3-4 times, rendering the relatively higher RSD values insignificant due to the overall higher enhancements. Notably, the Raman signal deviation is relatively lower in small area mapping. Similar mapping studies were conducted for cytosine at a concentration of 10 µM, focusing on the 792 cm⁻¹ peak. Mapping regions of $100\times100 \ \mu\text{m}^2$ and $20\times20 \ \mu\text{m}^2$ are depicted in figures 4.14 d)-f). Figure 4.14 a) demonstrates better reproducibility for CV with large area Raman mapping (40×40 µm²). However, slightly inferior reproducibility is observed for the 20×20 µm² region [figure 4.14 b)], likely due to overlapping of the collection area throughout the region, leading to potential photodegradation effects in the dye and subsequently reducing the Raman signal. Figure 4.14 f) presents the Raman mapping data for cytosine under the same conditions, exhibiting improved reproducibility compared to the dye. Therefore, it is hypothesized that the lower reproducibility observed for the dye is potentially attributed to laser-induced effects caused by the overlap in the collection area.

The reproducibility during mapping can be increased significantly by working with low powers that would prevent the sample degradation. Selecting a specific peak of interest instead of a full range measurement could also reduce the duration of exposure of the sample to the laser. A detailed protocol on approaching SERS mapping has been provided for these samples in our earlier report [26].

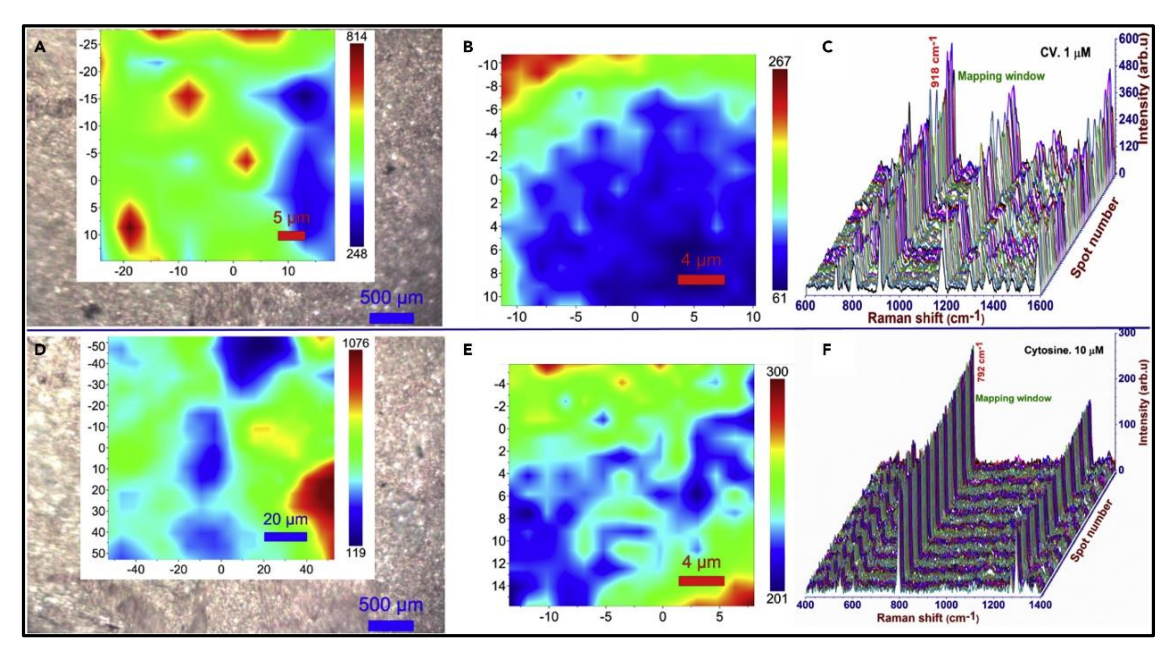


Figure 4.14: (a) Selected large-area Raman mapping $(45 \times 45 \ \mu m^2)$ of SERS substrate with 532 nm laser excitation, 10X microscope objective, 25 mW laser power with CV as probe molecule for 918 cm⁻¹ Raman mode with 3s acquisition time, averaged over 3 spectra (b) Small area $(20 \times 20 \ \mu m^2)$ SERS mapping of CV (c) corresponding representative spectra of the mapping region, (d) Selected large-area Raman mapping $(100 \times 100 \ \mu m^2)$ - cytosine as the probe molecule for the 792 cm⁻¹ Raman mode [with similar acquisition parameters mentioned in (a)] (e) Small area $(20 \times 20 \ \mu m^2)$ SERS mapping of 10 μ M cytosine (f) Corresponding representative spectra of the mapping region [presented in (e)]. The background (grey color) in (a) and (d) depicts the optical microscope images of the substrates.

4.3. 2-D, Hybrid SERS Substrates

2D materials, such as MoS2, h-BN, and graphene have gained significant attention as SERS substrates due to their unique properties and potential applications. These materials exhibit several advantages that make them valuable for enhancing Raman signals and improving the sensitivity of molecular detection. One key advantage of 2D materials is their large surface area-to-volume ratio owing to their atomically thin layers with a high density of edges and defects, which can provide numerous active sites for the adsorption of target molecules. This high surface area allows for efficient interaction between the analyte molecules and the substrate, leading to enhanced Raman signals. Furthermore, the electronic properties of 2D materials contribute to their SERS activity. MoS2 and GO possess unique band structures, including bandgaps, which can facilitate charge transfer processes and enhance the local electromagnetic field near the molecules of interest. This effect is particularly prominent in the presence of plasmonic nanoparticles or other metal structures, leading to increased Raman signal amplification. Another advantage of 2D

materials is their chemical tunability. Functionalization and doping of these materials can be achieved by introducing various chemical groups, such as metal ions or organic molecules. These modifications can enhance the interaction between the analyte molecules and the substrate, resulting in improved SERS performance. Additionally, the surface chemistry of 2D materials can be tailored to selectively capture specific analytes, enabling highly sensitive and selective detection. Using a combination of laser ablation (for preparation of MoS₂) and wet etching of Si, we have fabricated a highly durable and sensitive SERS substrate as represented in figure 4.15.

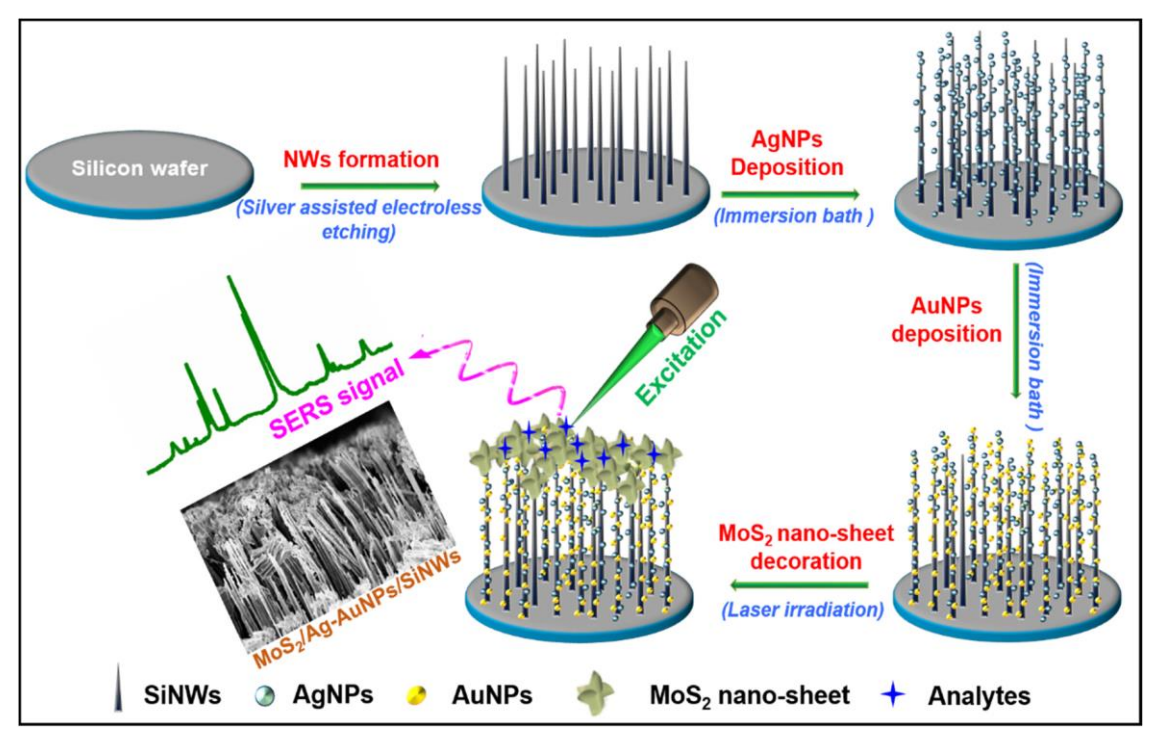


Figure 4.15: Schematic of application of MoS2 decorated plasmonic SiNWs for SERS based sensing.

4.3.1. Preparation and Characterization

In this study, we prepared vertically aligned silicon nanowires (SiNWs) through a Silver Assisted Electroless (SAE) etching method using p-type, boron-doped, (100) oriented Si wafers with a resistivity of 1-10 Ω -cm. The detailed cleaning and SAE process protocol can be found in our previous investigations [42]. To summarize, the Si wafers were thoroughly cleaned with acetone and ethanol to eliminate any chemical contaminants. Subsequently, the wafers were immersed in a 10% HF solution to remove the native oxide layer. The SAE process consisted of two consecutive steps: silver deposition and etching. Silver deposition involved dipping the Si wafer in a mixture of 0.02 M AgNO₃ and 4.6 M HF for 2 minutes. The Ag-deposited Si wafer was then immersed in an etching solution of

14.1 M HF and 1.9 M H₂O₂ at 60 0C for 30 minutes. Afterward, the Ag dendrites on the NWs surface were dissolved by sonicating with a 1:3 ratio of H₂O₂ to NH₄OH solution for 5 minutes. The resulting vertically aligned SiNWs were thoroughly rinsed with deionized water and dried with nitrogen gas to ensure a chemical-free substrate. In addition, we decorated Ag and Au nanoparticles onto the SiNWs using a simple immersion bath method [43]. Initially, the SiNWs were immersed in a solution of 5 mM AgNO₃ at 40^oC for 2 minutes to decorate AgNPs. Subsequently, the AgNPs-decorated SiNWs were immersed in a HAuCl₄ solution with a concentration of 4 mM at 50 ⁰C for 1 minute to achieve a better distribution of AuNPs in conjunction with AgNPs. Furthermore, ultra-pure MoS₂ micro-powder was irradiated using a femtosecond laser with a pulse duration of 50fs and a wavelength of 800 nm in different solvent environments such as ethanol, methanol, and water. Prior to ablation, 0.3g of MoS₂ powder was dissolved in 3 mL of solvent and sonicated. The laser beam was steered using reflective mirrors and focused in a glass beaker for irradiation. To maintain homogeneity and prevent particle settling, the solution was continuously stirred using a magnetic stirrer at 400 rpm. The laser power was controlled using a combination of a Brewster window and a half-wave plate, and a laser energy of 1.5 mJ was utilized. The irradiation time was set to 40 minutes, during which a noticeable color change occurred in the MoS₂ solution. Following careful observation of FESEM images as shown in figure 4.16, the resulting MoS₂ nanosheets obtained in a water environment were drop-casted onto the Ag-AuNPs/SiNWs structure to create a functional hybrid SERS-active substrate (MoS2/Ag-AuNPs/SiNWs). Additional data were obtained by conducting UV-Visible absorption spectra analysis of MoS₂ in different solvents, as depicted in Figure 4.16 d). The combination of plasmonic nanoparticles and MoS₂ sheets on SiNWs generated an effective SERS signal through the synergistic effect of electromagnetic and chemical mechanism mechanisms.

The study included field emission scanning electron microscopy investigations to unveil the morphological changes. As depicted in Figure 4.17, a distinct structure of SiNWs decorated with Ag-AuNPs is observed. The SiNWs exhibit estimated diameters ranging from 250 to 350 nm, with heights measuring approximately 11-12 µm. Notably, Figures 4.17 a) and 4.17 b) demonstrate a pronounced accumulation of Ag-AuNPs at the tips of the SiNWs. This observation suggests that the energy conditions at the NW tips are highly conducive to the reduction of Ag and Au ions during the immersion bath process.

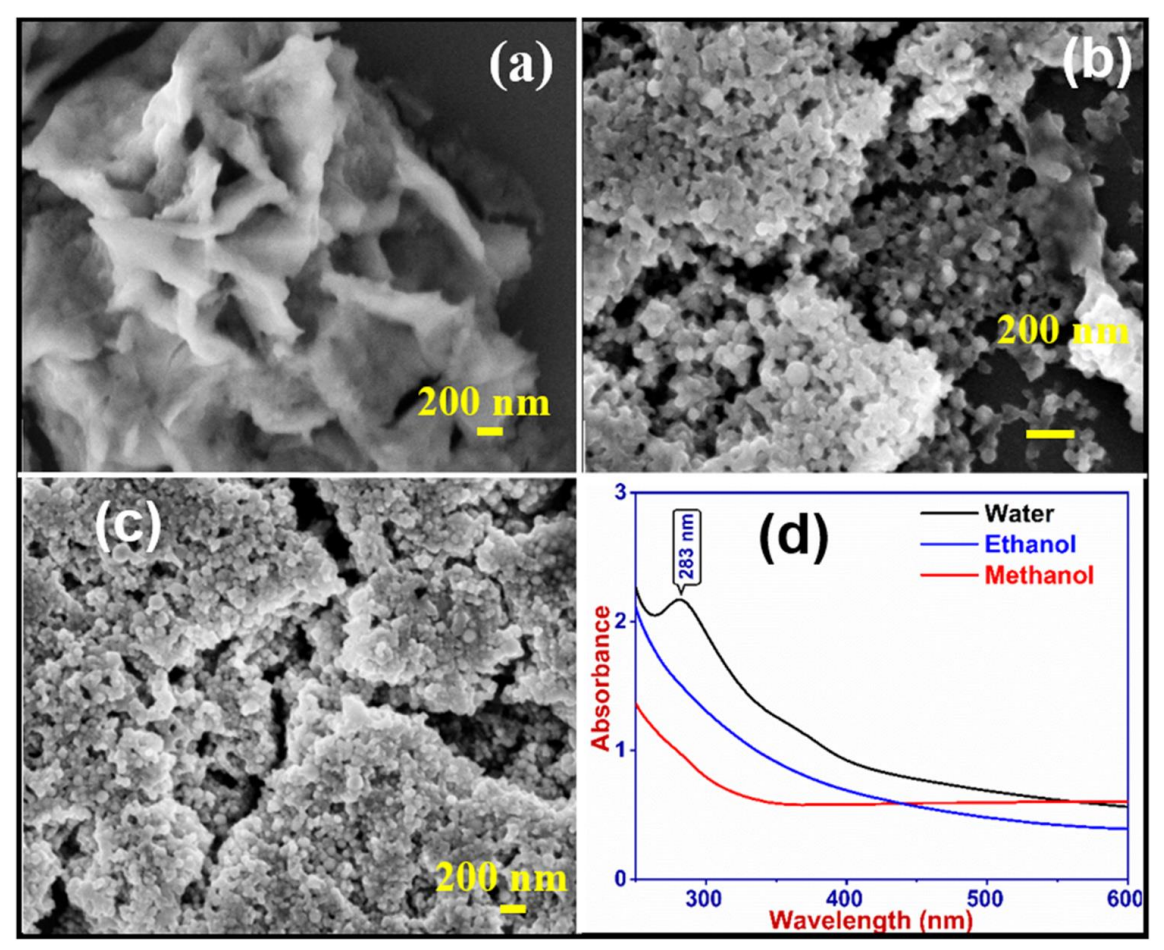


Figure 4.16: FESEM images of laser-irradiated MoS₂ in different liquid environments (a) Water, (b) Ethanol, (c) Methanol, and (d) Corresponding absorption spectra.

Moreover, Figures 4.17 d) and 4.17 e) clearly illustrate the uniform distribution of AgNPs and Ag-AuNPs along the walls of the SiNWs, respectively. These images confirm that the distribution of Ag-AuNPs on the vertically aligned SiNW walls is highly favourable for the generation of hotspots. Enhancements in the stability and sensitivity of Ag-AuNPs on SiNWs were achieved through the incorporation of MoS₂ nano-sheets as protective caps. Notably, MoS₂ synthesized in a water environment exhibited a prominent resonance band at approximately 300 nm. Subsequently, the as-prepared MoS₂ nano-sheets were carefully applied onto the Ag-AuNPs/SiNWs structure to create a hybrid SERS substrate, and the resulting morphology is illustrated in Figure 4.17 c). Elemental compositions of MoS₂-coated Ag-AuNPs@SiNWs were confirmed through EDS analysis, as demonstrated in Figure 4.17 f). The examination revealed prominent peaks corresponding to Si and Ag, indicating the presence of SiNWs and AgNPs, respectively.

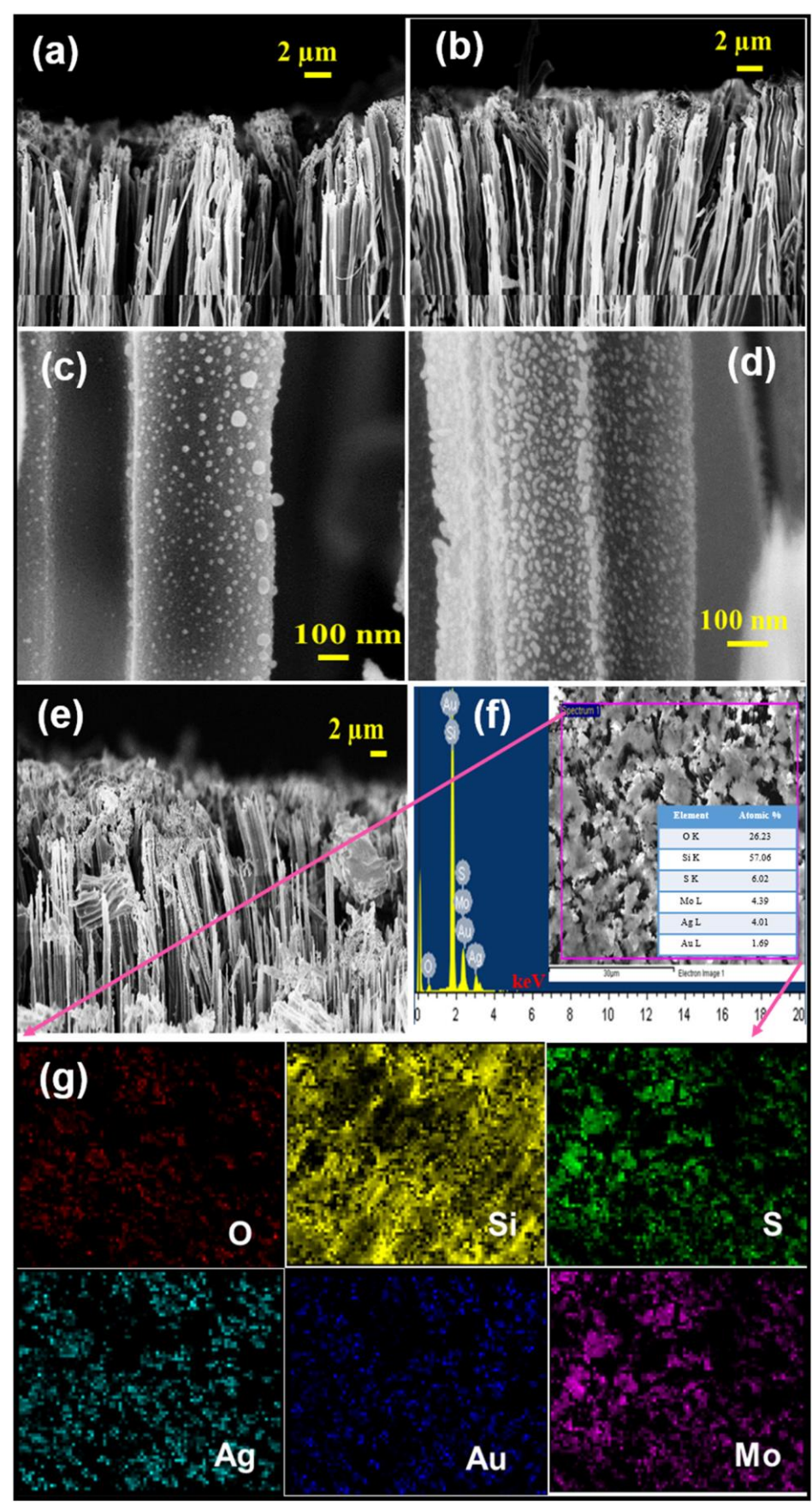


Figure 4.17: FESEM image of (a) AgNPs decorated SiNWs, (b) Ag-AuNPs decorated SiNWs, (c) MoS2 coated Ag-AuNPs/SiNWs, (d-e) higher magnifications of (b and c) images respectively, and (f) EDS spectrum of figure (c).

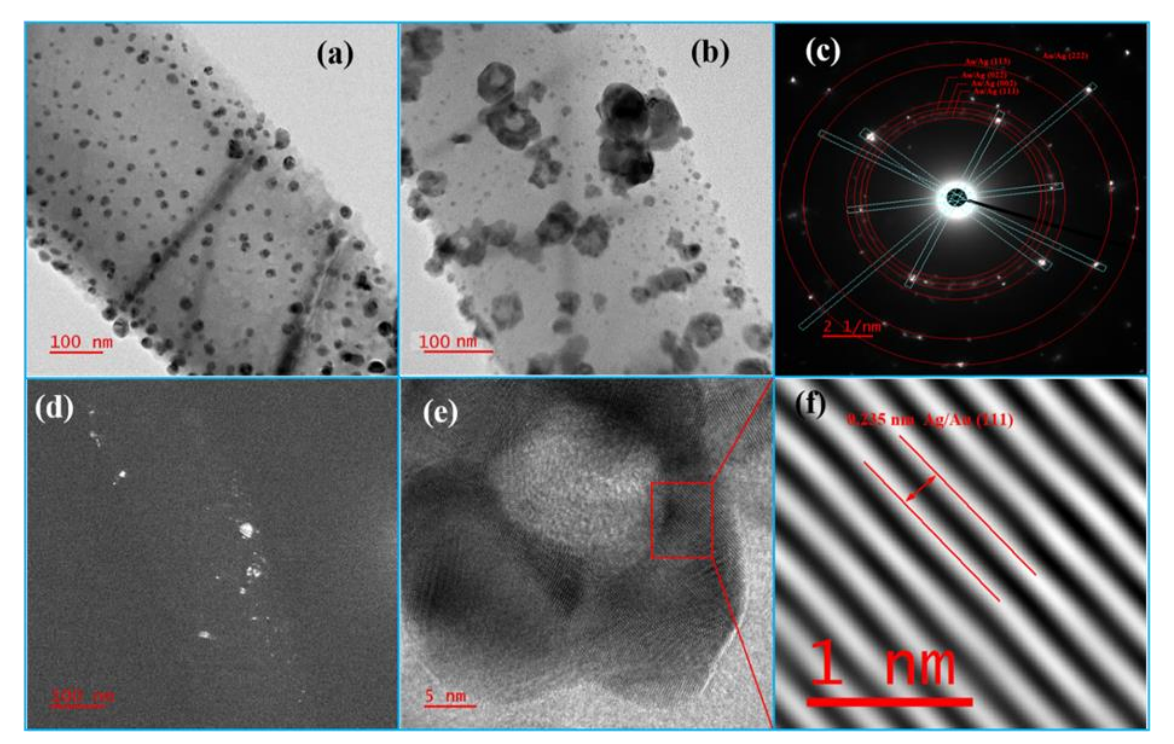


Figure 4.18: Bright-field images of (a) AgNPs distributed on the walls of SiNWs, (b) Ag-AuNPs distributed on the walls of SiNWs (c) SAED pattern of figure (b), (d) Dark-filed image of figure (b), (e) HRTEM image and the red rectangular line directs the area of selection for IFFT, and (f) IFFT data obtained from a selected area of figure (e).

Additionally, Au peaks were observed, indicating the presence of AuNPs. Furthermore, small amounts of oxygen, sulphur, and molybdenum were detected, which can be attributed to the presence of MoS₂ nano-sheets. The distribution of bimetallic (Ag-Au) nanoparticles (NPs) on vertically aligned SiNWs is revealed through TEM imaging, as depicted in Figure 4.18. The TEM images in Figure 14.8 a) and figure 4.18 b) exhibit the distribution of AgNPs and Ag-AuNPs on the walls of SiNWs, respectively. The average sizes of AgNPs and AuNPs are estimated to be approximately \sim 12 \pm 0.4 nm and \sim 20 \pm 0.6 nm, respectively, dispersed over the NW walls. Notably, the inter-particle separations between AgNPs and AuNPs are measured to be 17 nm and 23 nm, respectively, indicating a rapid enhancement in signal strength. The Selective Area Electron Diffraction (SAED) pattern displayed in Figure 4.18 c) and the corresponding dark-field image shown in Figure 4.18 d) provide authentic information about the distribution of AgNPs and AuNPs. Furthermore, Figure 4.18 f) presents a high-resolution TEM image along with the corresponding Inverse Fast Fourier Transform (IFFT) image of the bi-metallic NPs decorated SiNWs. The IFFT is derived from the region of interest highlighted by the red rectangular line in Figure 4.18 e). By analyzing the IFFT image, a d-spacing of 0.235 nm

is extracted for Ag (111)/Au (111), which corresponds to the JCPDS card No.98-005-0882.

4.3.2. SERS Measurements

The SERS measurements were performed using the advanced Horiba LabRam HR evolution Raman system, employing a 532 nm laser for excitation. To ensure precise data collection, a 50 × microscopic objective was utilized to focus the collection area. The study maintained a consistent laser power of 10 mW and an acquisition time of 5 seconds for all measurements. In evaluating the performance of the SERS substrate, parameters such as versatility, reproducibility, and durability played vital roles.

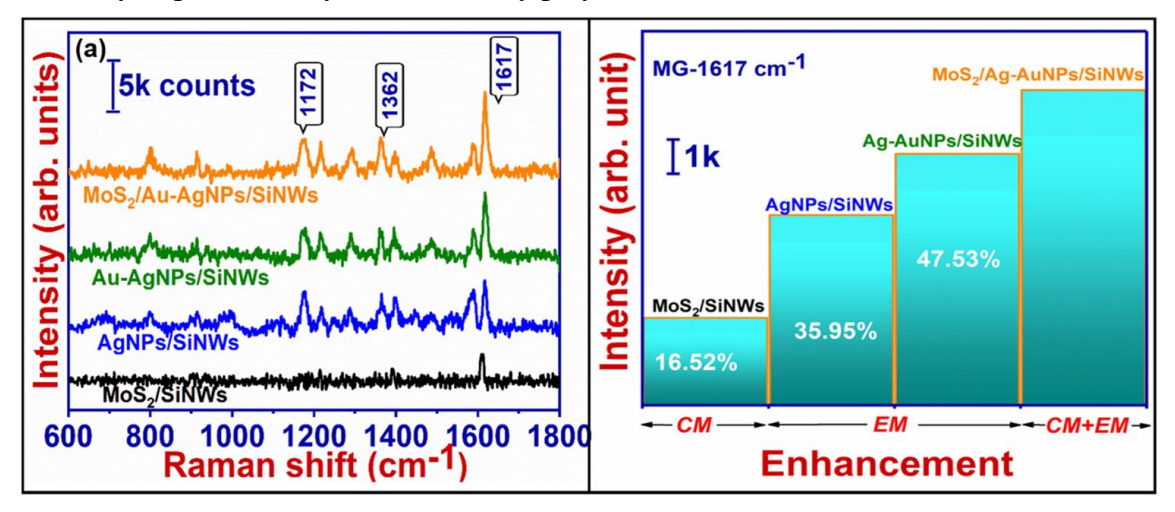


Figure 4.19: (a) SERS signal sensitivities of MG detected on various SERS-active substrates indicating signal enhancement at each stage (the spectra are shifted for clarity) (b) Bar-chart showing the quantitative CM and EM enhancements of MG detection [data has been taken from Fig. 4.19 a)].

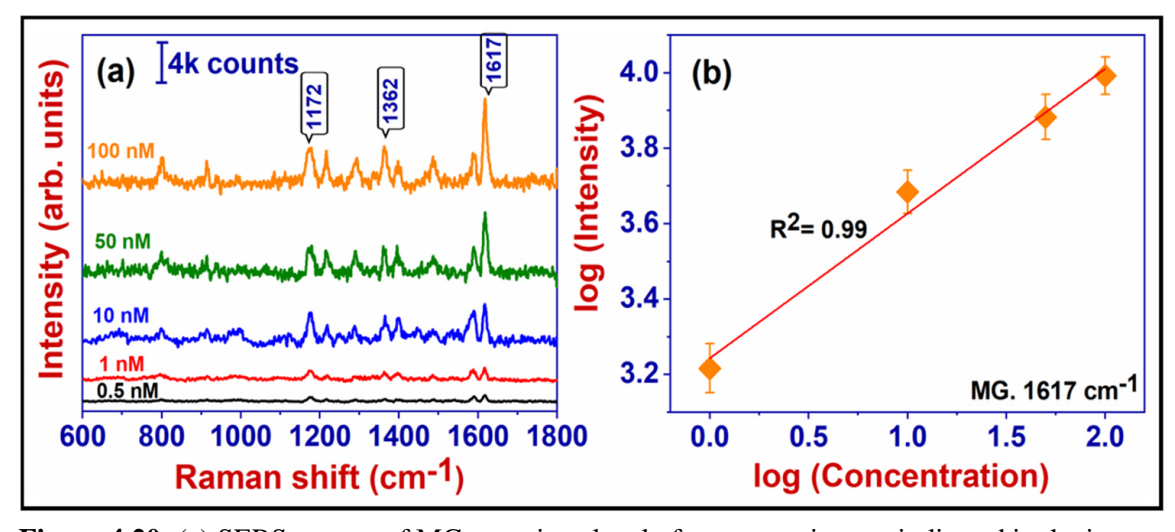


Figure 4.20: (a) SERS spectra of MG at various level of concentrations as indicated in the image, and (b) linear plot of log(concentration) vs log(intensity) of the peak 1617 cm⁻¹.

The distinct peak corresponding to MG at 1617 cm⁻¹ exhibits a noticeable change in intensity when comparing the Ag-AuNPs/SiNWs substrate to the mono-metallic (AgNPs/SiNWs) substrate as shown in figure 4.19. Additionally, the Raman strength of individual MoS₂ nano-sheets (NSs) on SiNWs shows a nominal intensity for the MG peak at 1617 cm⁻¹. However, upon incorporating the MoS₂ NSs onto the Ag-AuNPs/SiNWs substrate, we observed approximately a two-fold enhancement compared to the monometallic substrate. This enhancement can be attributed to the synergistic effect of electromagnetic interactions from Ag-Au bimetallic NPs and charge transfer mechanisms from MoS₂. The combination of these effects leads to a strong electric field generation at the hot-spot regions when subjected to laser excitation and studied in detail for MG and presented in figure 4.20. Furthermore, Figure 4.19 b) presents a bar chart displaying quantitative variations in intensity observed at different stages of substrate design. This statistical data highlights the significance of incorporating 2D materials onto the Ag-AuNPs/SiNWs substrate and their consequential impact on signal enhancements. The extent of these enhancements may vary depending on the specific analyte being studied.

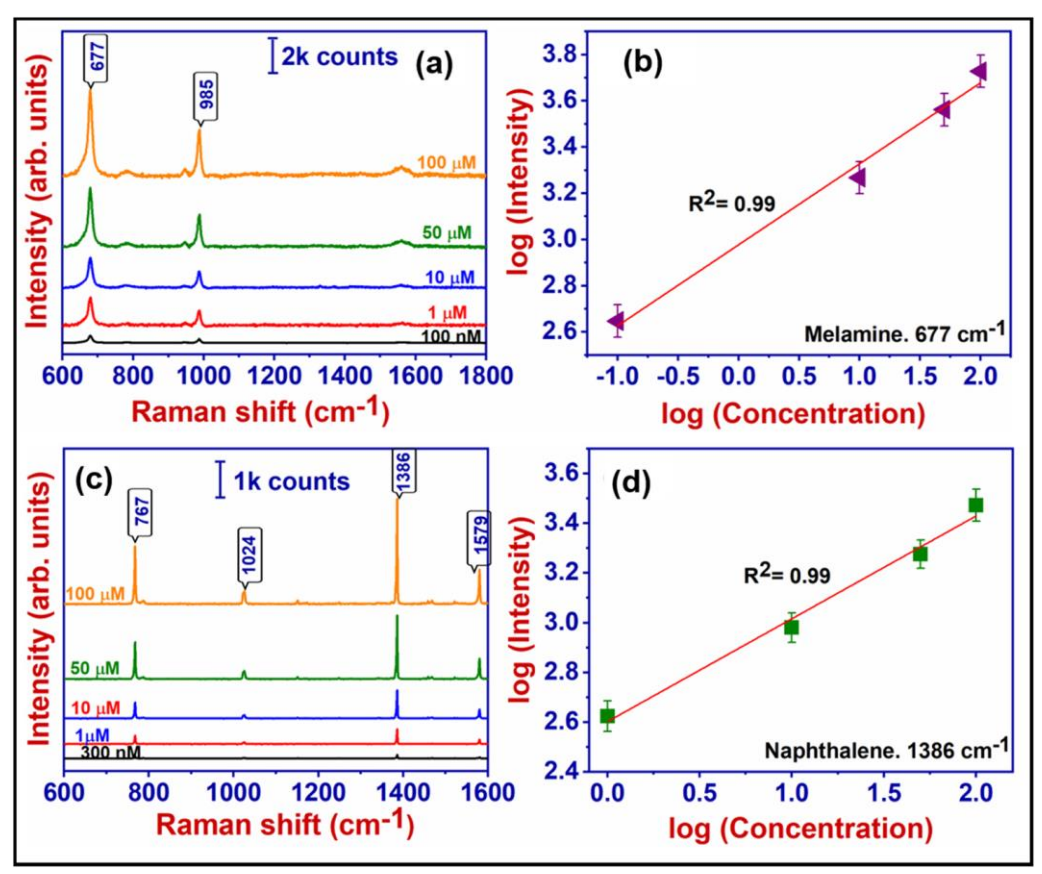


Figure 4.21: (a) SERS spectra of melamine at various concentrations (spectra are shifted for clarity) (b) Linear plot of log (intensity) versus log (concentration) of the peak at 677 cm⁻¹ (c) SERS spectra of naphthalene at various concentrations as indicated in the Fig. (spectra are shifted for clarity) and (d) Linear plot of log (intensity) versus log (conc.) of the peak at 1386 cm⁻¹.

The detection of naphthalene is important for several reasons. Naphthalene is a volatile organic compound (VOC) commonly found in various products such as mothballs, cleaning agents, and pesticides. It is also released during the combustion of fossil fuels and tobacco smoking. One significant reason for detecting naphthalene is its potential health hazards. Prolonged exposure to naphthalene vapours or ingestion of naphthalenecontaining substances can have adverse effects on human health. It is classified as a possible human carcinogen by several regulatory agencies, and long-term exposure has been linked to the development of lung and urinary tract cancers. Furthermore, naphthalene exposure can cause other health issues, such as respiratory problems, eye and skin irritation, and damage to the liver and kidneys. Another important aspect of naphthalene detection relates to environmental concerns. Naphthalene is released into the atmosphere through industrial processes, vehicle emissions, and burning of fossil fuels. It contributes to air pollution and can react with other pollutants to form secondary pollutants, including ozone and particulate matter, which have detrimental effects on air quality and human health. Efficient detection of naphthalene is crucial for monitoring and controlling its presence in indoor and outdoor environments and had been successfully demonstrated with our samples as shown in figure 4.21. The important peaks of naphthalene were identified with respect to reference [44] and detected with a sensitivity of 300 nM. Similar studies were carried out on melamine which is a common food adulterant and achieved a sensitivity of 100 nM which is lower than the reported value so far.

Three biomolecules, bovine serum albumin (BSA), cysteine and adenine were also detected with our samples establishing their versatility. The reported sensitivity for these molecules with our hybrid substrates is 100 nM for each analyte as represented in figure 4.22. The peaks were identified using the references [45][46]. The utilization of SERS has garnered significant attention in the realm of bacteria and microorganism detection [47]. One particular microorganism of concern is E. coli, a common contaminant in food and water that poses health risks. The rod-shaped E. coli cell from the B1121 bacterial strain, which is frequently employed in molecular biology, features a diameter of less than a micrometer.

In this study, E. coli was prepared using a standard method outlined elsewhere [48]. A depiction of the SERS spectrum of the strained B1121 E. coli bacteria, multiplied by a factor of five, can be seen in Figure 4.23. Several prominent Raman modes were identified

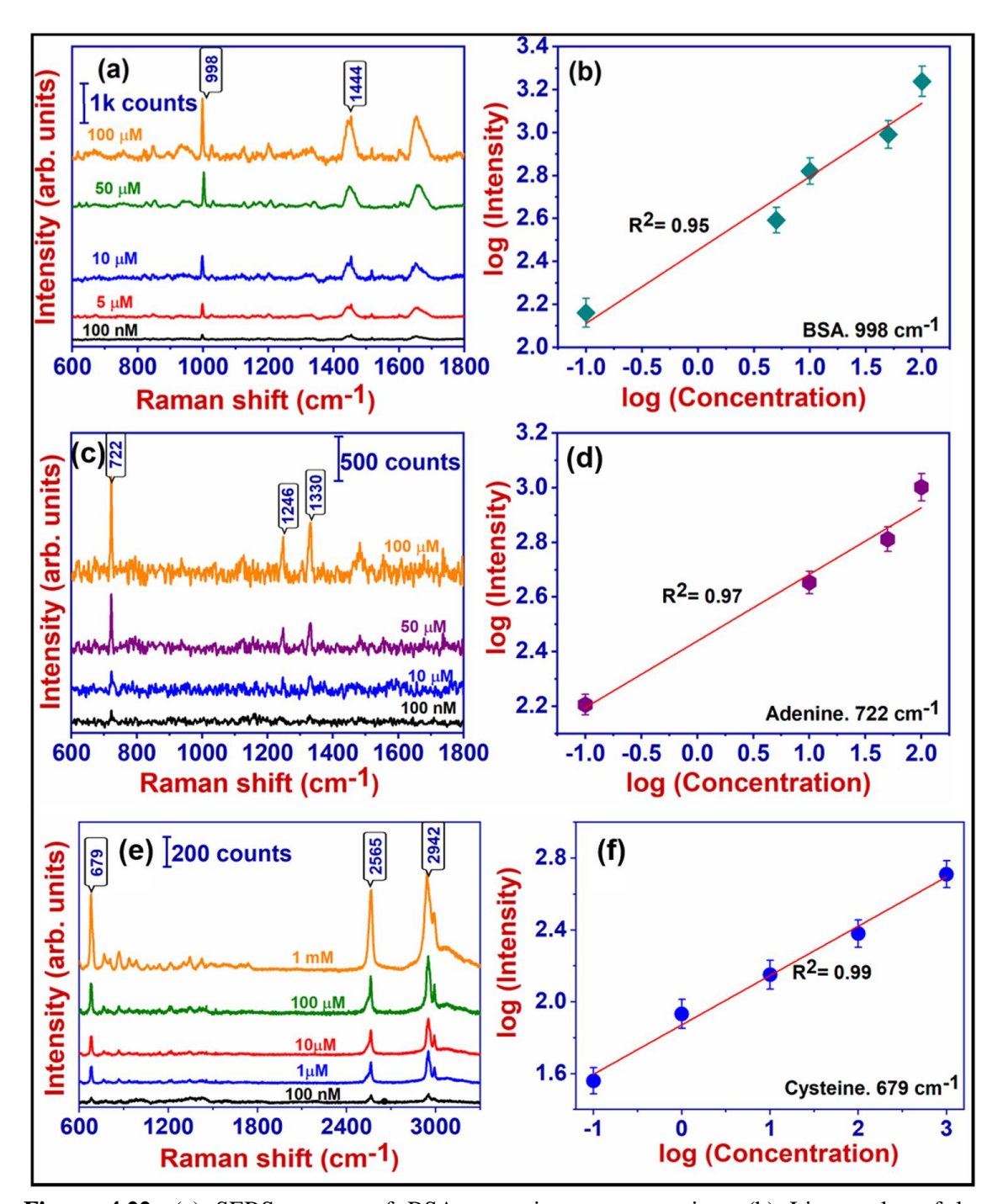


Figure 4.22: (a) SERS spectra of BSA at various concentrations (b) Linear plot of log (concentration) versus log (intensity) of the peak at 998 cm⁻¹ (c) SERS spectra of adenine at various concentrations (d) Linear plot of log (intensity) versus log (concentration) of the peak at 722 cm⁻¹ (e) SERS spectra of cysteine at various concentrations and (f) Linear plot of log (intensity) versus log (concentration) of the peak 679 cm⁻¹.

in our investigation of E. coli, specifically at 751 cm⁻¹, 1130 cm⁻¹, 1159 cm⁻¹, 1146 cm⁻¹, and 2937 cm⁻¹. These peaks within the overall organism spectrum are well-known to stem from amino acids, lipids, and nucleic acids [49]. To assess any potential alterations in the

SERS spectrum, measurements were conducted throughout the bacterial growth period. However, no significant changes were observed.

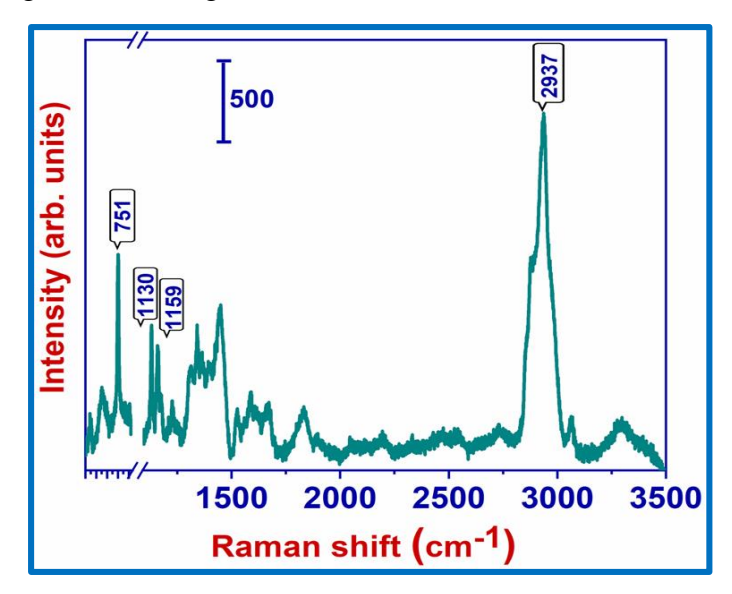


Figure 4.23: Whole organism SERS spectrum of B1121 strained E. coli bacteria detected on hybrid MoS₂/Ag-AuNPs/SiNWs substrate.

A trace explosive molecule tetryl has also been detected using the MoS₂/Ag-AuNPs/SiNWs substrate achieving a sensitivity of 50 nM as shown in figure 4.24.

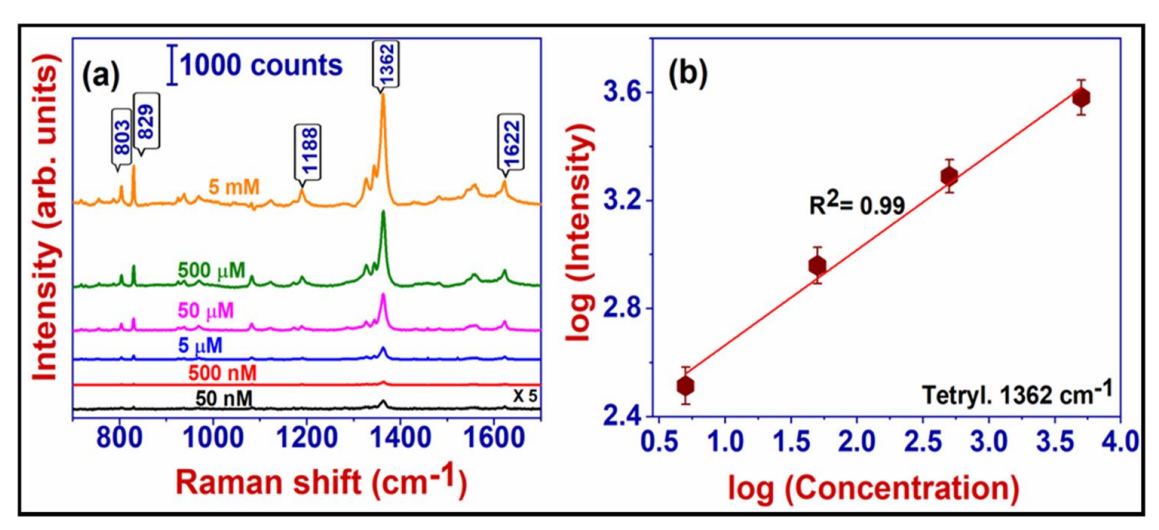


Figure 4.24: (a) SERS spectra of tetryl at various concentrations (spectra are shifted for clarity) and (b) Linear plot of log (intensity) versus log (concentration) of the Raman peak at 1362 cm⁻¹.

Large area Raman mapping has been carried out in order to understand the distribution of hotspots and ascertain the performance of the substrates as shown in the figure 4.25. The mapping data for tetryl with nearly 500 spectra in an area of $100 \ \mu m^2$ depicts an RSD of 6% establishing the practical applicability of the substrates. In addition to reproducibility, durability is also a crucial parameter for translating the lab scale substrates to field. The durability of the substrates has been studied with melamine as the probe molecule and the

data is presented in figure 4.26. The data indicates that even after a duration of 240 days, there is a significant presence of the melamine peak (~6%). The durability can be significantly improved if the samples were stored in vacuum sealed conditions as opposed to ambient conditions as performed in this study.

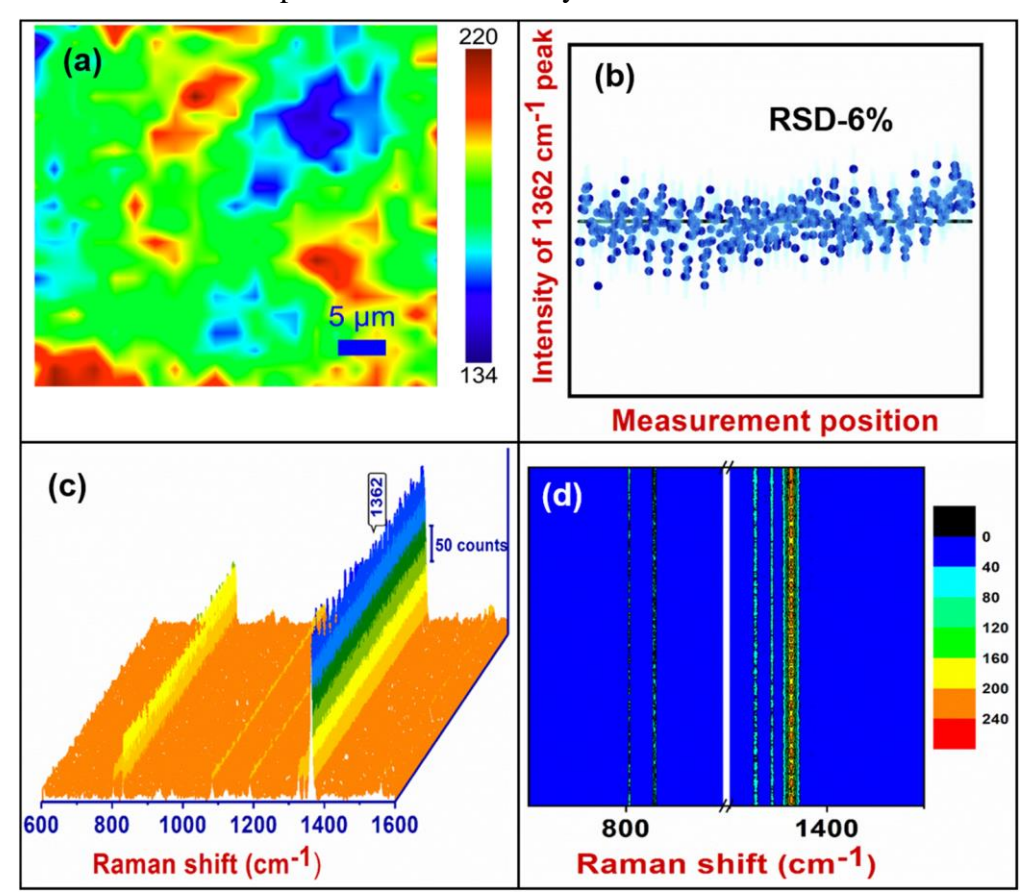


Figure 4.25: a) SERS mapping area ($50 \times 50 \ \mu m^2$) of 5 μM Tetryl with false colors for the peak intensity of 1362 cm⁻¹ mode b) Scatterplot for the peak intensity of ~ 500 spectra collected in mapping with RSD of 6%. The line indicates the mean value c) SERS spectra of the mapping region. d) The corresponding contour plot for the spectra depicted no significant peak shift at all collection points.

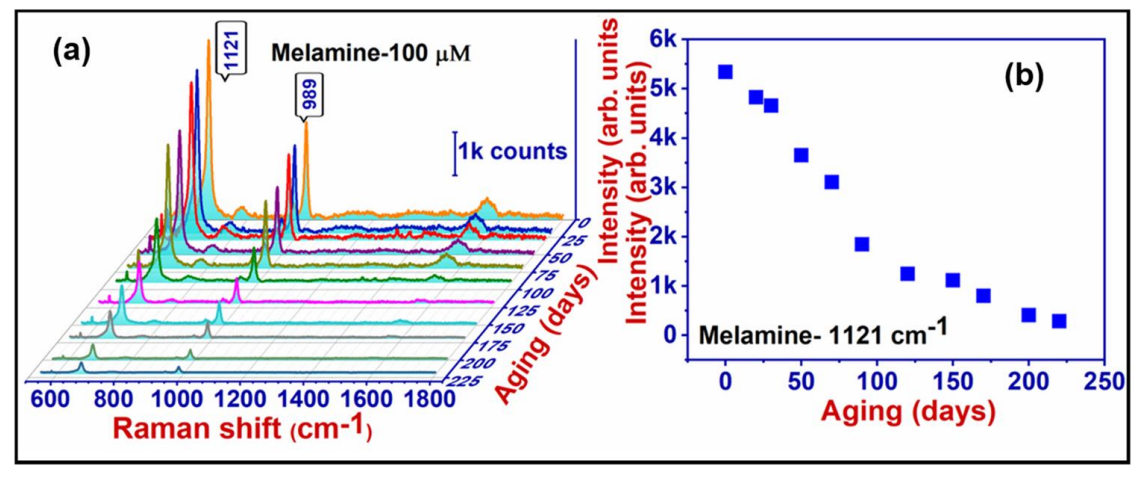


Figure 4.26: (a) SERS durability of melamine (100 μ M) as a function of the aging (days), and (b) Intensity variations as a function of aging (days).

4.4. Flexible SERS Substrates

Flexible SERS substrates hold great importance due to their unique characteristics and potential applications [50]. Flexible substrates refer to thin, bendable materials that can conform to various shapes and surfaces, enabling enhanced Raman signal amplification in a flexible and versatile manner. The importance of flexible SERS substrates lies in their ability to provide enhanced sensitivity and reproducibility in Raman spectroscopy while accommodating complex sample geometries. Traditional rigid substrates, such as glass or silicon, are limited in their adaptability to non-flat or irregular surfaces. Flexible substrates, on the other hand, can conform to curved or uneven surfaces, allowing for direct contact and improved signal collection from samples with complex topographies. The versatility of flexible SERS substrates extends to their integration into wearable devices, flexible electronics, and microfluidic systems. These substrates can be seamlessly incorporated into textiles, patches, or wearable sensors, enabling in-situ and real-time monitoring of chemical and biological analytes. This has significant implications in fields like healthcare, environmental monitoring, and food safety, where on-site and non-destructive analysis is crucial. Moreover, flexible SERS substrates offer advantages in terms of portability, ease of handling, and cost-effectiveness compared to their rigid counterparts. They can be fabricated using various materials, including polymers, metal foils, or nanoparticledeposited films, allowing for customizable designs and scalability. This flexibility in substrate material and fabrication methods further enhances their potential for widespread adoption and commercialization.

4.4.1. Novel Hydrophobic Filter Paper as SERS Substrate

Hydrophobic substrates play a crucial role in SERS, a powerful analytical technique used for sensitive detection and characterization of molecules. Hydrophobic substrates are highly desirable in SERS applications for several reasons including enhancing the SERS signal further. Hydrophobic substrates provide an ideal environment for SERS enhancement due to their ability to adsorb molecules with a strong affinity in a small area leading to concentration of hotspots. Hydrophobic surfaces tend to repel water molecules, preventing their interference with the adsorption of target molecules. This results in a higher concentration of analyte molecules on the substrate surface, leading to stronger Raman scattering signals. In addition, hydrophobic substrates are inherently more stable in aqueous environments compared to hydrophilic substrates. They are less prone to

degradation or alteration when exposed to water or other polar solvents. This stability ensures the longevity and reproducibility of SERS measurements, making hydrophobic substrates ideal for practical applications. These substrates also minimize unwanted background signals that can arise from the surrounding medium. The hydrophobic nature of the substrate reduces the adsorption of impurities, including water molecules and other contaminants present in the sample or solution. By reducing the background noise, the SERS signal-to-noise ratio is improved, enhancing the sensitivity and detection limits of the technique. Further, hydrophobic surfaces allow for better control over the moleculesubstrate interaction. The hydrophobicity can be tailored to specific requirements by modifying the substrate's surface chemistry or by employing appropriate surface coatings. This control enables precise manipulation of the molecule-substrate distance and orientation, optimizing the SERS enhancement for specific analytes. They are compatible with a broad range of analytes, including both hydrophobic and hydrophilic molecules. This versatility makes them suitable for the analysis of various chemical and biological species, such as drugs, proteins, nucleic acids, and environmental pollutants. Additionally, hydrophobic substrates can be utilized for SERS-based sensing in complex biological and environmental samples where hydrophilic substrates may not be as effective. The use of hydrophobic substrates expands the capabilities of SERS and contributes to its effectiveness in diverse fields, including chemistry, materials science, biology, medicine, and environmental monitoring.

Currently, there are different techniques to modify the wettability of a filter paper through both chemical and physical routes. Through a sequence of process of calendaring followed by treating the filter paper with alkyl ketene dimer, hydrophobicity was introduced on the surface resulting in a contact angle of nearly 110⁰ [51]. In a different study, hydrophobicity was achieved by treating the filter paper with (2- dodecen-1-yl)-succinic anhydride (DDSA, 95 %) in hexagonal followed by heating at high temperatures and the process was repeated for two to three cycles [20]. Agarose modified filter paper has been used for the trace detection of trace explosives [21]. Spin coating with polydimethylsiloxane followed by heating has also resulted in hydrophobicity with a contact angle of nearly 130⁰ [22]. Plasmonic filter paper was heated in the presence of 1H, 1H, 2H, 2H-Perfluoroalkyltriethoxysilane in vacuum at high temperature for 6 hours to achieve hydrophobicity enabling trace detection of melamine with sensitivity down to 1ppm [23]. All these methods are cost ineffective and require a series of procedures involving time

and resources. Si oil which costs nearly 15 USD for 500 ml combined with a spin coating method with duration of less than 4 minutes, is the cheapest and rapid alternative to the existing methods. This substrate was subsequently used for the quantification of trace explosives using machine learning as shown in the figure below (figure 4.27).

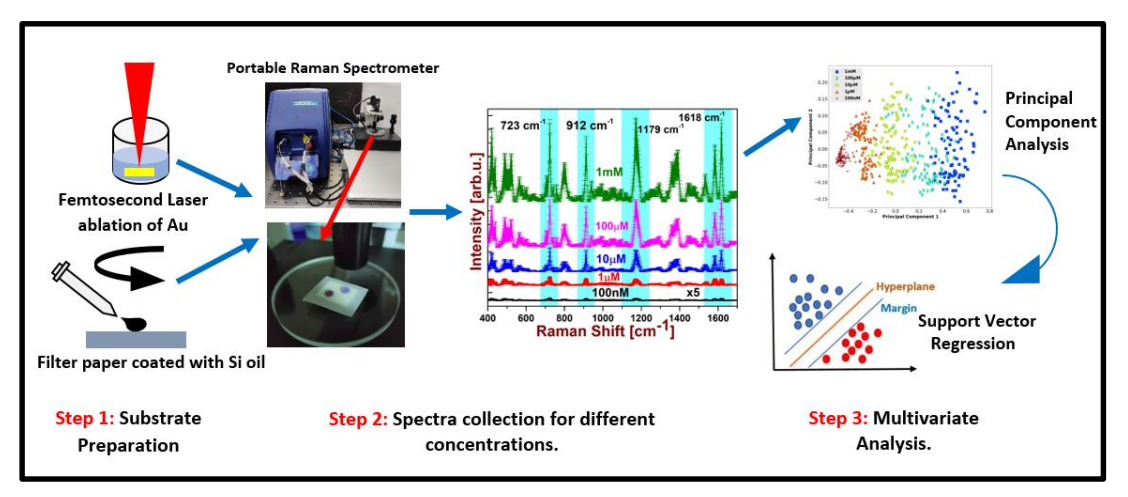


Figure 4.27: Schematic of HFP in combination with machine learning for rapid quantification of trace analyte molecules.

4.4.1.1. Preparation Method and Data Acquisition

To prepare the substrate, filter paper was initially treated with a coating of silicone oil using a spin coater (Holmarc Spin coater, India) for a duration of 4 minutes. The excess silicone oil was then eliminated by subjecting the samples to a temperature of 100 °C in an oven for one hour. For the synthesis of gold nanoparticles, pure gold was subjected to femtosecond laser ablation in water. This was accomplished using a Ti-Sapphire laser with a pulse duration of 50 fs, a repetition rate of 1 kHz, and a wavelength of 800 nm. The experimental setup was discussed in chapter 2. To prevent multiple-spot ablation at a single point, the sample was first cleaned and then placed in a 10 ml beaker containing 7 ml of water. It was then mounted on a two-dimensional X-Y stage and moved in a raster pattern within a 4x4 mm2 area at a scan speed of 1 mm/s. The laser power was controlled using a combination of a Brewster window and a half-wave plate, with an energy of 500 µJ utilized for the ablation process. The beam was focused on the target using a 25 cm convex lens until a cracking plasma sound was heard. For the SERS studies, the synthesized gold nanoparticles (Au NPs) were drop-casted onto the hydrophobic filter paper, followed by the addition of the analyte molecule. The sample was then allowed to dry, resulting in a drop size of approximately 2 mm on the filter paper. In the investigation, we have examined the dye molecule of CV at various concentrations, including 1 mM, 100 μM, 10 μM, 1 μM, and 100 nM. Additionally, an explosive molecule known as PA

was studied at concentrations of 1 mM, 100 μ M, 10 μ M, and 5 μ M. The SERS studies were conducted using a portable Raman spectrometer (BWTEK) with a laser excitation wavelength of 785 nm. The spectrometer offered a power scalable option ranging from 3 to 300 mW and was equipped with a micro-positioning system consisting of XYZ stages. A laser power of 10 mW was set as the input, and an acquisition time of 10 s was maintained for all the experiments. To acquire data, the samples were manually moved in a raster pattern using the translational stages. It is noteworthy that all the spectra were obtained under identical experimental conditions to ensure consistency and accuracy. To calculate the Enhancement Factor, higher concentrations of both analytes without nanoparticles were placed on the same filter paper, and the corresponding spectra were recorded. This allowed for a comparative analysis to determine the enhancement achieved with the addition of nanoparticles. In order to sample the sample surface well and collect statistically significant data 100 spectra were collected per concentration, adding to the total spectra of ~900.

4.4.1.2. Characterization

4.4.1.2.1. FESEM and TEM imaging

The characterization of the nanoparticles involved a comprehensive analysis of their structure, distribution, and shape using transmission electron microscopy (TEM). For imaging, the colloids were drop-casted onto TEM grids with a carbon coating and left to dry prior to measurements. TEM images at various magnifications were captured using a SEI cecnai G2 S-Twin 200 kV microscope, providing valuable insights into the morphology of the gold nanoparticles. Figure 4.28 displays these TEM images, showcasing different views of the nanoparticles. To determine the size distribution of the particles, multiple TEM images of the same colloids were utilized in conjunction with ImageJ software. Through analysis, it was observed that the frequency distribution of sizes exhibited a unimodal pattern, which was subsequently fitted to a Gaussian function. The average particle size was estimated to be approximately 20 nm, with a standard deviation of 1.8 nm. The full width at half maximum (FWHM) was measured to be around 4 nm. It is worth noting that the presence of larger particles beyond the average size was indicated by the extended tail of the Gaussian fit. This could potentially be attributed to the ejection of fragments during the ablation process or the coalescence of nanoparticles during the initial stages of ablation. Moreover, selected area electron diffraction (SAED) patterns were obtained, revealing the miller planes corresponding to (111), (2,0,0), (2,2,0), and

(3,1,1) of gold. These patterns were cross-referenced with the JCPDS file number Au: 04-0784 for confirmation and identification. The analysis revealed a unimodal size distribution, with the presence of larger particles beyond the average size. SAED patterns provided information about the crystallographic planes of gold.

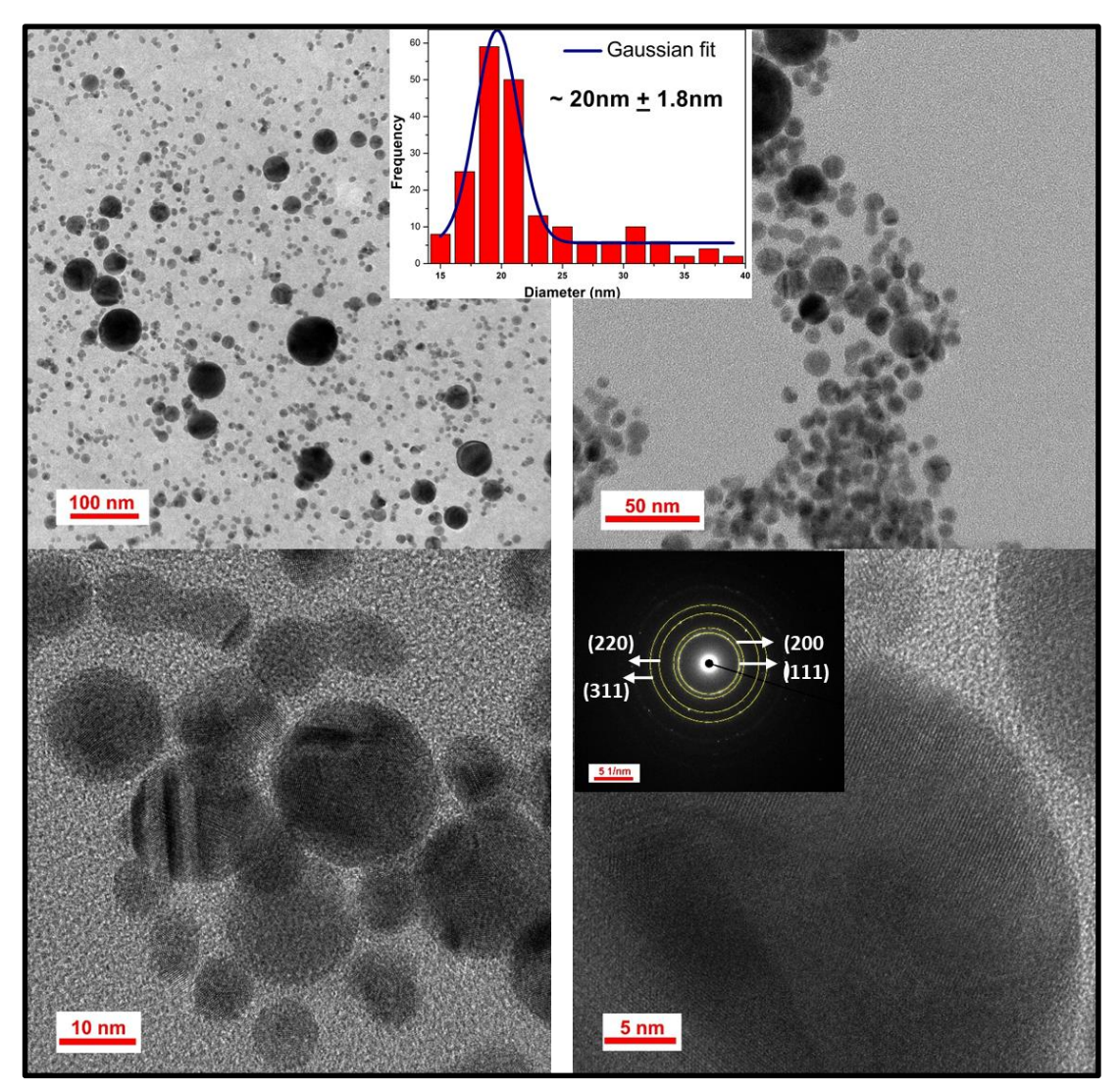


Figure 4.28: a) and b) TEM images of Au nanoparticles at different magnifications. c) and d) HRTEM images at different magnifications. Inset in a) and b) depicts the particle size distribution fitted to a Gaussian distribution and inset in d) shows the SAED pattern.

To gain insights into the morphology of the hydrophobic filter paper (HFP), field emission scanning electron microscopy (FESEM) was employed for characterization. The obtained micrographs are presented in Figure 4.29, showcasing the HFP at various magnifications. The FESEM images reveal notable differences compared to plain filter paper (FP) fibers observed in previous studies. In contrast to FP, the cellulose fibers of the HFP appear more planar and well-bounded. This distinctive morphology of the cellulose fibers in HFP provides a larger surface area for enhanced adsorption of nanoparticles. Consequently,

when observed at higher magnification, the nanoparticles are observed to be concentrated within a small region, highlighting the impact of the hydrophobic nature of the substrate. To quantify the hydrophobicity of the substrate, contact angle measurements were performed. The contact angle serves as an indicator of the degree of hydrophobicity, with higher angles indicating greater hydrophobic properties.

In this study, the Low Bond Axis Symmetric Drop Analysis (LBASDA) plugin in ImageJ was utilized for measuring the contact angle [52], yielding a value of approximately 110°. The inset in Figure 4.29 a) demonstrates the contact angle observed for the HFP, while Figure 4.29 b) provides a visual comparison of the spreading behaviour of the drop on the hydrophobic HFP versus the normal FP. The image clearly illustrates the undesired spreading of the drop on FP, contrasting with the contained shape observed on the hydrophobic HFP.

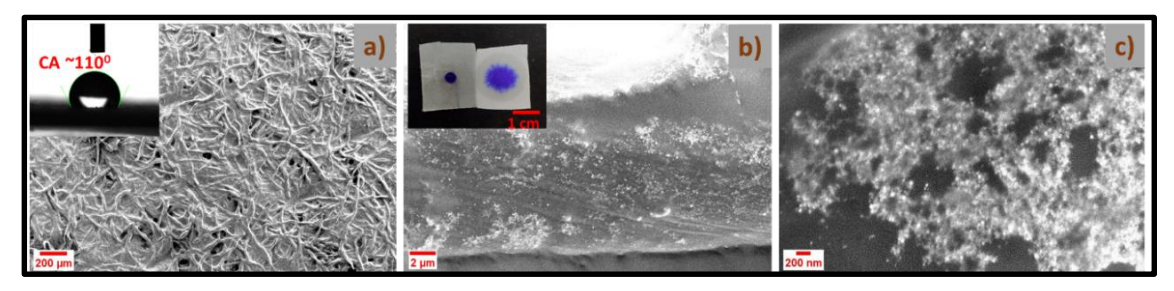


Figure 4.29: a), b), c) FESEM micrographs of HFP at different magnifications. Inset in a) shows contact angle measurement and b) shows a drop of CV on HFP and normal FP.

The micrographs revealed distinct cellulose fiber characteristics and concentrated nanoparticle distribution in the hydrophobic region. Contact angle measurements further confirmed the hydrophobic nature of the substrate, emphasizing its potential for preventing undesired drop spreading compared to the normal filter paper. These observations contribute to a better understanding of the morphology and properties of the hydrophobic filter paper used in the study.

4.4.1.2.2. UV-Visible Spectroscopy

The resulting AuNPs from fs laser ablation were subjected to characterization using UV-Visible spectroscopy to investigate their localized Surface Plasmon Resonance (LSPR) properties. The UV-visible absorption measurements were conducted within the wavelength range of 300-800 nm. Figure 4.30 displays the absorption spectra of the Au NPs, revealing a distinct LSPR peak observed at 521 nm. In the accompanying inset, a COMSOL simulation showcases the near-field enhancement around randomly spaced Au

NPs, which possess an average size of approximately 20 nm. The incident electric field is polarized in the X-direction, with an input wavelength of 785 nm. The simulated image provides valuable insights into the local field enhancement between the gaps of the nanoparticles. It demonstrates that as the nanoparticles are concentrated within a confined area, such as in the case of the HFP, a greater number of hotspots are formed. These hotspots are regions of heightened local field enhancement, which play a crucial role in intensifying the Raman signals. Moreover, the near-field enhancement gradually diminishes as the distance between the nanoparticles increases. Based on these observations, it can be inferred that the concentration of NPs within a small area, as facilitated by the HFP, holds promise for generating a greater number of hotspots and, consequently, stronger Raman signals. This highlights the potential significance of the spatial arrangement of NPs in enhancing the performance of SERS.

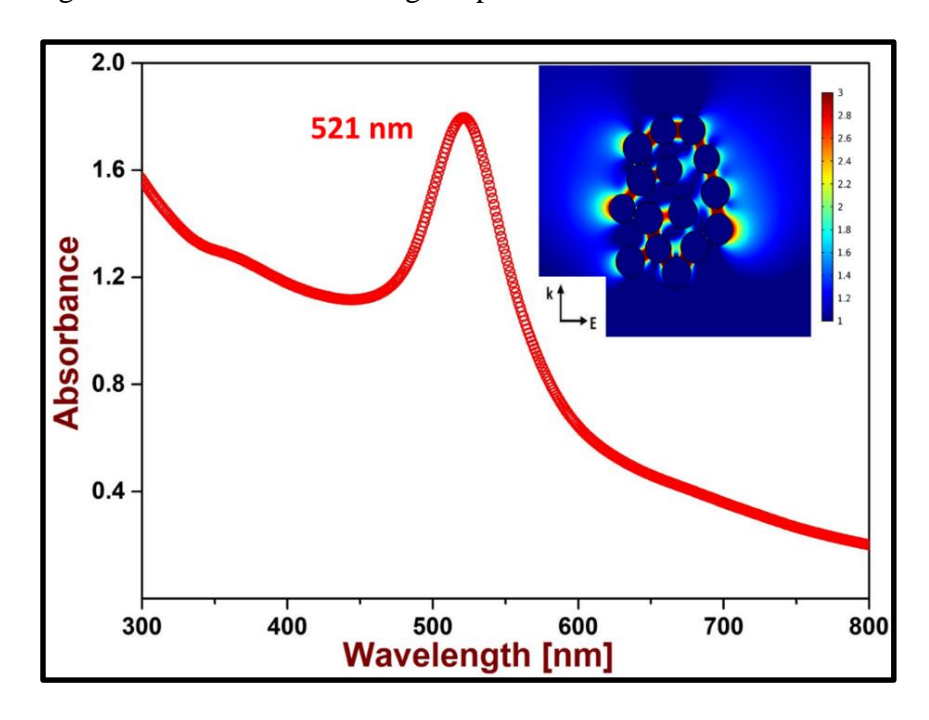


Figure 4.30: UV-Visible absorption spectrum of laser ablated Au NPs. Inset shows near field simulation of randomly spaced Au NPs of different sizes with 785 nm excitation using COMSOL.

4.4.1.2.3. Data Modelling and Quantification

All data pre-processing and multivariate analysis were conducted using Python 3.8.3. To ensure accurate analysis, baseline correction was implemented using the widely utilized asymmetric least square fitting method proposed by Eilers et al. [53]. Subsequently, the spectra were subjected to smoothening using a Savitzky-Golay filter [54]. Prior to performing PCA, the spectra were standardized using the RobustScaler function built into Scikit Learn, which effectively eliminated outliers (for details refer appendix A). The

analysis employed the inbuilt Kernel PCA and SVR algorithms available in the Python Scikit Learn library. Figure 4.31 illustrates the average of 100 SERS spectra obtained for each concentration of the analytes CV and PA.

Among the observed peaks, the Raman peak at approximately 1094 cm⁻¹ corresponds to the C–O–C bending mode of the filter paper [55]. In the case of CV, the Raman peaks at 1618 cm⁻¹, 1179 cm⁻¹, 912 cm⁻¹, and 723 cm⁻¹ correspond to the C-C stretching, C-H inplane bending, ring skeletal vibrations, and C-H out-of-plane bending modes, respectively [56]. For PA, the modes at 1345 cm⁻¹ and 827 cm⁻¹ correspond to the NO2 symmetric stretching and C-H bending modes, respectively [57].

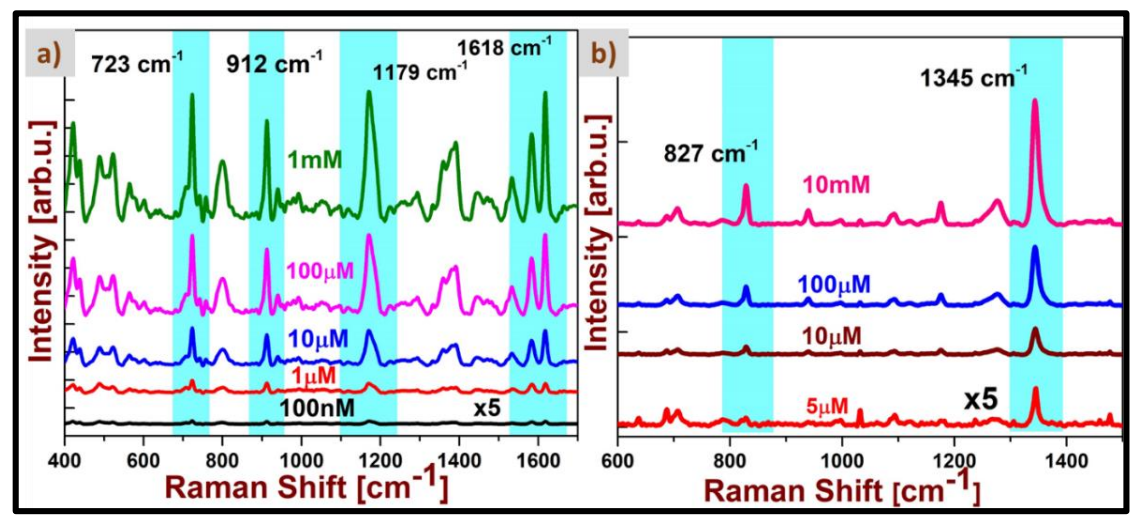


Figure 4.31: SERS spectra on HFP for different concentrations of a) CV, b) PA collected with a portable Raman spectrometer with laser excitation 785 nm and 10 mW laser power. Figures represent average and standard deviation of 100 spectra collected at random sites on the substrate for each concentration. The prominent peaks for each analyte molecule are highlighted in yellow colour. 'arb.u.' means arbitrary units.

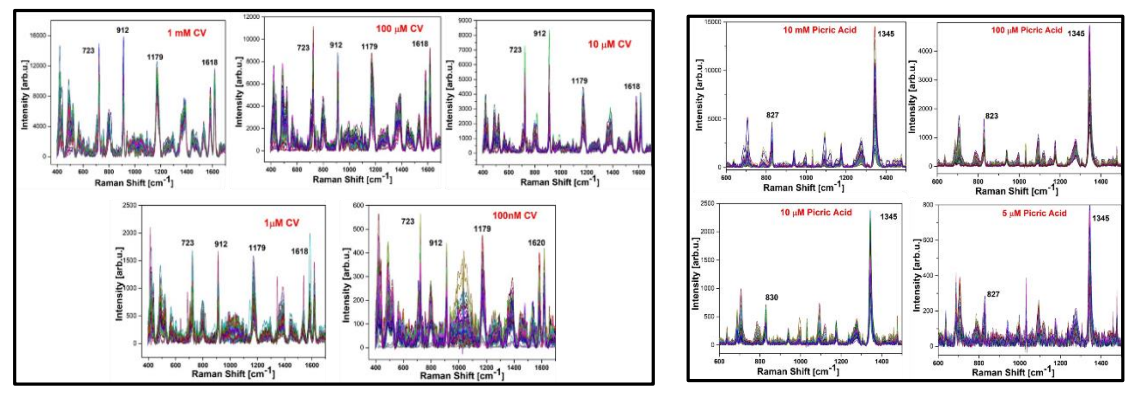


Figure 4.32: Individual SERS spectra of each concentration for the two molecules studied in the work.

Finally, the SERS enhancement factors were found to was found to be $3x10^4$ for PA and $5x10^6$ for CV. The relative standard deviation (RSD) was calculated, considering the 1345

cm⁻¹ peak for PA and the 1618 cm⁻¹ peak for CV, resulting in an RSD of approximately 27%. This data was considered for analysis using non-linear machine learning models. To reduce the dimensionality of the dataset while retaining relevant information, principal components explaining 95% of the total variance were selected as shown in figure 4.33. These principal components were then utilized as inputs for support vector regression (SVR).

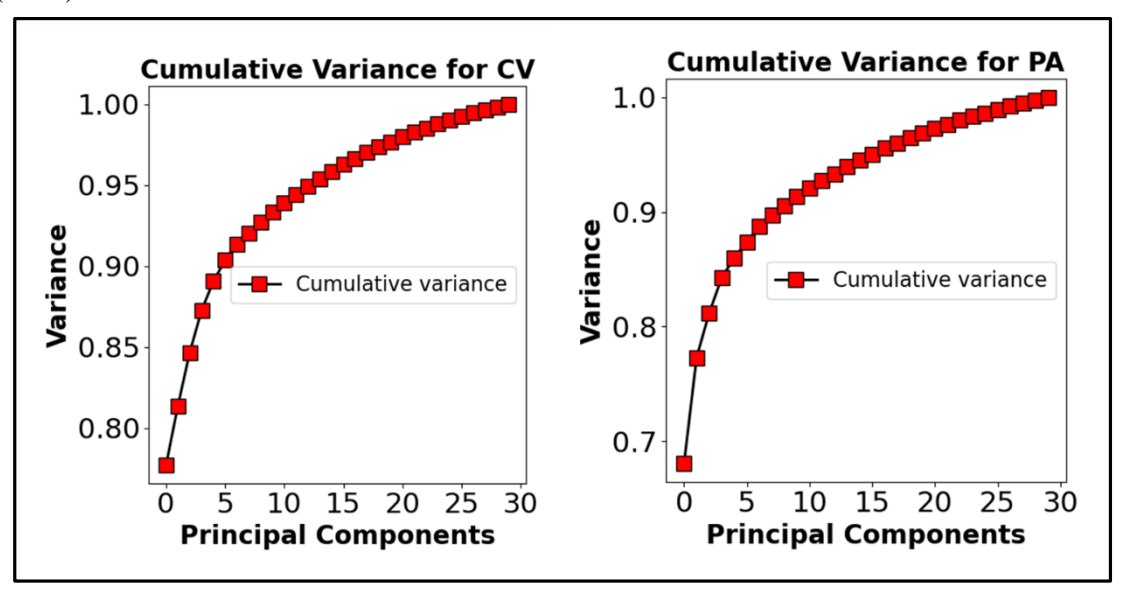


Figure 4.33: Cumulative variance as a function of number of Principal components for a) CV, b) PA.

Principal component analysis (PCA) is one of the most widely used ML algorithm for different applications including dimensionality reduction, classification and outlier detection. In this thesis work, we have exclusively used for the case of dimensionality reduction and hence the discussion is restricted to only that context. Dimensionality reduction techniques, such as PCA, offer a valuable approach for representing large datasets in a more concise manner, facilitating the efficiency and simplicity of subsequent algorithms. By reducing the dimensions of the data, computational resources and memory requirements are significantly alleviated. Traditional PCA operates on linear relationships between input and output features, but when confronted with nonlinear data patterns, alternative methods like Kernel PCA become necessary. Kernel PCA effectively addresses nonlinearity by employing a kernel function that maps the nonlinear variables onto a higher-dimensional space, where they can be linearly separated—an approach commonly referred to as the 'Kernel trick.' This transformation enables the identification of underlying linear structures in the data. Several kernel functions, such as polynomial, radial basis, cosine, and sigmoid, can be employed in Kernel PCA to accomplish this mapping task.

Each kernel function possesses unique properties that suit different datasets and nonlinearities. Given the nonlinearity present in the SERS data, we have utilized Kernel PCA for our analysis, specifically incorporating the sigmoid activation function. This choice of activation function contributes to capturing the complex relationships and nonlinear features inherent in the data, allowing for more accurate representation and subsequent analysis as shown in figure 4.34. The detailed mechanism of SVM is explained in appendix A. The PCs accounting for variance of greater than 90% were given as inputs to SVR with RBF as the kernel function and the results are summarised in the table 4.2.

Table 4.2: Summary of regression metrics for SVR.

Analyte	No. of PCs	\mathbb{R}^2	MSE	Bias	Variance
CV	8	0.9629	0.070	0.068	0.007
PA	17	0.9472	0.063	0.064	0.011

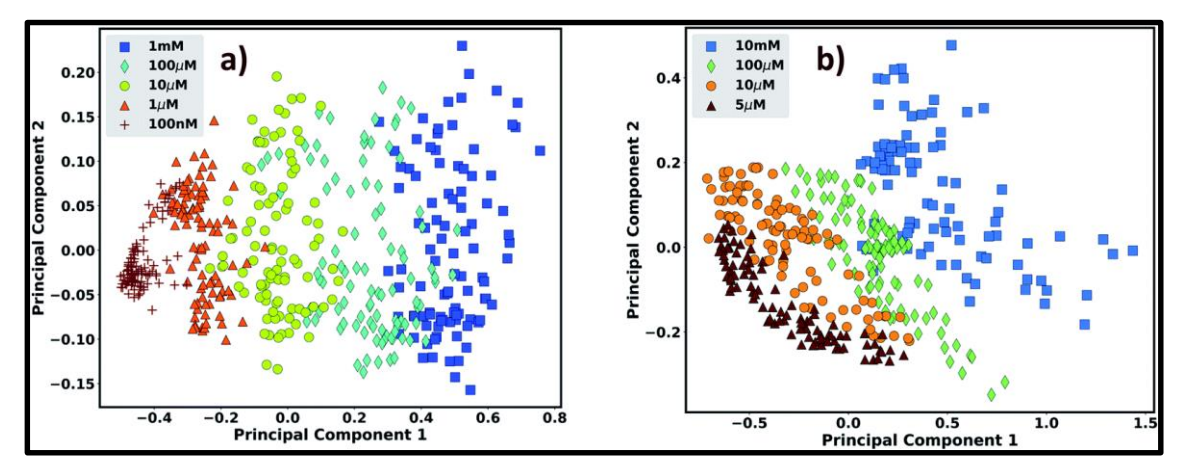


Figure 4.34: PCA for a) CV and b) PA for different concentrations as indicated in the labels.

4.4.2. Flexible Porous Si for SERS

A single silicon wafer is used as the starting material for the fabrication of porous silicon (pSi), a diverse porous nanostructure. pSi is created through electrochemical or anodic etching of crystalline silicon using an aqueous electrolyte containing hydrofluoric acid (HF) and alcohol. This process allows for precise control over pore size and porosity. pSi possesses micro, meso, and macro pores with cylindrical columns, offering a large surface area, unique optical properties, and chemical stability. These characteristics make pSi an ideal substrate for robust SERS activity. The utilization of pSi in SERS applications gained significant attention in the early 2000s ever since its discover in Bell labs [58], leading to the development of SERS-based substrates. To enhance flexibility and ease of handling, a free-standing single-crystal porous silicon (FS-pSi) substrate was developed by detaching

the pSi layer from the parent silicon substrate. The detachment process involved dissolving the silicon in alkaline solutions based on Fick's law. While the application of pSi as a flexible substrate in SERS sensing is a relatively unexplored area, SERS itself is a highly promising analytical technique with single-molecule detection capabilities. It offers high precision, sensitivity, and selectivity, making it suitable for various fields such as medicine, environmental pollutant detection, food safety, and military applications. The mechanism of plasmonic SERS involves electromagnetic (EM) and chemical (CM) enhancement mechanisms, with the charge transfer (CT) effect playing a crucial role in the chemical enhancement mechanism [16]. Plasmonic nanostructures are essential for effective molecular detection in SERS, as they induce localized surface plasmon resonance and enhance the electromagnetic field. To achieve high sensitivity, reproducibility, and selectivity in SERS, much attention has been devoted to preparing plasmonic SERS-active substrates. Therefore, the objective of the study was to synthesize flexible SERS substrates comprising a layer of silver NPs decorated on FS-pSi. These substrates aim to enable tracelevel molecular detection with stability and reproducibility, making them suitable for onsite applications.

4.4.2.1. Sample Preparation and Characterization

Nanocrystalline pSi with low dimensionality was prepared using a solution-based anodic etching process. Commercially available boron-doped silicon wafers (1×1 cm²) were subjected to cleaning with acetone and ethanol to eliminate surface contaminants. The cleaned wafers were then immersed in diluted hydrofluoric acid (HF) to etch away the native oxide layer, following previously established procedures [59] [60]. For the anodic etching, the pre-cleaned silicon wafer was directly mounted as the anode in an in-house etch-cell setup, while a platinum coil served as the cathode. The etch-cell was filled with an electrolyte containing a mixture of water, HF, and ethanol in a ratio of 1:1:2. The etching process was initiated using pulsed current densities, applying 30 mA/cm² for 60 minutes for anodization and 170 mA/cm² for 1 minute for electro-polishing using a Keithley-2400 DC current source and the results are shown in figure 4.37. Despite differences in resistivity, these current densities were utilized. Figure 4.35 illustrates the step-by-step synthesis of the free-standing pSi layers. After detachment from the etched silicon substrate, the pSi layer was retained on scotch tape to enhance flexibility.

Photographic representations of the detached free-standing pSi layer are shown in Figure 4.36, demonstrating the stability of the FS-pSi layers even after repeated folding attempts.

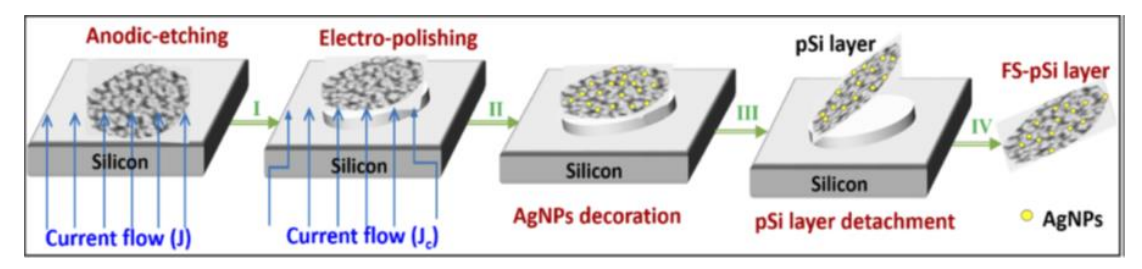


Figure 4.35: Processing steps for the fabrication of AgNPs@FS-pSi layer by anodic-etching followed by electro-polishing.

The FS-pSi layers were subjected to a two-step electroless deposition process, known as galvanic immersion, to decorate them with Ag NPs. In the first step, a solution of 0.002 M AgNO₃ was deposited onto the FS-pSi layer, followed by immersion in a 5 M hydrofluoric acid (HF) solution for 15 seconds in the second step. The density of Ag NPs was controlled by adjusting the deposition time, which was set at 30 minutes, 60 minutes, and 4 hours as shown in figure 4.38. These samples were designated as AgNPs@FSpSi-30min, AgNPs@FSpSi-60min, and AgNPs@FSpSi-4h, respectively. The AgNPs@FSpSi-60min.

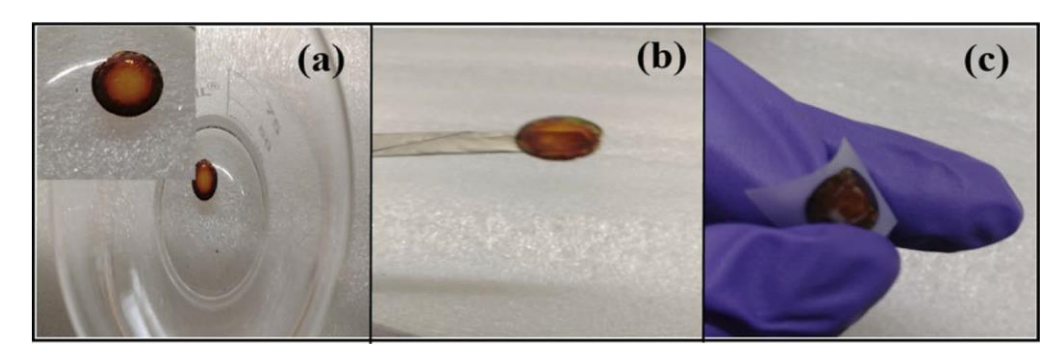


Figure 4.36: Photographs of FS-pSi (a) floating on water (b) freely held by a tweezer, and (c) mounted on a flexible scotch tape.

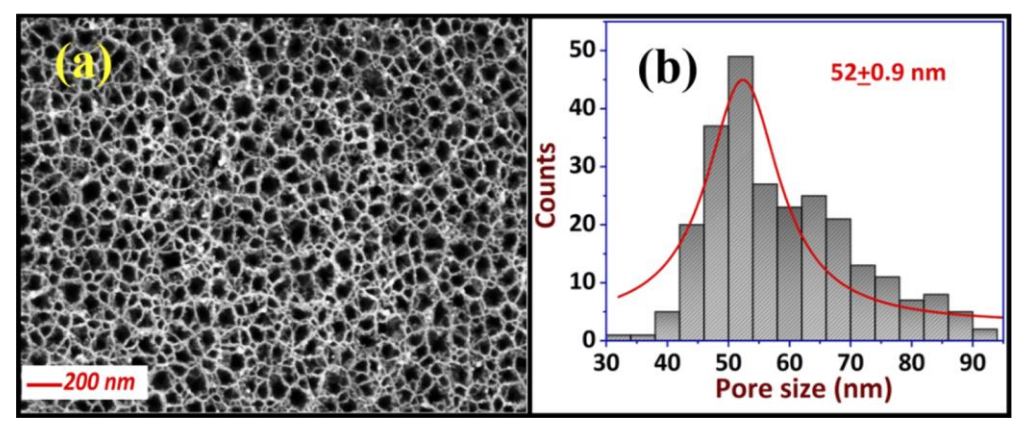


Figure 4.37: (a) The morphology of as-anodized FS-pSi layer and (b) the histogram of the pore size distribution (solid line indicates the Gaussian fit).

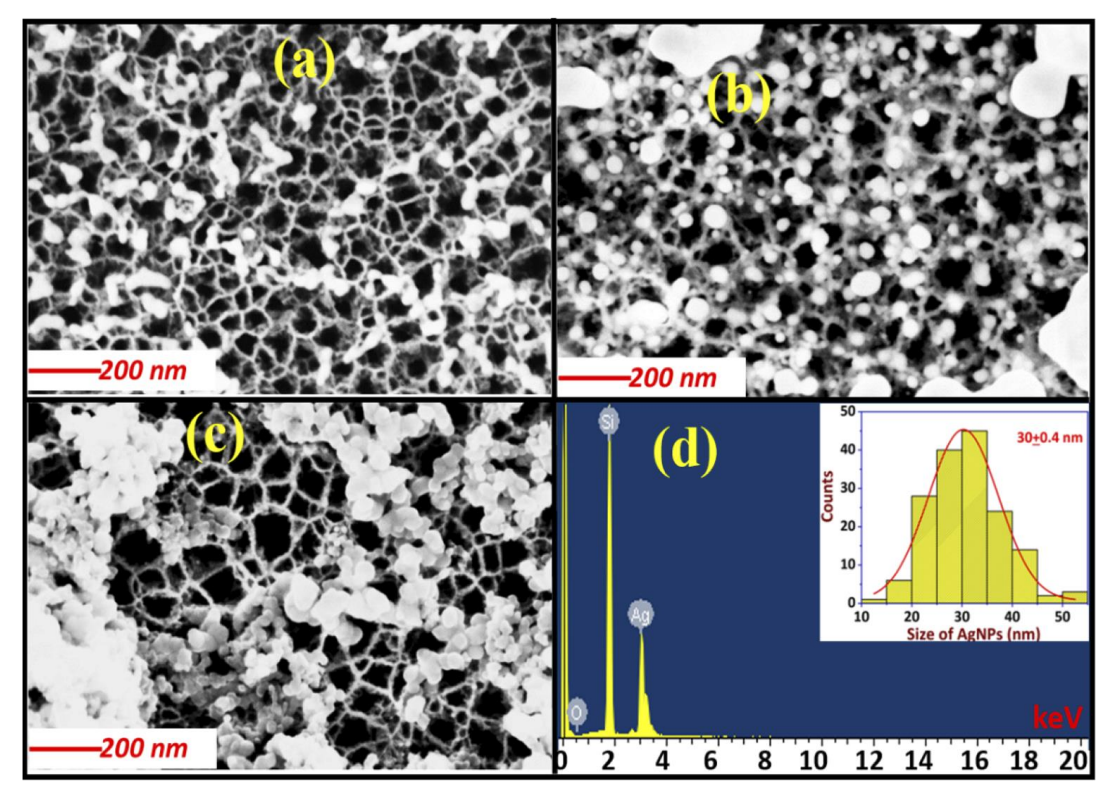


Figure 4.38: AgNPs decoration of FS-pSi at various deposition times (a) 30 min, (b) 60 min, (c) 4 hours, and (d) EDS spectrum of AgNPs@FSpSi-60min sample. [Inset of the figure (d) illustrates the distribution of AgNPs over the sample surface of FSpSi-60min [shown in (b)] and the solid line is a Gaussian fit].

sample was optimized and selected for further investigations. In this study, a 3-inch silicon wafer, costing approximately 25 USD, was sliced into pieces measuring 1.5×1.5 cm² for subsequent processing.

Each sliced piece, with an area of 2.25 cm² and a cost of less than \$5, was utilized for the fabrication of free-standing porous silicon. Importantly, the parent silicon used for etching could be recycled and repurposed for FS-pSi fabrication after appropriate cleaning and dusting of the samples. Depending on the measurement requirements, the resulting FS-pSi decorated with AgNPs, with a diameter of approximately 10 mm, was further divided into two pieces for characterization studies. Through comprehensive measurements and analyses, we demonstrate that a single piece of this cost-effective SERS-active substrate typically costs less than 1USD and possesses excellent capabilities for the rapid detection of hazardous materials.

4.4.2.2. SERS Measurements

SERS measurements were carried out using 532 nm laser excitation of the Horiba Raman spectrometer with 25 mW of laser power. Three molecules, methylene blue, picric acid and ammonium nitrate were studied and trace detection was demonstrated for each

molecule. Initially to assess the performance of the samples prepared for different deposition time, MB was chosen as a test molecule and SERS spectra for each sample has been collected (figure 4.39).

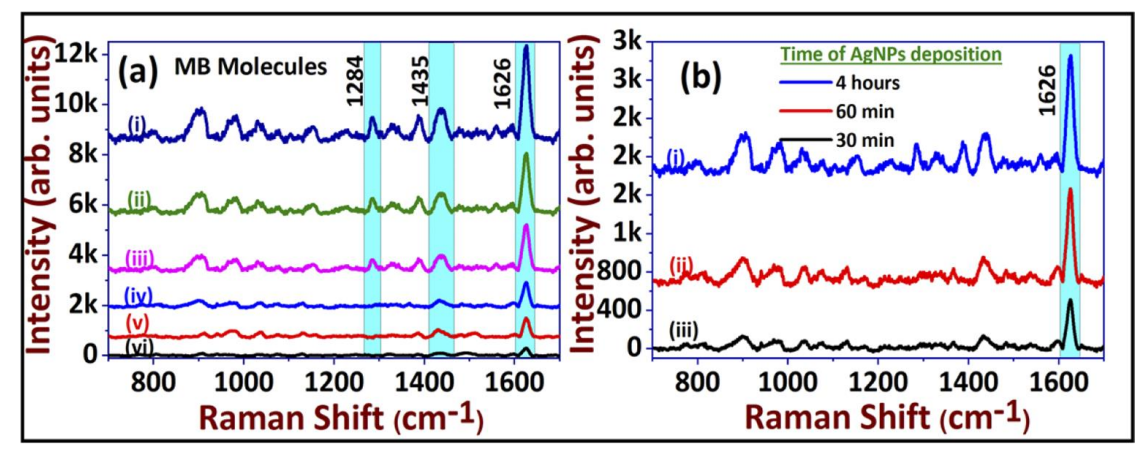


Figure 4.39: The SERS spectra of MB molecules on AgNPs@FS-60min substrate at a concentration of (a)-(i) 100 μ M (ii) 50 μ M (iii) 10 μ M (iv) 5 μ M (v) 1 μ M and (vi) 100 nM concentration (b) SERS spectra of MB (5 μ M) at various AgNPs deposition time on FS-pSi. Spectra in (a) and (b) are stacked in Y-axis to avoid ambiguity in the data.

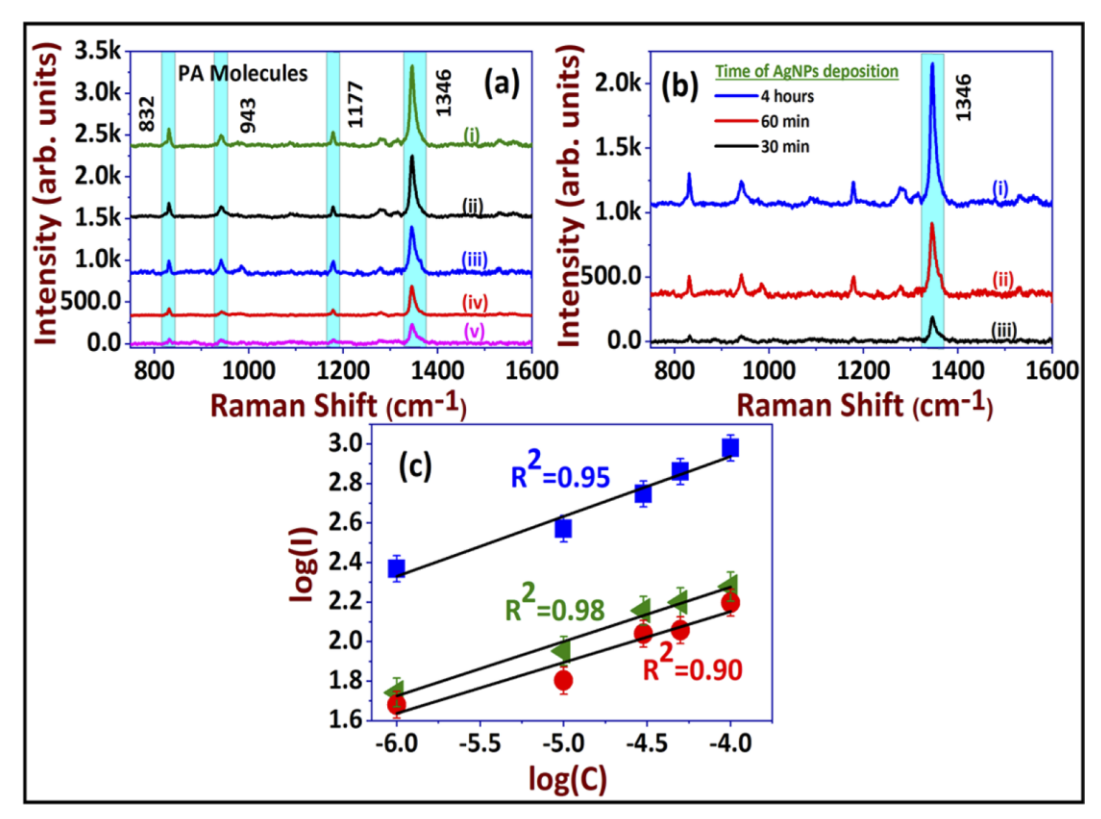


Figure 4.40: The SERS spectra of PA, an explosive molecule, on AgNPs@FSpSi-60min substrate at concentration of (a)-(i) $100 \,\mu\text{M}$, (ii) $50 \,\mu\text{M}$, (iii) $30 \,\mu\text{M}$, (iv) $10 \,\mu\text{M}$, and (v) $5 \,\mu\text{M}$ concentrations, (b) SERS spectra of PA ($30 \,\mu\text{M}$) at various AgNPs deposition time on FSpSi, and (c) corresponding linear calibration [log (SERS intensity) versus log (concentration)] of the different Raman modes observed at $832 \, \text{cm}^{-1}$, $1177 \, \text{cm}^{-1}$, and $1346 \, \text{cm}^{-1}$.

The data communicates that the AgNPs@FS prepared for 4 hours has outperformed slightly the sample at 1 hour. This is due to the high density of hotspots originating from the densely packed AgNPs produced at this deposition time. However, such aggregation of NPs also reflects as poor reproducibility and hence AgNPs@FS-60min sample was chosen for further SERS measurements. Measurements performed on PA also confirmed the same as indicated in figure 4.40.

The reproducibility of the signal has been measured with MB (10 μ M) and PA (50 μ M) and the RSD was found to be less than 10% as shown in figure 4.41. Though there is a significant room for improving the enhancement factors as shown in the table 4.3, the RSD for the given cost and flexibility outweighs the performance. Reproducibility of PA has also been studied and presented in figure 4.42.

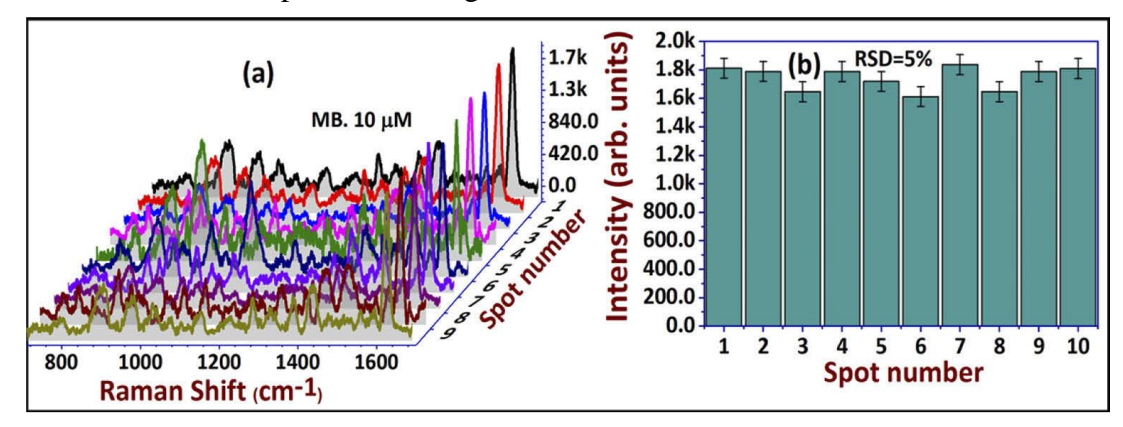


Figure 4.41: (a) Reproducibility of the SERS spectra of 10 μM MB molecules detected at 10 different spots on AgNPs@FSpSi-60min, and (b) the corresponding standard analysis with RSD values.

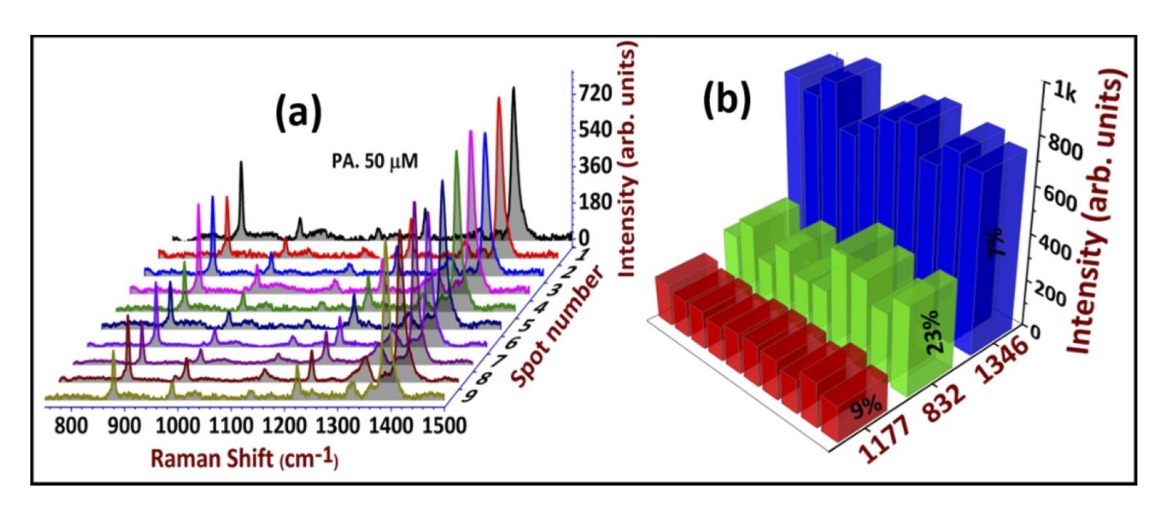


Figure 4.42: (a) Reproducibility of the SERS spectra of 50 μM PA molecules detected at 10 different spots on AgNDs@FSpSi-60min, and (b) the corresponding histogram with RSD values.

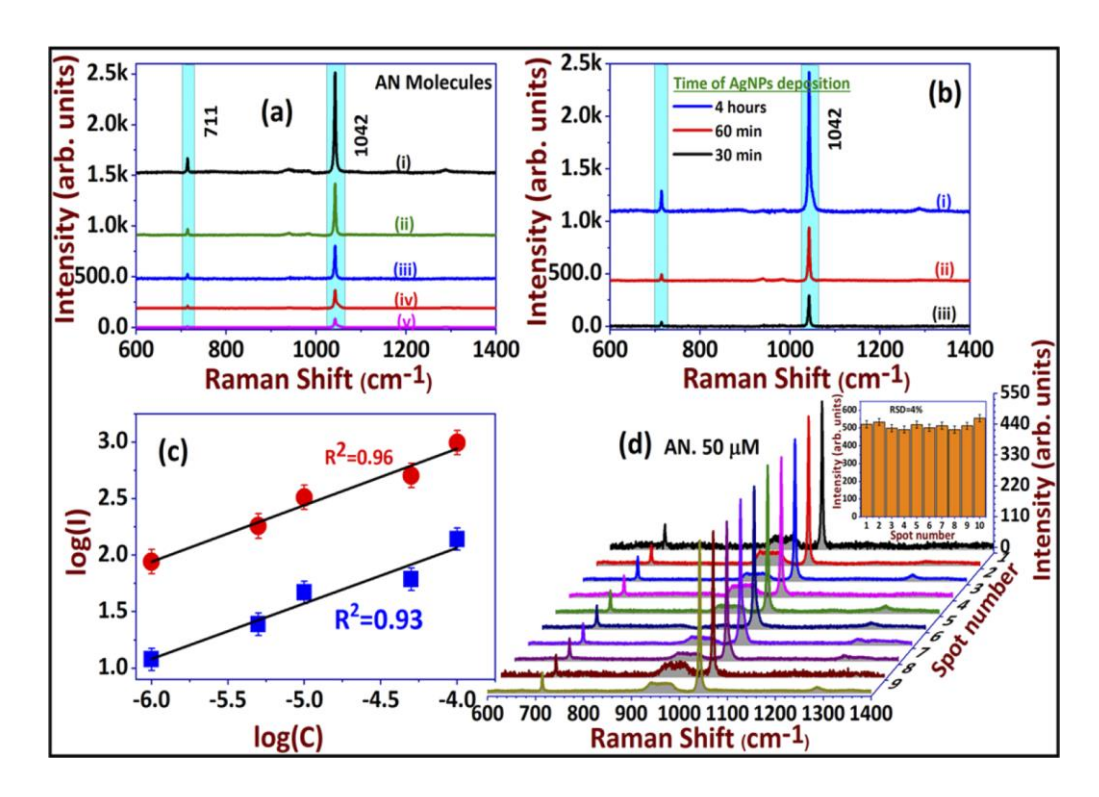


Figure 4.43: The SERS spectra of AN molecule on AgNPs@FSpSi-60min substrate at (a)-(i) 100 μM, (ii) 50 μM, (iii) 10 μM, (iv) 5 μM, and (v) 1 μM concentrations, (b) The SERS spectra of AN (50 μM) at various AgNPs deposition time on FS-pSi, and (c) corresponding linear calibration [log (SERS intensity) versus log (concentration)] of the Raman modes at 711 cm $^{-1}$, and 1042 cm $^{-1}$ (d) Reproducibility of AN (50 μM) on AgNDs@FSpSi-60min substrate and inset shows the corresponding standard deviation.

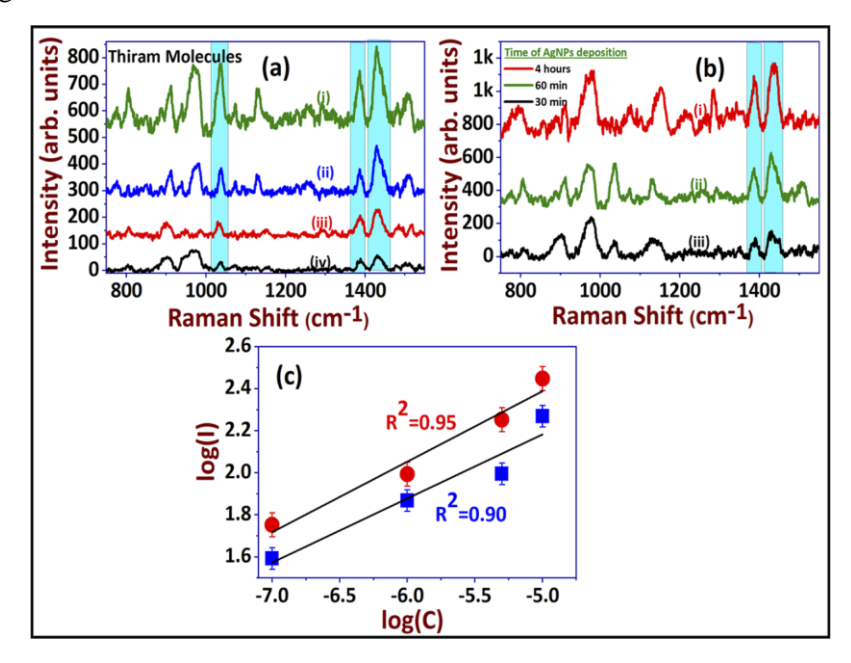


Figure 4.44: The SERS spectra of thiram (pesticide) on AgNPs@FSpSi-60min at (a) (i) 10 μ M (ii) 5 μ M (iii) 1 μ M and (iv) 100 nM concentrations (b) SERS spectra of thiram (10 μ M) at various AgNPs deposition time on FSpSi and (c) corresponding linear relationship of log (SERS intensity) versus log (concentration).

We have also studied ammonium nitrate reporting a sensitivity of $5\mu M$ with an RSD of 4% as shown in figure 4.43. A pesticide molecule thiram has also been studied with 100 nM sensitivity as shown in figure 4.44. The durability of the samples has been studied with 50 μM of MB at regular intervals of time and a recognisable fingerprint of MB was found until 90 days as shown in the figure 4.45.

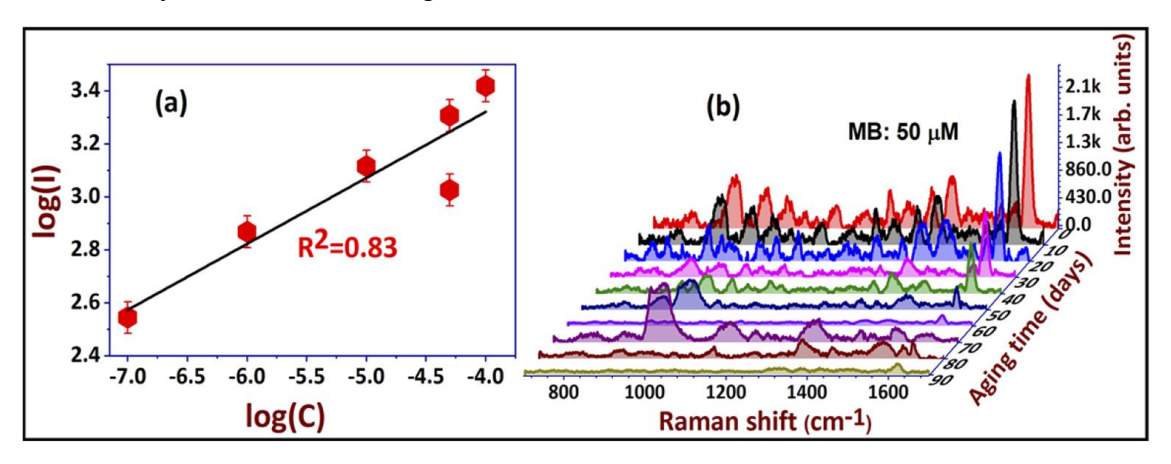


Figure 4.45: (a) Linear dependence of log (SERS intensity) versus log (analyte concentration) for the principal modes of MB molecules, (b) The durability estimation of AgNPs@FSpSi-60min substrate with 50 μ M concentration of MB over a period of 90 days.

The intensity and concentration fits that are used to calculate the LOD are presented in figure 4.46. The overall relation between intensity and concentration is non-linear and is linear for lower concentrations. The slope of the linear graphs is an important parameter for calculating LODs as presented in equation (1.1). The R² for the linear fits for all the analytes is greater than 95% and LODs are approximated using the slope. The results are summarised in the table 4.3.

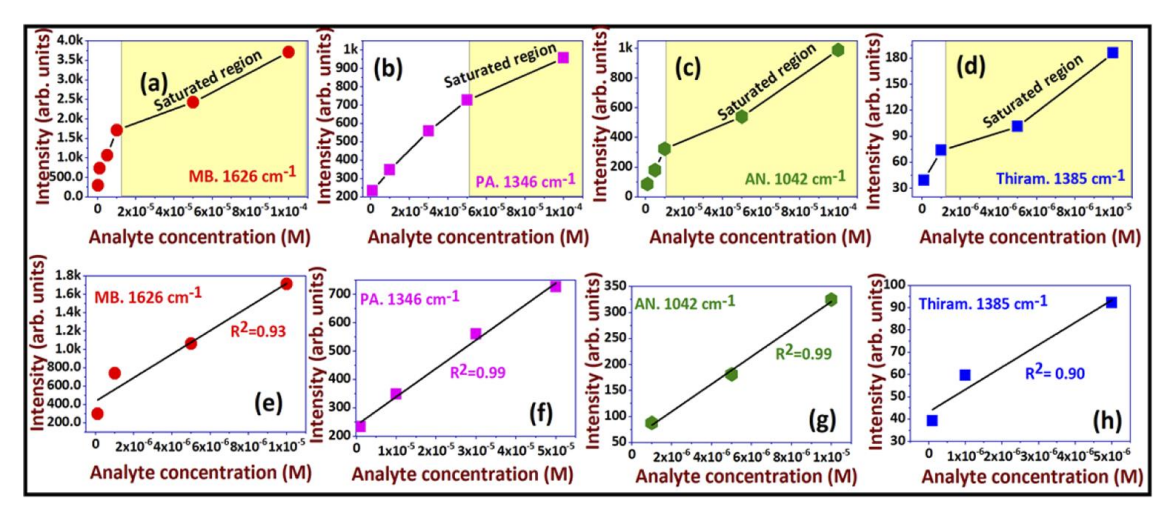


Figure 4.46: The SERS intensity versus analyte concentration for (a) MB - 1626 cm⁻¹ (b) PA - 1346 cm⁻¹ (c) AN - 1042 cm⁻¹ (d) thiram-1385 cm⁻¹, and (e)-(h) Linear dependence of the log SERS intensities verses lower molecular concentrations.

Table 4.3: Summary of analytes detected and the SERS parameter for studies on pSi.

Molecule	Raman peak	Lowest detected	AEF	LOD
	[cm ⁻¹]	conc. [M]		
Thiram	1385	10-7	2.9×10 ⁴	1 μM
AN	1042	10-6	1.0×10 ⁵	2 μΜ
PA	1346	5×10 ⁻⁶	1.3×10 ⁴	1 μM
MB	1626	10-7	7.4×10 ⁵	50 nM

4.6. Conclusion and Scope

This chapter summarises synthesis and application of novel anisotropic, flexible SERS substrates for SERS based trace detection of diverse analyte molecules including, explosives, pesticides, bacteria, food adulterants, environmental pollutants and biomolecules. Wafer scale, highly branched, dense Ag nanodendrites decorated with Au nanoparticles were synthesised by a simple electroless etching method of Si in the presence of HF. The samples have demonstrated trace detection with prolonged shelf life for antibiotics (penicillin, kanamycin and ampicillin), DNA bases (adenine, cytosine), explosive (AN) and pesticide thiram with nanomolar sensitivity. 2-D material, laser ablated MOS2 coated plasmonic SiNWs have demonstrated additional enhancement in addition to electromagnetic enhancement enabling trace detection of diverse analytes with increased durability. Hydrophobic filter paper that has been fabricated by spin coating with Si oil has been demonstrated as the so far cheapest method to modify the surface of the filter paper. This substrate has been used for quantification of trace analytes, CV and PA using machine learning algorithms, PCA and SVR. Using a portable Raman spectrometer coupled with algorithms that take less than 10s to run, this is a rapid low-cost method for quantification in SERS so far. Free standing, low cost, flexible porous Si decorated with Ag NPs has demonstrated trace detection of AN, thiram, and MB with a reproducibility of less than 8%. The durability of the samples can be significantly improved by storing them in vacuum sealed conditions in view of commercial application. The enhancement for the case HFP can be significantly increased if colloidal anisotropic NPS like stars and triangle are used instead of spherical NPs.

References

- [1] J. Reguera, J. Langer, D. Jiménez De Aberasturi, L.M. Liz-Marzán, Anisotropic metal nanoparticles for surface enhanced Raman scattering, Chem. Soc. Rev. 46 (2017) 3866–3885. https://doi.org/10.1039/c7cs00158d.
- [2] K. Rhee, A. Tukova, M. Tavakkoli Yaraki, Y. Wang, Nanosupernova: a new anisotropic nanostructure for SERS, Nanoscale. 15 (2023) 2087–2095. https://doi.org/10.1039/d2nr05287c.
- [3] B. Lim, M. Jiang, P.H.C. Camargo, E.C. Cho, J. Tao, X. Lu, Y. Zhu, Y. Xia, Pd-Pt bimetallic nanodendrites with high activity for oxygen reduction, Science. 324 (2009) 1302–1305. https://doi.org/10.1126/science.1170377.
- [4] B.D. Adams, G. Wu, S. Nlgro, A. Chen, Facile synthesis of Pd-Cd nanostructures with high capacity for hydrogen storage, J. Am. Chem. Soc. 131 (2009) 6930–6931. https://doi.org/10.1021/ja901798u.
- [5] A.Y. Li Fu, Tasnuva Tamanna, Wen-Jing Hu, Chemical preparation and applications of silver dendrites, Chem. Pap. 68 (2014) 1283–1297. https://doi.org/10.2478/s11696-014-0582-2.
- [6] A. Taleb, C. Mangeney, V. Ivanova, Electrochemical synthesis using a self-assembled Au nanoparticle template of dendritic films with unusual wetting properties, Nanotechnology. 22 (2011) 205301 https://doi.org/10.1088/0957-4484/22/20/205301.
- [7] S. Kaniyankandy, J. Nuwad, C. Thinaharan, G.K. Dey, C.G.S. Pillai, Electrodeposition of silver nanodendrites, Nanotechnology. 18 (2007) 125610. https://doi.org/10.1088/0957-4484/18/12/125610.
- [8] M. Matsushita, M. Sano, Y. Hayakawa, H. Honjo, Y. Sawada, Fractal structures of zinc metal leaves grown by electrodeposition, Phys. Rev. Lett. 53 (1984) 286–289. https://doi.org/10.1103/PhysRevLett.53.286.
- [9] D. Li, Z. Zheng, Y. Lei, S. Ge, Y. Zhang, Y. Zhang, K.W. Wong, F. Yang, W.M. Lau, Design and growth of dendritic Cu2-xSe and bunchy CuSe hierarchical crystalline aggregations, CrystEngComm. 12 (2010) 1856–1861. https://doi.org/10.1039/b919087m.
- [10] T. Qiu, X.L. Wu, Y.F. Mei, P.K. Chu, G.G. Siu, Self-organized synthesis of silver dendritic nanostructures via an electroless metal deposition method, Appl. Phys. A Mater. Sci. Process. 81 (2005) 669–671. https://doi.org/10.1007/s00339-005-3263-8
- [11] T.A. Witten, L.M. Sander, Diffusion-limited aggregation, Phys. Rev. B. 27 (1983) 5686–5697. https://doi.org/10.1103/PhysRevB.27.5686.
- [12] M. V Mandke, S.H. Han, H.M. Pathan, Growth of silver dendritic nanostructures via electrochemical route, CrystEngComm. 14 (2012) 86–89. https://doi.org/10.1039/c1ce05791j.
- [13] M.J. Lo Faro, C. D'andrea, A.A. Leonardi, D. Morganti, A. Irrera, B. Fazio, Fractal silver dendrites as 3D SERS platform for highly sensitive detection of biomolecules in hydration conditions, Nanomaterials. 9 (2019) 1630.

- https://doi.org/10.3390/nano9111630.
- [14] V.S. Vendamani, S.V.S.N. Rao, A.P. Pathak, V.R. Soma, Silicon Nanostructures for Molecular Sensing: A Review, ACS Appl. Nano Mater. 5 (2022) 4550–4582. https://doi.org/10.1021/acsanm.1c04569.
- [15] X. Li, P.W. Bonn, Metal-assisted chemical etching in HF/H2O2 produces porous silicon, Appl. Phys. Lett. 77 (2000) 2572–2574. https://doi.org/10.1063/1.1319191.
- [16] V.S. Vendamani, R. Beeram, S.V.S. Nageswara Rao, A.P. Pathak, V.R. Soma, Trace level detection of explosives and pesticides using robust, low-cost, free-standing silver nanoparticles decorated porous silicon, Opt. Express. 29 (2021) 30045. https://doi.org/10.1364/oe.434275.
- [17] A. Wang, L. Jiang, X. Li, Q. Xie, B. Li, Z. Wang, K. Du, Y. Lu, Low-adhesive superhydrophobic surface-enhanced Raman spectroscopy substrate fabricated by femtosecond laser ablation for ultratrace molecular detection, J. Mater. Chem. B. 5 (2017) 777–784. https://doi.org/10.1039/c6tb02629j.
- [18] Lee M, Oh K, Choi HK, Lee SG, Youn HJ, Lee HL, Jeong DH, Subnanomolar Sensitivity of Filter Paper-Based SERS Sensor for Pesticide Detection by Hydrophobicity Change of Paper Surface, ACS sensors, 3(2018), 151-159. https://doi.org/10.1021/acssensors.7b00782.
- [19] F. De Angelis, F. Gentile, F. Mecarini, G. Das, M. Moretti, P. Candeloro, M.L. Coluccio, G. Cojoc, A. Accardo, C. Liberale, R.P. Zaccaria, G. Perozziello, L. Tirinato, A. Toma, G. Cuda, R. Cingolani, E. Di Fabrizio, Breaking the diffusion limit with super-hydrophobic delivery of molecules to plasmonic nanofocusing SERS structures, Nat. Photonics. 5 (2011) 682–687. https://doi.org/10.1038/nphoton.2011.222.
- [20] N. V. Godoy, D. García-Lojo, F.A. Sigoli, J. Pérez-Juste, I. Pastoriza-Santos, I.O. Mazali, Ultrasensitive inkjet-printed based SERS sensor combining a high-performance gold nanosphere ink and hydrophobic paper, Sensors Actuators, B Chem. 320 (2020) 128412. https://doi.org/10.1016/j.snb.2020.128412.
- [21] A. Raza, B. Saha, In situ silver nanoparticles synthesis in agarose film supported on filter paper and its application as highly efficient SERS test stripes, Forensic Sci. Int. 237 (2014) 42–46. https://doi.org/10.1016/j.forsciint.2014.01.019.
- [22] D.J. Lee, D.Y. Kim, Hydrophobic paper-based SERS sensor using gold nanoparticles arranged on graphene oxide flakes, Sensors. 19 (2019) 8–14. https://doi.org/10.3390/s19245471.
- [23] C. Zhang, T. You, N. Yang, Y. Gao, L. Jiang, P. Yin, Hydrophobic paper-based SERS platform for direct-droplet quantitative determination of melamine, Food Chem. 287 (2019) 363–368. https://doi.org/10.1016/j.foodchem.2019.02.094.
- [24] D.Z. and W.S. Ruoyang Chen, Liyuan Zhang, Wetting and Drying of Colloidal Droplets: Physics and Pattern Formation, Advances in Colloid Science (2016), 3-25.
- [25] A. Nilghaz, L. Zhang, W. Shen, Coffee stains on paper, Chem. Eng. Sci. 129 (2015) 34–41. https://doi.org/10.1016/j.ces.2015.02.017.
- [26] V.S. Vendamani, R. Beeram, S.V.S.N. Rao, S.V. Rao, Protocol for designing AuNP-capped Ag dendrites as surface-enhanced Raman scattering sensors for trace

- molecular detection, STAR Protoc. 4 (2023) 102068. https://doi.org/10.1016/j.xpro.2023.102068.
- [27] R. Beeram, V.S. Vendamani, S.V. Rao, Flexible Paper Substrate with Silver Dendrites for Trace Detection of Dye and Explosive Molecules using SERS, Work. Recent Adv. Photonics, WRAP 2022. (2022). https://doi.org/10.1109/WRAP54064.2022.9758296.
- [28] V.S. Vendamani, S.V.S.N. Rao, A.P. Pathak, V.R. Soma, Robust and cost-effective silver dendritic nanostructures for SERS-based trace detection of RDX and ammonium nitrate, RSC Adv. 10 (2020) 44747–44755. https://doi.org/10.1039/d0ra08834j.
- [29] T.E. Agustina, W. Handayani, C. Imawan, The UV-VIS Spectrum Analysis From Silver Nanoparticles Synthesized Using Diospyros maritima Blume. Leaves Extract, in: Proc. 3rd KOBI Congr. Int. Natl. Conf. (KOBICINC 2020), Atlantis Press, 2021: pp. 411–419. https://doi.org/10.2991/absr.k.210621.070.
- [30] A. R. Bijanzadeh, A study of the surface plasmon absorption band for nanoparticles, Int. J. Phys. Sci. 7 (2012). https://doi.org/10.5897/ijps11.893.
- [31] Z. Cheng, Y. Qiu, Z. Li, D. Yang, S. Ding, G. Cheng, Z. Hao, Q. Wang, Fabrication of silver dendrite fractal structures for enhanced second harmonic generation and surface-enhanced Raman scattering, Opt. Mater. Express. 9 (2019) 860. https://doi.org/10.1364/ome.9.000860.
- [32] X. Wang, C. Liu, C. Gao, K. Yao, S.S.M. Masouleh, R. Berté, H. Ren, L. de S. Menezes, E. Cortés, I.C. Bicket, H. Wang, N. Li, Z. Zhang, M. Li, W. Xie, Y. Yu, Y. Fang, S. Zhang, H. Xu, A. Vomiero, Y. Liu, G.A. Botton, S.A. Maier, H. Liang, Self-Constructed Multiple Plasmonic Hotspots on an Individual Fractal to Amplify Broadband Hot Electron Generation, ACS Nano. 15 (2021) 10553–10564. https://doi.org/10.1021/acsnano.1c03218.
- [33] S. Fateixa, H.I.S. Nogueira, T. Trindade, Surface-Enhanced Raman Scattering Spectral Imaging for the Attomolar Range Detection of Crystal Violet in Contaminated Water, ACS Omega. 3 (2018) 4331–4341. https://doi.org/10.1021/acsomega.7b01983.
- [34] S. Hamad, G.K. Podagatlapalli, M.A. Mohiddon, V.R. Soma, Cost effective nanostructured copper substrates prepared with ultrafast laser pulses for explosives detection using surface enhanced Raman scattering, Appl. Phys. Lett. 104 (2014). https://doi.org/10.1063/1.4885763.
- [35] Y. Tzeng, B.-Y. Lin, Silver-Based SERS Pico-Molar Adenine Sensor, Biosensors. 10 (2020) 122. https://doi.org/10.3390/bios10090122.
- [36] F. Madzharova, Z. Heiner, M. Gühlke, J. Kneipp, Surface-Enhanced Hyper-Raman Spectra of Adenine, Guanine, Cytosine, Thymine, and Uracil, J. Phys. Chem. C. 120 (2016) 15415–15423. https://doi.org/10.1021/acs.jpcc.6b02753.
- [37] L.A. Wali, K.K. Hasan, A.M. Alwan, Rapid and Highly Efficient Detection of Ultra-low Concentration of Penicillin G by Gold Nanoparticles/Porous Silicon SERS Active Substrate, Spectrochim. Acta Part A Mol. Biomol. Spectrosc. 206 (2019) 31–36. https://doi.org/10.1016/j.saa.2018.07.103.
- [38] W.K. Kim, N. Karabasil, S. Bulajic, K.D. Dunkley, T.R. Callaway, T.L. Poole, S.C.

- Ricke, R.C. Anderson, D.J. Nisbet, Comparison of spontaneous antibiotic resistance frequency of Salmonella typhimurium growth in glucose amended continuous culture at slow and fast dilution rates, J. Environ. Sci. Heal. Part B Pestic. Food Contam. Agric. Wastes. 40 (2005) 475–484. https://doi.org/10.1081/PFC-200047598.
- [39] H. Zhou, Y. Liang, J. Zhang, F. Wang, Detection of benzylpenicillin sodium and ampicillin residue based on flower-like silver nanostructures using surface-enhanced Raman spectroscopy, Res. Chem. Intermed. 48 (2022) 117–128. https://doi.org/10.1007/s11164-021-04574-9.
- [40] A.K. Verma, Ultrasensitive surface-enhanced Raman spectroscopy detection of explosive molecules with multibranched silver nanostructures, J. of Raman Spectro., 53(2022), 694-708. https://doi.org/10.1002/jrs.6294.
- [41] R. Beeram, D. Banerjee, L.M. Narlagiri, V.R. Soma, Machine learning for rapid quantification of trace analyte molecules using SERS and flexible plasmonic paper substrates, Anal. Methods. 14 (2022) 1788–1796. https://doi.org/10.1039/d2ay00408a.
- [42] V.S. Vendamani, S.V.S. Nageswara Rao, S. Venugopal Rao, D. Kanjilal, A.P. Pathak, Three-dimensional hybrid silicon nanostructures for surface enhanced Raman spectroscopy based molecular detection, J. Appl. Phys. 123 (2018). https://doi.org/10.1063/1.5000994.
- [43] V.S. Vendamani, R. Beeram, V.R. Soma, MoS2 nanosheets decorated plasmonic silicon nanowires as SERS substrates for ultra-sensitive multiple analyte detection,
 J. Alloys Compd. 959 (2023) 170573. https://doi.org/10.1016/j.jallcom.2023.170573.
- [44] R.A. Alvarez-Puebla, D.S. Dos Santos, R.F. Aroca, Surface-enhanced Raman scattering for ultrasensitive chemical analysis of 1 and 2-naphthalenethiols, Analyst. 129 (2004) 1251–1256. https://doi.org/10.1039/b410488a.
- [45] V.S. Vendamani, R. Beeram, M.M. Neethish, S.V.S.N. Rao, S.V. Rao, Wafer-scale silver nanodendrites with homogeneous distribution of gold nanoparticles for biomolecules detection, IScience. 25 (2022) 104849. https://doi.org/10.1016/j.isci.2022.104849.
- [46] J.D. Reyes, B.D. Gilbert, L. College, Determination of the optimal conditions for bovine serum albumin surface enhanced Raman scattering on silver colloids, (2000) 97128.
- [47] K. Hamasha, Q.I. Mohaidat, R.A. Putnam, R.C. Woodman, S. Palchaudhuri, S.J. Rehse, Sensitive and specific discrimination of pathogenic and nonpathogenic Escherichia coli using Raman spectroscopy—a comparison of two multivariate analysis techniques, Biomed. Opt. Express. 4 (2013) 481. https://doi.org/10.1364/boe.4.000481.
- [48] M. Kahraman, M.M. Yazici, F. Sahin, O.F. Bayrak, M. Culha, Reproducible surface-enhanced Raman scattering spectra of bacteria on aggregated silver nanoparticles., Appl. Spectrosc. 61 (2007) 479–485. https://doi.org/10.1366/000370207780807731.
- [49] X. Zhou, Z. Hu, D. Yang, S. Xie, Z. Jiang, R. Niessner, C. Haisch, H. Zhou, P. Sun,

- Bacteria Detection: From Powerful SERS to Its Advanced Compatible Techniques, Adv. Sci. 7 (2020) 1–23. https://doi.org/10.1002/advs.202001739.
- [50] M.S.S. Bharati, V.R. Soma, Flexible SERS substrates for hazardous materials detection: recent advances, Opto-Electronic Adv. 4 (2021) 210048–210048. https://doi.org/10.29026/oea.2021.210048.
- [51] M. Lee, K. Oh, H.K. Choi, S.G. Lee, H.J. Youn, H.L. Lee, D.H. Jeong, Subnanomolar Sensitivity of Filter Paper-Based SERS Sensor for Pesticide Detection by Hydrophobicity Change of Paper Surface, ACS Sensors. 3 (2018) 151–159. https://doi.org/10.1021/acssensors.7b00782.
- [52] A.F. Stalder, T. Melchior, M. Müller, D. Sage, T. Blu, M. Unser, Low-bond axisymmetric drop shape analysis for surface tension and contact angle measurements of sessile drops, Colloids Surfaces A Physicochem. Eng. Asp. 364 (2010) 72–81. https://doi.org/10.1016/j.colsurfa.2010.04.040.
- [53] H.F.M. Boelens, R.J. Dijkstra, P.H.C. Eilers, F. Fitzpatrick, J.A. Westerhuis, New background correction method for liquid chromatography with diode array detection, infrared spectroscopic detection and Raman spectroscopic detection, J. Chromatogr. A. 1057 (2004) 21–30. https://doi.org/10.1016/j.chroma.2004.09.035.
- [54] R.W. Schafer, What is a Savitzky-Golay Filter? (2011) 111–117.
- [55] M.S.S. Bharathi, C. Byram, K. Nehra, P. Senthil Kumar, S.V. Rao, Filter paper loaded with gold nanoparticles as flexible SERS substrates for sensing applications, AIP Conf. Proc. 2265 (2020). https://doi.org/10.1063/5.0016882.
- [56] S.L. Kleinman, E. Ringe, N. Valley, K.L. Wustholz, E. Phillips, K.A. Scheidt, G.C. Schatz, R.P. Van Duyne, Single-molecule surface-enhanced raman spectroscopy of crystal violet isotopologues: Theory and experiment, J. Am. Chem. Soc. 133 (2011) 4115–4122. https://doi.org/10.1021/ja110964d.
- [57] C. Byram, S. Sathya, B. Moram, A.K. Shaik, V.R. Soma, Versatile gold based SERS substrates fabricated by ultrafast laser ablation for sensing picric acid and ammonium nitrate, Chem. Phys. Lett. 685 (2017) 103–107. https://doi.org/10.1016/j.cplett.2017.07.043.
- [58] A. Uhlir, Electrolytic Shaping of Germanium and Silicon, Bell Syst. Tech. J. 35 (1956) 333–347. https://doi.org/10.1002/j.1538-7305.1956.tb02385.x.
- [59] V.S. Vendamani, S.V.S.N. Rao, A.P. Pathak, Structural and optical properties of porous silicon prepared by anodic etching of irradiated silicon, Nucl. Instruments Methods Phys. Res. Sect. B Beam Interact. with Mater. Atoms. 315 (2013) 188– 191. https://doi.org/10.1016/j.nimb.2013.04.085.
- [60] V.S. Vendamani, S. Hamad, V. Saikiran, A.P. Pathak, S. Venugopal Rao, V. V. Ravi Kanth Kumar, S.V.S. Nageswara Rao, Synthesis of ultra-small silicon nanoparticles by femtosecond laser ablation of porous silicon, J. Mater. Sci. 50 (2015) 1666–1672. https://doi.org/10.1007/s10853-014-8727-9.

Intentional Blank Page

Chapter 5 Overcoming Signal Fluctuations in the SERS for Improved Field Applications

Abstract

This chapter attempts to address the challenge of signal fluctuations in SERS using deep learning techniques. SERS has demonstrated its enormous ability to detect trace analytes at the laboratory scale, with prospective applications in various fields. The undesirable signal reliability and blinking issues limit the onsite detection capabilities of SERS due to several factors, including analyte adsorption, an uneven distribution of hotspots, molecule orientation, and so on. SERS has an intrinsic tendency to exhibit signal variations, rendering it a stochastic process. Due to these signal fluctuations, identifying a spectrum as a molecule representative relies seriously on an expert. This chapter starts with understanding the origin of signal fluctuations in SERS-based trace detection and how machine learning techniques will be helpful. We will understand the working of NNs and develop a neural network-aided SERS model (NNAS) that effectively identifies reliable SERS spectra of trace explosives (Tetryl, Picric Acid) and a dye molecule, crystal violet, without an expert's influence. Massive SERS data has been collected using Ag-decorated Au nanodendrites synthesized by chemical methods described in Chapter 4. The model eliminates the reliability of the expert by classifying the spectra as representative (RS) and non-representative (NRS) using a unique signal-to-noise ratio technique. The experimental parameters of the SERS experiment, like excitation wavelength, laser power, and spot size, were systematically varied to simulate the general variation of experimental parameters in the SERS across instruments. A validation set and out-of-sample testing were used to validate the model, which had an accuracy of 98% (0.98) for all analytes. We believe that NNAS goes a long way in automating and bridging the gap between laboratory performance and field for the case of SERS-based trace detection.

5.1. Introduction

In recent years, machine learning (ML) has been shaping our lives in various ways offering convenience and newfound ways to discover deep insights through data. With its ability to extract information from large and complex datasets in diverse fields across sciences, there is a surge in the usage of ML for data analysis, especially in spectroscopy [1]. Traditional linear methods for processing the data are no longer sufficient to address real world applications through spectroscopy. With this need, there is an emergence of new field called 'chemometrics'. Chemometrics essentially deals with developing mathematical and statistical models to optimise measurements and experiments in analytical chemistry and also to extract useful insights from the experimental data in this discipline [2]. SERS being one of the popular spectroscopic tool, has also seen a welcoming change of usage in chemometrics for data analysis [3]. The emergence of SERS in biology and complex systems, increased computing power, and the availability of opensource machine learning libraries such as TensorFlow, Keras, and Scikitlearn, which are easy to implement, have facilitated this development [3].

Field applications concerning SERS has several characteristics that make it particularly suited for the usage of machine learning in data processing. Over the years, innovations in plasmonic materials have resolved the issue of low sensitivity and drastically improved the limit of detection (LOD) in SERS, allowing even for single molecule detection [4] [5]. However, the SERS spectra for the case of trace detection exhibit considerable variation in intensity and spectral profiles due to the orientation of the molecules concerning the SERS surface, uneven adsorption and inhomogeneous distribution of hotspots [6]. This stands in the way of translating well-established benefits of SERS to the field for practical applications. Conventional linear-based methods are unsuitable for capturing the various possible relations and identifying the spectra in complex matrices during trace identification. As a rescue, machine learning (ML) based methods are well-suited to capture complex relationships within large sets of spectra. Thus far, the usage of ML in SERS has focused only on post data processing applications like a) identification of the spectrum, b) classification, c) quantification [7] [8]. Attempts were also made to use ML algorithms to enhance the data collection process [9], estimate scattering efficiency [10] and to further enhance the SERS signal through PCA [11]. This chapter discusses how the ML algorithms can be trained to recognize features in the SERS spectra and assign

them to the proper label corresponding to the identity of the analyte and understand different correlations on the field devoid of any expert reliance.

5.1.1. Machine Learning Algorithms

Machine learning refers to a computer program or system that can acquire knowledge by analysing raw data and identifying key features through a process aptly called as 'training'. The knowledge gained through this process can then be utilized to solve real-world problems by making informed decisions after thorough 'evaluation'. Choice of the ML model, size of the data set, quality of the data, parameters in the model, play a key role in the performance of the model's predictions. By analysing and learning from the data through the model, ML systems can be trained to improve the accuracy and effectiveness, analogous to human learning. ML algorithms can be classified into three main categories: supervised learning, unsupervised learning, and reinforcement learning as shown in figure 14 of chapter 1. The discussion of these classifications and different machine learning algorithms is thoroughly discussed in chapter 1. We will limit the discussion in this section only to the models studied in this work.

5.1.1.1. Neural Networks (NNs)

Many scientific inventions have been inspired by observing living forms around us. Helicopters were invented inspiring from flying birds. Lotus leaves inspired many hydrophobic surface applications. Solar cells architecture that was inspired from leaf folds and so on. One such inspiration that revolutionized modern day life to an unimaginable scale are neural networks. The architecture of NNs is inspired from the functioning of human brain transferring information from one neuron to neuron and learning from the patterns. Though the current NNs have moved far away from their biological analogy, they have made incredible progress and became a part of our day-to-day life through recommendation systems, voice recognition tools, face recognition apps and computer vision applications to name a few. NNs are typically data hungry and need a large amount of data for training. The availability of big data and proven superior performance of NNs relative to other ML models has reinforced the development in NNs. Innovations in the direction of computation devices and development of libraries like Tensorflow and Keras has made the implementation of NNs easier in the recent years. NNs recognise complex patterns from given data by a series of mathematical operations classified as forward and backward propagation as shown in figure 5.1. NNs are known to extract features by themselves without any need for data pre-processing algorithms. The detailed mechanisms of their working are discussed in the sections that follow.

The fundamental unit of a NN is called as a 'node' and functions analogous to the neuron in the brain as represented in figure 5.2. Different nodes are put together in 'layers' depending on the complexity of the problem in order to build a model. The first layer is called as an input layer, the intermediate one is called hidden layers while the final layer is called an output layer. The user inputs a feature vector with N dimensions represented as x_i with i = 1, 2, ...N into an input layer with N neurons. At each of the neurons weighted sum of the input function along with a bias term is calculated as $h^{[j]}$, index j representing the layer number and is 1 for input layer (equation 1). A NN uses weights ($W^{[j]}$) to indicate the importance of a particular feature in predicting a final value based on the input value. A bias term, $b^{[j]}$, is also added which gives a flexibility to shift the activation function left or right. The goal of the training mechanism in NNs is to find optimum values of the weights and biases through iterations of forward and backward propagation (called as 'epochs'). The convergence of the model and its progression can be studied by analysing learning curves which are graphs of loss and iterations (epochs).

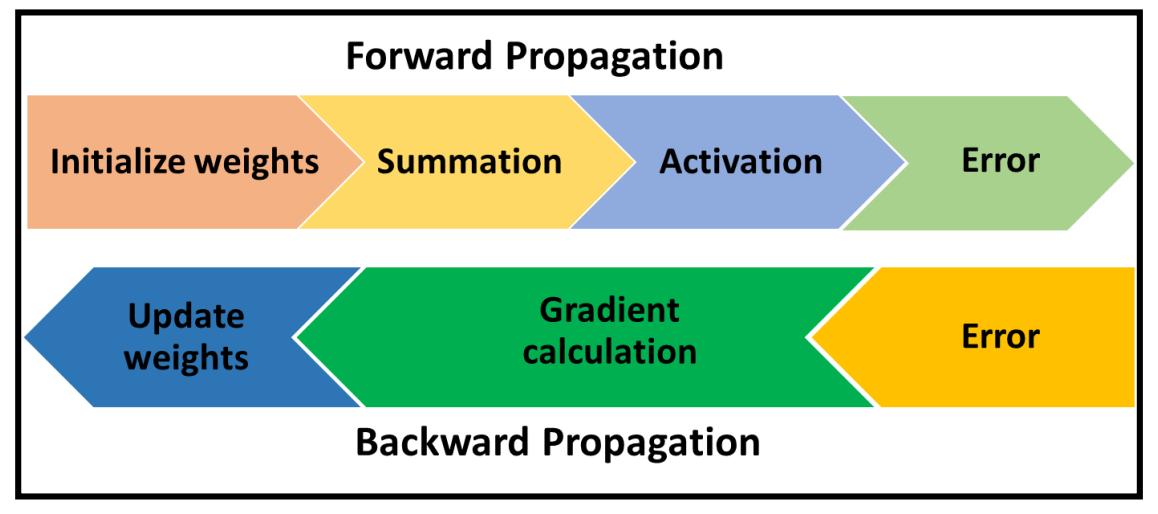


Figure 5.1: Schematic of flow of training mechanism in NNs through a series of mathematical operations classified as forward and backward propagation.

Once the input feature vector is given, the weighted sum of the input vector along with a bias term is calculated at each node. This summation is then passed through an activation function (A^[j]) in order to add non-linearity to capture complex patterns the model (equation 2). As the name suggests, activation function decides whether a neuron should be activated or not depending on the threshold. There are different activation functions like ReLU, sigmoid, SELU and tanh, and are used depending on the problem at hand. Of

all, ReLU is known to be computationally inexpensive and hence we have restricted to using ReLU in this thesis. At the output neuron we have used sigmoid as the activation function [equation (3)].

$$h^{[1]} = x_i W^{[1]} + b^{[1]} (5.1)$$

$$A^{[1]} = a(h^{[1]}) (5.2)$$

$$ReLU = \max(0, x)$$
, Sigmoid = $\frac{1}{1+e^{-x}}$ (5.3)

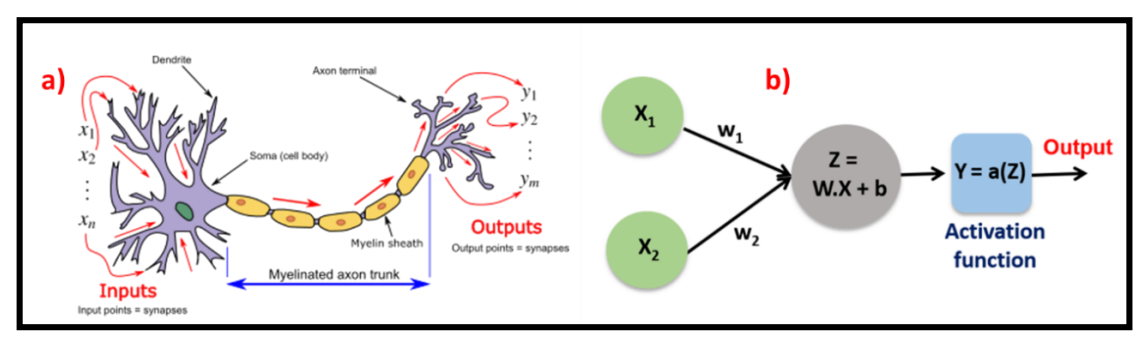


Figure 5.2: a) Representation of a single neuron with input and output (Image taken from Wikipedia), b) A single node of a NN with input, activation function and an output.

Followed by this, the input for the second layer will be the output of the first layer followed by an activation function as represented by equation 4 and 5. This process continues for all the hidden layers of the network until the output layer.

$$h^{[2]} = W^{[2]}A^{[1]} + b^{[2]} (5.4)$$

$$A^{[2]} = a(h^{[2]}) (5.5)$$

The ultimate goal of any ML model is to make predictions that are close to the actual value. This is achieved by a process aptly called as 'optimization'. In the specific case of NNs, the goal of the optimization algorithm is to find weights and biases that would eventually minimize the error. Gradient descent algorithms are very popular for this task. The optimization algorithm starts by randomly initializing the weight and updating them in an interactive process until they are close to the predicted values (\hat{Y}) . This deviation from actual values (Y) is calculated for each iteration through a function called as cost function, J, as given below in equation 6,

$$J = \frac{1}{2} (\hat{Y} - Y)^2 \tag{5.6}$$

The whole exercise discussed so far until calculation of weights is called as forward pass. The weights are updated in backward pass through calculating the gradient. The algorithm in each iteration moves step by step to the minimum and the size of the step depends on the 'learning rate (η)' of the NN and it determines the rate of convergence. The goal of this sequential iterations is to minimize the cost function. Each of such iteration is called as an 'epoch'. The number of gradients to be computed depends on the number of parameters in the model and are calculated using the chain rule in differential equations as below in equation (5.7),

$$\frac{dJ}{dW^{[1]}} = \frac{dJ}{dA^{[1]}} \frac{dA^{[1]}}{dh^{[1]}} \frac{dh^{[1]}}{dW^{[1]}}$$
(5.7)

After the gradient, in this process the weights are updated as below,

$$W_{new} = W_{old} - \eta \frac{dJ}{dW}$$
 (5.8)

For the case of NNAS, we have used a stochastic gradient descent (SGD) method as an optimiser and binary cross entropy as the cost function. Following the computation of loss on each training example, the model's parameters are changed for the case of SGD. Consequently, the model parameters will be updated m times in one cycle if the dataset contains m training values.

Neural networks have a tendency to overfit the data. Overfitting is a scenario where the model performs exceptionally well on the training data while performing poorly on validation and test data set. Regularization is a technique that is used to overcome the problem of overfitting in NNs. It is a slight perturbation to the cost function and penalizes certain weight matrices.

$$J = \frac{1}{2} (\hat{Y} - Y)^2 + Regularization term$$
 (5.9)

We have used accuracy as a measure of performance of the model. Accuracy for the case of classification is defined as below,

$$Accuracy = \frac{TP + TN}{TP + TN + FP + FN} \tag{5.10}$$

Here TP, TN, FP and FN are true positive, true negative, false positive and false negative respectively. Through a process, popularly called as hyperparameter tuning, different parameters like activation function, optimizer, scaler and learning rate are changed in order to get optimum accuracy. The final architecture of the neural network along is represented

in figure 5.3 b). Figure 5.3 a) depicts similar layers of interconnected neurons in the cerebral part of the brain that recognise patterns as an analogy.

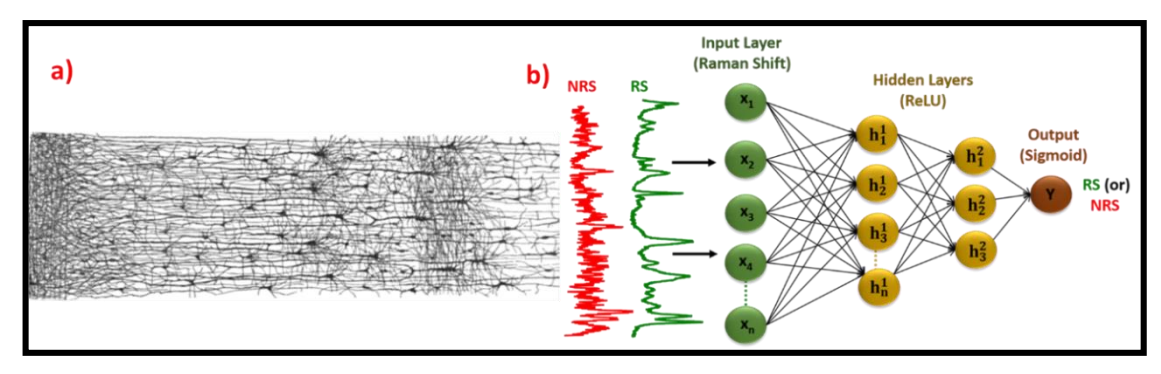


Figure 5.3: a) Sketch of cerebral cortex showing scheme of layers of interconnected neurons. Image taken from Wikipedia (https://en.wikipedia.org/wiki/Cerebral_cortex). b) Architecture of NNAS used in this study with two hidden layers, input and output layers.

5.2. Signal fluctuations in the SERS

The enhancement mechanisms in SERS are discussed elaborately in chapter 1 section 1.4. Electromagnetic enhancement is the significant contributor to the SERS signal enhancement and originates through high field intensity in the vicinity of metal nanoparticles popularly called as 'hotspots' [12]. Chemical enhancement is a consequence of change in polarizability that results from the interaction of probe molecules with the nanostructure either chemically or physically [13]. The ability of the SERS to detect trace or even single molecule and other merits are purely a consequence of these mechanisms. However, through the same mechanisms that lead to signal enhancement, SERS also experiences many signal fluctuations and deviations from the conventional Raman spectroscopy making it extremely reliable on an expert. In the following discussion we will focus on the origin of such signal fluctuations in first place.

The first fact comes from the fact that LSPR resonances that aid SERS are heavily dependent on the wavelength of the excitation source as studied in chapter 1, section 1.3. As a result of this dependence, some of the Raman modes might be selectively enhanced while the others might get quenched [14] [15]. Further, the orientation of the molecule with respect to the metal nanostructure and the symmetry of the Raman mode also dictates the selective enhancement and quenching of the modes[16]. These are guided by the surface selection rules in SERS [6]. The orientation of the molecule with respect to the polarization of the incident laser beam also plays a crucial role and contribute to the signal fluctuations spatially [17] [18]. Upon adsorbing on the metal surface, depending on the

molecule and metal nanostructure chemistry, the molecule might also undergo chemical changes resulting in drastic change of Raman signature with respect to the actual molecule [19]. Oxidation of metal substrates that are widely used in SERS, all cause undesirable changes in the Raman signal [15]. All these possibilities reflect as slight or large shift in Raman peaks or in some cases even broadening of peaks making the identification extremely reliable on expert's knowledge. Photo bleaching and the formation of different photo-products are also reported in SERS [20].

The preparation of SERS substrates through various techniques also adds to the inherent deviations/fluctuations in SERS. In many instances, colloidal NPs are used as SERS substrates for detection of the analyte. In this scenario, given the Brownian motion associated with these colloids causing diffusion of molecules from the collection area, the intensity of the signal is known to fluctuate at any point of time [21]. These can be classified as temporal fluctuations as opposed to spatial fluctuations. Another popular technique that is in use is drop-casting where colloidal NPs are dropped on to a planar surface like Si or metal and waited to dry. Though this technique is easy to implement, it is known to cause inhomogeneous distribution of both probe and NPs which will eventually reflect in the SERS intensity [22]. Nevertheless, often when aided with a microscope these distributions can also be used to our advantage, like the recently reported coffee-ring effect aided SERS [23] [24]. These can be classified as spatial fluctuations. An alternative that is generally considered for drop casting is spin coating. Spin coating however, is known to have low efficiency in terms of number of particles that are adhered to the surface relative to the input which manifests as poor density of hotspots in SERS. In addition to these, SERS intensities are also vulnerable to laser effects that are caused during the excitation [25]. The colloids in all the cases are known to undergo small movements under the laser exposure probably through the local heating caused by the laser [26]. Long acquisition times, which are often a prerequisite for trace detection also cause photo bleaching when the laser beam is focused at a single spot for very long time. In the case of trace detection and even further for single molecule detection, the orientation of the molecule with respect to the hotpots also plays a key role in the enhancement. Even though these fixed substrates seem unchanging/unmoving at a glance, at a nanoscale range which is where LFIE predominates, there is still movement. The incidence of laser aggravates these changes at the hotspots causing heating and even change in the roughness of the substrate [27] [28]. Through laser induced photo-chemistry or through indirect heating of the substrate, the molecules are also known to desorb, diffuse or even undergo chemical transformation [29]. It has been also reported that the molecules move in an out of these hotspots causing signal 'blinking' [30]. Further, the illumination of laser is also known to cause significant geometric changes like change in the distance between the NPs in addition to their shape and size [31]. The near field enhancement is also known to lead to the formation of cavities through various forces which in turn cause signal fluctuations [32]. Given these contributions, it is difficult to ascertain specific reasons for the case of signal fluctuations in a single experiment and needs an extensive statistical analysis as done by selected groups [33] [34]. Figure 5.4 depicts schematic of hotspot distribution, molecules distributed on the nanostructure and associated signal fluctuations.

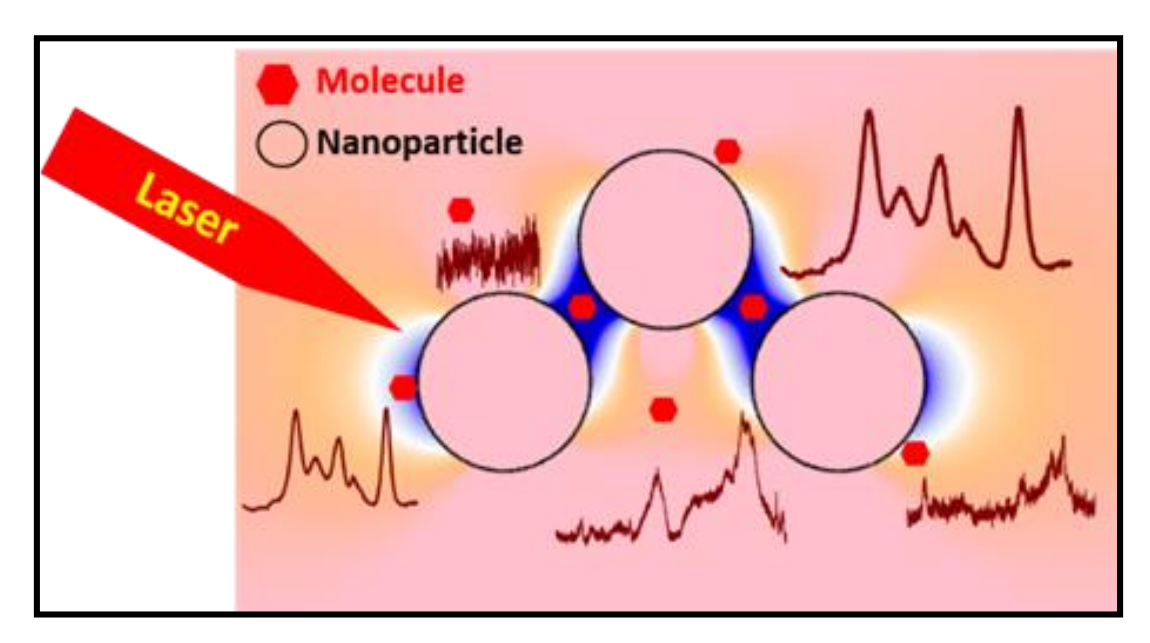


Figure 5.4: Schematic of distribution of probe molecules on a SERS substrate with hotspots and associated signal fluctuations.

All these effects are further magnified for the case of trace detection because the SERS signal originates from only a few molecules that are adsorbed on the substrate surface. Trace detection is heavily dependent on the hotspot enhancement and owing to the localization of the later, the signal intensity inherently fluctuates from point to point. On a SERS substrate typically these hotspots are known to occupy only a 1% or a fraction of the total area adding to the poor reproducibility of the signal [35]. Statistically this would mean that in the case of trace molecule detection, the detection is only possible if the molecule is present at that 1% surface area. In first stance this would convey that the role of hotspots is insignificant but it so happens that such small fraction contributes nearly 80% to the total signal emphasising their importance [36]. Diffusion of such molecules in

the presence of laser illumination either in or out of hotspots comes at a huge cost in terms of enhancement and could be a common occurrence especially for the case of physisorption [25,37,38]. On an other hand, a highly enhancing substrate comes at the cost of reproducibility analogous to the uncertainty relation [39]. The localization of hotspots restricts the number of molecules that can be adsorbed in these small fraction of area [18]. Photo bleaching of molecules in such enhanced local fields is also anticipated to happen [41] [42]. All these deviations are in many instances far from the mean value and often studied experimentally under the term long tailed distribution using statistics [35] [43]. Trace detection innovations in SERS focus on developing substrates with high density of hotspots but the very nature of these hotspots will eventually lead to the challenges in detection [44]. This temporal fluctuations in the intensity are in fact considered as a signature of single or few molecule detection [45]. Intensity fluctuations in the local field enhancement has been reported and discussed for the case of trace detection [46]. Detailed effects of temperature broadly called as thermal effects on the intensity fluctuation for trace detection were studied by both heating and cooling [40]. As an instance of this signal fluctuations, we have seen selective quenching, enhancement, photo bleaching and oxidation effects for the case of Picric Acid during our measurements. Figure 5.5 shows different SERS spectra observed under same experimental conditions but at different spatial point while performing mapping for the Picric Acid in this study supporting the discussions so far.

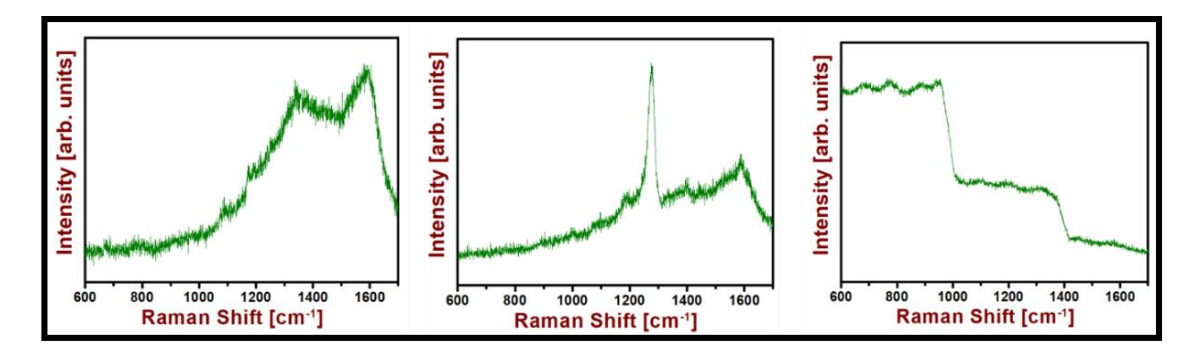


Figure 5.5: Different scenarios of SERS spectra of picric acid measured on same substrate of Au@Ag nanodendrites under experimental indication selective enhancement/quenching of peaks, effects of oxidation and photo bleaching.

5.3. Neural Network Aided SERS (NNAS)

All the shortcomings of SERS through its inherent signal fluctuations discussed so far make the measurements heavily dependent on an expert. In a lab scale environment, in the presence of an expert SERS has promised trace detection in the limits of attomolar [47,48],

femtomolar [39,49–51], and picomolar [52,53] molar detection. Single molecule SERS, through hugely debated has also been reported [54]. Xu et al. recently reported single haemoglobin molecule detection targeting hotspots between Ag nanoparticles [55]. Lin et al. have reported detection of single bacterium cell using immobilised plasmonic structures exploiting hotspots between Au nanoparticles[56]. Trace and ultra-trace detection of explosives using SERS has also been reported using different plasmonic materials by various research groups[57] [58]. However, in the present scenario these results are still at laboratory level and could not be translated onto the field [59].

ML techniques are being widely used in SERS focusing mainly on post data collection analysis, for example, in the case of classification [60–66], identification [64,67–72], and quantification [73–79] goals. Despite the promising application of ML, little or no work has been in SERS to automate the data collection process eradicating the huge dependence on expert. For the case of trace detection, any expert in the lab has to collect large volume of data before finding one representative spectra for various reasons discussed above. This is highly unreliable in field applications. Specifically, for the case of explosive detection, there are innovations in the direction of flexible substrates that offer easy collection of sample from surfaces through swabbing [80]. Low cost, durable, high density hotspot and reusable substrates have also been proposed for trace explosive detection [81]. It is also well known that high enhancement is a trade-off for reproducibility which would intern increase the reliability on an expert [36][82]. Despite these innovations in terms of plasmonic materials or instrumentations over the decades still did not take SERS to the field. In this regard, it is imperative to have an automated, streamlined and efficient SERS data collection system that would remove the reliance on expert. For this case we have employed a deep neural network model which we named as Neural Network Aided SERS (NNAS) as graphically depicted in figure 5.6.

In a recent work by Carney et al., they have attempted to improve the data collection efficiency and sampling in SERS through ML models [9]. Their model has used different ML algorithms like SVM, linear discriminant analysis (LDA), decision trees (DTs), random forest (RF) and an extreme gradient boosting (XGB) algorithms in order to classify and predict the SERS spectra as 'good', 'bad' and 'maybe'. The labelled data set that is used for training has been labelled by an expert manually when each spectrum is displayed to the user using a software. They have tested highly ordered commercial substrates and claim their model cannot be generalised to measurements done across different

instruments. Before building our own model, we have attempted to reproduce similar accuracy for trace explosives by manually labelling our data. In our observation, we have realised that the labelling is hugely prone to conformational bias and realised the boundary between what is representative and non-representative is thin especially for trace signals burring in noise. Confirmation bias in this case is an inevitable tendency to look for specific patterns in the signals with a pre-existing knowledge on how the signal looks like. Moreover, we realised the task is tedious specially to train algorithms that need huge amount of data to make accurate predictions. The present study proposes a novel approach to address the issue of spectra labelling for trace explosives detection without human intervention. The proposed method employs a unique SNR based analysis to differentiate between representative (R) and non-representative (NR) spectra. Additionally, we utilize an in-house, low-cost fabricated substrate for data collection rather than commercially available ones, catering to the needs of on-site defence applications. Our research results demonstrate that the proposed NNAS model exhibits a superior performance in terms of sensitivity, selectivity, and accuracy compared to the existing methods.

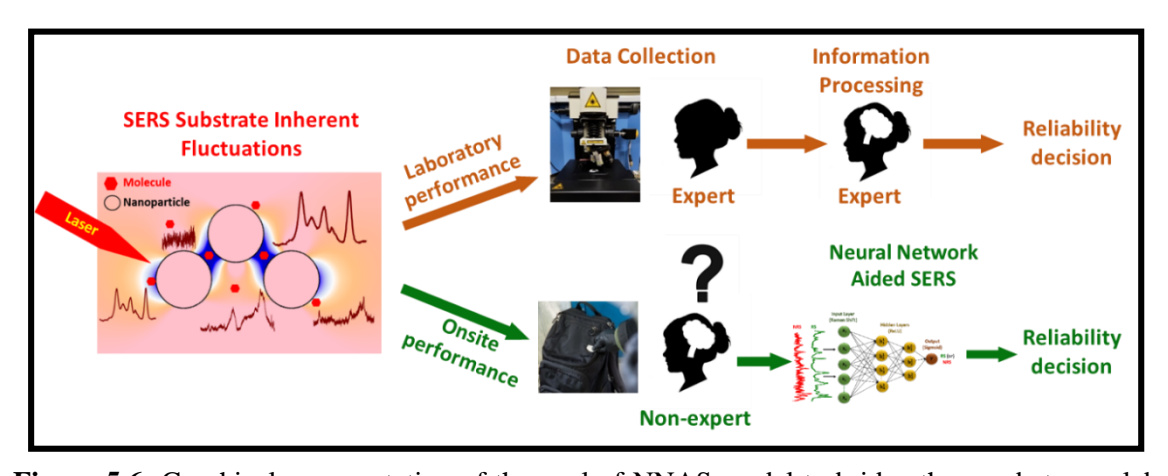


Figure 5.6: Graphical representation of the goal of NNAS model to bridge the gap between lab and field performance removing the reliance of expert by automating the identification of representative SERS spectra of trace explosives.

In this study, data was collected from our laboratory-fabricated substrates using Au nanoparticles on Ag nano-dendrites (AuNPs@AgNDs), which were prepared using a simple electroless deposition technique [83][84]. As training of NNs demands huge volume of data, large number of spectra were obtained by mapping the substrates with crystal violet (CV), tetryl (2,4,6-trinitrophenylmethylnitramine), and picric acid (PA) as analytes. Prior to modelling, data pre-processing baseline correction and spike removal were performed using python. The SNR for each prominent peak of the analytes was calculated using the first standard deviation (FSD) method as described elsewhere [85].

The average SNR was then used to represent the SERS spectrum. Based on the SNR, a threshold was set for labelling the spectra as either representative (R) or non-representative (NR) automated by a python code. The collected data was divided into training and validation sets, and a deep learning model with four layers was utilized to identify the spectra. The model was validated using the validation dataset, and out-of-sample predictions were made to evaluate the model's performance. A schematic of the model's end to end workflow, from data collection to model evaluation, is shown in the figure 5.7.

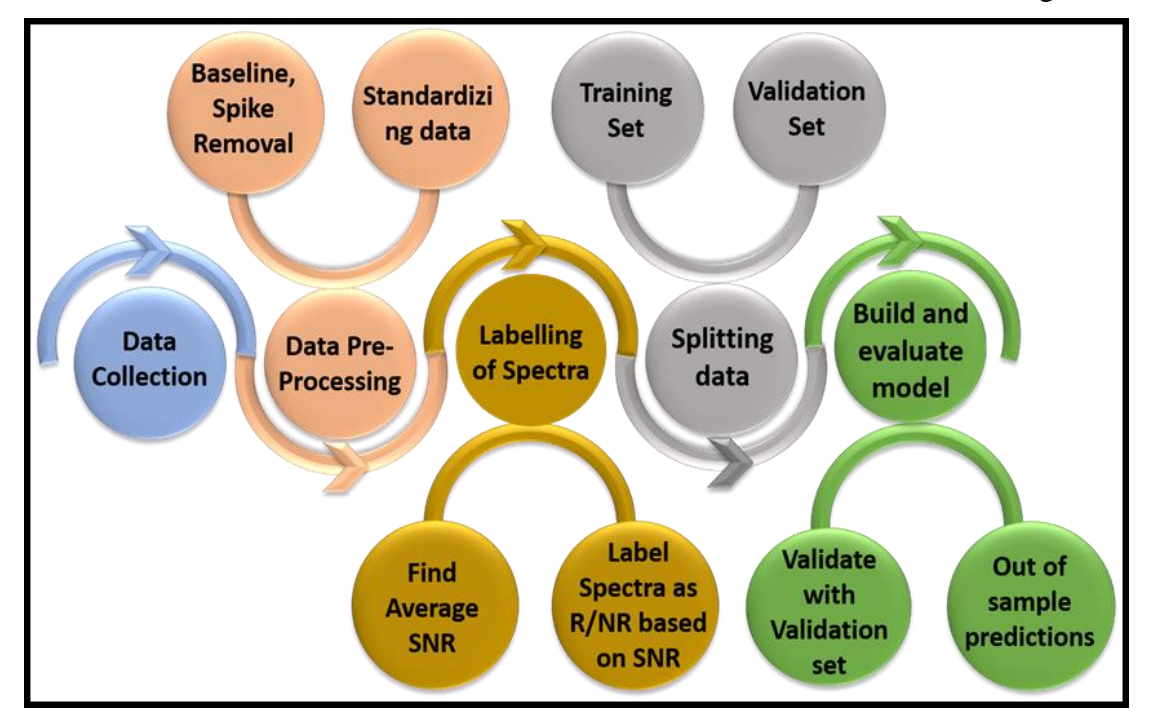


Figure 5.7: End to end streamlined workflow for the NNAS model starting from data collection to model evaluation.

A neural network, which includes the input and output layers, has various layers depending on the difficulty of the challenge. The input layer receives the input parameters, x_i . The bias term is used by the neuron to compute the total weighted inputs. An activation function processes the output from each layer. In a backpropagation mechanism, the weights are modified to reduce the loss function as discussed before. The majority of the codes were written in Python 3.8.3 utilising the Keras and Scikit-learn packages. Free Python tools like Scikitlearn and Keras will import various features including classification, functions, and neural networks. Baseline correction was carried out prior to modelling using the asymmetric least square fitting method suggested by Eilers and colleagues [86]. Each analyte's Raman shift was sent to the input layer as input. The hidden layers consist of 10 and 5 neurons, respectively, with each feature a rectified linear unit (ReLU) for their activation function. Comparatively speaking to other activation functions,

ReLU is computationally cheap. Each layer also receives a regularisation parameter (11 regularisation) to avoid overfitting. One neuron in the output layer is given sigmoid as activation function. Binary cross-entropy has been utilised as the loss function, while stochastic gradient descent has been used as the optimizer. The model's performance was measured using accuracy as a performance indicator, and the learning rate was optimised and set to 0.001. By using a minimum validation loss as a parameter and an early ending mechanism, the number of epochs was determined.

5.3.1. Signal to Noise Ratio Approach

The data used for modelling and prediction in our NNAS model has been collected using Horiba LabRam Raman spectrometer. Therefore, we have used the signal to noise ratio that has been discussed in Horiba documentation and is widely used in the context of Raman spectroscopy. HORIBA Scientific has been defining SNR as the difference between the peak signal and the background noise, divided by the square root of the background noise. This is the First Standard Deviation (FSD) approach. In Raman Spectroscopy, a combination of Raman peaks is often utilized as a molecular signature for detection, especially in the case of explosives. This is because all nitrogen-based explosive molecules tend to exhibit a peak at around 1300 wavenumbers, corresponding to the nitro stretching vibration. Taking that into account to label the analyte, we have employed the average SNR of all the prominent Raman modes of each molecule. The peak intensity of the Raman mode is denoted by I_{Peak}, while I_{Noise} is the average noise measured in the range corresponding to the signal's wings. The SNR is then computed as,

$$SNR = \frac{I_{Peak} - I_{Noise}}{\sqrt{I_{Noise}}} \tag{5.11}$$

The SNR, which measures the relative strength of the Raman signal to noise, is a valuable metric for determining the quality of the SERS spectra. By observation, a threshold SNR was chosen to label the spectra as R or NR, where if SNR is greater than threshold the signal is representative and is non-representative otherwise.

5.3.2 Sample Preparation

SERS substrates were fabricated using a facile, cost-effective two-step method, as illustrated in figure 5.8. Initially, the silicon (Si) substrate was subjected to a cleaning protocol involving acetone and diluted hydrofluoric acid (HF) to eliminate any native oxide layer. To generate silver nanodendrites (AgNDs), we employed an electroless

etching technique as previously discussed in our research [84]. The pre-cleaned Si wafer was submerged in an electrolyte solution comprising of (30 mM) silver nitrate (AgNO₃) and (4.6 M) HF at room temperature for 15 minutes, resulting in a uniform AgNDs growth. The AgNDs were then cleaned with de-ionized water and dried in ambient air. To circumvent the rapid oxidation and consequent substrate degradation, we decorated the AgNDs with gold nanoparticles (AuNPs). The AuNPs were deposited onto the AgNDs by immersing the AgNDs in an HF: HAuCl₄ solution for approximately three hours, leading to high-density distribution of AuNPs. The resulting AuNPs-decorated AgNDs (AuNPs@AgNDs) were employed for the detection of molecules as 1x1 cm² substrates. Stock solutions of the three analytes were prepared and serially diluted in order to achieve the desired concentrations. The FESEM images of the synthesized dendrites are presented in the previous chapter 4, section 4.2.

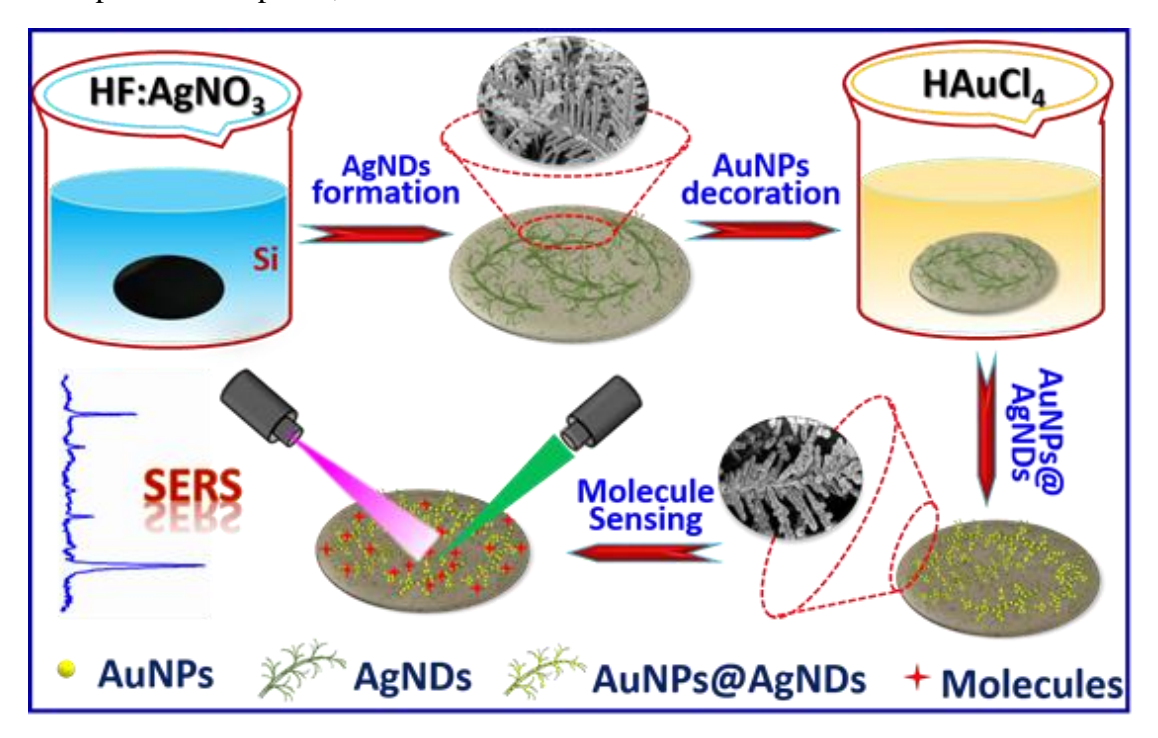


Figure 5.8: Schematic of preparation of AuNPs decorated on AgNDs (AuNPs@AgNDs) and their application for SERS.

5.3.3 Data collection

The SERS substrates that were prepared using a two-step method were utilized for the detection of three different analytes in this study. In addition to external parameters, SERS is also sensitive to instrument conditions that are used during data collection. In order to build a model that is universal, it is essential to take into account these experimental conditions that can influence the performance of the SERS substrates, such as laser

excitation wavelength [87], spot size, laser power, and collection optics [88]. Therefore, in this work, various experimental conditions were systematically varied to simulate real-world scenarios and to develop a generalizable model. Two concentrations of each analyte were studied, and for each, the input laser power, excitation wavelength, and spot size were varied as summarized in Table 5.1. Implementation of ML using python is described in appendix B.

Table 5.1: Summary of experimental parameters that were systematically varied during data collection.

S. No.	Molecule	Laser excitation	Spot size	Concentrations	Total Spectra
1	CV	532 nm	2.6 μM	1 μM, 100 nM	1806
2	Tetryl	532 nm	1.3 μΜ	1 μM, 100 nM	1936
3	Picric Acid	633 nm	3.8 μM	5 μM, 500 nM	1506

Dye molecules are often used as standards to measure the performance of SERS substrates because of their high Raman cross-section. However, the SERS signal from dye molecules is often prone to undesirable effects such as fluorescence and photo degradation. Moreover, the coupling of the molecule to the metal nanoparticles enhances specific modes, making it more challenging, particularly in trace detection. Dye molecules are also more sensitive to experimental conditions such as laser power, spot size, and acquisition time. In this study, crystal violet of concentrations 1 µM and 100 nM was used for analysis. For the detection of explosives such as Tetryl and PA, SERS has shown tremendous potential, particularly for trace detection to the limits of picomolar and nanomolar, respectively. In this study, different concentrations of Tetryl and PA were used under various experimental conditions as summarized in Table 5.1. To collect enough data for the model, 3 µl of analyte was drop-casted on the prepared SERS substrate and allowed to dry. Large area Raman mapping was performed, and a random area of 80×70 μm² was chosen on the substrate for mapping. By varying the experimental conditions and analysing the collected data, a unified model was developed to take into account the general variations in experimental conditions in SERS. Figure 5.9 a) shows how data is split for model training, validation and out of sample evaluation and figure 5.9 b) shows a code snippet of the model.

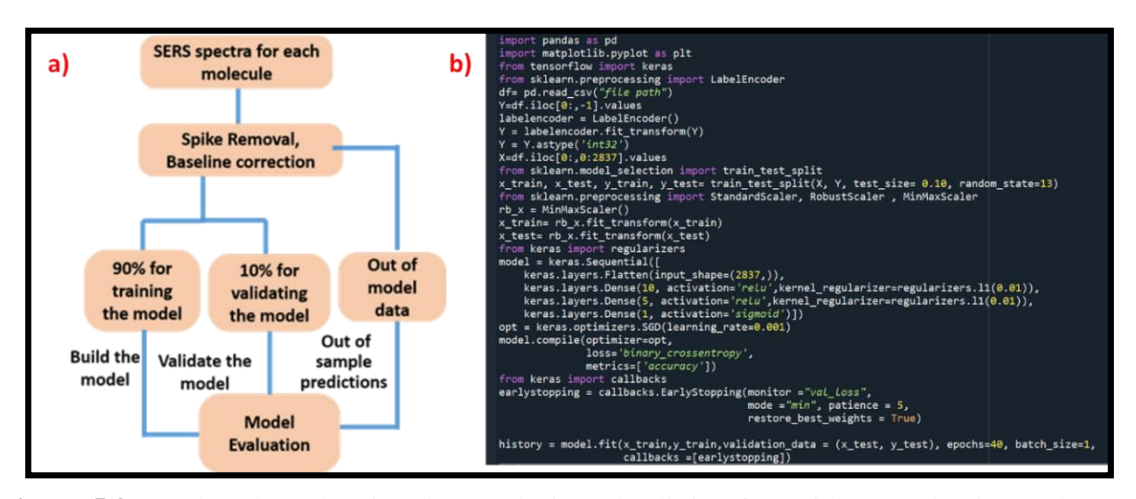


Figure 5.9: a) Flowchart showing data analysis and splitting for training, evaluation and out of sample evaluation, b) Code snippet of the NNAS model showing implementation of various techniques discussed in the section.

5.3.4 Results and Discussion

The target analyte molecule in the initial experiment was Crystal Violet. Figure 5.10 a) shows the characteristic Raman modes of CV, which correspond to the C-C stretching, C-H in-plane bending, ring skeletal vibrations, and C-H out-of-plane bending modes, at 1620 cm⁻¹, 1176 cm⁻¹, 912 cm⁻¹, and 723 cm⁻¹, respectively [89]. These particular Raman modes were chosen for SNR investigation, and the average SNR was calculated since they are suggestive of CV. The classification of spectra as representative or non-representative required an SNR threshold of 10 by observation. A random subset of typical spectra was deleted in order to provide an equal number of spectra for each label (903 R spectra and 903 NR spectra) and to eliminate sampling bias during modelling. Given that the spectra were spatially localised tending to the distribution of hotspots, the dataset was randomly shuffled in order to add randomization. Figure 5.10 b) depicts the intensity distribution of the spectra for each prominent Raman mode of CV that were used to calculate SNR, whereas Figure 5.10 c) shows the SERS spectra, containing both RS and NRS, that were used to model the data. By using a minimum validation loss as a parameter and an early stopping mechanism, the number of epochs was determined. The alike intensity distribution of all peaks of the CV as shown in figure 5.10 b) is an indication that the contribution of chemical enhancement is negligible in comparison to the electromagnetic enhancement [90].

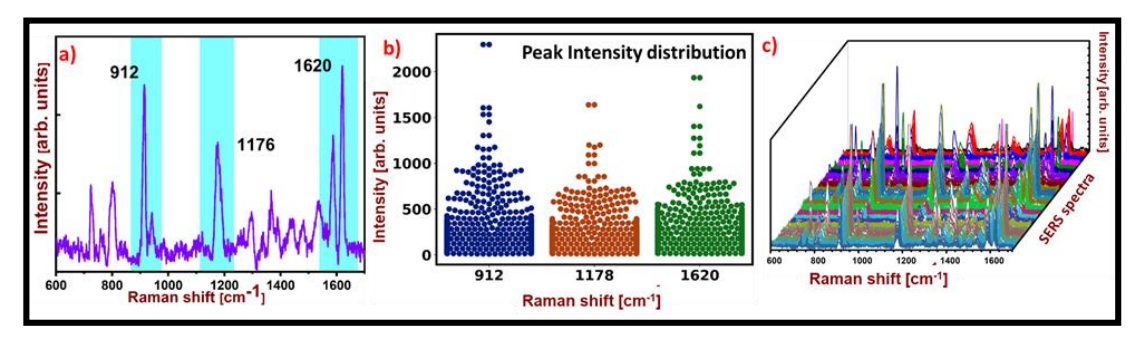


Figure 5.10: a) A representative spectrum of CV with prominent peaks used for calculating SNR labelled in blue. b) Swarm plot showing distribution of the prominent peaks highlighted in blue. c) Input SERS data for CV that is used for modelling.

Previous investigations have been conducted on two explosive molecules, Tetryl and PA. In this study, Tetryl with concentrations of 1 μM and 100 nM were utilized for large area mapping with similar parameters to CV, except the microscopic objective was altered to change the laser spot size to 1.3 μM. The laser spot size is a crucial parameter in SERS data collection as it influences the number of molecules in the collection area and, as a result, the SERS signal. A total of 1938 spectra were collected, consisting of 969 RS and 969 NRS, for Tetryl modeling. The RS of Tetryl is depicted in Figure 5.11 a), with notable peaks identified in grey for calculating SNR. The Raman mode of tetryl at 1358 cm⁻¹ corresponds to the symmetric stretching of the nitro group [91]. Figure 5.11 b) illustrates the intensity distribution of the spectra for each significant Raman mode of tetryl, which are employed to calculate SNR. Figure 5.11 c) depicts the SERS spectra utilized for modelling, which include both RS and NRS.

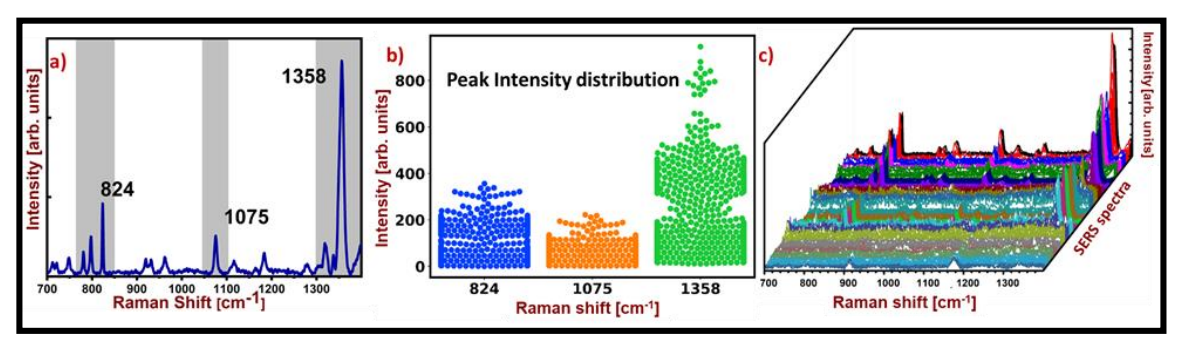


Figure 5.11: a) A representative spectrum of tetryl with prominent peaks used for calculating SNR labelled in grey. b) Swarm plot showing distribution of the prominent peaks highlighted in grey. c) Input SERS data for tetryl that is used for modelling.

0To enhance the applicability of the model to variations in instrument facilities from laboratory to on-site, PA was examined at different concentrations of 5 μ M and 500 nM using 633 nm laser excitation. Approximately 1506 spectra were acquired for both concentrations and processed according to the flowchart. The RS of PA is presented in Figure 5.12 a), with prominent bands highlighted in pink, which was utilized for SNR calculation. The Raman modes at 1345 cm⁻¹ and 827 cm⁻¹ correspond to the NO₂ symmetric stretching mode and C-H bending mode, respectively [92]. Figure 5.12 b) displays the intensity distribution of the spectra for each significant Raman mode of PA, which are used for calculating SNR. Figure 5.12 c) illustrates the SERS spectra employed for modelling, comprising both RS and NRS.

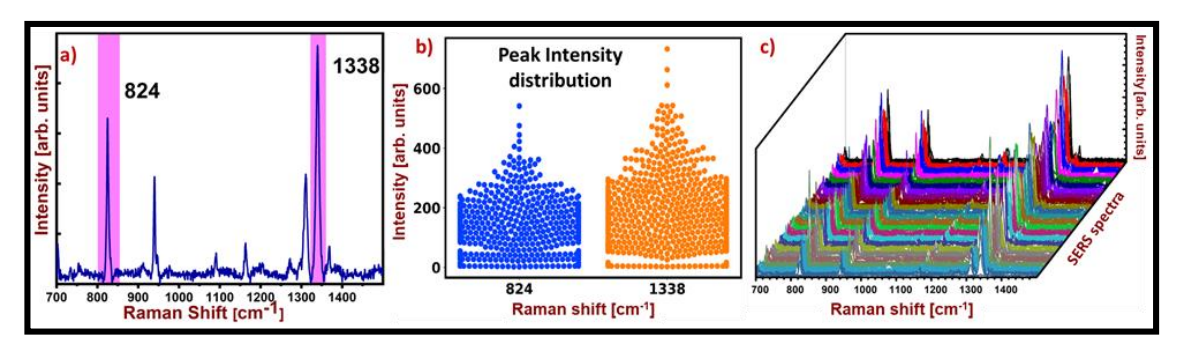


Figure 5.12: a) A representative spectrum of picric acid with prominent peaks used for calculating SNR labelled in pink. b) Swarm plot showing distribution of the prominent peaks highlighted in blue. c) Input SERS data for picric acid that is used for modelling.

Learning curves in neural networks depict the progress of training accuracy and loss metrics over time, such as the number of epochs or iterations. These curves are useful for evaluating model performance and identifying overfitting or underfitting problems. During the training process, the model is exposed to a set of training data, and the learning curves display the changes in model performance metrics with respect to the amount of training data. Initially, as more data is added, the model performance improves, leading to a decrease in loss and an increase in accuracy. However, as the model approaches its capacity to learn from the training data, its performance may reach a plateau. This indicates that additional data may not enhance the model's performance. Learning curves are an important tool for diagnosing problems in neural network models, such as overfitting, underfitting, or insufficient training data. Overfitting occurs when the model is too complex, and it performs well on the training data but poorly on the test data. Underfitting occurs when the model is too simple, and it performs poorly on both the training and test data. By analyzing learning curves, it is possible to determine if the model is overfitting or underfitting, as well as identify the optimal number of training iterations or epochs to

achieve the desired performance. Therefore, learning curves are a valuable tool for assessing neural network model performance during the training phase, detecting overfitting or underfitting, and determining the optimal number of training iterations or epochs. They can provide valuable insights into the behaviour of the model, allowing for adjustments to be made to enhance its performance. In the case of overfitting the training loss is very low (meaning accuracy is high) and validation loss is high (meaning accuracy is low) indicating good performance on training set and poor performance in validation set (the opposite is true for under fitting) [93]. In the case of a good fit, the training and validation losses decrease with each epoch and converge as shown in the figure 5.13 for the case of NNAS.

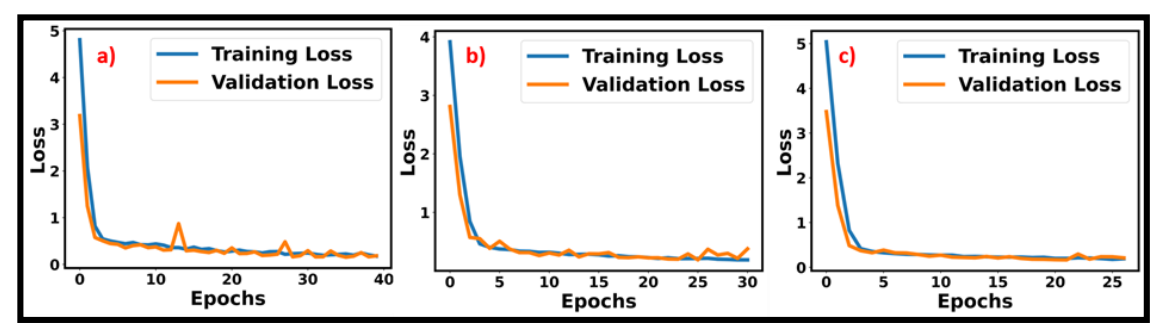


Figure 5.13: Learning curves for training and validation data of NNAS model with loss as a parameter for a) CV, b) Tetryl, and c) Picric Acid.

In order to examine the events of "by chance" we have changed the 'random_state' parameter while splitting the data sets to study different split cases and looked into the learning curves and accuracy. Random state controls the shuffling of the data while splitting the data set. Different random state numbers mean different splits and hence different training and validation data set. Figure 5.14 shows learning curves for the different random states with similar results indicating that the accuracy is not an event of chance.

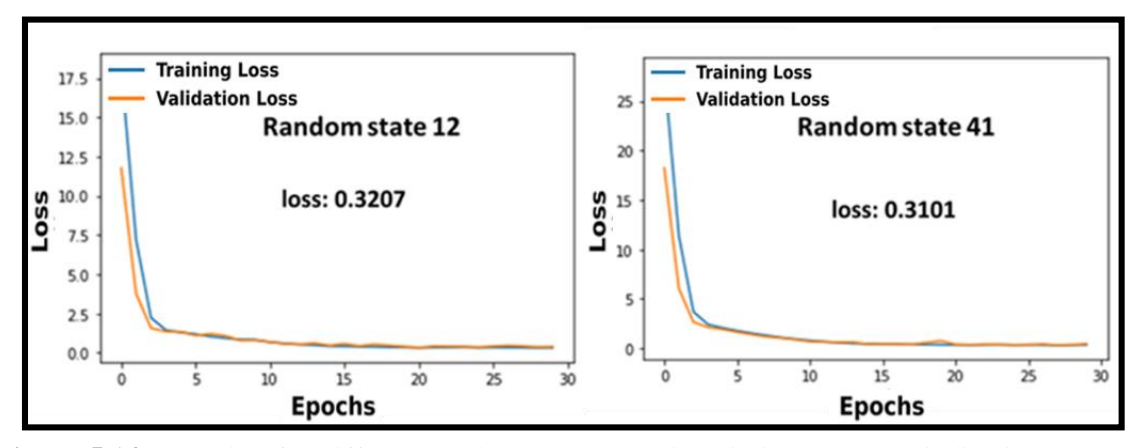


Figure 5.14: Learning for different random states resulting similar accuracy indicating that the accuracy of the model is not an event of chance.

5.3.5 Spatial Representation of the Data

In the interest of defence applications, it is often important to spatially map a selected area to identify the presence of trace hazardous materials. This is more so important for the case of SERS which is known to exhibit matrix effects and hugely relies on the distribution of the hotspots. Mapping tools in SERS always come with huge instrumentation and are expensive, unemployable on the field. In order to overcome this challenge, we propose a simple spatial representation tool using python and the model predictions from NNAS. To assess the model's performance spatially, we generated a spectral data image that included RS and NRS for both actual and predicted validation datasets. True validation spectral data is depicted spatially as RS and NRS in Figure 5.15 a), while the predicted validation spectra by the model is shown in Figure 5.15 b). The validation dataset's confusion matrix, which shows an accuracy of 0.983, is displayed in Figure 5.15 c). We also performed an out-of-sample evaluation by acquiring extra SERS data (~284 spectra) at a distinct concentration (50 nM) to assess the model further. The out-of-sample prediction's confusion matrix, with an accuracy of 0.982, is depicted in Figure 5.15 d), which confirms the model's performance.

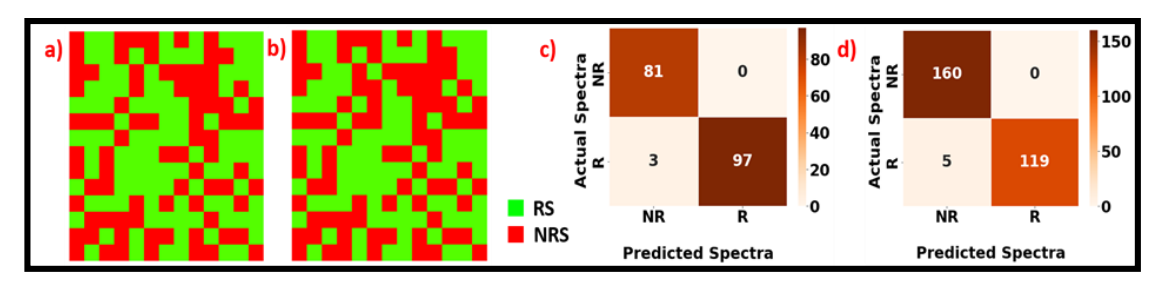


Figure 5.15: Spatial representation of a) actual and b) NNAS predicted validation SERS data set for CV with green representing RS and red representing NRS, c) Confusion matrix of the validation data set indicating an accuracy of 0.983, d) Confusion matrix of 284 out of sample SERS spectra for a different concentration than the testing data set (50 nM) depicting an accuracy of 0.982.

With an interest of on-site performance for detection of explosives using SERS, we focused on two explosive samples. Figure 5.16 a) portrays the spatial representation of true validation spectral data, which is represented as RS (blue) and NRS (green), while Figure 5.16 b) illustrates the predicted validation spectra by the model. Figure 5.16 c) exhibits the validation dataset's confusion matrix, with an accuracy of 0.984. To further evaluate the model, we gathered extra SERS data (~777 spectra) at a distinct concentration (50 nM) for an out-of-sample evaluation. Figure 5.16 d) presents the out-of-sample

prediction's confusion matrix, indicating an accuracy of 0.981, thereby affirming the model's performance.

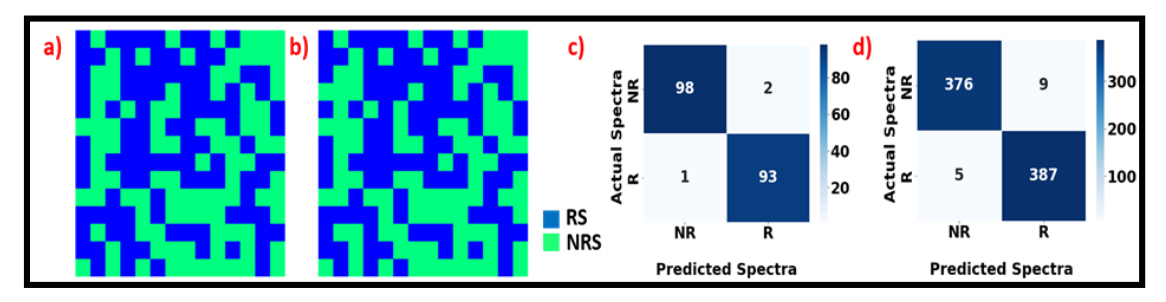


Figure 5.16: Spatial representation of a) actual and b) NNAS predicted validation SERS data set for Tetryl with blue representing RS and green representing NRS, c) Confusion matrix of the validation data set indicating an accuracy of 0.984, d) Confusion matrix of 777 out of sample SERS spectra for a different concentration than the testing data set (50 nM) depicting an accuracy of 0.981.

Analogous investigations were conducted on PA, which is a commonly used explosive molecule. The authentic validation spectral data of PA is demonstrated spatially as RS (yellow) and NRS (blue) in Figure 5.17 a), while the predicted validation spectra by the model is presented in Figure 5.17 b). The validation data set confusion matrix depicted in Figure 5.17 c) has an accuracy of 0.993. To evaluate the model further, additional SERS data (~1026 spectra) at a different concentration (100 nM) were collected for out of sample evaluation. The confusion matrix for the out-of-sample forecast with an accuracy of 0.985 is illustrated in Figure 5.17 d), which validates the model's performance. Figure 5.18 shows spatial representation of out of sample data for all the three analytes studied in the model. The distribution of the spectra through this kind of representation also provides insights into the distribution of hotspots on the substrates without the need of any SERS microscopy.

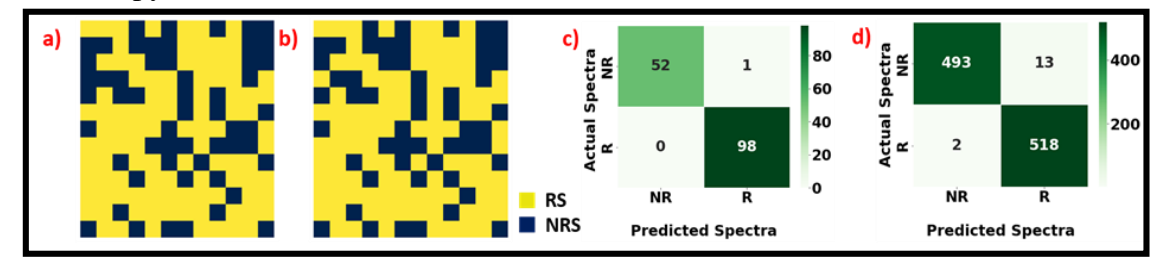


Figure 5.17: Spatial representation of a) actual and b) NNAS predicted validation SERS data set for picric acid with yellow representing RS and dark blue representing NRS, c) Confusion matrix of the validation data set indicating an accuracy of 0.993, d) Confusion matrix of 1026 out of sample SERS spectra for a different concentration than the testing data set (100 nM) depicting an accuracy of 0.985.

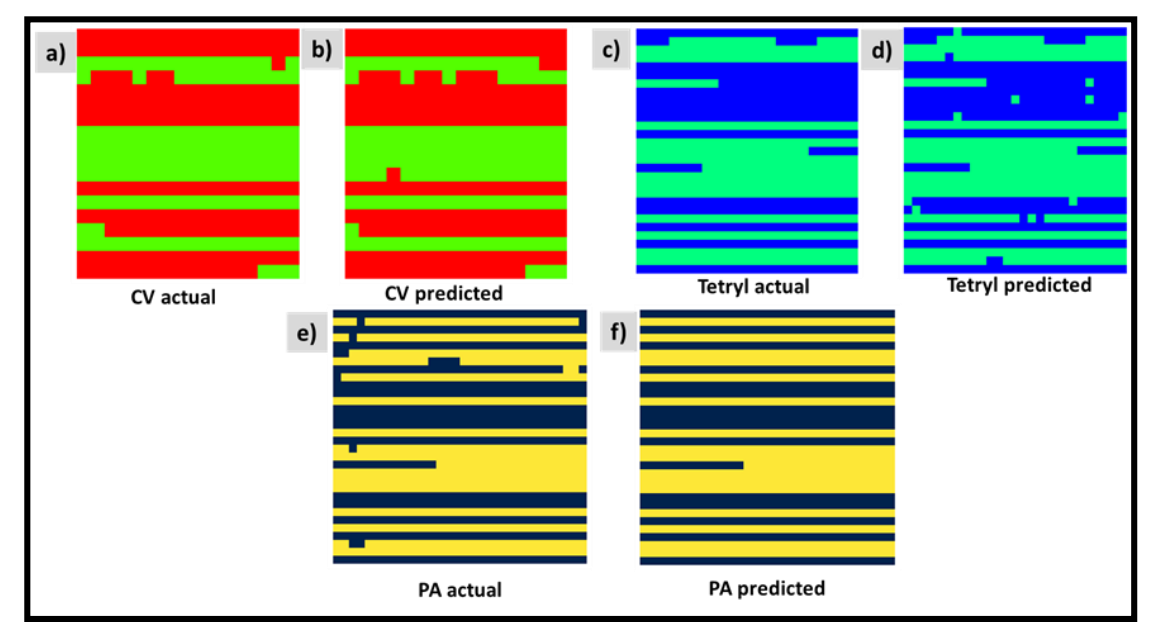


Figure 5.18: Spatial mapping of representative and non-representative spectra for actual, predicted data for a), b) CV, c), d) Tetryl, e),f) Picric Acid.

SERS has been widely analysed using well-liked classification technique Support Vector Machine (SVM). In order to compare the performance of NNAS, we have applied SVM technique for the same data and evaluated. For the classification of NRS and RS for all analytes, we have utilised SVM with Gaussian Kernel Radial Basis Function (RBF), and the accuracies for CV, Tetryl, and PA are 0.889, 0.874, and 0.887, respectively. Even with carefully controlled variations in the experimental settings, the NNAS model outperformed SVM with greater accuracy for all analytes. Figure 5.19 presents the confusion matrix for the SVM model with three analytes. Table 5.2 summarizes the performance of the two models in terms of accuracy.

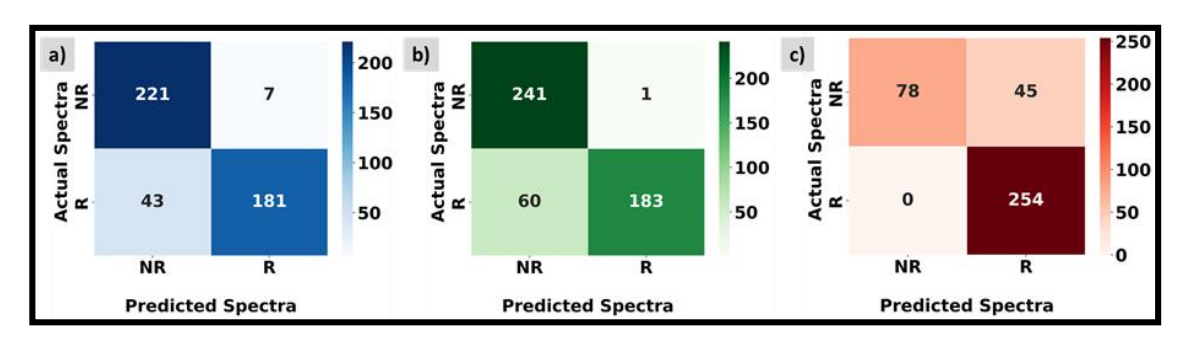


Figure 5.19: Confusion matrix for the classification based on SVM for a) CV, b) Tetryl and c) Picric Acid indication accuracy of 0.889, 0.874, and 0.887, respectively.

Table 5.2: Comparison of performance of SVM and NNAS model.

Analyte	SVM Accuracy	Validation set accuracy of NNAS	Out of Sample Accuracy of NNAS
Crystal Violet (CV)	0.889	0.983	0.982
Tetryl	0.874	0.984	0.981
Picric Acid (PA)	0.887	0.993	0.985

5.4. Conclusion and Scope

ML techniques are being widely used in SERS to analyse data and to extract meaningful information beyond the linear analysis models [94] [95] [96]. SERS is known to have inherent signal fluctuations through same mechanisms that lead to enhancement like a) dependence of LSPR on the wavelength, b) non-uniform adsorption of molecules, c) change in molecular structure through chemisorption, d) hotspot dynamic under the influence of a laser, e) thermal effects caused by the laser, f) surface oxidation of the metal NS and f) diffusion of hotspots in and out of hotspots. All these mechanisms make SERS measurements extremely reliable on a trained experimentalist and thus stand in the way of field applications [6] [97]. NNs are known to recognise complex data patterns without any data pre-processing and are hence widely used for automation. The efforts to use ML algorithms in SERS have been severely restricted to pre-processing artefacts like baseline correction, removal of cosmic spike and noise elimination [98] [99] [100]. The goal of the NNAS model studied in this work is to overcome signal fluctuations in SERS without any expert's reliance in view of field applications. We have used in-house (AuNPs@AgNDs) SERS substrates prepared using an easy and affordable electroless deposition technique. In order to incorporate different parameters that typically influence SERS, we have carefully changed the experimental parameters, such as the laser wavelength and spot size, to study three analyte molecules at trace levels. The model was evaluated using validation and out of sample data after being trained on a training set. For out-of-sample testing of CV, Tetryl, and picric acid, the model's accuracy was found to be 0.982, 0.981, and 0.985, respectively. The model's performance was compared against SVM, which demonstrated an accuracy of less than 89% across all analytes. The model has also accurately predicted CV spectrum from a portable Raman device indicating cross-functionality of the model. The trained NNAS model on one analyte needed no change for other two analytes,

implying that the model can be extended to any molecule of interest without any further parameter tuning. Data collected has been performed on randomly ordered and highly anisotropic nanostructures ensuring that the model works well for both ordered and disordered substrates unlike previous works [9]. We foresee that our model can close the performance gap between onsite and laboratory detection of SERS substrates.

This model can be utilised as a tool to understanding the distribution of hotspots on a surface. Often SERS substrates are characterised by high quality imaging tools like FESEM or TEM prior to measurements. However, in the presence of the analyte molecules and under the exposure of laser, the distribution and dynamics of hotspots is known to change significantly. In that regard, the spatial mapping tool prescribed in this model can be a useful tool in understanding the adsorption and hotspot distribution. This tool is also extremely useful for field applications where a suspicious area can be mapped successfully using SERS spectra characteristics in order to successfully identify suspicious materials. NNAS is an end-to-end model including data pre-processing and hence can be used as a plug in for field applications. The model can be made more rigorous if it is trained with data containing common field background elements like soil, clothes, luggage materials and plastic. The calculation of SNR in this model was based on identifying significant peaks that are characteristic of the molecule by the expert. This process can be improved by using peak identification algorithms that are widely discussed elsewhere [101] [102]. The data collection for this model was performed using mapping tool of Horiba LabRam Raman spectrometer which has automatic movable stages. It is also possible to extend data collection using portable instruments by using programmable, user-controlled stages. The model can be further extended for quantification analysis where the algorithms studied in chapter _ can be sued in streamline with the output of the NNAS model. NNAS can be extremely useful in analysing complex biological fluids and in situ measurements that are being extensively carried out using SERS recently [3].

References

- [1] L.M. Narla, S.V. Rao, Identification of metals and alloys using color CCD images of laser-induced breakdown emissions coupled with machine learning, Appl. Phys. B Lasers Opt. 126 (2020) 113. https://doi.org/10.1007/s00340-020-07469-6.
- [2] F. Cui, Y. Yue, Y. Zhang, Z. Zhang, H.S. Zhou, Advancing Biosensors with Machine Learning, ACS Sensors. 5 (2020) 3346–3364. https://doi.org/10.1021/acssensors.0c01424.
- [3] R. Beeram, K.R. Vepa, V.R. Soma, Recent Trends in SERS-Based Plasmonic Sensors for Disease Diagnostics, Biomolecules Detection, and Machine Learning, 5 (2023) 328. https://doi.org/10.3390/bios13030328.
- [4] Katrin Kneipp, Yang Wang, Harald Kneipp, Lev T. Perelman, Irving Itzkan, Ramachandra R. Dasari, Single Molecule Detection Using Surface-Enhanced Raman Scattering (SERS), Phys. Rev. Lett. 78 (1997) 1667. https://doi.org/10.1103/PhysRevLett.78.1667.
- [5] P.G. Etchegoin, E.C. Le Ru, A perspective on single molecule SERS: Current status and future challenges, Phys. Chem. Chem. Phys. 10 (2008) 6079–6089. https://doi.org/10.1039/b809196j.
- [6] A.I. Pérez-Jiménez, D. Lyu, Z. Lu, G. Liu, B. Ren, Surface-enhanced Raman spectroscopy: Benefits, trade-offs and future developments, Chem. Sci. 11 (2020) 4563–4577. https://doi.org/10.1039/d0sc00809e.
- [7] J. Liu, M. Osadchy, L. Ashton, M. Foster, C.J. Solomon, S.J. Gibson, Deep convolutional neural networks for Raman spectrum recognition: A unified solution, Analyst. 142 (2017) 4067–4074. https://doi.org/10.1039/c7an01371j.
- [8] R. Luo, J. Popp, T. Bocklitz, Deep Learning for Raman Spectroscopy: A Review, Analytica 3 (2022) 287–301. https://doi.org/10.3390/analytica3030020.
- [9] T. Rojalin, D. Antonio, A. Kulkarni, R.P. Carney, Machine Learning-Assisted Sampling of Surfance-Enhanced Raman Scattering (SERS) Substrates Improve Data Collection Efficiency, Appl. Spectrosc. 76 (2022) 485–495. https://doi.org/10.1177/00037028211034543.
- [10] G. Moon, T. Son, H. Lee, D. Kim, Deep learning approach for enhanced detection of surface plasmon scattering, Anal. Chem. 91 (2019) 9538–9545. https://doi.org/10.1021/acs.analchem.9b00683.
- [11] A.K. Gupta, C.H. Hsu, C.S. Lai, Enhancement of the Au/ZnO-NA plasmonic SERS signal using principal component analysis as a machine learning approach, IEEE Photonics J. 12 (2020). https://doi.org/10.1109/JPHOT.2020.3015740.
- [12] R. Pilot, R. Signorini, C. Durante, L. Orian, M. Bhamidipati, L. Fabris, A review on surface-enhanced Raman scattering, Biosensors. 9 (2019) 57. https://doi.org/10.3390/bios9020057.
- [13] E.C. Le Ru, E. Blackie, M. Meyer, P.G. Etchegoint, Surface enhanced raman scattering enhancement factors: A comprehensive study, J. Phys. Chem. C. 111 (2007) 13794–13803. https://doi.org/10.1021/jp0687908.
- [14] M. Futamata, Y. Maruyama, LSP spectral changes correlating with SERS activation

- and quenching for R6G on immobilized Ag nanoparticles, Appl. Phys. B Lasers Opt. 93 (2008) 117–130. https://doi.org/10.1007/s00340-008-3179-z.
- [15] Ertürk Ü, Pettenkofer C, Otto A, 'Sers activity' of coldly deposited Ag and Cu films quenched by oxygen, J. Electron Spectrosc. Relat. Phenomena, 38 (1986) 113–122. https://doi.org/10.1016/0368-2048(86)85081-2.
- [16] A.R.L. Marshall, J. Stokes, F.N. Viscomi, J.E. Proctor, J. Gierschner, J.S.G. Bouillard, A.M. Adawi, Determining molecular orientation: Via single molecule SERS in a plasmonic nano-gap, Nanoscale. 9 (2017) 17415–17421. https://doi.org/10.1039/c7nr05107g.
- [17] J.M. McLellan, Z.Y. Li, A.R. Siekkinen, Y. Xia, The SERS activity of a supported ag nanocube strongly depends on its orientation relative to laser polarization, Nano Lett. 7 (2007) 1013–1017. https://doi.org/10.1021/nl070157q.
- [18] P.G. Etchegoin, C. Galloway, E.C. Le Ru, Polarization-dependent effects in surface-enhanced Raman scattering (SERS), Phys. Chem. Chem. Phys. 8 (2006) 2624–2628. https://doi.org/10.1039/b603725a.
- [19] D.P. Dos Santos, G.F.S. Andrade, M.L.A. Temperini, A.G. Brolo, Electrochemical control of the time-dependent intensity fluctuations in surface-enhanced Raman scattering (SERS), J. Phys. Chem. C. 113 (2009) 17737–17744. https://doi.org/10.1021/jp907389v.
- [20] E.C. Le Ru, P.G. Etchegoin, Sub-wavelength localization of hot-spots in SERS, Chem. Phys. Lett. 396 (2004) 393–397. https://doi.org/10.1016/j.cplett.2004.08.065.
- [21] Y. Yuan, Y. Lin, B. Gu, N. Panwar, S.C. Tjin, J. Song, J. Qu, K.T. Yong, Optical trapping-assisted SERS platform for chemical and biosensing applications: Design perspectives, Coord. Chem. Rev. 339 (2017) 138–152. https://doi.org/10.1016/j.ccr.2017.03.013.
- [22] A. Kaliyaraj Selva Kumar, Y. Zhang, D. Li, R.G. Compton, A mini-review: How reliable is the drop casting technique?, Electrochem. Commun. 121 (2020) 106867. https://doi.org/10.1016/j.elecom.2020.106867.
- [23] Y. Hong, Y. Li, L. Huang, W. He, S. Wang, C. Wang, G. Zhou, Y. Chen, X. Zhou, Y. Huang, W. Huang, T. Gong, Z. Zhou, Label-free diagnosis for colorectal cancer through coffee ring-assisted surface-enhanced Raman spectroscopy on blood serum, J. Biophotonics. 13 (2020) 201960176. https://doi.org/10.1002/jbio.201960176.
- [24] S. Juneja, J. Bhattacharya, Coffee ring effect assisted improved S. aureus screening on a physically restrained gold nanoflower enriched SERS substrate, Colloids Surfaces B Biointerfaces. 182 (2019) 110349. https://doi.org/10.1016/j.colsurfb.2019.110349.
- [25] A. Kudelski, Fluctuations of Raman spectra of hydrogenated amorphous carbon deposited on electrochemically-roughened silver, Chem. Phys. Lett. 427 (2006) 206–209. https://doi.org/10.1016/j.cplett.2006.06.043.
- [26] R.C. Maher, L.F. Cohen, E.C. Le Ru, P.G. Etchegoin, A study of local heating of molecules under Surface Enhanced Raman Scattering (SERS) conditions using the anti-Stokes/Stokes ratio, Faraday Discuss. 132 (2006) 77–83.

- https://doi.org/10.1039/b510413k.
- [27] E.C. Le Ru, P.G. Etchegoin, Vibrational pumping and heating under SERS conditions: fact or myth?, Faraday Discuss. 132 (2006) 63–75. https://doi.org/10.1039/b505343a.
- [28] W. Zhang, T. Schmid, B. Yeo, R. Zenobi, Near-Field Heating, Annealing, and Signal Loss in Tip-Enhanced Raman Spectroscopy, J. Phys. Chem. C. 112 (2008) 2104–2108. https://doi.org/10.1021/jp077457g.
- [29] A. Mezni, T. Dammak, A. Fkiri, A. Mlayah, Y. Abid, L.S. Smiri, Photochemistry at the surface of gold nanoprisms from surface-enhanced raman scattering blinking, J. Phys. Chem. C. 118 (2014) 17956–17967. https://doi.org/10.1021/jp5038188.
- [30] B.L. Scott, K.T. Carron, Dynamic Raman Scattering Studies of Coated Gold Nanoparticles: 4-Mercaptopyridine, 4-Mercaptophenol, and Benzenethiol, J. Phys. Chem. C. 120 (2016) 20905–20913. https://doi.org/10.1021/acs.jpcc.6b02617.
- [31] L.O. Herrmann, V.K. Valev, C. Tserkezis, J.S. Barnard, S. Kasera, O.A. Scherman, J. Aizpurua, J.J. Baumberg, Threading plasmonic nanoparticle strings with light, Nat. Commun. 5 (2014) 4568. https://doi.org/10.1038/ncomms5568.
- [32] F.B. Magalhães, R.F.V. V. Jaimes, P. Cório, W.J. Salcedo, SERS fluctuations of NAD molecules adsorbed on arrays of Au nanocylinders, Opt. Mater. Express. 11 (2021) 3154. https://doi.org/10.1364/ome.434894.
- [33] P.G. Etchegoin, M. Meyer, E. Blackie, E.C. Le Ru, Statistics of single-molecule surface enhanced Raman scattering signals: Fluctuation analysis with multiple analyte techniques, Anal. Chem. 79 (2007) 8411–8415. https://doi.org/10.1021/ac071231s.
- [34] P. Kusch, S. Mastel, N.S. Mueller, N. Morquillas Azpiazu, S. Heeg, R. Gorbachev, F. Schedin, U. Hübner, J.I. Pascual, S. Reich, R. Hillenbrand, Dual-Scattering Near-Field Microscope for Correlative Nanoimaging of SERS and Electromagnetic Hotspots, Nano Lett. 17 (2017) 2667–2673. https://doi.org/10.1021/acs.nanolett.7b00503.
- [35] D.D.D. Ying Fang, Nak-Hyun Seong, Measurement of the Distribution of Site Enhancements in Surface-Enhanced Raman Scattering, Science. 321 (2008) 388–393. https://doi.org/10.1126/science.1159499.
- [36] E.C.L. Ru, Principles of Surface Enhanced Raman Spectroscopy and Related Plasmonic effects, Elsevier, 2008.
- [37] M.A. Osborne, S. Balasubramanian, W.S. Furey, D. Klenerman, Optically biased diffusion of single molecules studied by confocal fluorescence microscopy, J. Phys. Chem. B. 102 (1998) 3160–3167. https://doi.org/10.1021/jp9715078.
- [38] A. Kudelski, Some aspects of SERS temporal fluctuations: Analysis of the most intense spectra of hydrogenated amorphous carbon deposited on silver, J. Raman Spectrosc. 38 (2007) 1494–1499. https://doi.org/10.1002/jrs.1799.
- [39] R. Beeram, V.R. Soma, Ultra-trace detection of diverse analyte molecules using femtosecond laser structured Ag Au alloy substrates and SERRS, Opt. Mater. 137 (2023) 113615. https://doi.org/10.1016/j.optmat.2023.113615.
- [40] S.R. Emory, R.A. Jensen, T. Wenda, M. Han, S. Nie, Re-examining the origins of spectral blinking in single-molecule and single-nanoparticle SERS, Faraday

- Discuss. 132 (2006) 249–259. https://doi.org/10.1039/b509223j.
- [41] A. Nitzan, L.E. Brus, Theoretical model for enhanced photochemistry on rough surfaces, J. Chem. Phys. 75 (1981) 2205–2214. https://doi.org/10.1063/1.442333.
- [42] G.M. Goncher, C.A. Parsons, C.B. Harris, Photochemistry on rough metal surfaces, J. Phys. Chem. 88 (1984) 4200–4209. https://doi.org/10.1021/j150663a003.
- [43] M.G. R. C. Maher, T. Zhang, L. F. Cohen, J. C. Gallop, F. M. Liub, Towards a metrological determination of the performance of SERS media, Phys. Chem. Chem. Phys. 11 (2009) 7348–7349. https://doi.org/10.1039/b913171j.
- [44] Robert C. Maher, SERS Hot Spots, 2012. https://doi.org/10.1007/978-3-642-20620-7.
- [45] A. Szeghalmi, S. Kaminskyj, P. Ro, K.M. Gough, Time Fluctuations and Imaging in the SERS Spectra of Fungal Hypha Grown on Nanostructured Substrates, J. of Phy. Chem. B, 111(2007) 12916–12924. https://doi.org/10.1021/jp075422a.
- [46] J.T. Krug, G.D. Wang, S.R. Emory, S. Nie, Efficient raman enhancement and intermittent light emission observed in single gold nanocrystals, J. Am. Chem. Soc. 121 (1999) 9208–9214. https://doi.org/10.1021/ja992058n.
- [47] C.C. Huang, W. Chen, A SERS method with attomolar sensitivity: a case study with the flavonoid catechin, Microchim. Acta. 185 (2018) 1-8. https://doi.org/10.1007/s00604-017-2662-9.
- [48] W. Lee, B.H. Kang, H. Yang, M. Park, J.H. Kwak, T. Chung, Y. Jeong, B.K. Kim, K.H. Jeong, Spread spectrum SERS allows label-free detection of attomolar neurotransmitters, Nat. Commun. 12 (2021) 159. https://doi.org/10.1038/s41467-020-20413-8.
- [49] A.S.D.S. Indrasekara, S. Meyers, S. Shubeita, L.C. Feldman, T. Gustafsson, L. Fabris, Gold nanostar substrates for SERS-based chemical sensing in the femtomolar regime, Nanoscale. 6 (2014) 8891–8899. https://doi.org/10.1039/c4nr02513j.
- [50] M.B. Bhavya, R. Prabhu B., B.M. Shenoy, P. Bhol, S. Swain, M. Saxena, N.S. John, G. Hegde, A.K. Samal, Femtomolar detection of thiram: via SERS using silver nanocubes as an efficient substrate, Environ. Sci. Nano. 7 (2020) 3999–4009. https://doi.org/10.1039/d0en01049a.
- [51] H. Shao, H. Lin, Z. Guo, J. Lu, Y. Jia, M. Ye, F. Su, L. Niu, W. Kang, S. Wang, Y. Hu, Y. Huang, A multiple signal amplification sandwich-type SERS biosensor for femtomolar detection of miRNA, Biosens. Bioelectron. 143 (2019) 111616. https://doi.org/10.1016/j.bios.2019.111616.
- [52] S. Bettini, S. Pal, S. Sawalha, A. Licciulli, L. Valli, G. Giancane, R. Pagano, Cellulose-Based Substrate for SERS-Promoted Histamine Picomolar Detection in Beverages, ChemistrySelect. 4 (2019) 2968–2975. https://doi.org/10.1002/slct.201803323.
- [53] X. Huang, Y. Liu, J. Barr, J. Song, Z. He, Y. Wang, Z. Nie, Y. Xiong, X. Chen, Controllable self-assembled plasmonic vesicle-based three-dimensional SERS platform for picomolar detection of hydrophobic contaminants, Nanoscale. 10 (2018) 13202–13211. https://doi.org/10.1039/c8nr02778a.
- [54] K. Kneipp, H. Kneipp, H.G. Bohr, Single-molecule SERS spectroscopy, Top. Appl.

- Phys. 103 (2006) 261–278. https://doi.org/10.1007/11663898_13.
- [55] H. Xu, E.J. Bjerneld, M. Käll, L. Börjesson, Spectroscopy of single hemoglobin molecules by surface enhanced raman scattering, Phys. Rev. Lett. 83 (1999) 4357–4360. https://doi.org/10.1103/PhysRevLett.83.4357.
- [56] H.Y. Lin, C.H. Huang, W.H. Hsieh, L.H. Liu, Y.C. Lin, C.C. Chu, S.T. Wang, I.T. Kuo, L.K. Chau, C.Y. Yang, On-line SERS detection of single bacterium Using Novel SERS Nanoprobes and a microfl uidic Dielectrophoresis device, Small. 10 (2014) 4700–4710. https://doi.org/10.1002/smll.201401526.
- [57] A.K. Verma, R.K.Soni, Ultrasensitive surface-enhanced Raman spectroscopy detection of explosive molecules with multibranched silver nanostructures, J. of Raman Spectro., 53(2022), 694-708.. https://doi.org/10.1002/jrs.6294.
- [58] A. Hakonen, P.O. Andersson, M. Stenbæk Schmidt, T. Rindzevicius, M. Käll, Explosive and chemical threat detection by surface-enhanced Raman scattering: A review, Anal. Chim. Acta. 893 (2015) 1–13. https://doi.org/10.1016/j.aca.2015.04.010.
- [59] K.W. Kho, C.Y. Fu, U.S. Dinish, M. Olivo, Clinical SERS: Are we there yet?, J. Biophotonics. 4 (2011) 667–684. https://doi.org/10.1002/jbio.201100047.
- [60] A. Barucci, C. D'Andrea, E. Farnesi, M. Banchelli, C. Amicucci, M. De Angelis, B. Hwang, P. Matteini, Label-free SERS detection of proteins based on machine learning classification of chemo-structural determinants, Analyst. 146 (2021) 674–682. https://doi.org/10.1039/d0an02137g.
- [61] Y. Yang, B. Xu, J. Haverstick, N. Ibtehaz, A. Muszyński, X. Chen, M.E.H.H. Chowdhury, S.M. Zughaier, Y. Zhao, Differentiation and classification of bacterial endotoxins based on surface enhanced Raman scattering and advanced machine learning, Nanoscale. 14 (2022) 8806–8817. https://doi.org/10.1039/d2nr01277d.
- [62] Q. Hu, C. Sellers, J.S.-I. Kwon, H.-J. Wu, Integration of surface-enhanced Raman spectroscopy (SERS) and machine learning tools for coffee beverage classification, Digit. Chem. Eng. 3 (2022) 100020. https://doi.org/10.1016/j.dche.2022.100020.
- [63] R. Breuch, D. Klein, E. Siefke, M. Hebel, U. Herbert, C. Wickleder, P. Kaul, Differentiation of meat-related microorganisms using paper-based surface-enhanced Raman spectroscopy combined with multivariate statistical analysis, Talanta. 219 (2020) 121315. https://doi.org/10.1016/j.talanta.2020.121315.
- [64] N. Banaei, J. Moshfegh, A. Mohseni-Kabir, J.M. Houghton, Y. Sun, B. Kim, Machine learning algorithms enhance the specificity of cancer biomarker detection using SERS-based immunoassays in microfluidic chips, RSC Adv. 9 (2019) 1859– 1868. https://doi.org/10.1039/C8RA08930B.
- [65] Q. Cao, C. Chen, J. Huang, D. Shen, H. Chen, H. Zhong, Z. Liu, Z. Guo, Mussel-inspired hydrogels for fast fabrication of flexible SERS tape for point-of-care testing of β-blockers., 147(2022) 3652–3661. https://doi.org/10.1039/d2an00688j.
- [66] X. Fang, Q. Zeng, X. Yan, Z. Zhao, N. Chen, Q. Deng, M. Zhu, Y. Zhang, S. Li, Fast discrimination of tumor and blood cells by label-free surface-enhanced Raman scattering spectra and deep learning, J. Appl. Phys. 129 (2021). https://doi.org/10.1063/5.0042662.
- [67] A. Skvortsova, A. Trelin, P. Kriz, R. Elashnikov, B. Vokata, P. Ulbrich, A.

- Pershina, V. Svorcik, O. Guselnikova, O. Lyutakov, SERS and advanced chemometrics Utilization of Siamese neural network for picomolar identification of beta-lactam antibiotics resistance gene fragment, Anal. Chim. Acta. 1192 (2021) 339373. https://doi.org/10.1016/j.aca.2021.339373.
- [68] F. Uysal Ciloglu, A.M. Saridag, I.H. Kilic, M. Tokmakci, M. Kahraman, O. Aydin, Identification of methicillin-resistant: Staphylococcus aureus bacteria using surface-enhanced Raman spectroscopy and machine learning techniques, Analyst. 145 (2020) 7559–7570. https://doi.org/10.1039/d0an00476f.
- [69] R.M. Jarvis, R. Goodacre, Characterisation and identification of bacteria using SERS, Chem. Soc. Rev. 37 (2008) 931–936. https://doi.org/10.1039/b705973f.
- [70] B. Li, M.N. Schmidt, T.S. Alstrøm, Raman spectrum matching with contrastive representation learning, Analyst. 147 (2022) 2238–2246. https://doi.org/10.1039/d2an00403h.
- [71] A. Lebrun, H. Fortin, N. Fontaine, D. Fillion, O. Barbier, D. Boudreau, Pushing the Limits of Surface-Enhanced Raman Spectroscopy (SERS) with Deep Learning: Identification of Multiple Species with Closely Related Molecular Structures, Appl. Spectrosc. 76 (2022) 609–619. https://doi.org/10.1177/00037028221077119.
- [72] S. Horii, M. Ando, A.Z. Samuel, A. Take, T. Nakashima, A. Matsumoto, Y.K. Takahashi, H. Takeyama, Detection of Penicillin G Produced by Penicillium chrysogenum with Raman Microspectroscopy and Multivariate Curve Resolution-Alternating Least-Squares Methods, J. Nat. Prod. 83 (2020) 3223–3229. https://doi.org/10.1021/acs.jnatprod.0c00214.
- [73] H. Dies, J. Raveendran, C. Escobedo, A. Docoslis, Rapid identification and quantification of illicit drugs on nanodendritic surface-enhanced Raman scattering substrates, Sensors Actuators, B Chem. 257 (2018) 382–388. https://doi.org/10.1016/j.snb.2017.10.181.
- [74] D. Li, Q. Zhang, B. Deng, Y. Chen, L. Ye, Rapid, sensitive detection of ganciclovir, penciclovir and valacyclovir-hydrochloride by artificial neural network and partial least squares combined with surface enhanced Raman spectroscopy, Appl. Surf. Sci. 539 (2021) 148224. https://doi.org/10.1016/j.apsusc.2020.148224.
- [75] S. Yan, C. Liu, S. Fang, J. Ma, J. Qiu, D. Xu, L. Li, J. Yu, D. Li, Q. Liu, SERS-based lateral flow assay combined with machine learning for highly sensitive quantitative analysis of Escherichia coli O157:H7, Anal. Bioanal. Chem. 412 (2020) 7881–7890. https://doi.org/10.1007/s00216-020-02921-0.
- [76] W.J. Thrift, R. Ragan, Quantification of Analyte Concentration in the Single Molecule Regime Using Convolutional Neural Networks, Anal. Chem. 91 (2019) 13337–13342. https://doi.org/10.1021/acs.analchem.9b03599.
- [77] Q. Bao, H. Zhao, S. Han, C. Zhang, W. Hasi, Surface-enhanced Raman spectroscopy for rapid identification and quantification of Flibanserin in different kinds of wine, Anal. Methods. 12 (2020) 3025–3031. https://doi.org/10.1039/d0ay00741b.
- [78] R. Beeram, D. Banerjee, L.M. Narlagiri, V.R. Soma, Machine learning for rapid quantification of trace analyte molecules using SERS and flexible plasmonic paper substrates, Anal. Methods. 14 (2022) 1788–1796.

- https://doi.org/10.1039/d2ay00408a.
- [79] L. Morelli, F.A. Centorbi, O. Ilchenko, C.B. Jendresen, D. Demarchi, A.T. Nielsen, K. Zór, A. Boisen, Simultaneous quantification of multiple bacterial metabolites using surface-enhanced Raman scattering, Analyst. 144 (2019) 1600–1607. https://doi.org/10.1039/c8an02128g.
- [80] M.S.S. Bharati, V.R. Soma, Flexible SERS substrates for hazardous materials detection: recent advances, Opto-Electronic Adv. 4 (2021) 210048–210048. https://doi.org/10.29026/oea.2021.210048.
- [81] B. Sharma, R.R. Frontiera, A.I. Henry, E. Ringe, R.P. Van Duyne, SERS: Materials, applications, and the future, Mater. Today. 15 (2012) 16–25. https://doi.org/10.1016/S1369-7021(12)70017-2.
- [82] P.G. Etchegoin, E.C.L. Ru, Basic Electromagnetic Theory of SERS, Surface Enhanced Raman Spectroscopy: analytical, biophysical and life science applications, 2010, 1-37. https://doi.org/10.1002/9783527632756.ch1.
- [83] V.S. Vendamani, S.V.S.N. Rao, A.P. Pathak, V.R. Soma, Robust and cost-effective silver dendritic nanostructures for SERS-based trace detection of RDX and ammonium nitrate, RSC Adv. 10 (2020) 44747–44755. https://doi.org/10.1039/d0ra08834j.
- [84] V.S. Vendamani, R. Beeram, M.M. Neethish, S.V.S.N. Rao, S.V. Rao, Wafer-scale silver nanodendrites with homogeneous distribution of gold nanoparticles for biomolecules detection, IScience. 25 (2022) 104849. https://doi.org/10.1016/j.isci.2022.104849.
- [85] Horiba Scientific, Determining Signal to Noise Ratio of a Spectrofluorometer Methods and formulas to ensure accurate sensitivity comparisons, (2019). https://www.horiba.com/en_en/technology/measurement-and-control-techniques/spectroscopy/fluorescence-spectroscopy/how-to-calculate-signal-to-noise-ratio/.
- [86] H.F.M. Boelens, R.J. Dijkstra, P.H.C. Eilers, F. Fitzpatrick, J.A. Westerhuis, New background correction method for liquid chromatography with diode array detection, infrared spectroscopic detection and Raman spectroscopic detection, J. Chromatogr. A. 1057 (2004) 21–30. https://doi.org/10.1016/j.chroma.2004.09.035.
- [87] R.A. Álvarez-Puebla, Effects of the excitation Wavelength on the SERS spectrum, J. Phys. Chem. Lett. 3 (2012) 857–866. https://doi.org/10.1021/jz201625j.
- [88] M. Shutova, A.M. Sinyukov, B. Birmingham, Z. Zhang, A. V. Sokolov, Adaptive optics approach to surface-enhanced Raman scattering, Opt. Lett. 45 (2020) 3709. https://doi.org/10.1364/ol.394548.
- [89] S.L. Kleinman, E. Ringe, N. Valley, K.L. Wustholz, E. Phillips, K.A. Scheidt, G.C. Schatz, R.P. Van Duyne, Single-molecule surface-enhanced raman spectroscopy of crystal violet isotopologues: Theory and experiment, J. Am. Chem. Soc. 133 (2011) 4115–4122. https://doi.org/10.1021/ja110964d.
- [90] M. Sackmann, S. Bom, T. Balster, A. Materny, Nanostructured gold surfaces as reproducible substrates for surface-enhanced Raman spectroscopy, 38(2007) 277–282. https://doi.org/10.1002/jrs.
- [91] K. Milligan, N.C. Shand, D. Graham, K. Faulds, Detection of Multiple

- Nitroaromatic Explosives via Formation of a Janowsky Complex and SERS, Anal. Chem. 92 (2020) 3253–3261. https://doi.org/10.1021/acs.analchem.9b05062.
- [92] S.S.B. Moram, C. Byram, S.N. Shibu, B.M. Chilukamarri, V.R. Soma, Ag/Au Nanoparticle-Loaded Paper-Based Versatile Surface-Enhanced Raman Spectroscopy Substrates for Multiple Explosives Detection, ACS Omega. 3 (2018) 8190–8201. https://doi.org/10.1021/acsomega.8b01318.
- [93] M.M. Rahaman, C. Li, Y. Yao, F. Kulwa, M.A. Rahman, Q. Wang, S. Qi, F. Kong, X. Zhu, X. Zhao, Identification of COVID-19 samples from chest X-Ray images using deep learning: A comparison of transfer learning approaches, J. Xray. Sci. Technol. 28 (2020) 821–839. https://doi.org/10.3233/XST-200715.
- [94] F. Lussier, V. Thibault, B. Charron, G.Q. Wallace, J.F. Masson, Deep learning and artificial intelligence methods for Raman and surface-enhanced Raman scattering, TrAC Trends Anal. Chem. 124 (2020) 115796. https://doi.org/10.1016/j.trac.2019.115796.
- [95] S. Weng, H. Yuan, X. Zhang, P. Li, L. Zheng, J. Zhao, L. Huang, Deep learning networks for the recognition and quantitation of surface-enhanced Raman spectroscopy, Analyst. 145 (2020) 4827–4835. https://doi.org/10.1039/d0an00492h.
- [96] S.K. Seongyong Park, Abdul Wahab, Minseok Kim, Self-Supervised learning for inter-laboratory variation minimization in surface-enhanced Raman scattering spectroscopy Analyst, 148(2023), 1473-1482. https://doi.org/10.1039/D2AN01569B.
- [97] B. Sharma, M. Fernanda Cardinal, S.L. Kleinman, N.G. Greeneltch, R.R. Frontiera, M.G. Blaber, G.C. Schatz, R.P. Van Duyne, High-performance SERS substrates: Advances and challenges, MRS Bull. 38 (2013) 615–624. https://doi.org/10.1557/mrs.2013.161.
- [98] G. Lopez-Reyes, F. Rull Pérez, A method for the automated Raman spectra acquisition, J. Raman Spectrosc. 48 (2017) 1654–1664. https://doi.org/10.1002/jrs.5185.
- [99] M.D.M. Francis W.L. Esmonde-White, Matthew V. Schulmerich, Karen A. Esmonde-White, Automated Raman Spectral Preprocessing of Bone and Other Musculoskeletal Tissues, Proc SPIE Int Soc Opt Eng. 7166 (2009). https://doi.org/10.1177/0022146515594631.Marriage.
- [100] H.G. Schulze, S. Rangan, J.M. Piret, M.W. Blades, R.F.B. Turner, Developing Fully Automated Quality Control Methods for Preprocessing Raman Spectra of Biomedical and Biological Samples, Appl. Spectrosc. 72 (2018) 1322–1340. https://doi.org/10.1177/0003702818778031.
- [101] F. Scholkmann, J. Boss, M. Wolf, An efficient algorithm for automatic peak detection in noisy periodic and quasi-periodic signals, Algorithms. 5 (2012) 588–603. https://doi.org/10.3390/a5040588.
- [102] Peak indentification, https://terpconnect.umd.edu/~toh/spectrum/PeakFindingandMeasurement.htm (Accessed 15 May 2023).

Intentional Blank Page

Chapter 6

Summary and Future Scope

Abstract

This thesis work explored different projects to address several pressing challenges in the SERS measurements for trace detection. The conclusion chapter of this thesis work emphasizes the significance of contributions made through this thesis and also their short comings. Our findings have not only addressed the research objectives but have also provided valuable insights to envision SERS for real field applications making a potential impact for explosives and other hazardous materials detection. Furthermore, this thesis work has identified several avenues for future research and development. The future scope of this work encompasses extension of the current application of machine learning techniques and also prospects to extend the SERS studies for biology applications. The conclusions drawn from this research lay the foundation for further advancements and investigations. It is our hope that this work will serve as a catalyst for future research endeavours and inspire future researchers to refine the results and applications.

6.1. Summary

In the last decade the SERS technique has seen a tremendous increase in applications addressing tenacious causes like homeland security, forensics, environmental safety, and disease detection including the recent covid-19 [1] [2]. However, translating the benefits from research to the field has been a challenge limiting the performance only to lab scale. The challenges on the way of field, especially for achieving real world applications of SERS can be summarized as [3],

Reproducibility: SERS is known to have poor spatial reproducibility caused by signal fluctuations from point to point owing to the localization of hotspots. This manifests more prominently during trace detection when the molecules on the plasmonic surface are sparse. Higher enhancement factor, as is the case for trace detection, often comes at the cost of reproducibility.

Durability and cost: Most often than not, gold and silver nanostructures are used as SERS substrates as they have desirable optical properties for enhanced field in the visible region. However, these samples are expensive and often prone to rapid oxidation (especially silver-based substrates). Having a semiconductor substrate as a template for gold and silver nanoparticles would bring down the cost of the substrate.

Signal fluctuations: Signal fluctuations are inherent to SERS through the same mechanism of signal enhancement. Electromagnetic and chemical enhancement are known to cause signal fluctuations through various mechanisms as discussed elaborately in chapter 5. This makes SERS hugely reliable on an expert thus limiting the measurements to be carried out outside the lab atmosphere.

Quantification: Though SERS has a potential for quantitative trace detection, accurate quantification is limited for very reasons of signal fluctuations and reproducibility. The intensity and the quantity are not directly correlated for reasons broadly discussed in chapter 5.

Ultra-trace detection: Making the best of the SERS substrates in order to achieve ultra-trace detection goes beyond fabrication of plasmonic substrates. Choosing the right wavelength close to the resonant excitation would enable achieving lower detection limits through SERRS.

Flexible substrates for easy sampling: Ease of sample collection is a key feature for field applications. Flexible substrates are not only low cost but would enable sample collection through swabbing as on when needed unlike rigid substrates.

This thesis successfully attempted to address these challenges with different projects that have been taken up as shown in figure 6.1. Table 6.1 presents summary of all the substrates and their highlights.

6.1.1. Machine Learning for Quantification in SERS

Novel hydrophobic filter paper substrate has been fabricated by a simple method of spin coating it with Si oil followed by drop-casting, drying of Au nanoparticles to use it as a SERS substrate [4]. Machine learning techniques namely, PCA and SVR were used for quantification of trace explosive picric acid and a dye molecule with a remarkable accuracy of greater than 96%. The measurements were done with a portable Raman spectrometer and the total time to run the model was less than 10 s making it a promising tool for field applications. Some of the significant contributions made in this work are,

- a) For the first time, using a simple method of coating with Si oil, low-cost alternative for modifying the wettability of the Si oil has been proposed. HFPs had previously been reported to be either expensive or to require extensive pre- and post-processing. For the SERS experiments, FP was coated in a few prior works with alkyl ketene dimer (AKD) [5], (2-dodecen-1-yl)-diluted PDMS [6], succinic anhydride [7](60 USD for 100 g), agar [8], and spin-coating perfluoroalkyltriethoxysilanes [9] (150 USD for 5 g). In contrast coating with Si oil (15 USD for 500 mL) is a single step, cost effective method that has been prescribed so far.
- b) Using a portable Raman spectrometer, two analyte molecules, PA and CV were detected with sensitivity of 5 μ M and 100 nM, respectively. Significant data of nearly 900 spectra has been collected for both the analytes with nearly 100 per concentration in order to full sample the substrate surface.
- c) Nonlinear machine learning models, PCA and SVR have been used in sequence in order to quantify the analyte molecule under study. The time required to run the program was less than 10s and this is the fastest algorithm so far used for quantification in SERS.

6.1.2. Femtosecond Laser Ablation of Metals and Semiconductors

Femtosecond laser ablation has been utilised to fabricate nanostructures on metals and semiconductors and effects of different experimental parameters have been thoroughly studied. Some of the significant contributions made in these studies have been summarised below.

6.1.2.1. Studies on Ag-Au nanostructures

- a) Using an amplifier system and Ag-Au as a substrate, effects of angle of incidence on the resulting nanostructures and consequently their SERS performance has been studied [10].
- b) It was found that at a particular angle of incidence of 10⁰ the substrate has outperformed the other substrates at 0⁰, 20⁰, and 30⁰ with rhodamine 6G as a probe molecule. This has been attributed to increase in ablation yield at this particular angle of incidence.
- c) Using contrasting nanostructures with debris deposited samples and periodic nanostructures after cleaning, the relationship between enhancement factor and reproducibility has been explored for the first time. An inverse relationship between these two has found implying good reproducibility in trace detection comes at the cost of enhancement.
- d) Further, these nanostructures were utilised for ultra-trace detection of R6G, CV, PA and cysteine, respectively with sensitivity of 10 fM, 100 fM, 100 nM, and 100 nM using resonant excitation through SERRS.

6.1.2.2. Studies on Si Nanostructures

- a) As opposed to conventional laser ablation with amplifier system, a fs oscillator has been used to fabricate web-like nanostructures on Si as a low cost alternative for SERS substrate [11].
- b) Effects of scanning speed and fluence on the web-like structures have been studied in detail and correlated with the existing literature [12].
- c) The mechanism of formation of these web-like Si nanostructures has been thoroughly understood and the results obtained were analysed.
- d) After coating it with Au of 10 nm through thermal evaporation method, the substrates were utilised for SERS based detection of MB with a sensitivity of 1 μM.

6.1.2.3. Studies on Ag, Cu using Cylindrical Focusing

- a) Using fs laser ablation through cylindrical focusing, large area ripple like structures were obtained on Ag and Cu unlike the resulting structures from Gaussian beam ablation.
- b) The Ag nanostructures were utilised for the detection of tetryl, RDX, and cytosine with a sensitivity of 50 nM, 1 μ M, 100 nM with a significant reproducibility of ~6%.
- c) Using the Ag structures and PCA, different species of bacteria, E. coli. have been classified and identified using the SERS data.
- d) Low cost, Cu NSs were utilised for the detection of tetryl, ammonium nitrate, MB with a sensitivity of 100 μ M, 50 μ M and 5 μ M with a remarkable RSD of 5%.

6.1.3. Anisotropic Ag-Au dendrites for SERS

Highly branched and anisotropic Ag dendrites decorated with Au have been synthesised using a simple electroless deposition on Si [13].

- a) The near field enhancement in the vicinity of the nanostructures has been studied using COMSOL Multiphysics clearly showing the advantage of anisotropic structures.
- b) Establishing the versatility of the substrates, they have used for the detection of diverse analyte molecules including explosives, dye molecules, pesticide and biomolecules. CV, adenine, cytosine, penicillin G, kanamycin, ampicillin, AN, and thiram were detected with sensitivity of 1 nM, 100 nM, 10 nM, 10 nM, 100 nM, 10 nM, 100 nM, 10 nM, respectively.
- c) These substrates were utilized for developing a neural network model named neural network aided SERS (NNAS) to overcome signal fluctuations in the SERS data.
- d) Using a unique signal to noise ratio approach the spectra has been labelled as representative and non-representative of the molecules under study. Using the labels, the model has been trained for three analyte molecules, CV, PA, and Tetryl using SERS data from the Raman mapping.
- e) Out of sample predictions were also made to evaluate the model's performance and resulted in accuracy of 0.982, 0.981 and, 0.985 for CV, Tetryl and, Picric Acid, respectively.
- f) The model has been compared with standard classification algorithm, SVM (accuracy 89%) and was found to outperform.

- g) We believe that our NNAS can bridge the performance gap of SERS substrates between lab and onsite detection.
- h) Through this work, a detailed protocol for SERS-based detection has been prescribed to encourage beginners in the field [14].

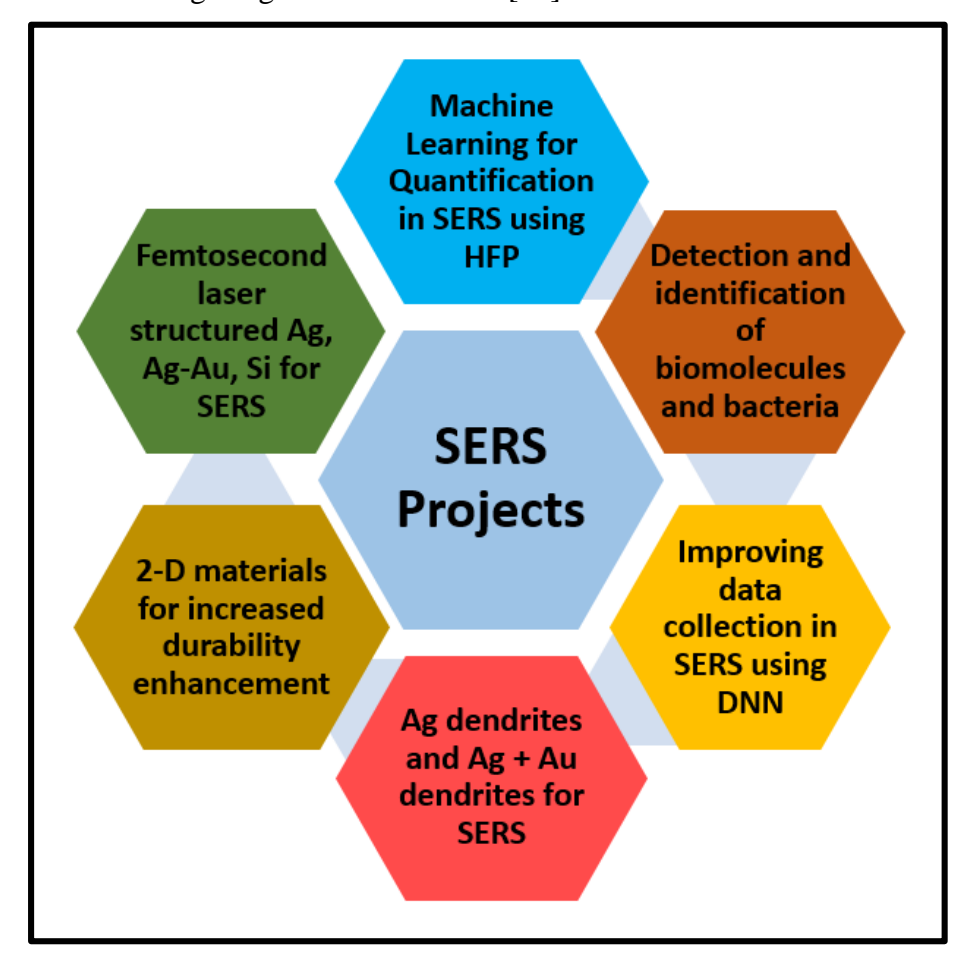


Figure 6.1: Summary of different contributions made in SERS in this thesis work.

6.1.4. 2-D materials for SERS

- a) Femtosecond laser irradiation of MoS₂ has been carried out in ethanol, water and methanol and the results were characterised using FESEM, UV-visible spectroscopy.
- b) Nano-plates like morphology was observed in water ablated samples and were subsequently used for SERS in combination with Si nanowires decorated with plasmonic nanoparticles.
- c) MoS₂ has resulted in nearly ~2-fold enhancement in addition to the enhancement from plasmonic materials and has significantly increased the durability of the substrate to more than 200 days.
- d) Different molecules, malachite green, melamine, naphthalene, L-cysteine, and tetryl have been studied for trace detection and achieved sensitivity of 0.5 nM, 100 nM, 300

nM, 100 nM, 50 nM, respectively. In addition, the substrates have also demonstrated successful detection of E. coli in water.

Table 6.1: Summary of all the substrates, analyte molecules, and highlights of the studies performed in this thesis.

S. No.	SERS Substrate	Molecules	Lowest detected	Highlights
1	fs laser structured Cu	Tetryl, AN, MB	100 μM, 50 μM and 5 μM	Low cost, reproducible (5 %)
2	fs laser structured Ag	Tetryl, RDX, Cytosine	50 nM, 1 μM, 100 nM	Highly reproducible with RSD of 6%.
3	Chemically synthesised AuNPs@AgNDs	CV, adenine, cytosine, penicillin G, kanamycin, ampicillin, AN, and Thiram	1 nM, 100 nM, 10 nM, 10 nM, 100 nM, 10 nM, 100 nM, 10 nM	Low cost, durable substrates. Substrates were used to develop NNAS model to overcome signal fluctuations in SERS
4	Hybrid MoS ₂ layered plasmonic Si nanostructures	Malachite Green, Melamine, Naphthalene, L- Cysteine, tetryl and E.coli	0.5 nM, 100 nM, 300nM, 100 nM, 50 nM	Highly durable and low-cost substrates that could be even used for live organism sensing
5	Flexible porous Si substrate	MB, PA, AN, and Thiram	50 nM, 1 μM, 2 μM, and 1 μM	Free standing, flexible and low-cost substrate.
6	Hydrophobic plasmonic filter paper	Picric Acid and Crystal Violet	5 μM and 100 nM	Novel substrate, fabricated for the first time and used for rapid quantification using ML techniques.
7	fs laser structured web-like Si coated with Au	Methylene blue	1 μΜ	Formation of web- like NSs is studied and the mechanism is understood.
8	fs laser structured Ag-Au	Rhodamine 6G, crystal violet, picric acid, and cysteine	10 fM, 100 fM, 100 nM, and 100 nM	SERRS has been used for ultra-trace detection. The relationship between enhancement and reproducibility is studied.

6.1.5. Flexible, Free Standing Porous Si Substrate for SERS

- a) Through a simple technique of wet etching in the presence of electric field, porous Si has been fabricated and was further decorated with Ag through etching in the presence of HF and AgNO₃ [15].
- b) Studies on the concentration and duration of etching has been carried out to optimise the SERS performance based on the hotspot density.
- c) These samples were employed for the trace detection of MB, PA, AN, and thiram with sensitivity of 50 nM, 1 μ M, 2 μ M, and 1 μ M, respectively.
- d) With significant durability of ~90 days and cost much lower than the available commercial substrates, these samples are suitable for real world applications.

A five-axis representation to visualise SERS performance has also been formulated for the first time and is presented in appendix C.

6.2. Future Scope

In many aspects, there is a significant room for improvement in the studies that have been carried out in this thesis.

- a) One important aspect is to focus on commercializing the substrates proposed in this thesis. In almost all the cases, the substrates have outperformed the commercially available substrates in terms of durability, sensitivity, versatility, and reproducibility. The HFP, for example can be commercialised by making paper strips analogues to pH strips and can be used, on the go, in the field as done in some of the previous studies. A hand-held Raman system will help in analyzing the data within a short period of time. Large scale, single step synthesis of anisotropic nanostructures on Si wafer with preparation time of less than 2 hours has an enormous potential of commercial usage given the cost and superior performance.
- b) In the study of HFP for SERS, the enhancement could be significantly improved by using alloy or anisotropic nanostructures like stars or triangles as reported before [16]. In addition to trace detection, the substrates can be utilised for vapour detection of different explosives.
- c) A simple alternative for contact angle measurements have been temporarily used using a Samsung camera and a combination of lenses as shown in figure 6.2. The contact angle measured using the setup was found to have a difference of ~40 compared with

- the angle measured using the commercial setup. The quality of the image and the setup can be significantly improved by using appropriate illumination and a better camera.
- d) The regression model used for quantification can be improved by collecting data for more intermediate concentrations for the analyte molecules under study. However, care here must be taken to ensure that the intensity distribution does not overlap as a part of exploratory data analysis.



Figure 6.2: Images of a drop of Au nanoparticles and CuSO₄ on HFP taken using home built contact angle setup.

- e) For the neural network model used in the thesis, the peaks used for calculating SNR were identified manually. Instead, a moving window algorithm can be used to identify the peaks, removing expert dependence at one more stage.
- f) Early identification of diseases using the SERS potential for trace detection is the current trend in the research concerning SERS [17]. The substrates prescribed in this thesis have a huge potential to be used for different applications in biology as well. The machine learning algorithms studied in this thesis will be a foundation for the analysis of complex data obtained from the biological systems.
- g) The COMSOL studies carried out in the thesis can be extended beyond plasmonics to study enhancements originating from Si nanostructures and MoS₂ in combination with plasmonic materials. Studies on effects of light polarization can also be initiated.
- h) Gaussian distribution of the laser pulse during SERS measurements lead to inhomogeneous illustration and hence excitation of the hotspots in the selected area. Modifying the wave front for carrying out SERS measurements using adaptive optics can be considered to achieve uniform illustration and effective plasmonic resonance which would probably reflect in the reproducibility, sensitivity of the Raman signal [18].

References

- [1] B. Sharma, R.R. Frontiera, A.I. Henry, E. Ringe, R.P. Van Duyne, SERS: Materials, applications, and the future, Mater. Today. 15 (2012) 16–25. https://doi.org/10.1016/S1369-7021(12)70017-2.
- [2] F. Saviñon-Flores, E. Méndez, M. López-Castaños, A. Carabarin-Lima, K.A. López-Castaños, M.A. González-Fuentes, A. Méndez-Albores, A review on sersbased detection of human virus infections: Influenza and coronavirus, Biosensors. 11 (2021). https://doi.org/10.3390/bios11030066.
- [3] A.I. Pérez-Jiménez, D. Lyu, Z. Lu, G. Liu, B. Ren, Surface-enhanced Raman spectroscopy: Benefits, trade-offs and future developments, Chem. Sci. 11 (2020) 4563–4577. https://doi.org/10.1039/d0sc00809e.
- [4] R. Beeram, D. Banerjee, L.M. Narlagiri, V.R. Soma, Machine learning for rapid quantification of trace analyte molecules using SERS and flexible plasmonic paper substrates, Anal. Methods. 14 (2022) 1788–1796. https://doi.org/10.1039/d2ay00408a.
- [5] M. Lee, K. Oh, H.K. Choi, S.G. Lee, H.J. Youn, H.L. Lee, D.H. Jeong, Subnanomolar Sensitivity of Filter Paper-Based SERS Sensor for Pesticide Detection by Hydrophobicity Change of Paper Surface, ACS Sensors. 3 (2018) 151–159. https://doi.org/10.1021/acssensors.7b00782.
- [6] N. V. Godoy, D. García-Lojo, F.A. Sigoli, J. Pérez-Juste, I. Pastoriza-Santos, I.O. Mazali, Ultrasensitive inkjet-printed based SERS sensor combining a high-performance gold nanosphere ink and hydrophobic paper, Sensors Actuators, B Chem. 320 (2020) 128412. https://doi.org/10.1016/j.snb.2020.128412.
- [7] A. Raza, B. Saha, In situ silver nanoparticles synthesis in agarose film supported on filter paper and its application as highly efficient SERS test stripes, Forensic Sci. Int. 237 (2014) 42–46. https://doi.org/10.1016/j.forsciint.2014.01.019.
- [8] D.J. Lee, D.Y. Kim, Hydrophobic paper-based SERS sensor using gold nanoparticles arranged on graphene oxide flakes, Sensors. 19 (2019) 8–14. https://doi.org/10.3390/s19245471.
- [9] C. Zhang, T. You, N. Yang, Y. Gao, L. Jiang, P. Yin, Hydrophobic paper-based SERS platform for direct-droplet quantitative determination of melamine, Food Chem. 287 (2019) 363–368. https://doi.org/10.1016/j.foodchem.2019.02.094.
- [10] R. Beeram, V.R. Soma, Ultra-trace detection of diverse analyte molecules using femtosecond laser structured Ag Au alloy substrates and SERRS, Opt. Mater. 137 (2023) 113615. https://doi.org/10.1016/j.optmat.2023.113615.
- [11] R. Beeram, D. Banerjee, A. Mangababu, S.V. Rao, Femtosecond Laser Processed Web-like Silicon Nanostructures and Application in Surface Enhanced Raman Spectroscopy, Presented in CLEO-PACIFIC 2022, Japan. (Yet to be online)
- [12] B. Tan, K. Venkatakrishnan, Synthesis of fibrous nanoparticle aggregates by femtosecond laser ablation in air, Opt. Express. 17 (2009) 1064. https://doi.org/10.1364/oe.17.001064.
- [13] V.S. Vendamani, R. Beeram, M.M. Neethish, S.V.S.N. Rao, S.V. Rao, Wafer-scale

- silver nanodendrites with homogeneous distribution of gold nanoparticles for biomolecules detection, IScience. 25 (2022) 104849. https://doi.org/10.1016/j.isci.2022.104849.
- [14] V.S. Vendamani, R. Beeram, S.V.S.N. Rao, S.V. Rao, Protocol for designing AuNP-capped Ag dendrites as surface-enhanced Raman scattering sensors for trace molecular detection, STAR Protoc. 4 (2023) 102068. https://doi.org/10.1016/j.xpro.2023.102068.
- [15] V.S. Vendamani, R. Beeram, S.V.S. Nageswara Rao, A.P. Pathak, V.R. Soma, Trace level detection of explosives and pesticides using robust, low-cost, free-standing silver nanoparticles decorated porous silicon, Opt. Express. 29 (2021) 30045. https://doi.org/10.1364/oe.434275.
- [16] S.S.B. Moram, C. Byram, V.R. Soma, Gold-nanoparticle- and nanostar-loaded paper-based SERS substrates for sensing nanogram-level Picric acid with a portable Raman spectrometer, Bull. Mater. Sci. 43 (2020) art. # 53. https://doi.org/10.1007/s12034-019-2017-8.
- [17] R. Beeram, K.R. Vepa, V.R. Soma, Recent Trends in SERS-Based Plasmonic Sensors for Disease Diagnostics, Biomolecules Detection, and Machine Learning, 5 (2023) 328. https://doi.org/10.3390/bios13030328.
- [18] M. Shutova, A.M. Sinyukov, B. Birmingham, Z. Zhang, A. V. Sokolov, Adaptive optics approach to surface-enhanced Raman scattering, Opt. Lett. 45 (2020) 3709. https://doi.org/10.1364/ol.394548.

Intentional Blank Page

Appendix A

Support Vector Machine

Support Vector Machine (SVM) is a powerful machine learning algorithm that is used for both classification and regression problems. It falls under supervised learning technique. It is extremely useful in solving both linear and non-linear problems and an even for outlier detection in some cases. Unlike many ML algorithms, SVMs are known to work well for small data sets as well. SVM operates on the principle of identifying a hyperplane capable of effectively separating data points into distinct classes. This hyperplane is carefully chosen to maximize the distance between itself and the nearest data points from each class, known as support vectors. Termed as a 'decision boundary,' the hyperplane is defined by a set of parameters that are learned through the training process. In binary classification scenarios, SVM seeks to discover a hyperplane that optimizes the margin, representing the gap between the hyperplane and the closest data points from both classes. To achieve this, an optimization problem is formulated, aiming to minimize classification errors while simultaneously maximizing the margin. Several techniques, such as quadratic programming, gradient descent, and interior point methods, can be employed to solve this constrained optimization problem effectively. SVM can be extended to address multiclass classification tasks by adopting a one-vs-all approach. This strategy involves training multiple binary classifiers, each focused on differentiating one class from the rest. By combining the results from these binary classifiers, the overall classification of multiple classes is achieved. One notable advantage of SVM is its proficiency in handling highdimensional data efficiently. Unlike certain machine learning algorithms like decision trees and artificial neural networks, SVM exhibits reduced susceptibility to overfitting, a common concern where a model becomes excessively complex and struggles to generalize to new data points.

The mathematics behind SVM can be understood using a simple binary classification problem. Let the input parameters be represented by a vector, x with a dimension, D. Each data point is called as a support vector. y be the label corresponding to the vector x and is the prediction variable. The equation of the hyperplane for this case can be given as,

$$wx - b = 0$$

Where, w is a vector with same dimensionality as the input parameter, x and b is a real number. The above equation is equivalent to,

$$w^1x^1 + w^2x^2 + w^3x^3 + \cdots + w^Dx^D - b = 0$$

Using a mathematical function, depending on the sign of the input vector relative to the hyperplane, the classification of different classes is performed. This can be constructed as,

$$y = sign(wx - b)$$

The problem then remains to find the hyperplane that best classifies the data i.e. to find optimum values of w, b represented hereafter as w^* and b^* . The job of the algorithm is to find these optimum values defined by a function, f(x) as,

$$f(x) = sign(w^*x - b^*)$$

Finding the right w^* and x^* is an optimization problem that is typical in any machine learning algorithm under given constraints. The constraints for the case of a binary classification problem that is shown in figure A.1 is,

$$wx_i - b \ge 1$$
 if $y_i = +1$

$$wx_i - b \le 1 \text{ if } y_i = -1$$

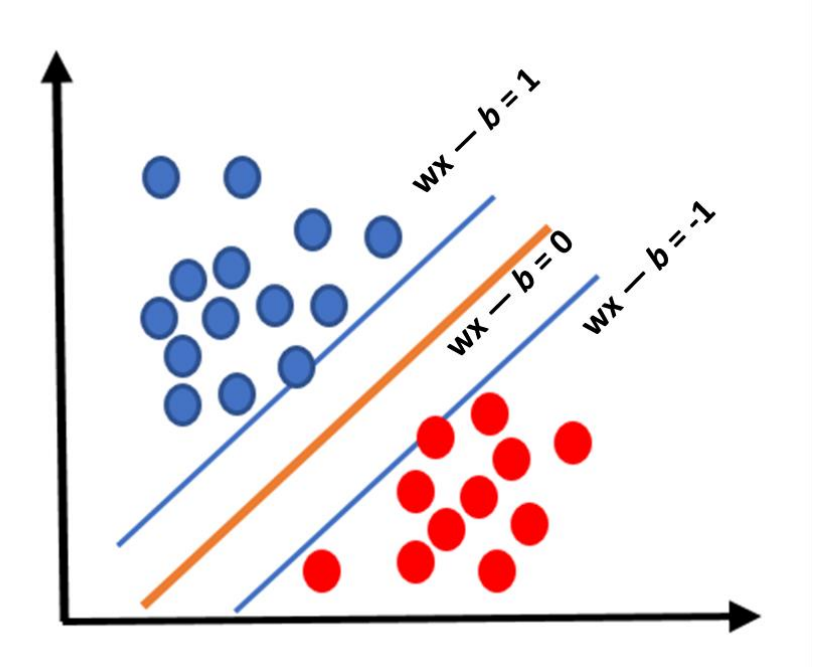


Figure A.1: Schematic of SVM for classification of two classes through a hyperplane.

The decision boundary given by the hyperplane in SVM also has a 'margin' which is the distance between two support vectors that are closest to the hyperplane. The optimization problem of SVM can be derived as,

$$\min \frac{1}{2} ||\mathbf{w}||^2$$
 with the constraint of $y_i(\mathbf{w} x_i - b) \ge 1$

The example above is a simple binary classification making the hyperplane linear in a twodimensional plane. However, for higher dimensions the problem is complex and SVM in this case uses a kernel function. Kernel function is an alternative to polynomials functions which when used in higher orders tend to overfit the data, by using something called as 'kernel trick'.

Appendix B

Guide to Implementing Machine Learning Using Python

Python is a preferable language for implementing machine learning as it has a rich ecosystem of libraries and frameworks specifically designed for machine learning. Popular libraries like TensorFlow, Pandas, and scikit-learn provide extensive functionality and support for various machine learning tasks, making it easier to develop and deploy machine learning models. Python is also known for its simplicity and readability. Its clean syntax and easy-to-understand code make it accessible for both beginners and experienced developers. Here, we are providing a step-by-step guide to implement machine learning models for spectroscopy using python.

- 1) Data curation: Machine learning models always perform better if there is statistically significant data. In fact, in a breakthrough study, it was found that any model performs equally good as the best model if the data set is large enough¹. However, the quality of data is crucial keeping in mind the problem of interest (It is popularly said that 'Garbage in, Garbage out'). It always helps to formulate the problem before data collection. It has to be ensured that the data collected is a complete representation of the sample under study. Pandas is a popular library for reading and writing large data in python.
- 2) Data Pre-processing: Spectroscopic data like SERS often need certain pre-processing before building a model. Baseline correction, peak identification and spike removal are a few such steps. Machine learning algorithms are sensitive to the magnitude of the data and hence often need any kind of scaling like normalization or standardization before progressing. This can be implemented by importing scalars like 'StandardScalar' or Normalizer from the 'sklearn.preprocessing' library.
- 3) Exploratory Data Analysis: It is important to have a fair understanding of data in hand before choosing a model. Exploratory data analysis includes finding the mean, distribution and outliers in the data to name a few. Finding relation between the variables under study (linear or nonlinear, for example) will be a guide for choosing a machine learning model.
- **4) Choosing a model:** Choosing a model is a crucial step and is guided by the following prescriptions.

- a) Gain a thorough understanding of the problem you are trying to solve. Identify the type of machine learning problem, such as classification, regression, clustering, or recommendation. Different problems require different types of models.
- b) Consider the size of the dataset, the number of features, and the presence of any patterns or relationships. Understanding your data will help you determine which models are appropriate and whether any preprocessing or feature engineering is required.
- c) Models are built on certain assumptions about the data. Evaluate whether your data aligns with the assumptions of the model you are considering. For example, linear regression assumes a linear relationship between variables.
- d) Assess the complexity of the problem at hand. Simple models like linear regression or decision trees may be sufficient for straightforward problems, while complex problems with intricate patterns may require more advanced models like deep neural networks.
- e) Determine the performance requirements for your model. Consider factors such as accuracy, speed, interpretability, and scalability. Some models may trade off interpretability for better accuracy, so consider the trade-offs that align with your specific needs. Evaluate the performance of different models using appropriate evaluation metrics. Split your data into training and validation sets or use cross-validation techniques to assess how well each model generalizes to unseen data. Compare metrics like accuracy, precision, recall, F1-score, or mean squared error to select the model that performs the best. Data splitting can be implemented using scikit-learn library.
- f) Take into account the computational resources required to train and deploy the model. Some models may have higher memory or processing requirements, so ensure that you have the necessary infrastructure to support them.
- g) Leverage the knowledge and experience of the machine learning literature that is existing in the area of your study. Stay updated on the latest research, read papers, and participate in online forums and discussions to understand which models are commonly used and recommended for similar problems.
- h) It is often an iterative process to find the best model. Experiment with different models, fine-tune hyperparameters, and analyze the results. Refine your approach based on insights gained from each iteration. Hyperparameters are

model variables that can be changed in order to improve the accuracy of the model, like for example number of layers in an artificial neural network.

- 5) Implementing the model of choice: Python provides an easy way to implement any complex model with its standard libraries. Scikit-learn offers a wide range of machine learning algorithms and techniques, including supervised and unsupervised learning, classification, regression, clustering, dimensionality reduction, and model selection. It covers many popular algorithms such as decision trees, random forests, support vector machines (SVM), k-nearest neighbours (KNN), PCA and more. For implementing neural networks, Keras is a popular library and is extremely easy to use.
- 6) **Results representation:** Data visualization in python is made easy with libraries like matplotlib, and seaborn. Depending on the model and results of interest any representation of choice can be implemented using these models.

A deeper understanding of the models and theory implementation can be achieved by attending Prof. Andrew Ng's course on ML on Coursera. A screenshot of code implementing PCA is presented in figure B.1.

```
import pandas as pd
from sklearn.model_selection import train_test_split
import matplotlib.pyplot as plt
from sklearn.preprocessing import StandardScaler, Normalizer, MinMaxScaler, RobustScaler
from sklearn.decomposition import KernelPCA as kpca
from pca import pca
from sklearn.svm import SVR
from sklearn.metrics import r2_score
#Reading data
df = pd.read_csv('file path')
lab = df.values[:,0].astype('uint8')
feat = df.iloc[:,1:].values
nfeat1 = RobustScaler().fit_transform(feat)
# np.savetxt('C:/Python Programs/Spyder_programs/Normal.csv',nfeat1,delimiter=',')
skpca1 = kpca(n_components=10, kernel='sigmoid')
X1 = skpca1.fit(nfeat1)
kpca_transform = skpca1.fit_transform(nfeat1)
explained_variance = np.var(kpca_transform, axis=0)
ev = explained_variance / np.sum(explained_variance)
         -- Bar Graph for Explained Variance Ratio
plt.bar([1,2,3,4,5,6,7,8,9,10],list(ev*100),label='Principal Components',color='b')
plt.legend()
plt.xlabel('Principal Components ')
```

Figure B.1: Screenshot presenting implementation of ML model on python.

Appendix C

Five Axis Representation of SERS Performance

In this thesis we have illustrated a novel and graphic way to represent the performance of any SERS substrate. There are five important metrics to evaluate a SERS substrate, namely a) Cost, b) Durability, c) Reproducibility, d) Enhancement Factor and, e) Sensitivity. Our visualization is a summary of this parameters which communicates complex information in one image. In our representation we have given a false scale for each of the parameter based on a range of values for each rank. These five parameters are further represented on five axes along concentric circles where each circle represents a number on the scale bar as shown in figure C1. A polygon is drawn joining all the points for each parameter for a given substrate. The colour of the polygon is also assigned based on an overall score calculated for all the five parameters.

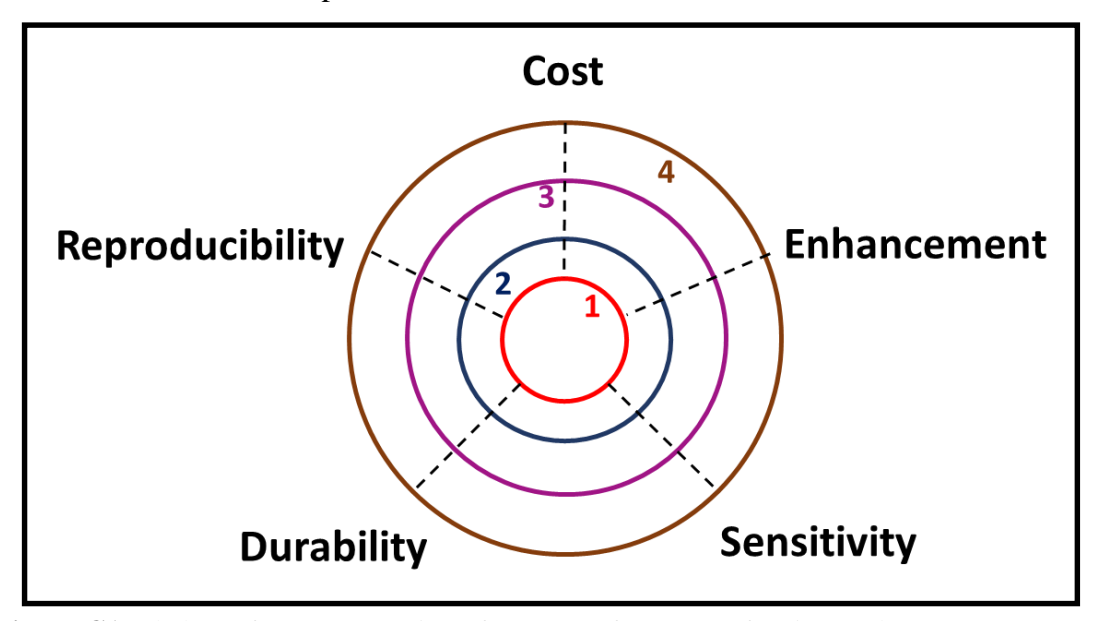


Figure C1: Skeleton for representation of SERS performance of a given substrate.

The scale that is set for each parameter are as below in table C1.

Table C1: Summary of scale of parameters.

Cost	RSD	Durability	Sensitivity	Enhancement	Score	Overall Score
<1 USD	<7%	>3 months	10 nM – few pM	>10 ⁷	4	20-18 Green
1 USD- 5 USD	7-12%	3-2 months	1-100 nM	10 ⁷ - 10 ⁵	3	18- 16 Yellow
5 USD- 10 USD	12-20%	2 -3 weeks	1-100 μΜ	$10^5 - 10^3$	2	16-12 Orange
>10 USD	>20%	<3 weeks	<μΜ	<10 ³	1	<12 Red

Based on this representation, two substrates, AuNPs@AgNDs and hydrophobic filter paper has been evaluated and the representation are presented in figure C2. It is evident from the representation of the two substrates that AuNPs@AgNSs has clearly outperformed HFP in terms of durability, sensitivity and reproducibility, while the cost being comparable. These representations can also be used as a guide to improve the performance of a particular substrate based on the short comings. For example, the representation communicates that HFP has relatively low enhancement which can be improved on if focused specifically by using alloy or anisotropic NPs. Durability can also be improved by storing in vacuum atmosphere. Hence, this representation is a powerful tool to analyse, compare and estimate room for improvement for different SERS substrates.

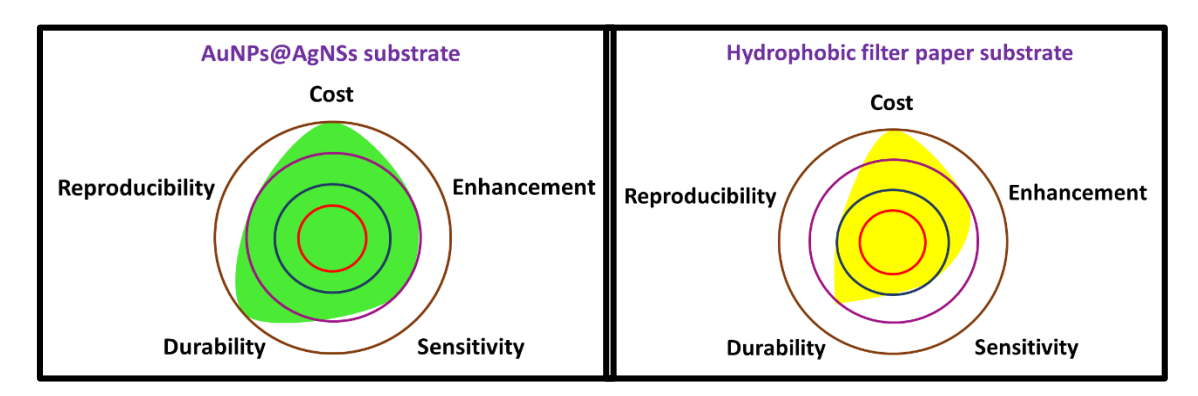


Figure C2: Representations of AuNPs@AgNDs substrate and hydrophobic filter paper.

List of Publications

- 1) **Beeram Reshma,** Dipanjan Banerjee, Linga Murthy Narlagiri, and Venugopal Rao Soma. "Machine learning for rapid quantification of trace analyte molecules using SERS and flexible plasmonic paper substrates." *Analytical Methods* 14, no. 18 (2022): 1788-1796.
- 2) **Beeram Reshma**, V. S. Vendamani, and Venugopal Rao Soma. "Deep learning approach to overcome signal fluctuations in SERS for efficient On-Site trace explosives detection." *Spectrochimica Acta Part A: Molecular and Biomolecular Spectroscopy* 289 (2023): 122218.
- 3) **Beeram Reshma**, and Venugopal Rao Soma. "Ultra-trace detection of diverse analyte molecules using femtosecond laser structured Ag—Au alloy substrates and SERRS." *Optical Materials* 137 (2023): 113615.
- 4) Vendamani, V. S., **Reshma Beeram,** SVS Nageswara Rao, and Soma Venugopal Rao. "Protocol for designing AuNP-capped Ag dendrites as surface-enhanced Raman scattering sensors for trace molecular detection." *STAR protocols* 4, no. 1 (2023): 102068.
- 5) **Beeram Reshma**, Kameswara Rao Vepa, and Venugopal Rao Soma. "Recent trends in SERS-based plasmonic sensors for disease diagnostics, biomolecules detection, and machine learning techniques." *Biosensors* 13, no. 3 (2023): 328.
- 6) Vendamani, V. S., **Reshma Beeram**, SVS Nageswara Rao, A. P. Pathak, and Venugopal Rao Soma. "Trace level detection of explosives and pesticides using robust, low-cost, free-standing silver nanoparticles decorated porous silicon." *Optics Express* 29, no. 19 (2021): 30045-30061.
- 7) Vendamani, V. S., **Reshma Beeram,** M. M. Neethish, SVS Nageswara Rao, and S. Venugopal Rao. "Wafer-scale silver nanodendrites with homogeneous distribution of gold nanoparticles for biomolecules detection." *iScience* 25, no. 8 (2022): 104849.
- 8) Vendamani, V. S., **Reshma Beeram**, and Venugopal Rao Soma. "MoS₂ nanosheets decorated plasmonic silicon nanowires as SERS substrates for ultra-sensitive multiple analyte detection," *Journal of Alloys and Compounds* 959 (2023): 170573.
- 9) Narlagiri, Linga Murthy, M. S. S. Bharati, **Reshma Beeram**, Dipanjan Banerjee, and Venugopal Rao Soma. "Recent trends in laser-based standoff detection of hazardous molecules." *TrAC*, *Trends in Analytical Chemistry* 153 (2022): 116645.

10) Byram, Chandu, Sree Satya Bharati Moram, Dipanjan Banerjee, **Reshma Beeram**, Jagannath Rathod, and Venugopal Rao Soma. "Review of ultrafast laser ablation for sensing and photonic applications." *Journal of Optics* 25 (2023): 043001.

Conference Proceedings:

- 1) **Beeram Reshma,** Dipanjan Baneerjee, and Soma Venugopal Rao. "Sand Dune Like Copper Nanostructures Fabricated by Femtosecond Laser Ablation for Trace Explosive Detection." In Frontiers in Optics/Laser Science 2022, 16 20 October, Rochester, New York, USA., pp. JTu4A-27. Optica Publishing Group, 2022.
- 2) Beeram Reshma, Dipanjan Banerjee, A. Mangababu, and Soma Venugopal Rao, "Femtosecond Laser Processed Web-like Silicon Nanostructures and Application in Surface Enhanced Raman Spectroscopy." In Conference on Lasers and Electro-Optics/Pacific Rim (CLEO-PR), Sapporo, Japan, 31st July- 5th August, p. CThP5D_04. Optica Publishing Group, 2022.
- 3) **Beeram Reshma**, V. S. Vendamani, and Soma Venugopal Rao. "Flexible Paper Substrate with Silver Dendrites for Trace Detection of Dye and Explosive Molecules using SERS." Workshop on Recent Advances in Photonics (WRAP), 04 March- 06 March, 2022, IIT Bombay,1-2. IEEE, 2022.
- 4) Beeram Reshma, and Soma Venugopal Rao. "Studies on Effects of Size, Morphology and Composition in Ag, Au and Ag-Au Plasmonic Nanoparticles." International Conference on Recent Trends in Photonics' (NPS 2021), 27th February- 1st March, International School of Photonics, Cochin University of Science and Technology.
- 5) Banerjee, Dipanjan, **Reshma Beeram,** and Venugopal Rao Soma. "Ultrafast Bessel Beam Induced Finger-like Silver Nanostructures for Trace-level Picric Acid Sensing." In Frontiers in Optics/Laser Science 2022, 16th 20th October, Rochester, New York, USA., pp. LM2B-5. Optica Publishing Group, 2022.

Achievements/Awards:

- 1) **Best Oral Presentation Award** at 7TH THEME MEETING ON ULTRAFAST SCIENCES (UFS-2021), 12th-13th November, 2021, UM-DAE Centre for Excellence in Basic Sciences, Mumbai University, for the presentation titled "Femtosecond Laser Structured Web-like Silicon Structures for Surface Enhanced Raman Spectroscopy".
- 2) **Best Poster presentation Award** at The Indo-French Conference on Frontiers in Photonics and Metamaterials (IFCFPM)-2023, 20th-22nd, April, 2023, Mahindra University, Hyderabad, for presentation on "Deep Learning Approach to Overcome Signal Fluctuations in SERS".



Cite this: Anal. Methods, 2022, 14, 1788

Machine learning for rapid quantification of trace analyte molecules using SERS and flexible plasmonic paper substrates†

Reshma Beeram, Dipanjan Banerjee, Linga Murthy Narlagiri and Venugopal Rao Soma $^{\odot}$ *

Given the intrinsic nature of low reproducibility and signal blinking in the surface enhanced Raman scattering (SERS) technique, especially while detecting trace/ultra-trace amounts, it remains a major challenge to quantify the analyte under study. Here we present a simple and economically viable, flexible hydrophobic plasmonic filter paper-based SERS substrate for the quantification of two trace analytes [crystal violet (CV) and picric acid (PA)] using machine learning techniques and SERS data. The wettability of the substrate was modified with an easy and low-cost technique of coating it with silicone oil. Gold nanoparticles were synthesized using a femtosecond laser ablation in water technique. The prepared nanoparticles were characterized using UV, TEM, and SEM techniques and subsequently loaded onto filter papers before using them for SERS studies. We have considered the SERS intensities of the analytes at different concentrations with over 900 spectra to train the model. Principal component analysis (PCA) was used to reduce the dimensionality and, hence, the complexity of the model. Furthermore, support vector regression was used to quantify the analyte molecules and we achieved an R^2 error of 0.9629 for CV and 0.9472 for PA. In conjunction with a portable Raman spectrometer and a computation time of less than <10 s, we believe that this is an affordable and rapid method for quantification of analytes using the SERS technique.

Received 9th March 2022 Accepted 6th April 2022

DOI: 10.1039/d2ay00408a

rsc.li/methods

Spectrochimica Acta Part A: Molecular and Biomolecular Spectroscopy 289 (2023) 122218



Contents lists available at ScienceDirect

Spectrochimica Acta Part A: Molecular and Biomolecular Spectroscopy

journal homepage: www.journals.elsevier.com/spectrochimica-acta-part-a-molecular-and-biomolecular-spectroscopy





Deep learning approach to overcome signal fluctuations in SERS for efficient On-Site trace explosives detection

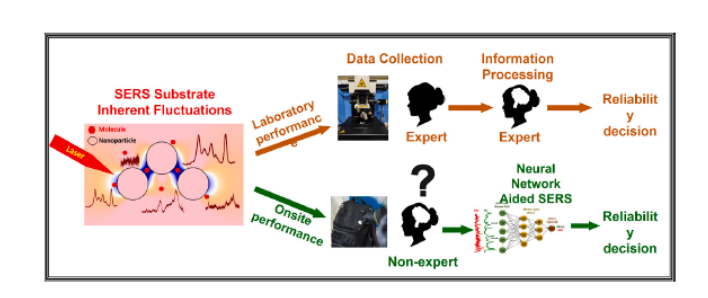
Reshma Beeram, V.S. Vendamani, Venugopal Rao Soma

Advanced Centre of Research in High Energy Materials (ACRHEM), University of Hyderabad, Hyderabad 500046, Telangana, India

HIGHLIGHTS

- We present a neural network-aided SERS model without expert interference.
- We have efficiently identified reliable SERS spectra of trace explosives and a dua.
- The deep learning model has been validated.
- An out-of-sample testing was achieved with an accuracy of 98%.

GRAPHICAL ABSTRACT





Contents lists available at ScienceDirect

Optical Materials

journal homepage: www.elsevier.com/locate/optmat



Research Article

Ultra-trace detection of diverse analyte molecules using femtosecond laser structured Ag—Au alloy substrates and SERRS



Reshma Beeram, Venugopal Rao Soma

Advanced Centre of Research in High Energy Materials (ACRHEM), DRDO Industry Academia – Centre of Excellence (DIA-COE), University of Hyderabad, Hyderabad, 500046, Telangana, India

ABSTRACT

Choosing a wavelength close to the electronic excitation of the analyte molecules is known to enhance the Surface Enhanced Raman Spectroscopy signal further. This technique is often referred to as Surface Enhanced Resonance Raman Spectroscopy (SERRS). Here we use SERRS for sensing different classes of molecules and demonstrate how it can be used for ultra-trace detection. Diverse SERS substrates were fabricated by femtosecond laser ablation of Ag-Au alloy (1:1) in the air by changing the angle of incidence. Further, we have examined the SERRS performance of each substrate. Often in laser ablation in air, the surface debris is considered undesirable. Here we have shown that this debris of nanoparticles can be used as an advantage for ultra-trace detection of different molecules. Further, with the advantage of having randomly stacked nanoparticles in debris and periodic substrates without debris from a single experiment, we have examined the much-debated relationship between enhancement and reproducibility in SERS and found that they are inversely correlated. The sensitivity of the substrate for rhodamine 6G, crystal violet, pieric acid, and cysteine was found to be 10 fM, 100 fM, 100 nM, and 100 nM, respectively, with good reproducibility.

iScience



Article

Wafer-scale silver nanodendrites with homogeneous distribution of gold nanoparticles for biomolecules detection

V.S. Vendamani, ¹ Reshma Beeram, ¹ M.M. Neethish, ² S.V.S. Nageswara Rao, ^{3,4} and S. Venugopal Rao^{1,5,*}

Journal of Alloys and Compounds 959 (2023) 170573



Contents lists available at ScienceDirect



journal homepage: www.elsevier.com/locate/jalcom



MoS₂ nanosheets decorated plasmonic silicon nanowires as SERS substrates for ultra-sensitive multiple analyte detection



V.S. Vendamani, Reshma Beeram, Venugopal Rao Soma *

Advanced Centre for Research in High Energy Materials (ACRHEM), DRDO Industry Academia - Centre of Excellence (DIA-COE), University of Hyderabad,

Flexible Paper Substrate with Silver Dendrites for Trace Detection of Dye and Explosive Molecules using SERS

Reshma Beeram ACRHEM, School of Physics University of Hyderabad V.S. Vendamani ACRHEM, School of Physics University of Hyderabad Soma Venugopal Rao ACRHEM, School of Physics University of Hyderabad

JTu4A.27

Frontiers in Optics + Laser Science (FiO/LS) @ Optica Publishing Group 2022

Sand Dune Like Copper Nanostructures Fabricated by Femtosecond Laser Ablation for Trace Explosive Detection

Reshma Beerama, Dipanjan Baneerjeea, and Soma Venugopal Raoa,

^aAdvanaced Center for Research in High Energy Materials (ACRHEM) University of Hyderabad, Hyderabad 500046, Telangana, India * soma_venu@uohyd.ac.in OR soma_venu@yahoo.com

Abstract: We report the fabrication of cost-effective Cu nanostructured surfaces as potential SERS substrates for the detection of a trace explosive, Tetryl. Novel sand dunes-like nanostructures were achieved by femtosecond laser ablation and cylindrical focusing. © 2022 The Author(s)

CThP5D-04

CLEO-PR2022/ISOM'22/ODF'22

Femtosecond Laser Processed Web-like Silicon Nanostructures and Application in Surface Enhanced Raman Spectroscopy

Reshma Beeram¹, Dipanjan Banerjee¹, A. Mangababu ², Soma Venugopal Rao¹

¹Advanced Centre of Research in High Energy Materials (ACRHEM). ² School of Physics

University of Hyderabad, Hyderabad 500046, Telangana, India.

Author e-mail address: soma_venu@nohyd.ac.in OR soma_venu@yahoo.ac.in

Abstract: Web-like Si nanostructures were fabricated by laser ablation of Silicon in air with a femtosecond laser oscillator. Further, after gold coating, these nanostructures were used for SERS studies with methylene blue as a probe molecule.



Trace level detection of explosives and pesticides using robust, low-cost, free-standing silver nanoparticles decorated porous silicon

V. S. VENDAMANI, RESHMA BEERAM, S. V. S. NAGESWARA RAO, 2,3,4 A. P. PATHAK, AND VENUGOPAL RAO SOMA 1,5,6 (5)

 $^{1} A dvanced\ Centre\ of\ Research\ in\ High\ Energy\ Materials\ (ACRHEM),\ University\ of\ Hyderabad,\ Hyderabad\ 500046,\ India$

² Centre for Advanced Studies in Electronics Science and Technology (CASEST), School of Physics, University of Hyderabad, Hyderabad 500046, Telangana, India

³School of Physics, University of Hyderabad, Hyderabad 500046, Telangana, India

4svnsp@uohyd.ac.in

5 soma_venu@uohyd.ac.in

6 somavenu@gmail.com

STAR Protocols



Volume 4, Issue 1, 17 March 2023, 102068

Protocol

Protocol for designing AuNP-capped Ag dendrites as surface-enhanced Raman scattering sensors for trace molecular detection





Revieu

Recent Trends in SERS-Based Plasmonic Sensors for Disease Diagnostics, Biomolecules Detection, and Machine Learning Techniques

Reshma Beeram, Kameswara Rao Vepa and Venugopal Rao Soma *🗅

 $Advanced\ Centre\ of\ Research\ in\ High\ Energy\ Materials\ (ACRHEM),\ DRDO\ Industry\ Academia—Centre\ of\ Excellence\ (DIA-COE),\ University\ of\ Hyderabad,\ Hyderabad\ 500046,\ Telangana,\ India$

* Correspondence: soma_venu@uohyd.ac.in or soma_venu@yahoo.ac.in

Abstract: Surface-enhanced Raman spectroscopy/scattering (SERS) has evolved into a popular tool for applications in biology and medicine owing to its ease-of-use, non-destructive, and label-freapproach. Advances in plasmonics and instrumentation have enabled the realization of SERS's full potential for the trace detection of biomolecules, disease diagnostics, and monitoring. We provide a brief review on the recent developments in the SERS technique for biosensing applications, with a particular focus on machine learning techniques used for the same. Initially, the article discusses the need for plasmonic sensors in biology and the advantage of SERS over existing techniques. In the later sections, the applications are organized as SERS-based biosensing for disease diagnosis focusing on cancer identification and respiratory diseases, including the recent SARS-CoV-2 detection. We then discuss progress in sensing microorganisms, such as bacteria, with a particular focus on plasmonic sensors for detecting biohazardous materials in view of homeland security. At the end of the article, we focus on machine learning techniques for the (a) identification, (b) classification, and (c) quantification in SERS for biology applications. The review covers the work from 2010 onwards, and the language is simplified to suit the needs of the interdisciplinary audience.

Novel, Hybrid Plasmonic Materials aided with Machine Learning Techniques for SERS based Trace Detection

by Reshma Beeram

Submission date: 26-Jul-2023 11:45AM (UTC+0530)

Submission ID: 2136989230

File name: 18ACPP01_Thesis_Draft.pdf (788.67K)

Word count: 47052

Character count: 255432

Nempopae Rao 26/1/2013

Prof. SOMA VENUGOPAL RAO

DRDO Industry Academic-Centre of Excellence (DIA-COE)

University of Hyderabad Hyderabad-500046. Telangana, INDIA.

Novel, Hybrid Plasmonic Materials aided with Machine Learning Techniques for SERS based Trace Detection

by Reshma Beeram

Indira Gandhi Memorial Library UNIVERSITY OF HYDERABAD

Central University P.O.

Submission date: 26-Jul-2023 11:45AM (UTC+0530)

Submission ID: 2136989230

File name: 18ACPP01_Thesis_Draft.pdf (788.67K)

Word count: 47052

Character count: 255432

Nempopae Rao 26/1/2013

Prof. SOMA VENUGOPAL RAO F.N.A.Sc., F.Inst.P., FRSC

ACRHEM

DRDO Industry Academic-Centre of Excellence (DIA-COE)

University of Hyderabad Hyderabad-500046. Telangana, INDIA.

Novel, Hybrid Plasmonic Materials aided with Machine Learning Techniques for SERS based Trace Detection

ORIGINALITY REPORT

15% SIMILARITY INDEX

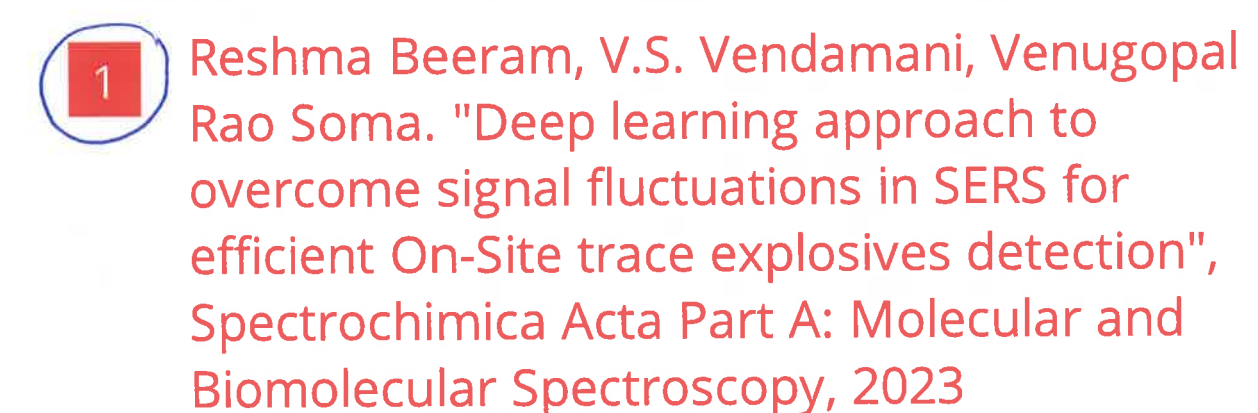
6%
INTERNET SOURCES

13% PUBLICATIONS

3%

STUDENT PAPERS

PRIMARY SOURCES



Publication

Reshma Beeram, Venugopal Rao Soma.
"Ultra-trace detection of diverse analyte
molecules using femtosecond laser structured
Ag-Au alloy substrates and SERRS", Optical
Materials, 2023

Publication



Submitted to University of Hyderabad, Hyderabad

Student Paper

2%

7%



Reshma Beeram, Dipanjan Banerjee,
Lingamurthy N., Venugopal Rao Soma.
"Machine Learning for Rapid Quantification of
Trace Analyte Molecules using SERS and G,

1)-4 of are students own works.
The similarity after removing these is

<10°/.

Evenyopal how 26/7/20

Prof. SOMA VENUGOPAL RAO
F.N.A.Sc., F.Inst.P., FRSC
ACRHEM

DRDO Industry Academic Control of Excellence

DRDO Industry Academic-Centre of Excellence (DIA-COE) University of Hyderabad Hyderabad-500046. Telangana, INDIA.

Flexible Plasmonic Paper Substrates", Analytical Methods, 2022 Publication

Internet Source

	dbileadon				
5	www.ncbi.nlm.nih.gov Internet Source		1 %		
6	V.S. Vendamani, Reshma Beeram, Venugopal Rao Soma. "MoS2 Nanosheets Decorated Plasmonic Silicon Nanowires as SERS Substrates for Ultra-sensitive Multiple Analyte Detection", Journal of Alloys and Compounds, 2023 Publication				
7	Reshma Beeram, Dipan Murthy Narlagiri, Venug "Machine learning for ra trace analyte molecules flexible plasmonic pape Analytical Methods, 202 Publication	gopal Rao Soma. apid quantification of susing SERS and er substrates",	1 %		
8	www.fulviofrisone.com Internet Source		<1%		
9	worldwidescience.org	Nemporallas rol7/2013 Prof. SOMA VENUGOPAL RAO	<1%		
10	www.science.gov Internet Source	F.N.A.Sc., Finst.P, FRSC ACRHEM DRDO Industry Academic-Centre of Excellence (DIA-COE) University of Hyderabad Hyderabad-500046. Telangana, INDIA.	<1%		
11	www.osapublishing.org		<1%		

12	coek.info Internet Source	<1%			
13	V.S. Vendamani, Reshma Beeram, M.M. Neethish, S.V.S. Nageswara Rao, S. Venugopal Rao. "Wafer-scale silver nanodendrites with homogeneous distribution of gold nanoparticles for biomolecules detection", iScience, 2022 Publication				
14	Pilot, Signorini, Durante, Orian, Bhamidipati, Fabris. "A Review on Surface-Enhanced Raman Scattering", Biosensors, 2019 Publication	<1%			
15	hdl.handle.net Internet Source	<1%			
16	"Surface Enhanced Raman Spectroscopy", Wiley, 2010 Publication	<1%			
17	core.ac.uk Internet Source	<1%			
18	lia.scitation.org Internet Source Prof. SOMA VENUGOPAL RAO F N.A.Sc., Finst.P, FRSC ACRHEM	<1%			
19	d-nb.info Internet Source DRDO Industry Academic Centre of Excellence (DIA-COE) University of Hyderabad Hyderabad-500046. Telangana, INDIA.	<1%			
20	V. S. Vendamani, Reshma Beeram, S. V. S. Nageswara Rao, A. P. Pathak, Venugopal Rao	<1%			

